Deep convection processes off the coast of Adélie Land, East Antarctica

Author:
Wong, Ann-Marie May Yi

Publication Date:
2004

DOI:
https://doi.org/10.26190/unsworks/11099

Deep Convection Processes off the Coast of Adélie Land, East Antarctica.

by

ANN-MARIE MAY YI WONG

A thesis submitted for

the degree of Doctor of Philosophy

at The University of New South Wales

June 2004

CERTIFICATE OF ORIGINALITY

I hereby declare that this submission is my own work and to the best of my knowledge it contains no materials previously published or written by another person, nor material which to a substantial extent has been accepted for the award of any other degree or diploma at UNSW or any other educational institution, except where due acknowledgement is made in the thesis. Any contribution made to the research by others, with whom I have worked at UNSW or elsewhere, is explicitly acknowledged in the thesis.

I also declare that the intellectual content of this thesis is the product of my own work, except to the extent that assistance from others in the project's design and conception or in style, presentation and linguistic expression is acknowledged.

Ann-Marie M Wong

To my parents

Acknowledgements

I would like to thank Jason Middleton for his guidance and supervision, Mark Baird and Matthew England for their advice, Rob Massom for the sea-ice images, Rick Smith for the GEBCO data, and Nathan Bindoff for access to unpublished work. APAC for the time on the computers for my numerous runs and the staff for all there assistance.

The constant support of my family, Pat for taking me out climbing, Yoong for providing me with lots of energy food, the emails from Joe, John and Ying encouraging me to finish up and visit them (at their expense) overseas, and Shim for hiking up the stairs to my office and being a great little sister.

I would like to thank my friends who have always been good company, Eric and Kylea for the home cooked dinners, Simon and Kylie for the coffee breaks, Frank for the afternoon tea breaks, Van and Trung for the African Violets which are just flowering as I finish writing up, Paul and Glenn for the entertaining telephone calls, Lili for always being around to chat to and Franca for always making me laugh. I'd especially like to thank Simon and Paul who went beyond the call of friendship and spent hours proof reading my work.

Last, but not least, I'd like to thank Andrew for being there for me.

Abstract

The East Antarctic region between 140 and 146°E, sometimes referred to as Adélie Land, Wilkes Land or George V Coast is believed to produce a substantial amount of deep convection, including Antarctic Bottom Water (AABW). This region is characterised by the Adélie Depression, a shallow sill at the shelf break, a channel connecting the shelf to the slope and canyons in the slope. The Mertz polynya above the Adélie Depression facilitates the atmospheric forcing required for the formation of dense water.

The bottom water that is produced in the Adélie Land region has a distinctive cold fresh signal that allows it to be distinguished from the Ross Sea Bottom Water formed farther to the east and found flowing westward along the continental slope rise. Previously known sources of AABW, the Weddell and Ross Seas, are characterised by wide shelves and western boundaries which allow the recirculation of water on the shelf allowing it to become dense enough to form Shelf Water (SW). This SW is an important constituent of bottom water.

A series of numerical studies reported here incorporates the depression, sill and channel in the Adélie Land region, and describes for the first time the role of these features in modifying circulation and AABW formation. It is shown that the depression acts to trap dense water beneath the Mertz polynya so that it is resident beneath this forcing region for a longer period. The sill at the shelf break acts to reduce cross-shelf buoyancy fluxes by preventing dense water from flowing from the shelf onto the slope and reducing the transport of less dense water found offshore onto the shelf. The channel through the sill at the shelf break provides a pathway to allow dense water to flow onto the slope.

The results of the numerical simulations agree with a range of observations from the Adélie Land region during winter and summer. The numerical simulations were

able to reproduce the observation that the densest water on the shelf is present in the depression and that this water is younger than the water immediately above it. The numerical simulations also reproduce the observations of the production of dense water in this region, its transport off the shelf through the channel and its westward movement along the slope.

Contents

Chapter 1

Introduction

The world's oceans play a major role in regulating the climate; they are an important heat and carbon dioxide sink. Antarctic Bottom Water (AABW) drives a conveyor belt (Figure 1.1), that takes carbon dioxide and heat out of the atmosphere and transfers it to the deep ocean where it is stored for hundreds of years before it comes to the surface again (Broecker, 1991). This conveyor is responsible for bringing heat to the higher latitudes moderating heat at higher latitudes. Temporary shutdown of the conveyor was possibly responsible for about a millenium of very cold conditions known as the Younger Dryas (Broecker, Sutherland, and Peng, 1999).

All around Antarctica the cold shelf waters are made saltier and denser by the injection of brine into the water column as sea-ice is produced. These dense shelf waters flow off the continental shelf and down the continental slope by their greater density in plumes. AABW is the name given to those water masses that are sufficiently dense that they reach the abyssal plains. If AABW is defined as the body of water denser than the Circumpolar Deep Water (CDW) of the Antarctic Circumpolar Current (ACC), i.e., with a neutral density $\gamma^n \geq 28.27$, then $\sim$3.5% of the world ocean's volume can be classified

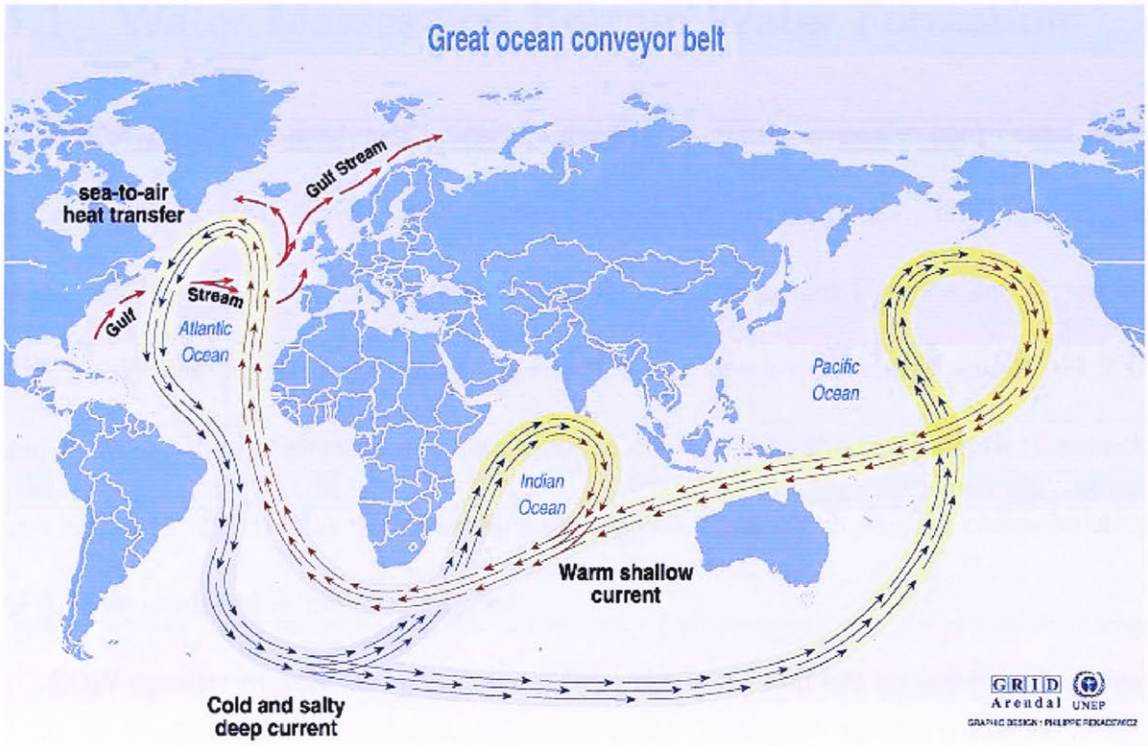

Figure 1.1: *The great ocean conveyor logo from Broecker (1991).*

as AABW (Orsi, Johnson, and Bullister, 1999). The major sources of AABW are the Weddell Sea, the Ross Sea and the region off Adélie Land (also referred to as Wilkes Land and George V Coast). Bottom water formed in each region has a characteristic signature that distinguishes it from bottom water formed in others. Weddell Sea Bottom Water (WSBW) is characterised by water with potential temperature less than $-0.7°C$ and a salinity range of $34.63 - 34.64$ psu (Carmack and Foster, 1975). Ross Sea Bottom Water (RSBW) is the most saline due to the highly saline shelf water produced in the Ross Sea. The salinity of RSBW is greater than 34.7 psu and is only found in the Southwest Pacific Basin (Rintoul, 1998). AABW formed off the coast of the Adélie Land region has a temperature of $-0.7°C$ and a salinity of 34.560 psu (Gordon, 1974, Table 1). Adélie Land Bottom Water (ALBW) is somewhat colder and fresher than RSBW and contributes to the bottom waters found in the Australian-Antarctic Basin (Rintoul, 1998).

1.1 Water Masses and Bottom Water Formation

Shelf Water (SW) is produced by the freezing of sea water over the continental shelf to form sea-ice which leaves behind dense brine in the waters below. The high oxygen levels of SW indicate that the water was recently near the surface (Gordon and Tchernia, 1972). SW has high salinity values around 34.6 psu, low temperatures around $-1.9°C$ and is denser than offshore water masses when compared at the same depth (Carmack and Killworth, 1978). SW varies in different regions, resulting in varying characteristics of AABW produced in different regions.

CDW consists of deep waters advected from the north and has an upper and a lower layer. Upper CDW has an oxygen minimum resulting from deep waters of the Pacific and Indian Oceans and Lower CDW has a salinity maximum derived from the North Atlantic Deep Water (Whitworth, Orsi, Kim, and Nowlin, 1998). CDW is carried around the continent by the Antarctic Circumpolar Current beneath the Antarctic Surface Water and above AABW, and is found up to 100 km north of the continental slope depending on how far north the slope is situated. It is characterised by warm temperatures above $0°C$, high salinities $\sim$34.68 psu and low oxygen levels (Foster and Middleton, 1987).

As SW moves offshore over the shelf break it mixes with the CDW to form Modified Circumpolar Deep Water (MCDW). MCDW is denser than any linear combination of SW and CDW due to the non-linearity of the equation of state (Foster and Carmack, 1976) known as the thermobaric effect. Typically it has a temperature of $-0.7°C$ and a salinity range of $34.5 - 34.6$ psu (Foster and Middleton, 1987). MCDW can be found intruding onto the shelf to mix with SW. This water mass flows down the continental slope entraining CDW found adjacent to the slope between 600 and 1,800 m (Carmack and Foster, 1975). The entrainment of CDW is important in the mass flux increase

(Carmack and Killworth, 1978).

As the MCDW moves down the slope it entrains more CDW, and if the mixture reaches the same density as the surrounding water before it reaches the bottom then it leaves the slope. If the water is dense enough to reach the bottom it forms AABW.

Estimates of AABW formation rates are of the order of 10 Sv (1 Sv = 10^6 m^3 s^{-1}). Orsi et al. (1999) estimate 8−12 Sv of AABW production and report estimates of AABW formation ranging from 5 (Carmack, 1977) to 15 Sv (Gill, 1973). The discrepancies between the various estimates of bottom water formation can be attributed to (Hellmer and Beckmann, 2001):

- the temporal variability over which bottom water formation occurs;
- the undetected sources and spreading paths around Antarctica;
- uncertain techniques using various tracers such as chloroflurocarbons (CFC-11), phosphate star (PO_4^*) and radiocarbon (C-14); and
- a lack of a common definition of water masses.

The direct measurement of AABW formation rates is difficult because of the distribution of sources along 18,000 km of remote Antarctic coastline which is often inaccessible due to ice coverage (Orsi, Jacobs, Gordon, and Visbeck, 2001).

The major sources of AABW are the Weddell Sea, the Ross Sea and the Adélie Land region and observations of downslope flows are limited to a small number of regions (Baines and Condie, 1998). The Weddell Sea produces 60 − 70% of the total volume of bottom water formed (Orsi et al., 1999; Rintoul, 1998; Hellmer and Beckmann, 2001). In the past, the Ross Sea was believed to be the second largest source of AABW. This conclusion was in error as much of the bottom water formed in the Adélie Land region

was attributed to the Ross Sea. Reanalysis of the data by Rintoul (1998) attributes a larger volume to the Adélie Land region, making ALBW the second largest source of AABW. He attributes 66% of bottom water formation to the Weddell Sea, 25% to the Adélie-Wilkes Land region and 7% to the Ross Sea. Using the AABW formation rate of $8-12$ Sv (Orsi et al., 1999), $2-3$ Sv of AABW is formed in the Adélie Land region. Most of the bottom water in the Australian-Antarctic basin is formed on the Adélie Coast. West of 143°E low salinity ALBW flows beneath the high salinity RSBW (Gordon, 1974) and is able to erode the deep salinity maximum signal of RSBW (Rintoul, 1998).

1.2 Numerical Modelling of AABW Formation

Numerical modelling has been used since the 1970s to study the physical processes that drive the ocean (Böning and Semtner, 2001). AABW plays an important part in driving the thermohaline circulation in the oceans and must therefore be included in ocean general circulation models. Some models are diagnostic models which restore temperature and salinity towards observations and do not "form" bottom water, but in order to model global climate the ventilation process of the world's oceans must be represented realistically (England, 1992).

The Fine Resolution Antarctic Model (FRAM) modelled the circumpolar region around Antarctica from 24°S to 79°S, concentrating mainly on the dynamics of the ACC. The model resolves the eddies of the ACC with a resolution of 1/4° latitude by 1/2° longitude and 32 z-level co-ordinates in the vertical, the resolution at the surface is 21 m and at the bottom is 233 m. The model is relaxed to Levitus data for the first 6 years and is then run without relaxation (The FRAM Group, 1991). Good agreement is found between the distribution of kinetic energy in the model and observations (Stevens

and Killworth, 1992). The transport, heat and salt fluxes from the model are found to be generally realistic (Saunders and Thompson, 1993), and the circulation from the FRAM results show many features of the Southern Ocean circulation (Stevens and Stevens, 1999).

Goosse, Campin, and Tartinville (2001) studied the sources of AABW in a z-level ice-ocean model. In a z-level model the production of AABW by the export of dense shelf waters is sensitive to the effect of downsloping parameterisation, i.e., the movement of water from a shallower region to a deeper one. They concluded that open ocean convection is generally overestimated in global models.

A terrain-following model with the ability to model the advection and diffusion of bottom water water was configured by Beckmann, Hellmer, and Timmermann (1999) to investigate the large scale structure of the Weddell Gyre. The model is circumpolar from 50°S to 82°S, and the highest resolution is found in the Weddell Sea sector (20 km) and includes major ice shelves. The study showed that shallow shelf areas near the Filchner-Ronne Ice Shelf are important in the production of bottom water.

Many coupled sea-ice ocean models only consider the upper layers of the ocean and can be used to delineate oceanic heat fluxes and their effect on the sea-ice. Some coupled models use a full three dimensional terrain-following model. For example, Häkkinen (1995) uses a full three-dimensional terrain-following circumpolar model with a coarse resolution that did not resolves eddies. Nonetheless, the model did show the realistic production of 12 Sv of AABW in the Weddell Sea and 5 Sv in the Ross Sea. Marsland and Wolff (1998) configured a circumpolar coupled model with high resolution (the same as FRAM) in the East Antarctic between 120 and 140°E to study the seasonal variability of oceanic heat fluxes and its effect on the ice. Nøst and Foldvik (1994) modelled the

circulation under the Filchner-Ronne and Ross Ice Shelves and concluded that Ice Shelf Water is formed from the interaction of the Western Shelf Water with the ice shelves.

Most modelling studies around Antarctica have been configured as circumpolar models. FRAM had 1/2° longitude resolution all around Antarctica while some other models concentrated resolution in selected areas (e.g., the Weddell Sea) but the resolution was still only ~25 km (Beckmann et al., 1999). In global ocean modelling dense water formation often happens through open ocean convection (Stössel and Kim, 1998). Higher resolution modelling of dense water formation is done through a more idealised approach. These models are discussed further in Section 3.7.

1.3 AABW in the Adélie Land region

Gordon and Tchernia (1972) and Gordon (1974) identified the Adélie Land region as a source of AABW, observing that the water in the Adélie Depression having $T \simeq -1.9$°C and $S \simeq 34.6 - 34.7$ psu was dense enough to combine with upper CDW to form AABW. Further evidence of bottom water formation in this region was the increase in oxygen levels and decrease in salinity of the bottom water from the Ross Sea travelling west along the continental rise.

An anomalous water mass of low salinity, low temperature and higher oxygen lies west of the Ross Sea, offshore of the Adélie coast. Carmack and Killworth (1978) suggested that this water could be formed from a mixture of shelf water in the Adélie Depression and the CDW, but that the mixture was not always dense enough to form bottom water. The range of depths of neutral buoyancy calculated using a range of buoyancy and mixing parameters is $1,300 - 2,500$ m. This is consistent with the depths where the anomalous water has been observed.

Foster (1995) observed anomalous water masses distinct from RSBW between 147 and 162°E. This region lies north-east of the Adélie Depression, and as the slope current is westward, the source of the anomalous water is probably east of the Adélie Depression, possibly the Cook Depression. Model estimates from the geochemical data suggest that there is $0.2 - 0.4$ Sv of subsurface water exchanged offshore over the shelf break.

(Whitworth, 2002) proposed two modes of bottom water in the Australian-Antarctic basin. One mode of water is fresher than the other by about 0.02 psu when compared at the same temperature. This anomaly is likely to be due to a variability of the Adélie Coast source waters.

Observations of bottom water in the South Indian Basin to the north west of the Adélie Land region suggest that this water is a mixture of RSBW and ALBW (Speer and Forbes, 1994). The Kerguelen Plateau forms the western boundary of the South Indian Basin, and to the south of the plateau lies the Princess Elizabeth Trough which separates the plateau from Antarctica. Hydrographic sections along the eastern flank of the Kerguelen Plateau indicate a northward near-bottom transport of 6 Sv. This northward near-bottom transport includes the flow of the bottom water along the plateau and the water that is entrained by this flow, implying that this is an upper limit to the amount of bottom water formed in this region. If Speer's (1994, Figure 5) mixture comprising of 2 parts ALBW to 1 part RSBW makes up the bottom water observed here, then it is estimated that up to 4 Sv of ALBW is formed.

In Baines and Condie's (1998) review of observations on the Antarctic shelves they identified active downslope flow at a cross-shelf section at 140°E in the Adélie Land region. This means that dense water must be forming somewhere on the shelf near 140°E. East of 140°E in the Adélie Land region they identified passive downslope flow,

i.e., sections which showed evidence of downslope flow at some other time or within the local region.

The presence of a 'V' shaped Antarctic Slope Front between 140 and 150°E is indicative of bottom water formation (Gill, 1973; Jacobs, 1991; Whitworth et al., 1998; Bindoff, Rosenberg, and Warner, 2000b). As the ALBW moves westward along the continental rise, it becomes warmer and fresher. At 150°E, RSBW is observed, while 10° to the west at 140°E, the RSBW is replaced by colder and fresher ALBW on the continental rise.

1.4 Objectives

To date there have been no high resolution numerical studies of circulation and deep water production in the Adélie Land region. The resolution of circumpolar models has been too coarse to resolve the topographic features in this region. Regional models of the Weddell Sea have been configured but the key topographic features of this region are quite different from those of the Adélie Land region.

It is clear that there are significant questions which remain to be answered concerning dense water production on the Antarctic continental shelves. The objectives in this study are to examine the effects on deep water production of

- size of forcing region and the strength of the forcing,
- topography including depression, sill and channel,
- wind, including steady uniform wind, pulsating wind and a wind stress curl.

This present study configures a high resolution model which includes the key topographic features of the Adélie Land region. The results of the numerical simulations are

compared with observations from the region to answer the objectives listed above. Chapter 2 is a review of the literature related to conditions in the Adélie Land region which may affect the production of AABW. Chapter 3 describes the theory of the processes involved in the production of dense water. Chapters 4 through 6 describe the results from the process studies. Chapter 7 compares the results from the numerical simulations to observations in the Adélie Land region and Chapter 8 discusses the findings from this study.

Chapter 2

The Adélie Land Region

The region between 66 and 67°S, and from 136°20' to 142°20'E is referred to as the Adélie Coast. It is situated within Wilkes Land, the coastal region of East Antarctica between 102° and 142°20'E. To the east of this region lies the George V Coast which is also relevant to this study. The principal region of interest of the studies in this thesis is from 140° to 147°E and for simplicity is referred to here as the Adélie Land region.

2.1 Bathymetry

Much of the coastal ocean off the Wilkes Land region is permanently covered in sea-ice, and as a result the bathymetry in not well mapped. Of the data sets available for this region, the GEBCO97 bathymetry is believed to be the most reliable, and is shown here in Figure 2.1. As with most shallow regions near the coast, global ocean data sets determined by satellite atlimetry eg., Smith and Sandwell (1997) are not as reliable in shallower regions near the coast. It was found that topographic features that were present in the Smith and Sandwell (1997) were not observed (*V Lytle - personal comm*) and that the GEBCO97 dataset was more relibable.

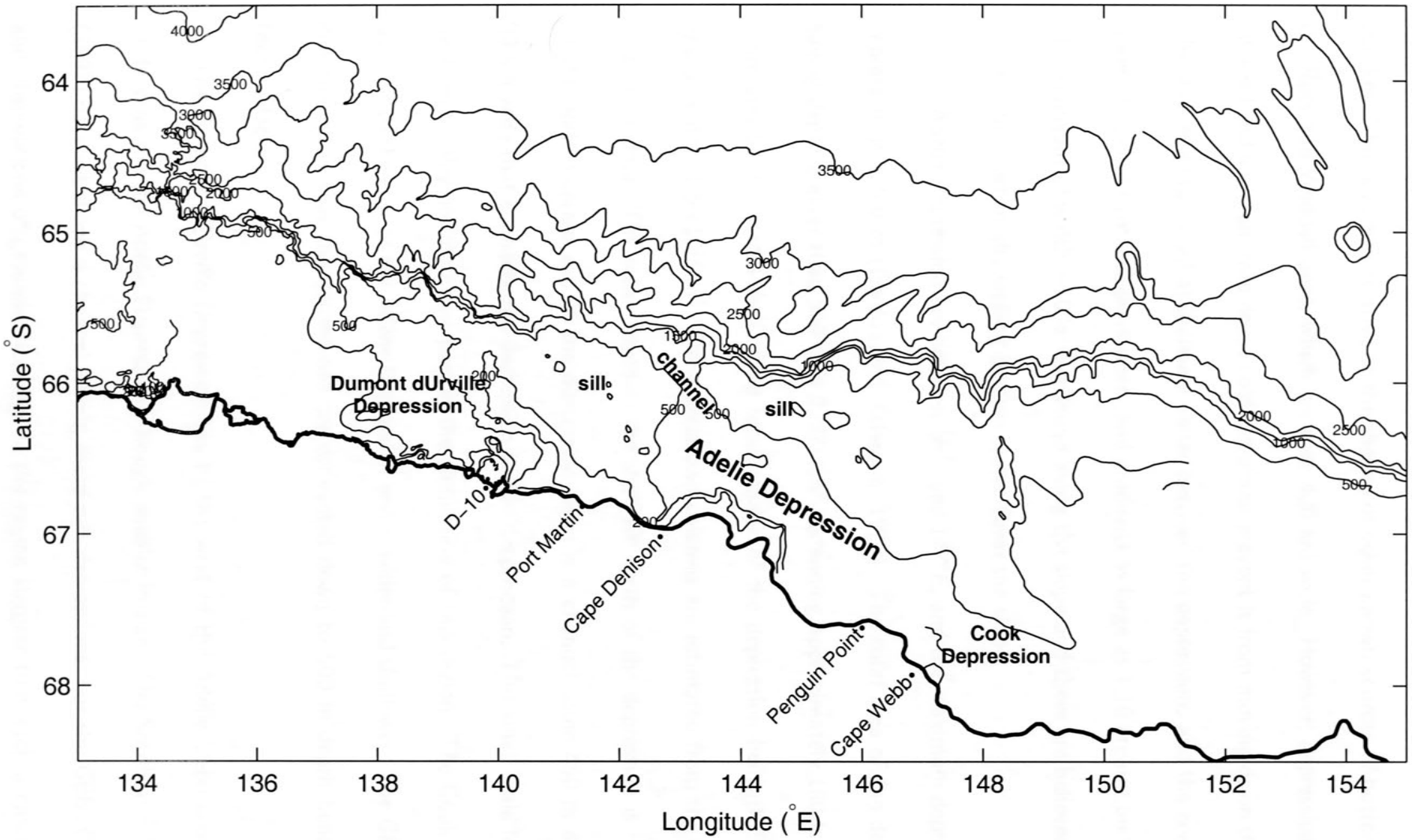

Figure 2.1: *GEBCO97 data for Wilkes Land, Antarctica with depth contours expressed in metres. Automatic Weather Station (AWS) locations are labeled. The Mertz Glacier lies between Cape Denison and Penguin Point.*

The continental shelf is typically 500 m deep and varies in width between 100 and 200 km. This is narrow relative to the shelves of other known sources of bottom water, the Ross and Weddell Seas, which are over 400 km wide. However, depressions in the Wilkes Land shelf can trap dense cold water and prevent it from moving down the slope. The shelf edge has a sill of shallower water between the depressions and the continental slope. The continental slope is steep, and gradients as large as 1:10 are not uncommon. Many canyons of width $\sim$10 km are found along the slope and these are believed to play a significant part in channelling bottom water down the slope.

The Adélie Depression lies between 142° and 147°E, and the maximum depth of this depression is 1,300 m (Gordon and Tchernia, 1972). The total area of the depression having depth greater than 500 m is 9,000 km^2, extending approximately 180 km alongshore and 50 km across-shelf. The total volume of the depression beneath 500 m is approximately 1.5×10^{12} m^3. These areas and volumes are estimated from the digitised GEBCO97 data. The mean depth of the shelf sill north of the depression is $\sim$250 m. At the north western end of the depression there is a channel some 450 m deep and 20 km wide that connects the depression to the deep ocean. This small scale feature is believed to play an important part in the circulation of this region. The Cook Depression lies to the east of the Adélie Depression and is wider and shallower. The GEBCO97 contours show that the depressions are connected down to 500 m depth beneath the Mertz Glacier.

The Dumont d'Urville Depression lies to the west of the Adélie Depression and is as deep as the the Adélie Depression, though smaller in size. The Smith and Sandwell (1997) data set shows a channel joining these two depressions, but the GEBCO97 data and observations of grounded icebergs in the region suggest that such a channel may

not exist (*V Lytle – personal communication*).

The Mertz and Ninnis Glaciers protrude some 100 km north from the Antarctic coast at 145° and 147°E respectively. The Mertz Glacier lies over the eastern end of the Adélie Depression. Grounded icebergs extend the Mertz Glacier by up to 160 km offshore, and comprise the feature labeled as the "Finger" in Figure 2.3 from Massom, Hill, Lytle, Worby, Paget, and Allison (2001). The region of open water to the west of the Mertz Glacier is generally referred to as the Mertz polynya. The Ninnis Glacier protrudes into the Cook Depression and modifies the circulation to create a polynya on the western side. This polynya is smaller and not as persistent as the Mertz polynya (Potter, 1995) which has been reported as being ice-free for most of winter.

2.2 Wind

Katabatic winds are density currents that drain cold air off the continent. They are topographically modified and converge in valleys along the coast. Once these winds reach the coast, they turn left due to the Coriolis force and blow alongshore to the west, forming the East Wind Drift close to the coast. Offshore wind measurements are scarce and offshore wind circulation has been obtained for this study from models by Parish and Wendler (1991) and Davis and McNider (1997). The Adélie Land region and adjacent coast are strongly impacted by these winds.

The winds in this region are strongly time-dependent, as a result of the intermittent surges of cold air draining from the interior (Parish and Bromwich, 1987). The monthly averaged temperatures and wind speeds for Cape Denison are plotted in Figure 2.2. Colder temperatures in winter lead to stronger temperature inversions and a greater katabatic flow (Wendler, Stearns, Weidner, Darguad, and Parish, 1997). During winter

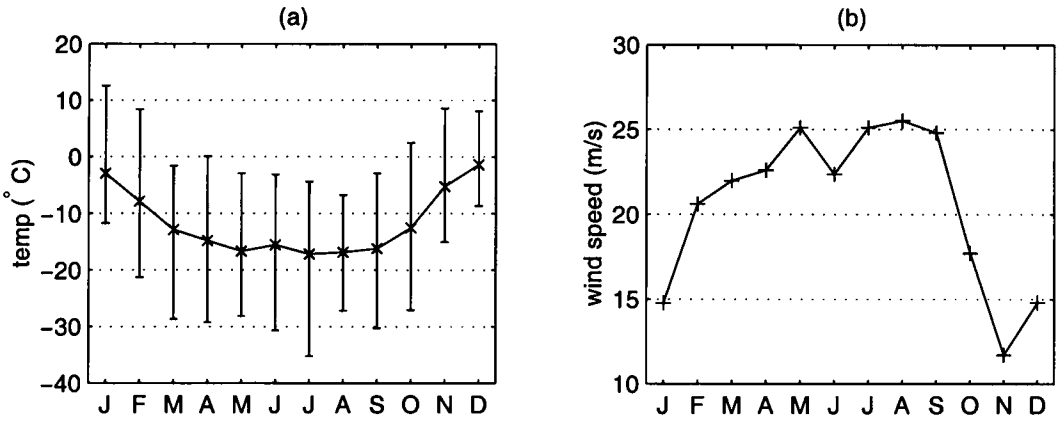

Figure 2.2: *(a) Mean monthly temperature data for Cape Denison (67.0°S, 142.7°E, 31 m above sea level) from Jan 1990 to Dec 1995, with bars showing the temperature range for each month, and (b) mean monthly wind speeds.*

the wind speeds are higher in the confluence zone of the katabatic wind. The wind speeds measured from the Automatic Weather Station (AWS) at D10 and Dumont d'Urville which are outside the confluence zone are half those in the jet. During the summer months of December and January the wind speeds are nearly the same for all the coastal AWSs.

The position of the AWSs are shown in Figure 2.1. Cape Denison and Port Martin are in the 150 km confluence zone of the katabatic winds. The monthly averaged wind speeds for Cape Denison from 1990 – 1995 are plotted in Figure 2.2b. These are the strongest winds observed close to sea level (Wendler et al., 1997) with an annual mean of 19 m s^{-1}. The average offshore wind velocity component is 12 m s^{-1} (Parish and Wendler, 1991). The highest monthly average wind speed recorded was 29 m s^{-1} at Port Martin in March 1951.

The direction of the wind is remarkably constant. At Cape Denison, the directional constancy of the wind is 0.97 (a directional constancy of 1.0 implies that the wind never changes direction) and the wind direction is ~20° to the left of the fall line. The other coastal AWS also show a high level of constancy (0.90). This suggests that the

wind regime is controlled by topographic steering. Streamlines from the Parish and Wendler (1991) model show the confluence zone at Cape Denison and Port Martin and a secondary confluence zone at Penguin Point.

Typically, katabatic winds extend $10 - 20$ km offshore before they die out, but in the confluence zone they are believed to extend $20 - 30$ km offshore (Bindoff, Williams, and Allison, 2001). However the region of influence of these winds on the ice is much greater, and areas of reduced ice concentration extend over 100 km offshore during winter (Adolphs and Wendler, 1995). Measurements from Dumont d'Urville which is situated on an island 5 km from the mainland are more easterly and have a lower constancy than those at D10 (inland). This is due to winds being affected by the Coriolis force and by synoptic weather processes as they move offshore. Low-pressure synoptic systems appear to pass through the region every $3 - 7$ days (Worby, Bindoff, Lytle, Allison, and Massom, 1996). The inertial period in this region is 13 hours resulting in reasonably quick geostrophic adjustment of the winds.

2.3 Glaciers, Ice Shelves and Sea Ice

The formation of sea-ice is one of the most important processes involved in AABW formation. When sea-ice forms, the sea surface temperature is reduced to $-1.8°C$, and salt is excluded from the ice to form a cold brine in the waters below. For bottom water formation to occur, the shelf water salinity must be greater than 34.63 psu (Cavalieri and Martin, 1985). Toggweiller and Samuels (1995) estimate that it takes approximately five years for shelf water to become cold and salty enough to contribute to AABW formation. The salinity enrichment of Shelf Water (SW) due to ice formation is small in comparison to the salinity contribution from Circumpolar Deep Water (CDW) but it is still a critical

part of the process. The high salinity of AABW is also due in part to the salty CDW that combines with the shelf water to form AABW. This process is described in more detail in Section 2.5.

An estimate of the salt flux in the East Antarctic region due to sea-ice formation (including ridging) between 60°E and 150°E is 9.41×10^{13} kg per year arising from the formation of 1.91×10^{12} m^3 of ice (Worby, Massom, Allison, Lytle, and Heil, 1998). Sea ice is formed around the coast of Antarctica during the winter which lasts 240 days from February until September (Zwally, Comiso, and Gordon, 1985; Worby et al., 1998). As the sea-ice becomes attached to the continent it becomes fast ice and can extend 100 km or more offsore (Massom - personal communication). The temperature difference between the ocean and atmosphere is 20°C, providing a heat flux of $\sim$500 W m^{-2} (Worby et al., 1998) where the air is in contact with the open ocean. The ice acts as an insulator between the ocean and atmosphere, with insulation increasing as the sea-ice thickens. On average, the heat flux through the sea-ice is $\sim$15 W m^{-2}.

Ice shelves and glaciers can "supercool" the shelf waters to below the surface freezing point. The freezing point of sea water decreases with increased pressure and salinity (Gill, 1982, p 602). The fast ice can lower the temperature to below -2.0°C, but the "warmer" shelf water can simultaneously melt the fast ice that is formed from the sea-ice. This results in a colder and fresher water mass, which is less dense.

2.4 Polynyas and Leads

Polynyas and leads are localised regions of open water within the ice. These areas have high rates of ice formation because of the more rapid heat loss to the atmosphere. Gill (1973) estimates that up to 10 m of ice per year are formed in polynyas. This is ten

times more than the surrounding ice-covered areas. More recent estimates of annual ice formation by Allison (*personal communication*) are $\sim$ 8 m of ice formation in polynya regions and 1.1 m in the surrounding ice covered areas. Ice growth rates in the first few days of ice formation of 8 cm day^{-1} with average salinity of 10 psu have been measured by Lytle, Worby, Massom, Paget, Allison, Wu, and Roberts (2001) in the Mertz Glacier polynya. Roberts, Allison, and Lytle (2001) have calculated ice formation rates as high as 25 cm day^{-1} in areas of high wind speeds near the coast. These higher rates of ice formation in areas of high wind speeds are due to the removal of ice which maintains the polynya which in turn results in the high rate of ice formation.

Latent-heat polynyas are maintained by wind and ocean currents moving ice away from a region. Sensible-heat polynyas are kept open by the upwelling of warm water which melts the ice and prevents further ice formation (Massom, Harris, Michael, and Potter, 1998) as well as adding fresh water and lowering the salinity of the surface waters in the region. Latent-heat polynyas are generally found near the coast over the continental shelf. They have a larger impact on the AABW formation than sensible heat polynyas found over deeper waters.

The distinction between latent and sensible heat polynyas is not as absolute as often assumed (Rintoul, 1998). The Mertz polynya has both latent and sensible polynya properties. The properties of the Mertz polynya associated with latent heat polynyas are the persistence of the polynya due to the strong katabatic winds and the advection of ice out of the polynya due to the East Wind Drift. The sensible heat properties of the polynya are reflected by the fact that the offshore extent of the polynya is $70 - 80$ km beyond the offshore extent of the wind, and that this part of the coastline becomes ice-free first in spring.

In the Wilkes Land region, Cavalieri and Martin (1985) found that the size of a polynya is associated with the synoptic winds. Temperature increases associated with the synoptic forcing melt the thin ice in the polynyas. At Casey (66°S, 110°E) the size of polynyas varies on a $5-6$ day period, consistent with synoptic variability in this area. Ice drift measurements in relation to the wind are $2-2.5\%$ of the wind speed, at an angle 15° to the left of the wind (Worby et al., 1996).

Large persistent polynyas are associated with strong constant winds and coastal protrusions. Stronger winds advects sea ice away faster, increasing the size of the polynya while colder temperatures increase the rate of ice formation reducing the size of a polynya. Under fairly constant meteorological conditions, the size of a polynya tends to remain constant as the advection of sea ice away from the polynya is balanced by the production rate of sea ice (Pease, 1987). The winds at the Adélie Coast are strong and constant whereas the winds at George V Coast are localised and intermittent. Correspondingly the Mertz polynya near the Adélie Coast is more persistent than the polynya at the George V Coast.

Figure 2.3 is an AVHRR image of the Mertz polynya region. The regions of thinnest ice (labelled A) are adjacent to the coast in the vicinity of the katabatic winds. The black arrows in the north east of the image show the westward advection of thick multi-year ice due to the East Wind Drift. The Mertz Glacier tongue and the grounded icebergs, which extend the Mertz Glacier protrusion another 100 km offshore to form a feature known as the "Finger", block the continuous advection of ice from the east and thereby create a polynya. This coastal protrusion forms the eastern boundary of the Mertz polynya. The south western boundary of the polynya is the fast ice extending $90-120$ km out from the coast east of Dumont d'Urville. The northern boundary is formed from multi-

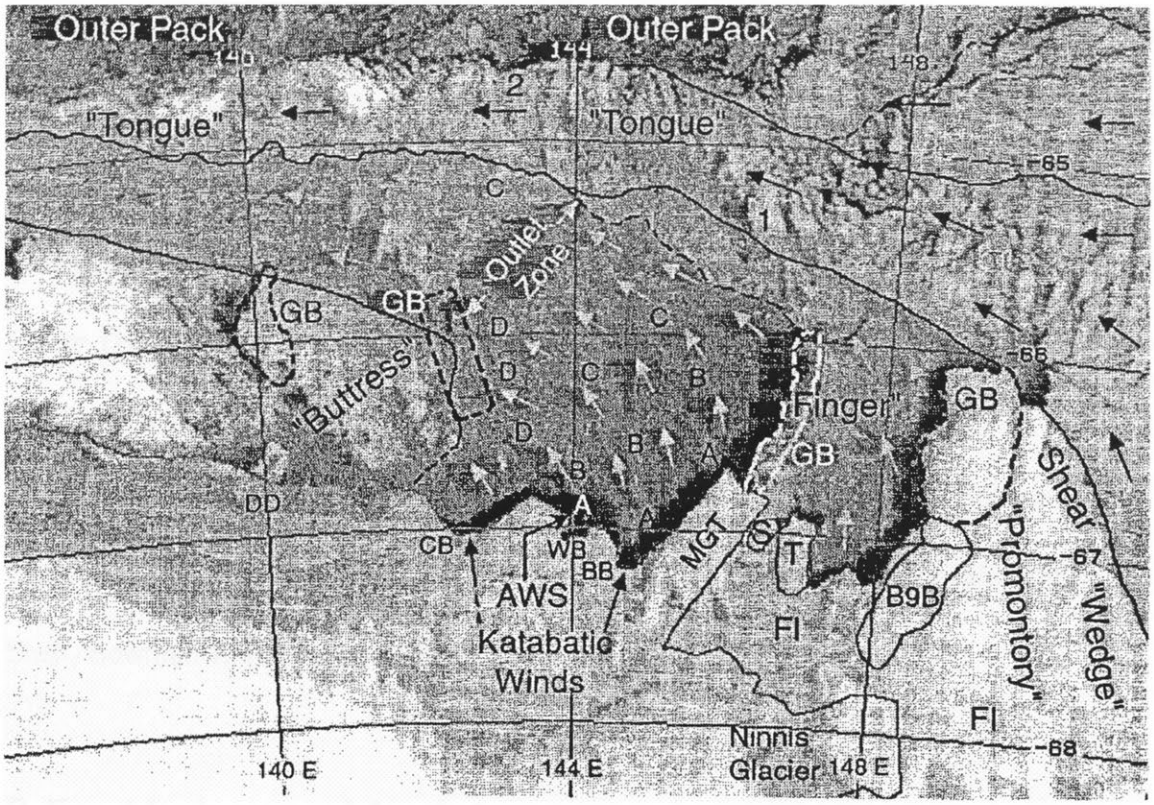

Figure 2.3: *An AVHRR image from June 14, 1999 (16:57 UTC) from Massom et al. (2001). DD = Dumont d'Urville, CB = Commonwealth Bay, WB = Watt Bay, BB = Buchanan Bay, MGT = Mertz Glacier tongue, GB, S, T = grounded icebergs, FI = fast ice. A–D is the ice thickness (A is the thinnest where the core of the Mertz polynya is located). Light arrows denote the large scale drift of new ice (dark arrows for the multi-year ice).*

year ice floes, following the 3,000 m isobath. These features are labeled the "Buttress" and "Tongue" in Figure 2.3, respectively. The removal of ice formed in this polynya is confined to the passageway to the north west (Massom et al., 1998). This passageway occasionally gets blocked and the passageway back fills.

The averaged size of the Mertz polynya is 23,000 km^2 based on a maximum ice concentration of 75% (Massom et al., 1998), ranging in size from 15,346 km^2 to 30,275 km^2. This polynya has a core with a lower concentration of ice $< 65\%$ which is a small fraction of the polynya size (Figure 3 in Massom et al., 1998). The maximum extent of the polynya occurs during October, when it can grow to a size of 60,000 km^2. It then extends from Commonwealth Bay to the tip of the "Finger".

Polynyas are regions of high rates of ice formation. The Mertz polynya has the highest rate of ice production in East Antarctica (Cavalieri and Martin, 1985). Polynyas are also regions of large momentum fluxes due to the wind. Both the high rate of ice production and the high momentum fluxes are required to produce High Salinity Shelf Water (HSSW) according to Grumbine (1991). Temperature fluxes are important to the formation of ice but only make a small contribution to the buoyancy flux and can be neglected. Cavalieri and Martin (1985) concluded that the only regions in Wilkes Land capable of forming HSSW are the Mertz Glacier tongue and the Shackleton Ice Shelf/Bowman Island Region to the west.

2.5 Hydrographic data

ALBW is a mix of various water masses found in the Adélie Land region. North Atlantic Deep Water moves south and eventually circulates around the Antarctic continent as Circumpolar Deep Water (CDW). It has a warm core of $0.5 - 1.0°C$, is high in salinity, approximately 34.7 psu, and low in oxygen (Foster, 1995). The warm core of CDW is found at a depth of 500 m is located $20 - 100$ km offshore of the shelf break. CDW is found beneath the Antarctic Surface Water and above the cold dense waters flowing off the Antarctic shelf.

Sharp temperature and salinity gradients exist between the Antarctic Surface Water and the CDW. Where the thermocline and halocline separating the water masses drops sharply towards the slope is referred to as the Antarctic Slope Front (Whitworth et al., 1998). Associated with the Antarctic Slope Front is a westward flow relative to 1000 m depth.

Modified Circumpolar Deep Water (MCDW) is a mixture of shelf water and CDW.

This water mass is warm and saline relative to the SW. Strong intrusions of MCDW warmer than 0.5°C are observed as far as 50 km inshore of the shelf break near 143°E where there is a channel through the sill into the Adélie Depression, but MCDW is not found to the east and the west of the depression. The MCDW signal is stronger west of 150°E, perhaps due to the shelf being further north (Rintoul, 1998).

The densest water reported by Gordon and Tchernia (1972) on the Adélie shelf in summer (January to February 1969) had properties of $T = -1.9$°C and $S = 34.6 - 34.7$ psu, and was found in the Adélie Depression. Later Bindoff et al. (2001) sampled the water beneath the Mertz polynya during winter (July to September 1999) and identified four water masses:

- Highly Modified Circumpolar Deep Water (HMCDW), found intruding above the shelf sill. This water mass has $T > -1.88$°C, has low salinity, is oxygen poor and has potential density $\sigma_\theta < 27.88$ kg m^{-3};

- Ice Shelf Water (ISW), which is "super-cooled" to $T < -2.0$°C, $\sigma_\theta < 27.88$ kg m^{-3} and contains melt water from the ice shelves;

- High Salinity Shelf Water (HSSW), which is located in the depression beneath 500 m and is strongly stratified. This water mass is the densest $\sigma_\theta > 27.91$ kg m^{-3}, most saline ($S > 34.66$ psu) and most oxygen-rich water mass in the depression; and

- Winter Water (WW), a homogeneous layer of colder, less saline water, of density $27.88 < \sigma_\theta < 27.91$ kg m^{-3}, which is found above the HSSW.

Bindoff et al. (2001) found that HMCDW at the shelf break is converted to WW which is then converted to ISW. The HSSW (found in the depression) is not a constituent

of the ISW. Prior to this expedition, it was believed that HSSW was part of the process of ISW formation.

The HSSW found in the Adélie Depression is the most saline water found on the shelf in the Adélie region, with salinities greater than 34.70 psu being observed. This water is dense enough to reach the bottom of the ocean as AABW, but is confined to the continental shelf because of the sill, unless it overflows over the sill. The HSSW is a result of MCDW intruding onto the shelf and the large, persistent polynya (Rintoul, 1998).

A $100-300$ m thick layer of cold, fresh and highly oxygenated water is found on the continental slope. This is formed as the shelf waters move down the slope and entrain MCDW. If the water is sufficiently dense it finally forms Adélie Land Bottom Water (ALBW). Evidence of active downslope flow is noted by Baines and Condie (1998) at 140°E. This may be ALBW draining out from the Adélie Depression.

The bottom water formed here is colder and fresher than the high salinity ($S >$ 34.70 psu) Ross Sea Bottom Water (RSBW). The deep salinity maximum associated with RSBW is not found west of 143°E. It is replaced by ALBW which is cooler, fresher and is higher in oxygen. Oxygen-rich water is found along the shelf of the Adélie Land region, but only west of 147°E is it found on the abyssal sea floor.

An anomalous water mass observed by Carmack and Killworth (1978) between 150° and 170°E may be water from the Adélie coast that was not dense enough to sink to the bottom and displace the RSBW signal. Deep water formation, where dense slope waters descend and finally intrude into the ocean at their own density level, is observed in the Weddell Sea (Foster and Middleton, 1980).

2.6 Circulation

Bindoff et al. (2001) measured the currents above the shelf in the Mertz polynya during the winter of 1999. They found that HMCDW moved westward along the shelf break (0.7 Sv). Above the part of the depression where the depth is greater than 500 m, the flow is eastward, and this moves both HSSW and WW under the Mertz Glacier (2.0 Sv). The strongest flow (> 0.20 m s^{-1}) is the narrow westward flow at the coast (1.2 Sv).

The westward currents above the slope are 0.16 m s^{-1} for depths where the water depth is less than 500 m. These currents decrease to zero as the depth increases to 3,800 m northwards towards the Antarctic Circumpolar Current (ACC) where the current turns eastward (Bindoff et al., 2000b).

The cross-shelf flow appears to be limited to the vicinity of the channel at 143°E which is the main outflow for ALBW from the Adélie Depression (Rintoul, 1998). This channel is also the area where the CDW enters onto the shelf.

Chapter 3

Theoretical Background

In this chapter a description is made of some of the theory of processes involved in the formation of dense water. The forces that cause dense water formation are first considered, followed by the processes associated with the mixing and motion of dense water.

This chapter is set out to follow the Lagrangian path of the dense water. Section 3.1 describes some of the ocean surface fluxes that may result in the formation of dense water or the movement of water. The convection that occurs if dense water forms beneath the surface as a result of surface forcing is considered in Section 3.2. If dense water formation occurs over an isolated region, a lateral buoyancy flux develops, which is discussed in Section 3.3. An equilibrium state discussed in Section 3.4 occurs when the amount of dense water being formed is equal to the amount of dense water being removed. Section 3.6 describes the dynamics that govern the movement of dense water away from the region of formation and onto and down the slope.

3.1 Surface Fluxes

The atmosphere affects the ocean, through the transfer of buoyancy fluxes and momentum fluxes across the ocean-atmosphere interface. Buoyancy fluxes which occur through a heat flux, a salinity flux, or both and change the density of the water beneath the sea surface. Momentum fluxes from the wind add momentum to the ocean and drive the surface layer of the ocean.

Buoyancy Fluxes

Buoyancy fluxes arise from the combination of temperature and salinity fluxes. Sensible heat fluxes contribute to the temperature fluxes. Sensible heat fluxes result from temperature differences between the atmosphere and the ocean, with the flux being proportional to the temperature difference. The removal of freshwater by evaporation or freezing results in a positive salinity flux. Precipitation or melting of ice results in a negative salinity flux. In this region of study, the effects evaporation and precipitation are small in comparison to the freezing and melting of ice and have not been included in the buoyancy equation given below.

The buoyancy flux B_0 in units of $m^2\ s^{-3}$ can be calculated from the heat flux and salinity flux, and is

$$B_0 = c_w^{-1}\rho^{-1}g\alpha Q + g\beta(F_{ice} - M_{ice})(S_{surface} - S_{ice}) \tag{3.1}$$

where c_w is the specific heat of water, ρ is the density of the water, Q is the upward heat flux, $\alpha = -\rho^{-1}\ \partial\rho/\partial T$ is the thermal expansion coefficient of sea water at the surface and $\beta = \rho^{-1}\ \partial\rho/\partial S$ is the corresponding coefficient for salinity, F_{ice} and M_{ice} are the

freezing and melting rates of ice in m s^{-1} and $S_{surface}$ and S_{ice} are the salinities of the surface and the ice respectively (Gill, 1982). Where no ice is being formed or there is no ice to melt, the second term on the right hand side of equation 3.1 is zero. The freezing rate F_{ice} can be estimated by

$$F_{ice} = -\frac{Q}{\rho_i L_H} \tag{3.2}$$

where $\rho_i = 950$ kg m^{-3} is the density of ice and $L_H = 3.34 \times 10^5$ J kg^{-1} is the latent heat of fusion for water (Pease, 1987). The latent heat of fusion for newly formed ice with a salinity of 10 psu and temperature of -2°C is $L_H = 2.4 \times 10^5$ J kg^{-1} (Roberts et al., 2001). For the calculation of the freezing rate of ice, an average of the latent heat of fusion of $L_H = 2.92 \times 10^5$ J kg^{-1} is used as the latent heat of fusion of sea water.

The heat flux from open water typical of Antarctica (see Section 2.3) is $Q =$ 500 W m^{-2}, this generates a buoyancy flux $B_0 = 0.3{\times}10^{-7}$ m^2 s^{-3}. From equation 3.2, this heat flux will freeze sea water to produce sea-ice at the rate of 16 cm of sea-ice per day. The water on the continental shelf around Antarctica during winter typically has salinity 35 psu and temperature -1.8°C, and the salinity of newly formed ice is $\sim$ 8 psu. The resulting buoyancy flux due the salinity flux caused by the ice formation is $B_0 = 3.7{\times}10^{-7}$ m^2 s^{-3}. Thus, in practice the buoyancy flux due to the salt flux resulting from ice formation is typically 12 times greater than the buoyancy flux due to the heat flux. In the numerical experiments undertaken in the present study, the temperature remains constant and only the buoyancy flux due to the salt flux is considered.

Momentum flux

The wind stress on the ocean surface transfers momentum across the air-sea interface. The momentum transfer alone does not affect the buoyancy of the water, rather it mixes the surface layers of the ocean and contributes to creating a surface mixed layer. The depth over which the wind has influence is known as the Ekman depth h_E, and is given by (Cushman-Roisin, 1994, p 65)

$$h_E = \sqrt{\frac{2\nu}{|f|}}, \tag{3.3}$$

where $\nu = 10^{-2}$ m^2 s^{-1} is a typical value for the vertical eddy viscosity and $f = -1.33\times10^{-4}$ s^{-1} is the Coriolis parameter at 66°S. A typical Ekman depth for this area is $h_E \simeq 12$m.

The katabatic winds around Antarctica, described in Section 2.2, blow westward alongshore with the coast to the left. This causes onshore Ekman transport at the surface. The cross-shelf volume transport U due to the alongshore wind stress τ^y (Cushman-Roisin, 1994, p 69) is

$$U = \frac{1}{\rho f}\tau^y \tag{3.4}$$

per metre width of sea surface. The onshore transport increases the sea surface elevation near the coast and creates a negative elevation gradient that drives a barotropic westward alongshore current throughout the water column. The onshore transport of water in the surface layer is balanced by the offshore transport in the bottom Ekman layer, as described in Section 3.6.3, and eventually a steady state is reached.

The momentum flux can be calculated from the wind speed. Different parameterisations of the wind stress due to a wind acting on the ocean surface exist, the

parameterisation used by Pond and Pickard (1995, p108) is

$$\tau^y = \rho_a C_D v_{\text{wind}}^2 \tag{3.5}$$

where $\rho_a = 1.2$ kg m^{-3} is the density of air, the non-dimensional drag co-efficient $C_D \simeq 1.4 \times 10^{-3}$ and v_{wind} is the wind speed in m s^{-1}. Gill (1982, p29) quotes a drag co-effient value of $C_D \simeq 1.1 \times 10^{-3}$ for low wind speeds and

$$C_D = 10^{-3} \times (0.61 + 0.063 v_{\text{wind}}) \qquad \text{for} \qquad 6 < v_{\text{wind}} < 22 \text{ms}^{-1}.$$

The wind speed at Cape Denison during winter is 25 m s^{-1} (see Section 2.2). This is equivalent to a wind stress of $\tau^y = 1$ Pa and generates an onshore transport of 8 m^3 s^{-1} m^{-1}. For a shelf 100 km wide and 500 m deep, it takes ~72 days for this transport to flush the water on the shelf.

3.2 Convection

The stages of shallow convection which occur when a stratified fluid is subject to a negative buoyancy flux B_0 at the surface are shown in Figure 3.1, reproduced from Send and Marshall (1995). The water at the surface of the forcing region becomes denser than the water beneath it, creating an unstable water column. This creates a convectively modified layer of depth h shown in Figure 3.1 *"convective overturning"*. This convectively modified layer grows with time according to (Visbeck, Marshall, and Jones, 1996)

$$h = \frac{\sqrt{2B_0 t}}{N} \tag{3.6}$$

where N is the buoyancy or Brunt-Vaisala frequency. The layer is homogeneous, with a density anomaly ρ' equal to the ambient density at depth h (Chapman, 1998), i.e.,

$$\rho' = \frac{\rho_0 N^2 h}{g} = \frac{\rho_0 N \sqrt{2 B_0 t}}{g}. \tag{3.7}$$

If the buoyancy flux is limited to a region of radius r, the column of dense water beneath the forcing region forms a chimney. With continued buoyancy flux the density difference between the chimney of water and the ambient fluid grows, increasing the lateral buoyancy gradient.

The importance non-hydrostatic process

Convection is a non-hydrostatic process. As described in Appendix A, the Princeton Ocean Model which is used in this study uses the hydrostatic approximation. Marshall, Hill, Perelman, and Adcroft (1997) provide a non-dimensional parameter $m = \delta^2/Ri$ for non-hydrostatic effects. δ is the ratio of vertical to horizontal scales and $Ri = (NH/u)^2$ is the Richardson number, where u is the typical horizontal velocity. In this study the horizontal scales ($\sim$ 100 km) are significantly larger than the vertical scales ($\sim$ 500 m), rendering the non-hydrostatic effects fairly small.

3.3 Lateral buoyancy advection

If the chimney is large, it will be broken up by baroclinic instabilities, whereas small chimneys are broken up by gravity waves. A large chimney has a small Burger number

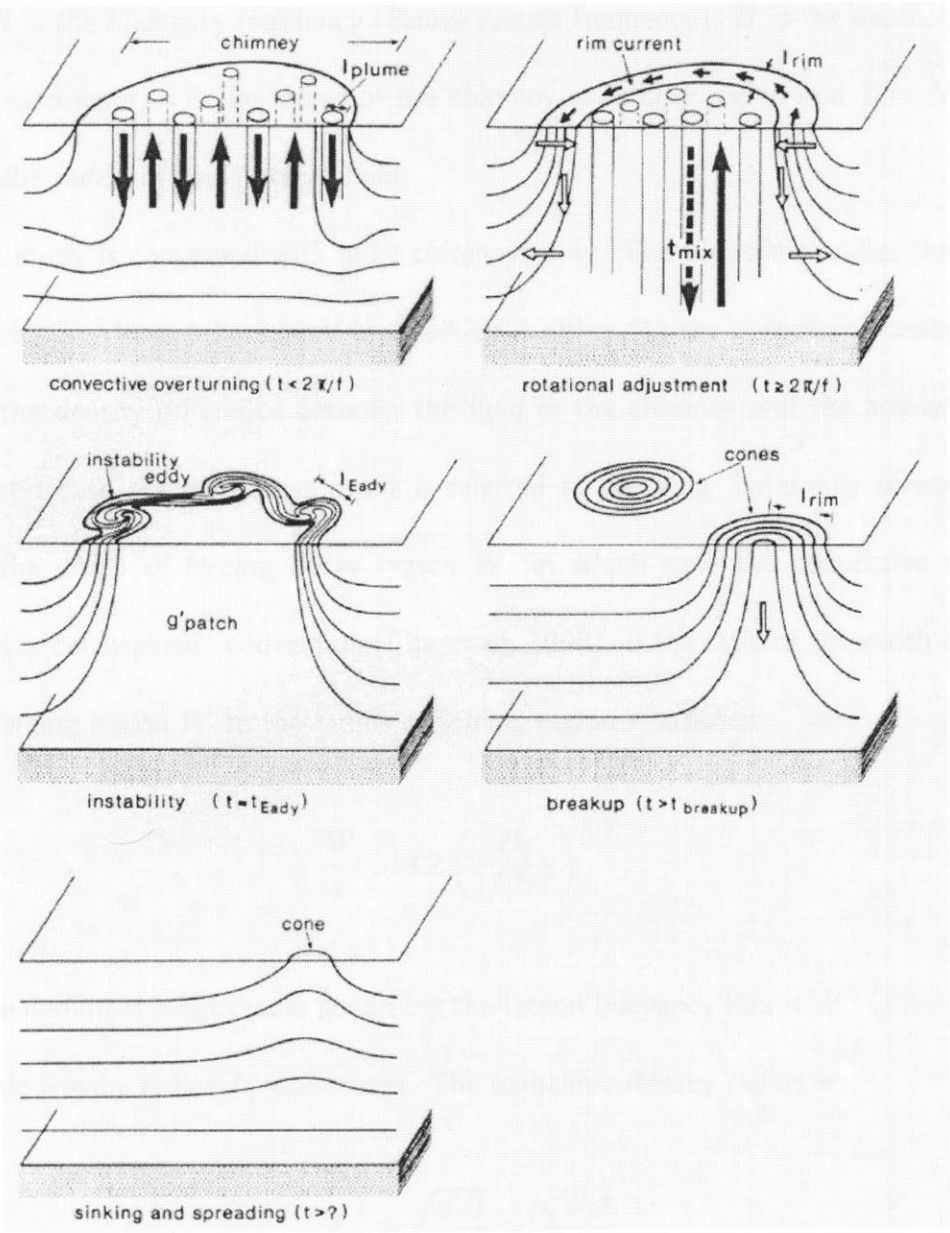

Figure 3.1: *Summary of the stages of shallow convection from Send and Marshall (1995).*

(Visbeck et al., 1996) defined by

$$Bu = \left(\frac{NH}{fr}\right)^2 = \left(\frac{L}{r}\right)^2$$

where N is the buoyancy frequency (Brunt-Vaisala frequency), H is the depth, f is the Coriolis parameter, r is the radius of the chimney or forcing region and $L = NH/f$ is the Rossby radius of the ambient fluid.

This study is concerned with large chimneys only. The baroclinic eddies that break up the chimney have a horizontal scale which is either (1) the baroclinic Rossby radius due to the density difference between the fluid in the chimney and the ambient fluid, and in this case the convective event is referred to as being "internally constrained"; or (2) the width of forcing decay region W, in which case the convective event is "externally constrained" convection (Chapman, 1998). If the ratio of the width of decay of the forcing region W to the radius of forcing region r satisfies

$$\frac{W}{r} > 3.2\left(\frac{B_0}{|f|^3 r^2}\right)^{1/3}, \tag{3.8}$$

then the dominant length scale governing the lateral buoyancy flux is W. Otherwise the baroclinic Rossby radius L_ρ dominates. The baroclinic Rossby radius is

$$L_\rho = \frac{\sqrt{g'H}}{|f|} = \frac{\sqrt{B_0 t}}{|f|}. \tag{3.9}$$

where $g' = \rho'/\rho_0 g$ is the reduced gravity, and ρ' is the density anomaly of the chimney given in equation 3.7.

The azimuthal rim current shown in Figure 3.1 *"rotational adjustment"* at the edge

of the chimney is determined from the thermal wind balance

$$\frac{\partial u}{\partial z} = \frac{g}{\rho_0 f}\frac{\partial \rho}{\partial y}.$$

Assuming that $u_{\text{surface}} = -u_{\text{bottom}}$ (Gawarkiewicz and Chapman, 1995) and constant $\partial u/\partial z$ with depth, then solving the thermal wind equation gives

$$u(z) = \frac{gH}{\rho_0 f}\frac{\partial \rho}{\partial y}(z + \frac{1}{2}H).$$

This will result in cyclonic circulation around the dense water at the surface, anti-cyclonic at the bottom and the rim current vanishes in the middle. The rim velocity and the eddies are dependent on whether the lateral scale is L_ρ or W, i.e., "internally" or "externally" constrained. From here on the surface rim current $u(0)$ will be denoted by u_{rim}.

Internally constrained convection

The vertical interface between the dense water beneath the forcing region and the ambient fluid is displaced inward at the surface and outward at the bottom to the baroclinic Rossby radius L_ρ. This sets up a horizontal density gradient $\partial\rho/\partial x = \rho'/L_\rho$, which using a thermal wind balance results in a rim velocity (Send and Marshall, 1995)

$$u_{\text{rim}} = \frac{1}{2}\sqrt{B_0 t}. \tag{3.10}$$

Externally constrained convection

If there is a forcing decay region of width W, then the horizontal scales that the eddies are formed are initially dominated by the width of the decay region. This is due to the

small difference in the density of the water beneath the forcing region and the ambient water initially, resulting in a small baroclinic Rossby radius L_ρ (equation 3.9) and W dominates the horizontal scale. By the same thermal wind balance as above, the rim velocity is

$$u_{\text{rim}} = \frac{B_0 t}{2fW}. \tag{3.11}$$

Over time, the density anomaly ρ' increases, causing the baroclinic Rossby radius L_ρ to increase. When $L_\rho = W$, the system goes from being "externally" constrained to being "internally" constrained. Using equation 3.9, the transition occurs at time (Chapman, 1998)

$$t^* = \frac{(fW)^2}{B_0}. \tag{3.12}$$

After the transition time, the rim velocity grows with time according to equation 3.10.

Breaking up of the chimney

The rim current does not grow indefinitely. The rim current begins to meander and then eddies develop (shown in Figure 3.1 *"convective instability"*). Initially the fastest growing perturbations have wavelength $\lambda = 3.912\ L$ (Cushman-Roisin, 1994), where $L = NH/f$ is the Rossby radius of deformation. Only perturbations of wavelength $\lambda > 2.619L$ are unstable and break up the cylinder of dense water (shown in Figure 3.1 *"breakup"*). The eddies that are formed play an important role in the transport of dense water over the shelf break and onto the slope.

3.4 Equilibrium state

The system comes to equilibrium when the lateral buoyancy flux balances the buoyancy flux at the surface. The lateral buoyancy fluxes act to remove dense water from beneath the forcing region and to force ambient water from outside the forcing region to beneath the forcing region. The change in density beneath the forcing region can be expressed as (Chapman, 1999, equation 1)

$$\frac{d}{dt}\int\int\int \rho' \, dA \, dz = \int\int \frac{\rho_0 B_0}{g} \, dA \, dz - \int \oint \overline{v'\rho'} \, dl \, dz \qquad (3.13)$$

where ρ' is the density anomaly beneath the polynya, A is the area over which a uniform surface buoyancy flux B_0 is imposed, $\overline{v'\rho'}$ is the lateral eddy flux of density normal to the edge of the polynya, l is the distance along the edge of the polynya. The first term on the right hand side represents the surface buoyancy flux and the second term represents the lateral buoyancy flux. Equilibrium is reached when there is no change in density beneath the forcing region, i.e., the left hand side of equation 3.13 is zero and the lateral buoyancy flux balances the surface buoyancy flux.

Deep Convection

Deep convection (and shallow convection) has been defined in different ways in different studies. Jones and Marshall (1993) refer to any convection in the deep ocean as deep convection whether or not it penetrates the whole water column. For these conditions the vertical scales are comparable to the horizontal scales and the hydrostatic condition is not satisfied. In the present work deep convection is defined as occurring when equilibrium is reached before the chimney of homogeneous water reaches the ocean bottom $z = -H$

(Visbeck et al., 1996). Deep convection occurs if the ocean is very deep or very stratified, such that

$$NH > \gamma(B_0 r)^{1/3} \tag{3.14}$$

where $\gamma = 3.9 \pm 0.9$ is the efficiency of the baroclinic eddies in breaking up the chimney and has been found by experiments (Visbeck et al., 1996).

This quasi-steady final state will be reached when

$$t_{\text{final}} = \frac{\gamma^2}{2}\left(\frac{r^2}{B_0}\right)^{1/3}. \tag{3.15}$$

At this time the chimney extends to a depth of

$$h_{\text{final}} = \gamma\frac{(B_0 r)^{1/3}}{N}$$

and the density of the chimney is the density at depth $z = -h_{\text{final}}$.

If the buoyancy flux continues then the depth and the density of the chimney are maintained at these values. If the buoyancy flux ceases then the restratification timescale of a cylinder of homogeneous water of depth h in a stratified fluid due to eddies spawned by baroclinic instabilities is

$$\tau_{\text{restrat}} \simeq 56\frac{r}{Nh}\text{days} \tag{3.16}$$

(Jones and Marshall, 1997).

The equilibrium density of the water in the chimney in a deep convection event is less than the densest water beneath the forcing region. In this study we are concerned with shallow convection events on the shelf which produce dense shelf water.

Shallow convection

In the case of shallow convection the whole water column is homogenised by the buoyancy flux, as shown in Figure 3.1 *"rotational adjustment"*. This initial stage is referred to as the pre-conditioning stage. The preconditioning stage ends once the modified convective layer reaches the bottom, i.e., $h = H$ in equation (3.6), this occurring at time

$$t_{\text{bot}} = \frac{(NH)^2}{2B_0}. \tag{3.17}$$

Once the water column has been homogenised, the time for the water to mix from the surface to the bottom is (Send and Marshall, 1995)

$$t_{\text{mix}} = \frac{2}{|f|Ro^*} = 2H\sqrt{\frac{|f|}{B_0}} \tag{3.18}$$

where Ro^* is the natural Rossby number

$$Ro^* = \frac{1}{H}\sqrt{\frac{B_0}{|f|^3}}. \tag{3.19}$$

The maximum density anomaly beneath the forcing region increases with time (Gawarkiewi and Chapman, 1995) according to

$$\rho' = \frac{\rho_0 B_0 t}{gH} \tag{3.20}$$

until it reaches an equilibrium. The equilibrium time can be internally or externally constrained as determined by equation 3.8.

Externally Constrained Equilibrium

Externally constrained convection will come to equilibrium when

$$t_{\text{ext\_eq}} = 5.7\sqrt{\frac{frW}{B_0}} \tag{3.21}$$

and the equilibrium density anomaly is

$$\rho'_{\text{ext\_eq}} = 5.7\frac{\rho_0}{gH}\sqrt{fB_0rW} \tag{3.22}$$

(Chapman, 1998). If the equilibrium time for the externally controlled convection occurs before the transition time t^* given in equation 3.12, from externally to internally constrained, then the convection is externally constrained.

Internally Constrained Equilibrium

For internally constrained convection, the system will come to equilibrium after time

$$t_{\text{int\_eq}} = \kappa\left(\frac{r^2}{B_0}\right)^{1/3} \tag{3.23}$$

at which time it reaches the equilibrium density anomaly

$$\rho'_{\text{int\_eq}} = \kappa\frac{\rho_0}{gH}\left(rB_0\right)^{2/3}. \tag{3.24}$$

The coefficient κ is a measure of how efficient the eddies are in transporting the buoyancy away from the convective region.

The value for κ varies from study to study, ranging from 5 to 23. Through laboratory and numerical experiments, Visbeck et al. (1996) found $\kappa = \gamma^2 \simeq 15.2$ where $\gamma =$

3.9 ± 0.9. Chapman (1998) found a value of $\kappa = (1/a)^{2/3} = 8.0$ where $a = 0.044$ is the eddy exchange efficiency. Spall and Chapman (1998) determined a theoretical efficiency constant $c_e = 0.045$, which gives a co-efficient of $\kappa = (1/2c_e)^{2/3} = 5.0$, but eddy-resolving numerical models gave an efficiency constant of $c_e = 0.02 - 0.04$ resulting in $\kappa = 5.4 - 8.5$. A study by Narimousa (1997) on turbulent convection at large aspect ratios ($r/H \gg 1$) for a homogeneous ambient fluid gives the maximum density of the mesoscale vortices with $\kappa = 10 \pm 1$.

3.4.1 Other factors affecting equilibrium density

Shape of forcing region

The time to reach equilibrium is dependent on the geometry of the forcing region, in particular the ratio of the perimeter that is subject to the forcing region to the area. The generalized form of the equilibrium time given in equation 3.21 is (Chapman, 1999, equation 4)

$$t_e q = \left(\frac{1}{c_e}\right)^{1/2} \left(\frac{fW}{B_0}\frac{A}{P}\right)^{1/2}$$

where c_e is the efficiency constant and A/P is the ratio of the area of the forcing region to the perimeter. The values of A/P for various geometries are found in Chapman (1999, Table 1). In equation 3.21 $A/P = r/2$.

Time dependent forcing

The typical time scale of a polynya event is same as the synoptic events which is a matter of a few days. The typical ocean response time is greater than 10 days which is longer than the typical polynya event (Chapman, 1999). Numerical calculations show that the ocean tends to integrate the polynya events such that the results achieved by

the time dependent forcing and steady time averaged forcing is similar.

Effect of ambient stratification

In the case where there is ambient stratification, the equilibrium density anomaly is equal to the equilibrium density calculated in equation 3.22 plus the density anomaly at the bottom at the coast (Gawarkiewicz, 2000, equation 11). This is give by

$$\rho'_{\text{strat\_eq}} = \rho'_{\text{eq}} + \frac{N^2 \rho_0 h_0}{g}, \tag{3.25}$$

where the first term on the right hand side is the equilibrium density anomaly determined by equation 3.22 or 3.24 and h_0 is the depth at the coast. The second term on the right hand side is the density at the coast on the bottom.

Effect of a sloping bottom

In the presence of a gently sloping bottom, the equilibrium time can be calculated by replacing H with the depth at the midpoint of the forcing decay region H_{new}, reducing the time by a factor of H/H_{new}. Since the equilibrium density is a linear function of the equilibrium time, the equilibrium density is reduced by the same amount (Gawarkiewicz, 2000).

The studies discussed in Chapters 4 through 6 have a forcing region over the shelf which contains a depression, and the bathymetry beneath the forcing region is neither flat nor of a constant slope. To date there is no literature that addresses this situation. The minimum, mean and maximum depths beneath the forcing region are used to determine the theoretical equilibrium densities in equation 3.22. The effect of the ambient stratification from equation 3.25 are added to the equilibrium density and these

values are converted to equilibrium salinity anomalies and listed in Table 4.1 for the experiments in this study. The equilibrium salinity anomaly calculated using the minimum depth beneath the forcing region gives the upper limit to the equilibrium salinity anomaly.

Effect of an alongshore current

Ambient alongshore currents change the density anomalies generated and the direction of the eddy transport of the dense water, but do not change the fundamental processes of instabilities generating eddies which move dense water away from the polynya (Chapman, 2000). An alongshore current will reduce the time of exposure of the water columns to the surface forcing as the water is advected beneath the forcing region. As a result the density anomaly of the water is decreased but the volume of water exposed to the forcing is increased. These effects tend to compensate each other and produce similar density anomaly fluxes in the direction of the current. The current increases the alongshore density flux downstream of the forcing region, whereas in the absence of the current, the alongshore density flux tends to be nearly absent.

3.5 Tidal Induced Mixing

Tidal mixing modifies the water masses on the shelf through lateral mixing. The energy from the tidal mixing causes water on the shelf to mix with water off the shelf. This results in water of lower density on the shelf. Areas of weak tidal exchange correspond well with areas of cross-shelf exchange of dense water (Beckmann and Pereira, 2003).

There are limited observations of tidal currents around Antarctica. Middleton and Foster (1977), Middleton, Foster, and Foldvik (1982), Foster and Middleton (1987) and

Foldvik, Middleton, and Foster (1990) have reported measurements of tides in the central and southern Weddell Sea. The tidal fluctuations are stronger on the shelf than on the slope and in the southern Weddell Sea the semidiurnal tides result in shear instability and mix the MCDW with the SW (Foster and Middleton, 1987).

3.6 Downslope flow

Once the dense water has formed on the shelf, it spills over the shelf break and moves down the slope. If the water is dense enough it will sink to the bottom to form Antarctic Bottom Water, otherwise it will settle at an equilibrium depth where it will leave the slope and interleave between other layers of water.

The water can move down the slope as a plume or separate eddies. The equilibrium depth at which the water leaves the slope is determined by its density which controls the bulk flow of the dense water, and by Ekman drainage which removes water from the plume in the bottom boundary layer and brings it to greater depths. Other factors such as entrainment lower the density of the dense water mass and increase its volume. Detrainment and interleaving occur when the outer layers of the plume have the same density as the ambient water at depth.

3.6.1 Equilibrium depth

The depth that a dense plume is expected to reach in a stratified fluid is the depth where the density of the plume matches the surrounding density. Though a descending plume with significant momentum may drop to slightly below the equilibrium level, it will eventually return to where the local density matches the density of the surrounding water. For an undiluted plume of original density ρ'_{eq} determined from equations 3.22 or

3.24, and 3.25, this depth is (Gawarkiewicz, 2000)

$$z_{\text{eq}} = \frac{g\rho'_{\text{eq}}}{\rho_0 N^2}. \tag{3.26}$$

Numerical experiments using parameters typical of the Arctic Ocean show that the plume generally reaches between 0.5 and 0.75 times the equilibrium depth due to the entrainment of less dense water.

3.6.2 Bulk Flow of a plume

The quasi-geostrophic speed and direction of the dense plume can be determined from the force balance between gravity, Coriolis and bottom friction, see Figure 3.2. The angle down slope of the isobaths ϕ at which the plume will travel is determined by

$$\tan\phi = \frac{c_D}{d\,|f|} \tag{3.27}$$

and the speed is determined by

$$v = \frac{1}{|f|}\, g' \sin s\, \cos\phi. \tag{3.28}$$

The co-efficient of bottom friction $c_D \simeq 0.0025$, d is the thickness of the plume, f is the Coriolis parameter and s is the angle of inclination of the slope to the horizontal. Small thicknesses imply a large offshore angle (due to the Ekman layer being a large fraction of the dense water layer) and the speed of the plume is determined by the density anomaly.

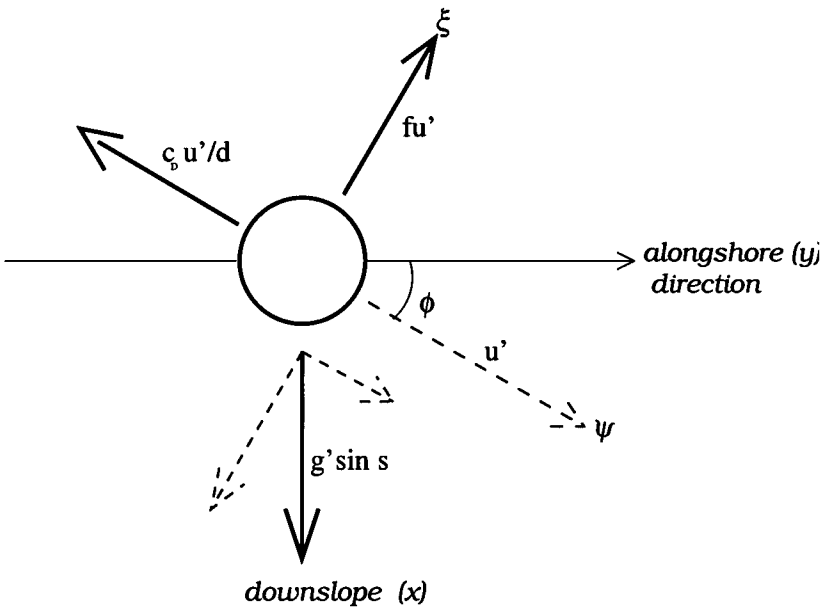

Figure 3.2: *The force balance between the gravitational force $g' \sin s$, Coriolis force fu' and friction $c_D u'/d$ acting on a plume of dense water on the slope. x and y are the downslope and alongshore directions, ψ is the direction that the plume is moving in and ξ is perpendicular to this - the direction the Coriolis force is working in.*

3.6.3 Ekman drainage

An alongshore flow will result in an Ekman bottom boundary layer. In the southern hemisphere, if this flow has the shallower water to the left of the direction of the flow then the drainage in the bottom boundary layer will be offshore. The effect of the Ekman drainage depends on the depth of the plume d, relative to the Ekman depth h_E given in equation 3.3. The eddy viscosity coefficient for h_E can be calculated (Shapiro and Hill, 1997) by

$$\nu = 2\frac{c_D^2 \overline{v}^2}{|f|} \tag{3.29}$$

where $\overline{v}$ is the alongslope or tidal current and $c_D \simeq 0.0025$ is the drag coefficient. The offshore volume transport caused by Ekman dynamics is (Cushman-Roisin, 1994)

$$U = \frac{\overline{v} h_E}{2}. \tag{3.30}$$

The offshore transport U is dependent on the speed of the current and the Ekman depth only; it is independent of the depth of the plume. Plumes that are much thicker than the Ekman depth only have a fraction of the transport in the lower layer and the plume is driven predominantly in the direction of the flow. Thin plumes with depth $d < 0.5\ h_E$ have a stronger downslope flow because friction plays a larger part in its motion. This can be measured by the Ekman number

$$E_k = \frac{\nu}{d^2\ |f|}. \tag{3.31}$$

Flows with $E_k < 10^{-3}$ are generally stable and do not form eddies (Condie, 1995).

Baines and Condie (1998) use the non-dimensional parameter

$$F = \frac{Q_{\mathrm{DW}}}{g's} \left(\frac{|f|^3}{\nu} \right)^{1/2}$$

where Q_{DW} is the rate of dense water production per unit length of slope, s is the gradient of the bottom slope. If $F < 1$ and Q_{DW} is small or the eddy viscosity is high, then the Ekman drainage removes most of the dense water down the slope. This will prevent eddies from forming (Land-Serff and Baines, 1998). If $F \gg 1$ then the dynamics of the plume are governed by geostrophy and the rate of dense water production. If $F > 1$ but not very large then geostrophic effects are important until the plume reaches intermediate depths and viscous drainage takes over.

3.6.4 Eddy formation on the slope

When eddies form on the slope the governing scale is the Rossby deformation radius

$$L_{\text{slope}} = \frac{\sqrt{g'd}}{f}, \tag{3.32}$$

where d is the height of the density current.

From experimental results by Land-Serff and Baines (1998) the downslope excursion of the flow before turning left (in the southern hemisphere) to flow alongslope is $(2.3 \pm 0.1)\ L_{\text{slope}}$. If the flow broke up into eddies, the radius of these eddies was $(1.25 \pm 0.05)\ L_{\text{slope}}$.

As eddies move along a slope, they may generate eddies in the fluid above provided that there is time to "capture" the fluid i.e., viscous draining is not dominant (either the viscous effects are not too high or the slope is too steep). Once the upper layer has been captured and moved into deeper water, the water column is stretched and develops cyclonic rotation. This cyclonic rotation is due to the conservation of potential vorticity

$$q = \frac{f + \zeta}{H + \eta} \tag{3.33}$$

where $\zeta = \frac{\partial v}{\partial x} - \frac{\partial u}{\partial y}$ is the relative vorticity and η is the sea surface elevation. As the water column is stretched, the vorticity ζ must increase, i.e. it must rotate cyclonically. This cyclonic rotation acts to draw water into the eddy and maintains the dome of dense water together rather than allowing the dense water to be diffused by viscous effects. It may then be propagated along the slope (Land-Serff and Baines, 1998).

The ratio of the time interval between eddies T_{int} and the period of rotation $T =$

$2 \times 2\pi/f$ is

$$\frac{T_{\text{int}}}{T} = \frac{0.19 \pm 0.02}{\Gamma} + (2.4 \pm 0.2)$$

where the relative stretching $\Gamma = L_{\text{slope}} s/D$ where D is the depth of the ambient fluid above the dense fluid and s is the bottom slope (Land-Serff and Baines, 1998).

Kikuchi, Wakatsuchi, and Ikeda (1999) found that when the slope was steeper, the period of eddy development decreases. This is consistent with the above equation as Γ increases and the interval between eddies T_{int} decreases.

3.6.5 Entrainment and detrainment

The process of entrainment occurs when turbulence in the plume captures the ambient fluid, and these are mixed into the plume modifying the plume properties. Shapiro and Hill (1997, eqn 26) parametrise the entrainment velocity as

$$w_e = \frac{0.32 f^3 h_E^2}{8\, c_D^{3/2} g'} F\left(\frac{h_E}{d}\right) \tag{3.34}$$

where $F(h_E/d) = h_E/d$ when $h_E/d \leq 1$ and $F(h_E/d) = 1$ when $h_E/d > 1$. Maximum entrainment will occur when the depth of the plume d is less than the Ekman depth h_E. This generally occurs at the head of the plume where Ekman transport constantly transports a thin layer of dense water offshore. The entrainment causes the front of the plume to thicken, allowing more water to feed into the head of the plume. This increases the propagation speed of the plume (see equations 3.27 and 3.28), and in turn increases the offshore Ekman transport.

Entrainment also results in a reduction of the initial density anomaly of the plume (Jiang and Garwood, 1998). This will decrease the penetration depth of the plume

(Gawarkiewicz, 2000) by $25-50\%$. Ambient stratification increases mixing and entrainment which further decreases the penetration depth of the dense water plume.

Detrainment occurs when elements of water in the plume leave the plume and become part of the ambient fluid. This has been observed in the stratified ocean e.g. Foster and Middleton (1980).

3.6.6 Thermobaric Effects

Water on the continental shelf around Antarctica is much colder than the water offshore. This water is cooled by the katabatic winds which are very cold, and have the most profound effect in cooling shelf waters. The ice shelves around Antarctica may also "supercool" the water to below surface freezing point which is $-1.90°C$ for salinity 34.6 psu. When cold water from the shelf moves down the slope and reaches depths greater than around 2,000 m it increases its negative buoyancy due to the thermobaric effect. The thermobaric effect is when a water mass colder than its surroundings in the deep ocean has negative buoyancy due to the non-linearity of the equation of state (Fofonoff, 1956; Gill, 1973). This results in increased downward velocity of the cold water mass.

3.6.7 Topographic Effects

Across-slope submarine canyons tend to enhance the penetration depth of the dense bottom currents by breaking down the effects of rotation in the canyon and allowing the dense water to be channeled along the side wall of the canyon, reducing entrainment. Wider and deeper canyons tend to transport more water offshore. A ridge on the slope has a similar effect in that it will provide a surface for the dense water to flow down and

hence penetrate deeper into the ocean (Jiang and Garwood, 1998).

Chapman (2000) studied the effect of canyons with an along shelf current on a gentle slope. The canyon started 75 km downstream and 20 km offshore of the forcing region. When the canyon was oriented normally or diagonally to the coast, the dense water tended to avoid the canyon because the along shelf flow is nearly geostrophic with a tendency to follow isobaths. When the canyon orientation was parallel to the coast, the alongshore current carries dense water parallel to the axis of the canyon and a substantial quantity of dense water flows into the canyon.

3.7 Numerical Studies

Kikuchi et al. (1999) investigated the transport process of dense shelf water from the continental shelf to the slope using the Princeton Ocean Model. They found that the eddy flux is dominant on the shelf and the bottom dense plume controls salinity transport on the shelf. The shelf break front develops a boundary between the two regions.

Jiang and Garwood (1995) studied the movement of three-dimensional dense bottom plumes on a continental slope by studying the adjustment of a vertical density front over a continental shelf break. They found that geostrophic adjustment takes place for the first 12 days where fresh warm deep ocean water intrudes onto the shelf near the surface, and saline cold shelf water penetrates downslope at the bottom. Frontal instabilities in the form of light plumes at the surface with length scales of 50 km intrude 50–60 km onshore and rotate anti-cyclonically.

At the bottom, dense plumes of width 50 km form and flow downslope and are slightly deflected by Coriolis force. The downslope penetration of the bottom plumes decreases mixing and entrainment of the surrounding water. After 18 days, the plumes

begin interacting with each other and form a bottom front. A quasi-steady state is reached when the front is nearly parallel to isobaths and has penetrated ~140 km from the shelf break where the depth is 1,800 m.

3.8 Summary

In this chapter a wide range of theoretical concepts concerning convection over a continental shelf has been described.

The negative buoyancy flux due to sea-ice formation at the sea surface increases the density of the beneath the surface, creating an unstable water column that mixes and deepens the mixed layer. If the time of the buoyancy forcing is too short, the topography too deep or the water column too stratified then the mixed layer does not reach the bottom and deep convection occurs. Otherwise if the mixed layer reaches the bottom, shallow convection occurs. If shallow convection occurs then water that is denser than the water initially present beneath the forcing region is formed.

Eddies form at the edge of the forcing region and break down the dense water chimney. When the lateral buoyancy flux is equal to the surface buoyancy flux, the system comes to equilibrium. The theoretical time to reach equilibrium is given by equation 3.21 (3.23) for externally (internally) constrained shallow convection and the equilibrium density is given by equation 3.22 (3.24). In a stratified fluid the equilibrium density anomaly is increased by the amount given in equation 3.25.

Once the dense water has formed on the shelf, some of it moves over the shelf break and onto the slope. The dense water plume moves down and along the slope under the influence of gravity, Coriolis force and friction in the bottom boundary layer. The quasi-geostrophic direction and speed of the plume on the slope can be determined by

equations 3.27 and 3.28. Entrainment of ambient water into the plume moving down the slope reduces the downslope penetration of the plume by $25 - 50\%$. Other factors affecting the movement of the plume include currents, detrainment, thermobaric effects and topographic effects.

These processes will be referred to in later chapters when the results of the numerical simulations are described.

Chapter 4

Process Studies

This chapter describes studies of the processes that are involved in the formation and deep convection of Antarctic Bottom Water. These processes are investigated using various experimental configurations of the Princeton Ocean Model with idealised topography of a continental shelf having a depression, and applying a negative buoyancy flux at the sea surface to simulate salt injection by sea-ice formation. A summary of the experiments in this chapter is listed in Table B.1.

4.1 The Princeton Ocean Model

The technical details of the Princeton Ocean Model (POM) are summarised in Appendix A. The model resolution on the shelf is 3 km by 3 km so that the model is able to resolve the perturbations that break up the chimney of dense convecting fluid. The external time step is 8 seconds and the internal time step is 240 seconds which satisfy the Courant-Fredrich-Levy conditions in equations A.28 and A.29.

Bathymetric configuration

The model bathymetry is configured to be that of the Adélie Land region which is described in Section 2.1. A schematic of the model bathymetry used in Section 5.3.1 is shown in Figure 4.1. The model is orientated such that the x-axis points northwards in the offshore direction and the y-axis points westward alongshore. The coast is assumed to be straight and is along the southern boundary at $x = 0$. The basic bathymetry consists of a flat shelf, 500 m deep and 100 km wide adjacent to a continental slope of slope 1.7°. The region of the shelf that is of interest is between $y = 160$ and 430 km. A rectangular depression is located on the shelf, of size 180 km alongshore between $y = 160$ and 340 km, and 60 km offshore between $x = 18$ and 78 km and has a maximum depth of 1,000 m, so the volume of the depression is 2,100 km^3. This basic bathymetry is used in the experiments in this chapter.

Initial state

The stratification is constant with Brunt-Vaisala frequency $N^2 = 0.8 \times 10^{-6}$ s^{-2}. This low stratification is typical of the stratification found offshore of the Antarctic Slope Front and beneath the pycnocline that separates the surface water from the Circumpolar Deep Water and Antarctic Bottom Waters beneath (Foster, 1995). The model is initialised with salinity

$$S_0(z) = 34.4 - \frac{0.1}{1000} z \tag{4.1}$$

where the depth ranges from $z = -H$ at the bottom to $z = 0$ at the surface.

The temperature is maintained at $T = 0$°C throughout the whole domain. This was done in order to simplify the modelling of the processes studied and minimise the number of variables that needed to be analysed in the results. Though the addition

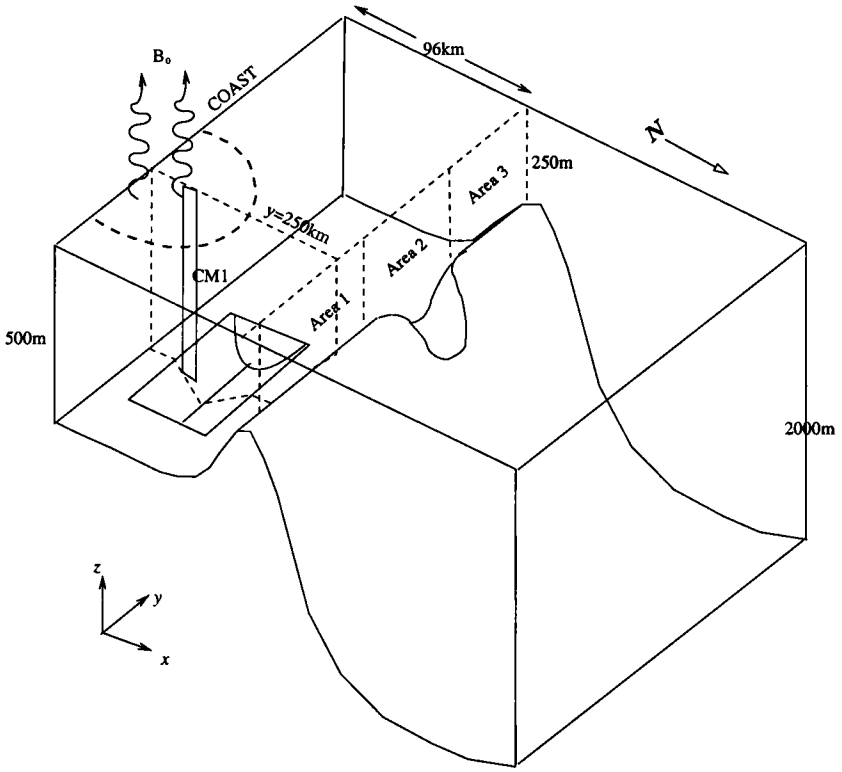

Figure 4.1: *Model bathymetry showing the location of the depression, shelf sill and channel for experiments that include these features. The dotted line at the surface outlines the basic forcing region used for most of the experiments. CM1 is the water column located at x=24 km, y=250 km where H=600 m. It is on the south bank of the depression beneath the forcing region. The three areas marked at the shelf break: Areas 1, 2 and 3 indicate the areas where the fluxes across the shelf break are measured.*

of temperature into the model would have been a small overhead to carry, analysis of the results would have to take into account the diffusion of temperature, generally in the opposite direction to the diffusion of salinity as the two dominant water masses are the cold saline water on the shelf and the warm slightly fresher CDW offshore. As the temperature-salinity balance is very delicate in the Antarctic region in keeping the hydrostatic stability, the effects of differring rates of diffusion of temperature and salinity would also have needed to be taken into account. In order to keep this study focussed on the deep water convection processes, the temperature was kept as a constant.

4.1.1 Forcing

The model is forced with a salinity flux at the surface to simulate the effects of sea-ice formation. The buoyancy forcing is ramped up to its full value over one day in order to prevent numerical instabilities. The winter period $T_{\text{winter}} = 240$ days. The forcing region is chosen to be a semi-circular area with the diameter parallel to the coast at $x = 10$ km as shown in Figure 4.1. It has a radius of 50 km surrounded by a decay width of 10 km and is centered in line with the centre of the depression. The total area of the forcing region is 7,000 km^2, and the effective open water area is $A_{\text{OW}} = 5,100$ km^2. The salt flux used in the basic experiment is equivalent to the salt released by the formation of 10 cm of ice per day, where the salinity released into the water by the ice formation is $S_{\text{surface}} - S_{\text{ice}} = 27$ psu. The buoyancy flux calculated from equation 3.1 due to the salinity flux is $B_0 = 2.39\times10^{-7}$ m^2 s^{-3}. The volume of ice formed is in this model is 1.2×10^{11} m^3, which releases 2.1×10^{12} kg of salt into the ocean.

Figure 4.2 contours the theoretical equilibrium time and salinity anomaly for externally constrained convection for forcing regions with radii $r = 0 - 150$ km and buoyancy flux

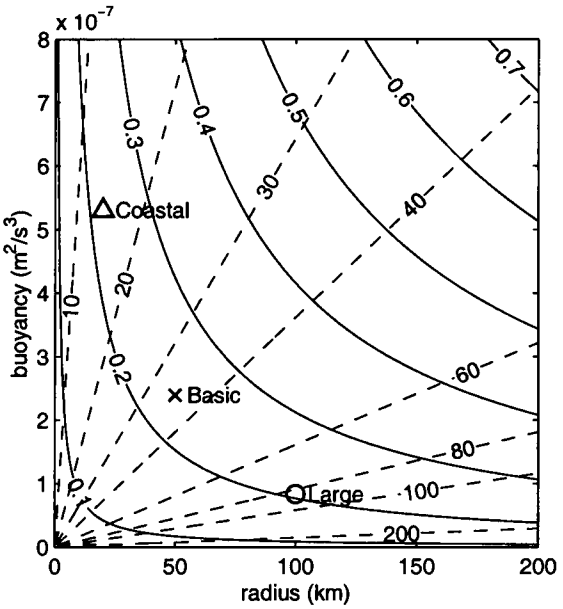

Figure 4.2: *Contours of equilibrium salinty anomaly in psu (solid line) and equilibrium time in days (dashed lines) for the externally constrained shallow convection with $W = 10$ km, $f = 1.33\times10^{-4}$ s^{-1}, $g = 9.8$ m s^{-2}, $H = 500$ m and $N^2 = 0.8 \times 10^{-6}$ s^{-2}. The '$\times$' marks the radius and buoyancy flux used for the forcing region for the basic experiment in Section 4.2, '$\bigcirc$' for the experiment with the large forcing region in Section 4.3.1 and '$\triangle$' for the experiment with the strong coastal forcing in Section 4.3.2.*

$B_0 = 0 - 8\times10^{-7}$ m^2 s^{-3}. The time to reach equilibrium, t_{eq}, is calculated from equation 3.21. The equilibrium salinity anomaly, S'_{eq}, is calculated from equations 3.22 and 3.25 for the density anomaly and multiplied by $dS/d\rho = 1.25$ psu m^3 kg^{-1} to convert to a salinity anomaly. The minimum depth beneath the forcing region, $H = 500$ m, is used to calculate the salinity anomaly plotted in Figure 4.2. Small forcing regions with strong buoyancy fluxes can have the same salinity equilibrium anomaly as large forcing regions with a weaker buoyancy flux. The smaller forcing regions reach equilibrium faster than the larger forcing regions but the larger forcing regions can affect a larger volume of water.

The buoyancy flux and the radius of the forcing region used in the experiments in this chapter are marked in Figure 4.2. Table 4.1 lists the equilibrium times and salinity anomalies calculated using the minimum, mean and maximum depths beneath the forcing

Section	Descr	radius (km)	B_0 ($\times 10^{-7}$ m^2 s^{-3})	t_{eq} (days)	S'_{eq} $H = 500$ (psu)	Mean depth (m)	S'_{eq} (psu)	Max depth (m)	S'_{eq} (psu)
4.2	Basic	50	2.39	35	0.238	668	0.191	963	0.148
4.3.1	Large	100	0.83	79	0.206	671	0.167	963	0.131
4.3.2	Coastal	20	5.30	15	0.227	510	0.223	553	0.210

Table 4.1: *Buoyancy flux and radius of the forcing regions used in this chapter, and the equilibrium times and salinities calculated using the minimum, mean and maximum depths beneath the forcing region.*

region. The salinity increase required to produce dense water with $S \geq 34.6$ psu from the initial configuration with initial surface salinity $S = 34.4$ psu is 0.2 psu. Figure 4.2 shows that the forcing used in all experiments in this chapter have an equilibrium salinity anomaly $S'_{eq} > 0.2$ psu when the minimum depth beneath the forcing region $H = 500$ m is used to calculate the equilbrium salinity anomaly.

The maximum production rate of dense water P_{DW} for the year in Sv (10^6 m^3 s^{-1}) averaged over a 360 day year is

$$P_{\mathrm{DW}} = \frac{F_{\mathrm{ice}}\,(S_{\mathrm{surface}} - S_{\mathrm{ice}})\,A_{\mathrm{OW}}\,T_{\mathrm{winter}}}{S_{\mathrm{DW}} - \overline{S}_{\mathrm{shelf}}} \times \frac{10^{-6}}{360 \times 86400} \tag{4.2}$$

where F_{ice} is the freezing rate of ice, S_{DW} is the salinity of the dense water, $\overline{S}_{\mathrm{shelf}}$ is the mean salinity of the water initially on the shelf. The above forcing is able to produce dense water with $S_{\mathrm{DW}} = 34.6$ psu at a maximum rate of 0.6 Sv, where $\overline{S}_{\mathrm{shelf}} = 34.425$ psu. The amount of salt released into the water, represented in equation 4.2 by $F_{\mathrm{ice}}\,(S_{\mathrm{surface}} - S_{\mathrm{ice}})\,A_{\mathrm{OW}}\,T_{\mathrm{winter}}$, and the $\overline{S}_{\mathrm{shelf}}$ is the same for all experiments in this chapter, therefore the maximum production rate of dense water is the same for all experiments.

The small buoyancy flux and the large radius of the forcing region result in small Rossby and Burger numbers, resulting in a system where rotation is important and

baroclinic instabilities break down the chimney. This is true for all experiments in this chapter.

4.2 Results from the basic experiment

Convection and pre-conditioning

The initial response to the negative buoyancy flux is a deepening of the mixed layer beneath the forcing region. Figure 4.3 plots the mean Brunt-Vaisala frequency N^2 of the water column CM1 depicted in Figure 4.1. CM1 is located above the south bank of the depression and beneath the forcing region. The mixed layer deepens in accordance with equation 3.6 until it reaches the bottom and the water column is homogeneous $N^2 = 0$ when $t = 6$ days. This time to homogenise CM1 is in close agreement with the time predicted $t_{bot} = 7$ days in equation 3.17. For 36% of the winter the water column is homogeneous or unstable $N^2 \leq 0$, and the mean Brunt-Vaisala frequency for the water column CM1 for winter is $N^2 = 0.6 \times 10^{-6}$ s^{-2}.

Figure 4.4a plots the mean salinity of the water column CM1. For the first 10 days the salinity of the water column increases linearly at a rate of 0.0045 psu day^{-1}. This agrees with the rate of maximum salinity increase expected from equation 3.20

$$\frac{\partial S}{\partial t} = \frac{\partial S}{\partial \rho}\frac{\rho_0 B_0}{gH} \qquad \text{where} \qquad \frac{\partial \rho}{\partial S} = 0.8 \tag{4.3}$$

(Gill, 1982, p 603) and $H = 600$ m is the depth of the water column.

Initially, the mean salinity of CM1 increases smoothly. High frequency fluctuations in the mean salinity after $t = 25$ days are evident from Figure 4.4a. These fluctuations are caused by eddies that move and mix the water, transferring dense water away from the

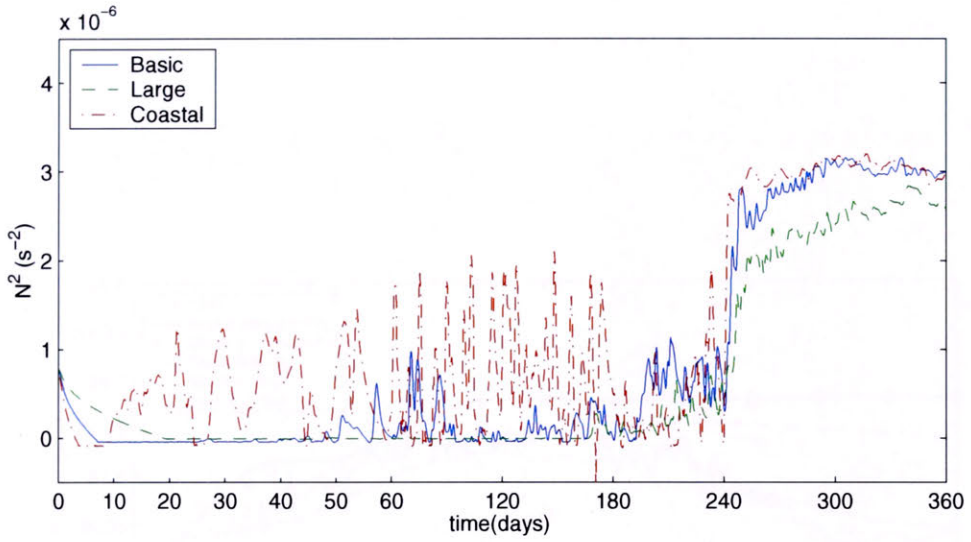

Figure 4.3: *Mean Brunt-Vaisala frequency squared N^2 in the water column CM1 in the polynya on the south bank of the depression for the basic experiment in Section 4.2 (solid line), weak forcing over a large area in Section 4.3.1 (dashed line) and strong coastal forcing in Section 4.3.2 (dash dot line). Note the extended scale for the first 60 days.*

forcing region and light ambient water beneath the forcing region. The 25 days taken by the first eddy to reach CM1, which is near the centre of the forcing region, is an indication of the time required for the eddies to break up the chimney of dense water being formed by the buoyancy forcing.

To measure the bulk effects of the forcing, the mean salinity of the water beneath the forcing region is calculated. In common with Chapman and Gawarkiewicz (1997), the area used to calculate the mean salinity does not include the area beneath the forcing decay region. The mean salinity initially increases at a rate of 0.0035 psu day^{-1} but the maximum salinity beneath the forcing region increases at a rate of 0.0039 psu day^{-1}. The maximum salinity increase predicted by equation 4.3 for a the mean depth beneath the polynya of $H = 668$ m is 0.0041 psu day^{-1}, which is very close to the value from this numerical simulation.

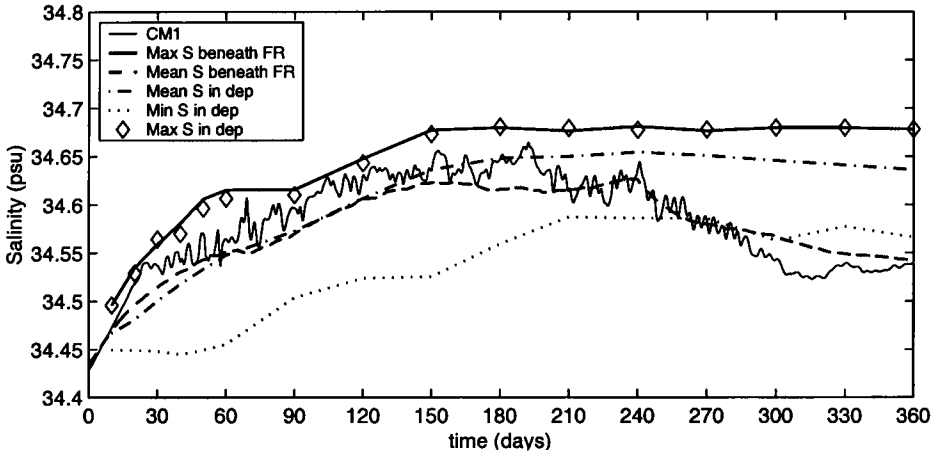

(a) Salinity

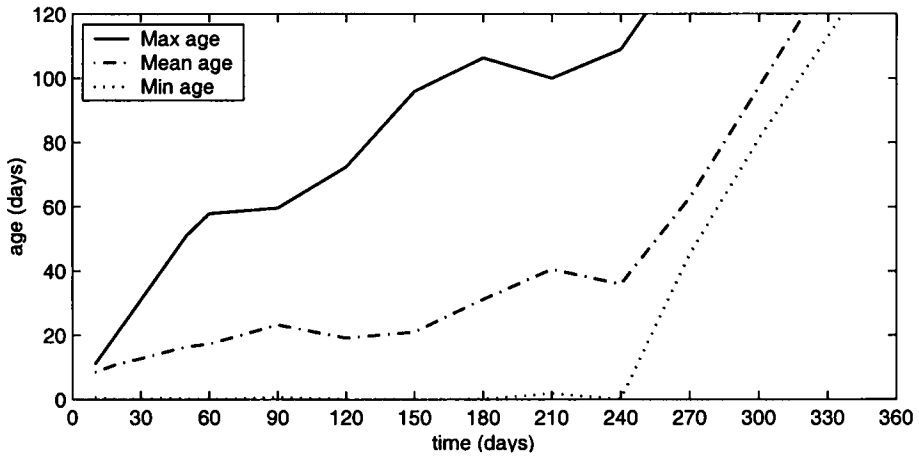

(b) Age in depression

Figure 4.4: *(a) Mean salinity of the water column CM1 (thin line), maximum (thick solid line) and mean (dashed line) salinities beneath the forcing region and mean (dash dot line), minimum (dotted) and maximum (◇) salinity in the depression for the basic experiment in Section 4.2. (b) Maximum (solid line), mean (dashed line) and minimum (dotted) age in the depression.*

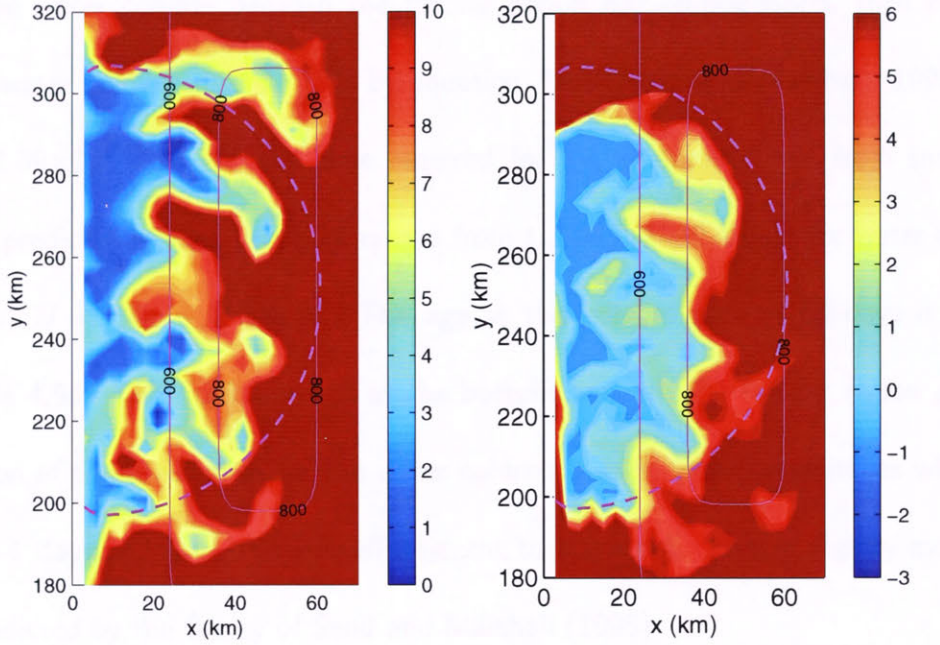

(a) Age

(b) Brunt-Vaisala freq ($\times 10^{-7}$)

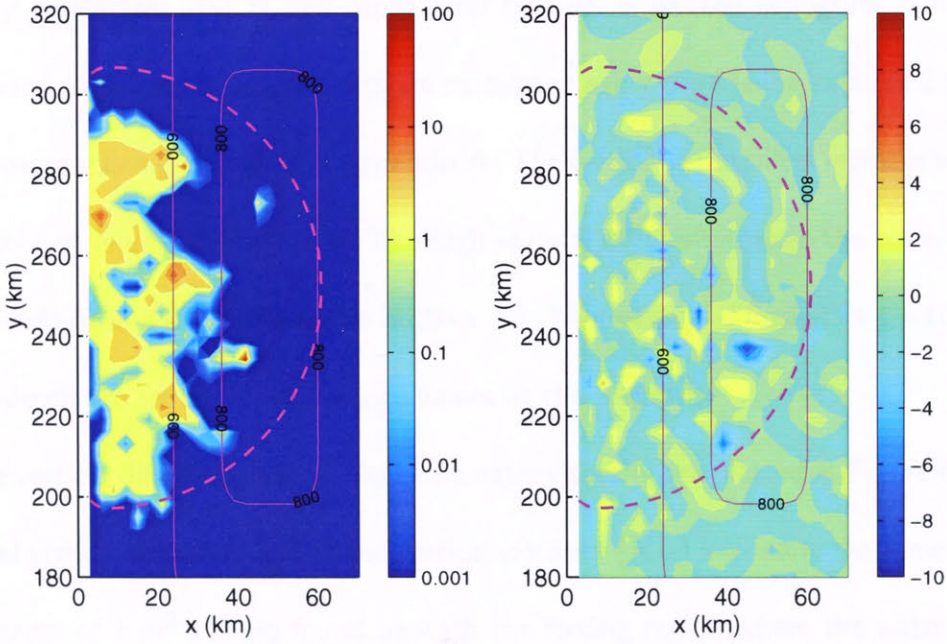

(c) Vertical diffusivity

(d) Vertical velocity

Figure 4.5: *Age at the bottom in days, mean Brunt-Vaisala frequency for the water column in s^{-2}, vertical diffusivity in $m^2\ s^{-1}$ and vertical velocity in mm s^{-1} at mid-depth after 60 days for the basic experiment in Section 4.2. The solid magenta lines are isobaths and the dashed line shows the forcing region.*

Vertical mixing beneath the forcing region

Once the water column beneath the forcing region has homogenised, then the time for the water column mix is given by equation 3.18 (Send and Marshall, 1995). For $B_0 = 2.39\times10^{-7}$ m^2 s^{-3} the time required for the column to mix from surface to bottom predicted by equation 3.18 ranges from $t_{\text{mix}} = 0.3 - 0.6$ days for water columns of height $H = 500 - 1,000$ m. The age at the bottom at $t = 60$ days is plotted in Figure 4.5a. The minimum age at the bottom beneath the forcing region gives an indication of the time taken for the water column to mix; extensive patches where the age is $\sim$1 day are found on the shelf adjacent to the coast. This is slightly more than that predicted by the theory of Send and Marshall (1995).

The mean Brunt-Vaisala frequency N^2 for the water column and the vertical diffusitivity co-efficient K_H at mid-depth after 60 days is plotted in Figures 4.5b and c. These vertical diffusivity co-efficients are calculated using the Mellor-Yamada 2.5 turbulence closure scheme described in Appendix A. The vertical diffusivities increase when the water column is unstable $N^2 < 0$. The high vertical diffusivity mixes the water column faster resulting in a lower age at the bottom, i.e., high vertical diffusivities $1 - 10$ m^2 s^{-1} at mid-depth are found above low age values at the bottom.

The vertical diffusivity and vertical kinematic viscosity are plotted in Figure 4.6. The values of vertical diffusivity (K_H) and vertical viscosity (K_M) are nearly the same. Values of the order of 1 m^2 s^{-1} are found beneath the forcing region where the water column is unstable and active vertical mixing is occuring, elsewhere the vertical kinetimatic viscosity and vertical diffusivity is less than 10^{-5} m^2 s^{-1}.

The vertical velocities at mid-depth are plotted in Figure 4.5d. The mean vertical velocity beneath the forcing region $\overline{w} \simeq 0$ mm s^{-1} suggesting that the plume beneath

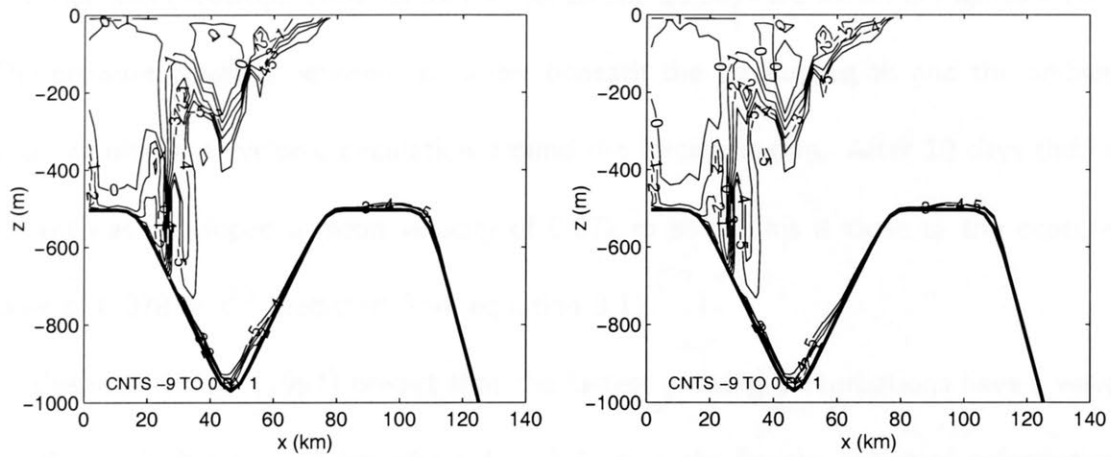

(a) Vertical diffusivity

(b) Vertical kinematic viscosity

Figure 4.6: *Vertical sections of the vertical diffusivity ($log_{10}(K_H)$) and vertical kinematic viscosity ($log_{10}(K_M)$) in $m^2\ s^{-1}$ at y=250 km after 60 days for the basic experiment in Section 4.2.*

the forcing region acts as a *"mixing agent"* (Send and Marshall, 1995). The vertical velocities beneath the forcing region in the model are $\sim$ 7 mm s^{-1}. These are smaller than the vertical velocities estimated by Send and Marshall (1995) $w_{\text{plume}} \sim u_{\text{rot}} = (B_0/f)^{1/2} = 42$ mm s^{-1}. The turbulence closure scheme used by POM is described in Appendix A. This turbulence closure scheme will enhance mixing of an unstable water column resulting in a more stable water column and lower vertical velocities.

The mixing times t_{mix} of the model are close to the theoretical values in Send and Marshall (1995). This "mixing" of the water columns beneath the forcing region predominantly takes place through vertical diffusion in the model.

Development of instabilities

As salt is added to the surface, the water near the surface becomes denser and the water parcels sink, compressing the water column. This results in an elevation gradient between the area beneath the forcing region and the water outside the forcing region. The

elevation and barotropic currents for $t = 10, 20$ and 30 days are shown in Figures 4.7a–c. The pressure gradient between the water beneath the forcing region and the ambient water results in a cyclonic circulation around the forcing region. After 10 days the rim current has developed a mean velocity of 0.072 m s^{-1}. This is close to the expected value of 0.078 m s^{-1} predicted from equation 3.11.

Cushman-Roisin (1994) predict that the fastest growing perturbations have a wavelength of $3.912 \times L = 13$ km where $L = 3.3$ km is the Rossby radius of deformation. By day 20 the rim current develops meanders of wavelength $\sim$12 km which is close to the size of the theoretical fastest growing perturbations. The mean speed beneath the forcing decay region is 0.11 m s^{-1}, while the maximum is 0.30 m s^{-1}. The velocity of the rim current predicted from equation 3.11 for $t = 20$ days is 0.15 m s^{-1}. This is greater than the mean speed of the rim current but less than the maximum speed in the numerical simulation.

The meander on the western side of the southern bank of the depression is fed by the dense water moving down the slope and turning to the left (to the west) as the dense water geostrophically adjusts. The closed depression traps this dense water. Eventually the meander separates from the uniform chimney of dense water beneath the forcing region to form an eddy. Initially this eddy is approximately 25 km in diameter. Over the next 10 days it builds momentum as it is fed by more dense water, growing to $\sim$35 km in diameter.

After day 30 the meanders around the forcing region have a regular wavelength of 15 km. These meanders develop into eddies. A spectral analysis of the time series of the velocities in the depression reveals an anti-cyclonic signal for frequecies of $1 - 2.5$ cycles per day. These eddies break up the chimney and bring the system towards equilibrium.

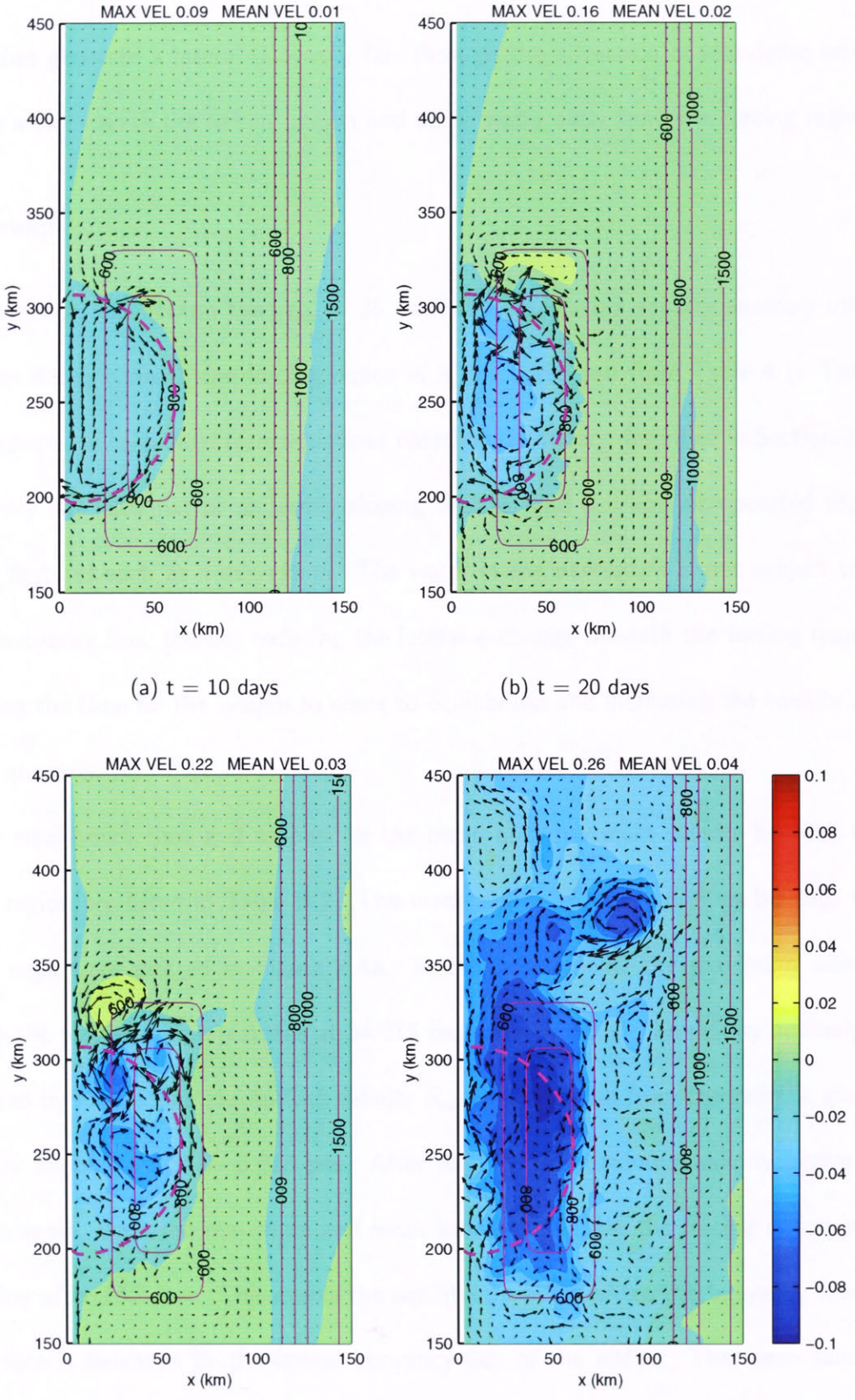

(a) t = 10 days

(b) t = 20 days

(c) t = 30 days

(d) t = 240 days

Figure 4.7: *Elevation and barotropic velocities for t = 10, 20, 30 and 240 days for the basic experiment in Section 4.2. The forcing region is marked by the magenta dashed line and the magenta isobaths are labelled in m. The units for the colorbar for the elevation are in m and the mean and maximum velocities are in m* s^{-1}.

The eddies generate a lateral buoyancy flux through the advection of less dense water into the area beneath the forcing region and dense water away from the forcing region.

Equilibrium

The theoretical equilibrium time t_{eq} = 35 days and equilibrium salinity anomaly using the mean depth beneath the forcing region is S'_{eq} = 0.191 psu from Table 4.1. These values have been calculated from equations based on the theory described in Section 3.4, this theory has used flat or uniformly sloping shelves, and has not incorporated topographic features such as a depression. The water in the depression is not subject to a lateral buoyancy flux, thereby reducing the lateral exchange beneath the forcing region, increasing the time for the system to come to equilibrium and increasing the equilibrium salinity anomaly.

The equilibrium time and salinity for the mean and maximum salinity beneath the forcing region are listed in Table B.2. The mean and maximum salinities beneath the forcing region are plotted in Figure 4.4a. In this experiment, the maximum salinity beneath the forcing region plateaus at 34.615 psu after 60 days. The salinity anomaly is calculated by subtracting the surface salinity S_{surf} = 34.40 psu from the salinity, giving a salinity anomaly of S' = 0.215 psu. After day 90, the maximum salinity begins to increase again. Both the maximum and mean salinities beneath the forcing region stop increasing after 150 days. This marks the equilibrium point where the buoyancy flux at the surface is balanced by the lateral buoyancy flux of the eddies. The mean salinity beneath the forcing region at t = 150 days is 34.623 psu (S' = 0.223 psu), this is greater than the equilibrium salinity anomaly calculated using the mean depth beneath the forcing region but less than the salinity equilibrium calculated using the depth at the

Water mass	Salinity range (psu)	Initial depth $-z$ (m)
Surface	34.4 – 34.425	0 – 250
Shelf	34.425 – 34.45	250 – 500
Depression	34.45 – 34.5	500 – 1000
Intermediate	34.5 – 34.6	1000 – 2000
Dense	34.6 –	2000 –

Table 4.2: *Water mass definitions and their initial depth range. Because temperature is kept constant in this study the water masses are defined by the salinity content only. Modified Circumpolar Deep Water (MCDW) is a combination of the water masses with* $S > 34.45$ *psu but has the added constraint that the surface tracer concentration* $c < 0.02$.

coast.

The equilibrium maximum salinity beneath the forcing region is 34.677 psu ($S' = 0.277$ psu). This salinity anomaly is higher than the expected equilibrium salinity anomaly for this forcing over flat topography of depth 500 m by 0.039 psu. The presence of the depression in the shelf beneath the forcing region increases the equilibrium maximum salinity. The maximum salinity beneath the forcing region remains at 34.679 ± 0.002 psu from day 150 to the end of the summer.

Water in the depression

The depression acts to trap and store dense water. The newly formed dense water flushes the less dense water out of the depression. Water masses defined by their salinity are listed in Table 4.2. The composition of water masses in the depression and on the shelf are plotted in Figure 4.8. Figure 4.8a shows that nearly all the water initially in the depression is replaced with 'intermediate' water in 60 days. 'Intermediate' water is newly formed water with salinity greater than that of the water initially in the depression. After all the water initially in the depression has been flushed out the minimum salinity in the depression shown in Figure 4.4a begins to increase and the maximum age shown in Figure 4.4b increases at a slower rate.

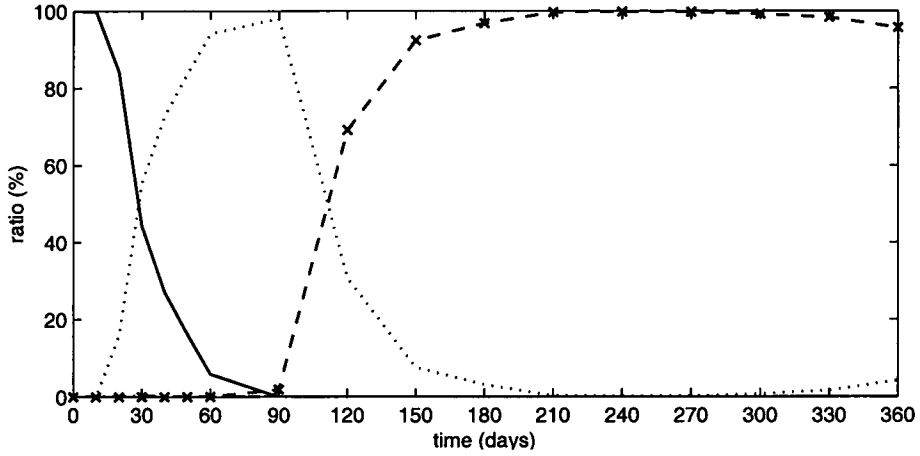

(a) Depression

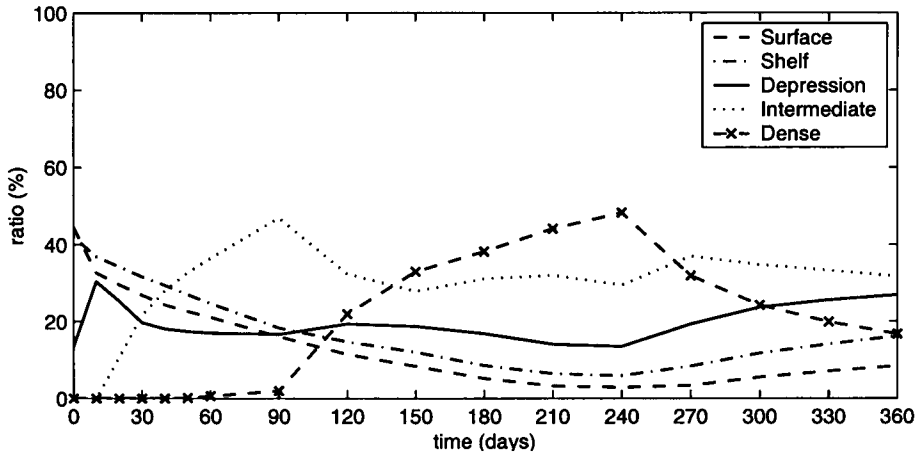

(b) Shelf

Figure 4.8: *Breakdown of water masses (a) in the depression and (b) on the shelf for the basic experiment described in Section 4.2. The water masses are defined in Table 4.2.*

The maximum salinities beneath the forcing region and in the depression are plotted in Figure 4.4a. These are generally the same as the area beneath the forcing region includes the deepest part of the depression where the maximum salinity on the shelf is generally located. From $t = 40 - 150$ days the maximum salinity beneath the forcing region is slightly greater than in the depression because the maximum salinity beneath the forcing region is located on the shelf between the coast and depression, this being where the bathymetry is the shallowest.

From day 120 onwards the mean salinity in the depression is significantly higher than the mean salinity beneath the forcing region as evident from Figure 4.4a. This is due to the lack of advection of less dense water into the depression which does occur above the depression. By day 150 when the mean salinity of the water beneath the forcing region has reached an equilibrium of 34.623 psu, the mean salinity in the depression is 34.636 psu and continues to increase by trapping the densest water from beneath the forcing region, until the end of winter when it reaches 34.654 psu and is completely filled with 'dense' water as shown in Figure 4.8a.

At the end of the winter, $t = 240$ days, the age of the water in the depression ranges from 0.01 to 109 days as shown in Figure 4.4b. The mean age is 36 days, which implies that the buoyancy forcing flushes the depression over $\sim$36 days. During the summer, when the forcing has stopped, there is little exchange of water in or out of the depression. This results in only a small decrease of 0.018 psu in the mean salinity in the depression. The decrease in the mean salinity beneath the forcing region during the summer is 0.147 psu, which is much larger and indicates a large influx of less dense water into the area beneath the forcing region.

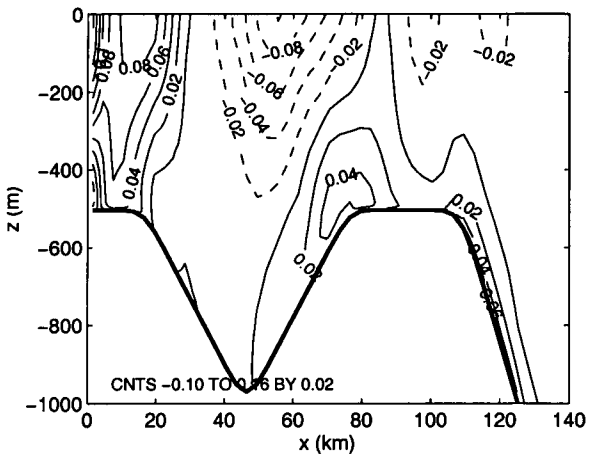

Figure 4.9: *Time averaged alongshore velocity at y=250 km for the basic experiment in Section 4.2.*

Kinetic energy on the shelf

During winter the circulation on the shelf consists a barotropic cyclonic circulation beneath the forcing region. This circulation breaks down into eddies of diameter ~20 km having velocities of $0.1 - 0.2$ m s^{-1}. Another feature of the circulation on the shelf is the westward coastal current with speeds reaching 0.2 m s^{-1}.

The elevation and barotropic velocity for $t = 240$ days is shown in Figure 4.7d. The kinetic energy on the shelf is predominantly stored in eddies of diameter $10 - 30$ km. These eddies break down the dense water chimney according to Cushman-Roisin (1994) who states that only perturbations greater than 9 km break up the chimney (see page 34).

As the density of the water beneath the forcing region increases and the density difference between the newly formed water and the ambient water increases, the horizontal density gradients also increase. This results in increases in the vertical shear through the thermal wind balance, and an increase in the baroclinic energy. This leads to kinetic energy being concentrated at the surface and at the bottom. On average the baroclinic energy is 1.5 times the barotropic energy.

The time averaged alongshore velocity at $y = 250$ km is plotted in Figure 4.9. At

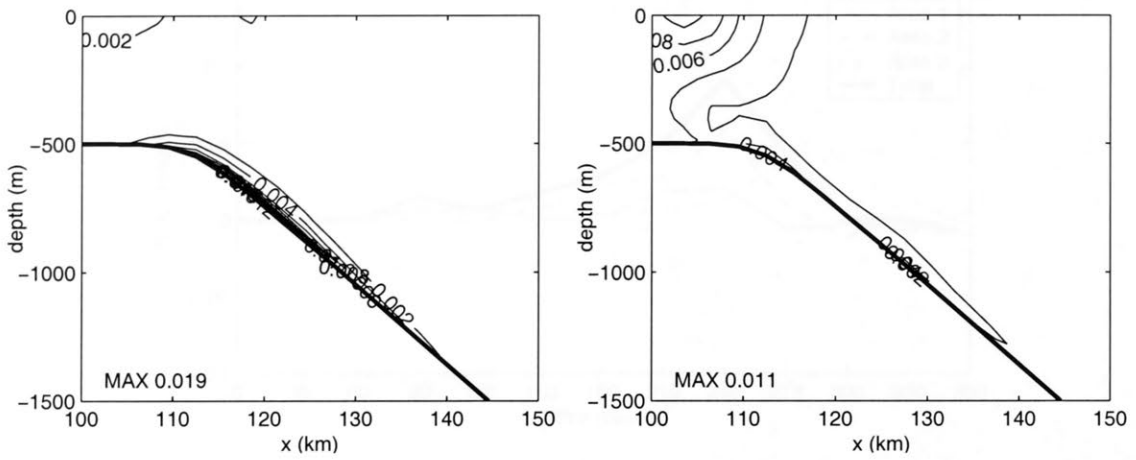

(a) Mean kinetic energy (b) Eddy kinetic energy

Figure 4.10: *Mean and eddy kinetic energy for day 240 for exp 197, calculated for by taking the alongshore mean and variance between $y = 160 - 430$ km. Offshore of the shelf break where the topography is uniform alongshore ($x > 90$ km), the alongshore averages of the velocities and their variances are calculated in order to determine the mean kinetic energy and the eddy kinetic energy. The contour are at 0.002 unit intervals and the units are in $m^2\ s^{-2}$.*

the coast there is a strong westward current of width 20 km and with average velocity of 0.1 m s^{-1}, this current is very persistent and reaches speeds of up to 0.2 m s^{-1}. A second westward current is found on the floor above the the northern bank of the depression at $x = 80$ km. A return eastward flow of $\sim$0.1 m s^{-1} exists beneath the surface above the depression.

Eddy variability

To determine the impact of eddy variability, the mean and eddy kinetic energy was calculated by taking the alongshore average of the velocity and squaring it and the alongshore variance of the velocity. The mean and eddy kinetic energy for day 240 are plotted in Figure 4.10.

On the shelf, the eddy kinetic energy dominates. Whereas on the slope, the mean kinetic energy dominates.

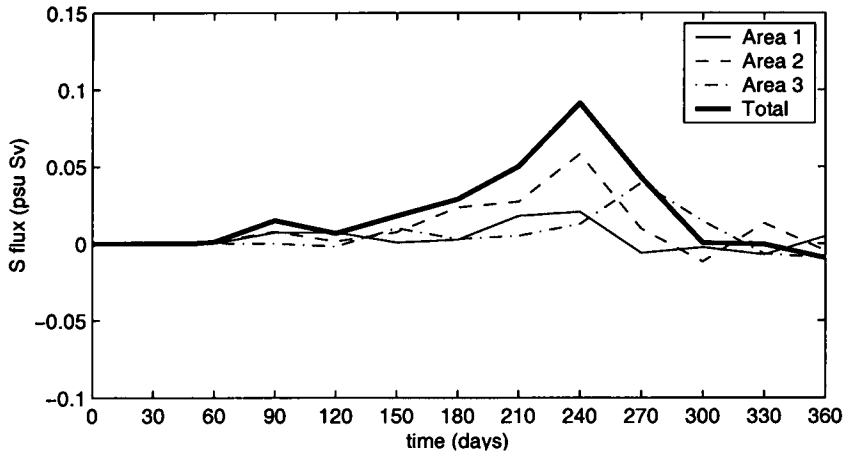

Figure 4.11: *Salinity fluxes across the shelf break (x=96 km) divided into three areas for the basic experiment in Section 4.2. Area 1 eastern half of the depression, Area 2 western half of the depression, Area 3 west of the depression.*

Fluxes across the shelf break

An estimation of the offshore component of the salt flux at $x = x_0$ is adapted from the density flux used by Gawarkiewicz (2000, equation 15), this being

$$\int_{-H}^{0} \int_{\text{alongshore}} u(x_0, y, z, t)\ [S(x_0, y, z, t) - S(x_0, y, z, t = 0)]\ dy\ dz \tag{4.4}$$

where $u(x_0, y, z, t)$ is the cross-shelf velocity at $x = x_0$ and $S(x_0, y, z, t)$ is the salinity at time t and $S(x_0, y, z, t = 0) = S_0(z)$ is the initial salinity defined in equation 4.1. The on and offshore volume transports and the net salinity transports across the shelf break $x = 96$ km between $y = 160$ and 430 km are listed in Table B.3. The 1.61 Sv onshore and 1.39 Sv offshore transport at the shelf break is predominantly caused by the eddies shown in Figure 4.7d. Figure 4.11 shows the salinity fluxes across the shelf break for three areas along the shelf break: Area 1 from $y = 160 - 250$ km, offshore of the eastern half of the depression; Area 2 from $y = 250 - 340$ km, offshore of the western half of the depression; and Area 3 from $y = 340 - 430$ km.

During winter, 60% of the salinity transport across the shelf break occurs through

Area 2 (western half of the depression), 27% through Area 1 (eastern half of the depression) and 13% through Area 3 (west of the depression). The maximum salt flux across the shelf break occurs at the end of winter when there is a large build up of dense water on the shelf, shown in Figure 4.8b and dense water formation is still occurring. This results in dense water being pushed over the shelf break.

Dense water is defined as water that has $S \geq 34.6$ psu, this water being potentially dense enough to reach the abyssal bottom depth of 2,000 m. During winter, the volume of dense water that is transported offshore over the shelf break is 1.40×10^{12} m^3, and a further 0.53 $\times 10^{12}$ m^3 flows over the shelf break during the summer. This total of 1.93×10^{12} m^3 per year equates to 0.062 Sv of dense water being transported over the shelf break.

Modified Circumpolar Deep Water (MCDW) is a warm water mass found offshore of the Antarctic shelf and intrusions of this water mass on the shelf are believed to assist in keeping the polynya open. In this study the temperature is kept constant and MCDW cannot be identified by its warmer temperature. Here, MCDW is defined as water with a low surface tracer concentration $c < 0.02$ and $S > 34.45$ psu. All water below a depth of $z = 500$ m is initialised as MCDW. Most of this water is located in the deep ocean, the only water on the shelf that is MCDW is found in the depression. The onshore transport of MCDW across the shelf break is 0.075 Sv.

On the slope

As the dense water forms on the shelf some of it overflows onto the slope in plumes. These plumes of dense water grow in width, height and become denser over time. At day 90 the plumes of dense water at the start of the slope ($x = 105$ km) have a width

of ~20 km, height 100 – 200 m and mean salinity of 34.477 psu. The mean salinity anomaly of the plume is

$$\overline{S'}_{pl} = \overline{S(x,y,z,t) - S_0(z)} \qquad \text{where} \qquad c \geq 0.02 \tag{4.5}$$

where $S_0(z)$ is the initial (and also the ambient) salinity defined in equation 4.1 and c is the concentration of the surface tracer. The surface tracer is a passive marker of the water that originates from the forcing region and is described in Appendix A. The mean salinity anomaly of the plume $\overline{S'}_{pl}$ is an indication of the buoyancy of the plume, as the plume approaches its equilibrium depth z_{eq}, $\overline{S'}_{pl} \rightarrow 0$. The mean salinity anomaly of the plume at $t = 90$ days and $x = 105$ km is $\overline{S'}_{pl} = 0.03$ psu. By day 210 the width of the plume grows to ~35 km, height 400 m, mean salinity 34.496 psu, and $\overline{S'}_{pl} = 0.06$ psu. The Rossby radius of deformation calculated from equation 3.32 is $L_{\text{slope}} = 1.6 - 3.2$ km. Land-Serff and Baines (1998) found that the downslope excursion of the flow before turning left is $2.3 \times L_{\text{slope}} = 3.7 - 7.4$ km offshore. When the plume first moves onto the slope, it turns left within 10 km of the start of the slope which is in close to the values predicted by Land-Serff and Baines (1998).

Figure 4.12 shows the salinity, salinity anomaly, surface tracer concentration, age, and across-shelf and alongshore velocities at $y = 372$ km (10 km west of the depression) at $t = 240$ days. The plume has a height of ~200 m and reaches a depth of 1,700 m. The core of the plume is found above the 1,000 m isobath, where the salinity anomaly, surface tracer concentration and alongshore velocity are maximum. The age of the water in the plume is younger than the surrounding water showing that this water has recently been at the surface.

The plume thins as it penetrates greater depths. This results in an increasing Ekman

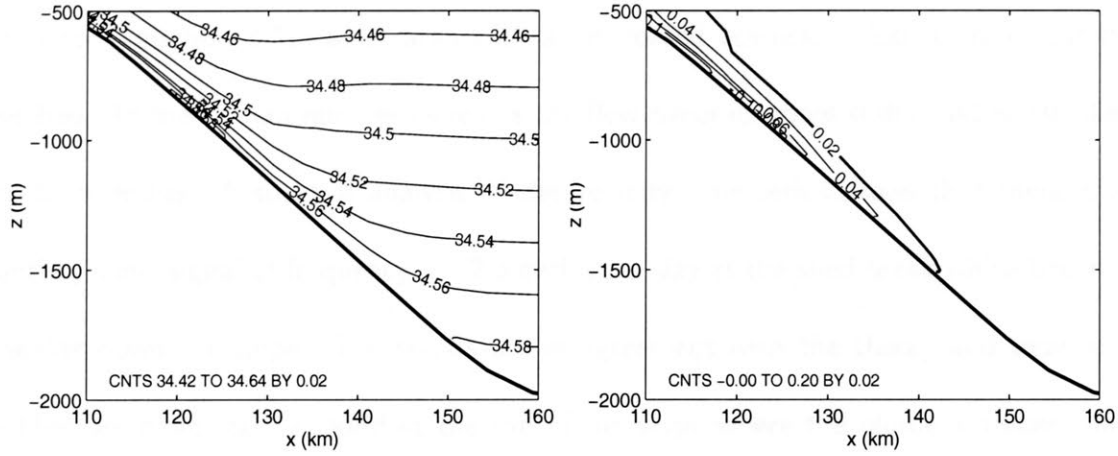

(a) Salinity

(b) Salinity anomaly

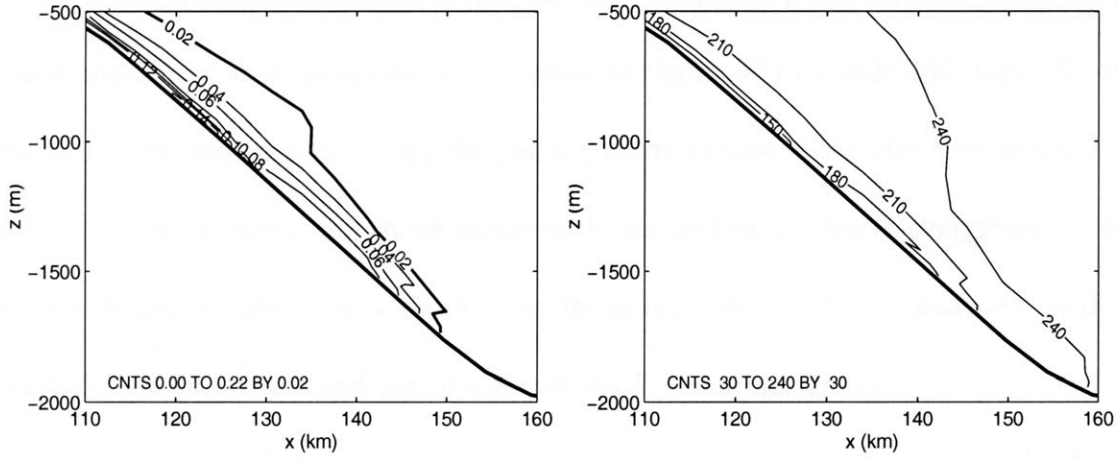

(c) Surface tracer concentration

(d) Age

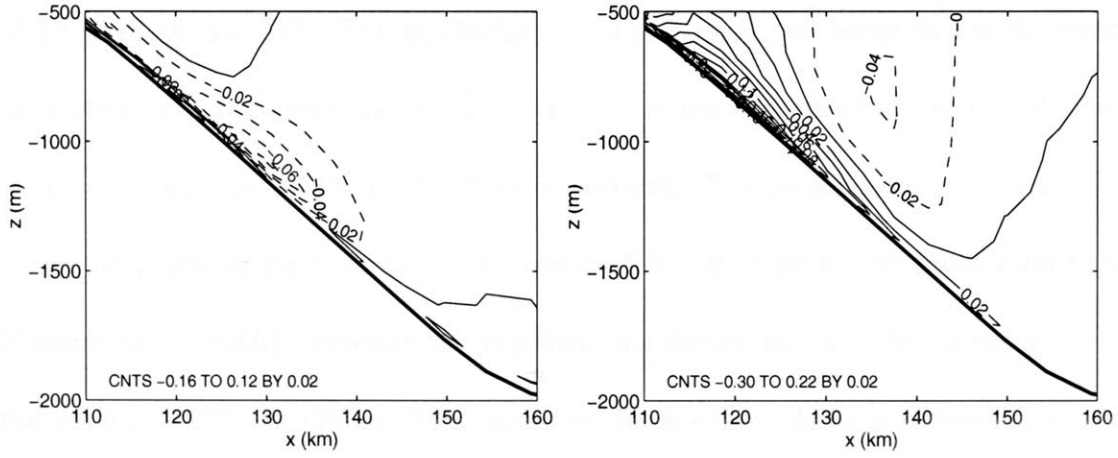

(e) Across-shelf velocity

(f) Alongshore velocity

Figure 4.12: *(a) Salinity (psu), (b) salinity anomaly (psu), (c) surface tracer concentration, (d) age (days), and (e) across-shelf and (b) alongshore velocities (m s^{-1}) on the slope at y=372 km after t=240 days for the basic experiment in Section 4.2.*

number (equation 3.31) associated with an increased downslope Ekman flux near the seabed. As the Ekman number increases the flow becomes more stable and is less likely to form eddies. A spectral analysis of the velocity time series shows that there is an anti-cyclonic signal of frequency $1 - 2.5$ cycles per day at the shelf break which becomes weaker down the slope. The results are in agreement with the theory and show that eddies are more readily found at the top of the slope where the plume is thicker than towards the bottom of the slope where the plume is thinner and more stable.

Figure 4.13 shows along-slope sections of salinity, surface tracer concentration, along-shore and across-shelf velocities on the slope at depth 970 m after 240 days. As the plume travels westward ($y \rightarrow \infty$) the plume becomes more saline, the concentration of surface tracer increases, the plume becomes thicker and moves faster alongshore. In the bottom boundary layer, the offshore velocities increase with distance westward, as does the salinity of the water and the concentration of the surface tracer.

Over time the plume of dense water continues to move westward and down the slope. The downslope extent of the plume increases until it reaches a maximum depth of 1,870 m by day 270. The equilibrium depths of undiluted water in the depression calculated using the mean and maximum salinity in the depression at the end of winter in equation 3.26 are 2,540 and 2,770 m respectively. Due to entrainment of less dense water the plume is expected to reach between $0.5 - 0.75$ times the equilibrium depth (Gawarkiewicz, 2000), therefore the expected equilibrium depth of the dense water on the slope is $1,270 - 2,080$ m. The maximum depth of the plume is within this range.

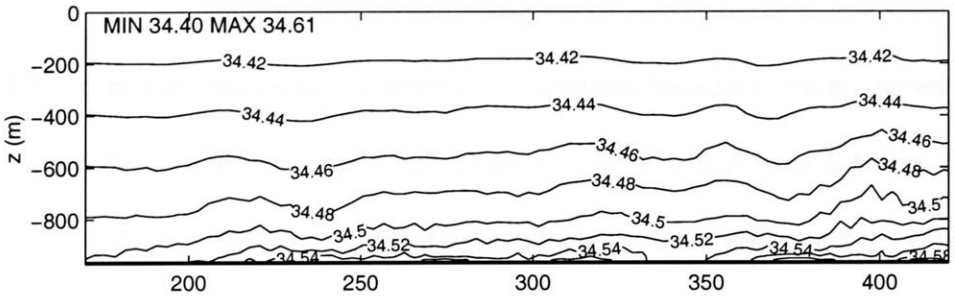

(a) Salinity

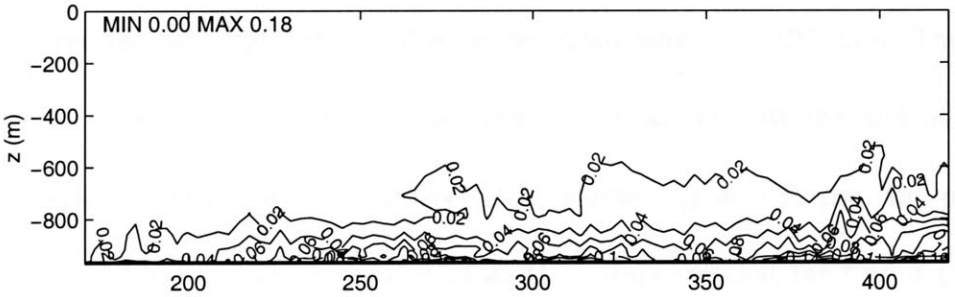

(b) Surface tracer concentration

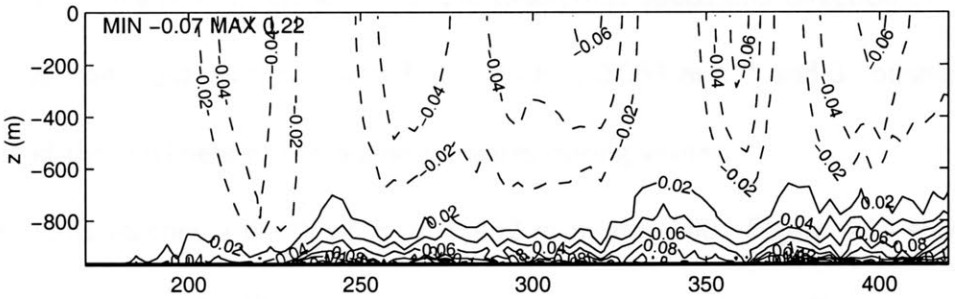

(c) Alongshore velocity

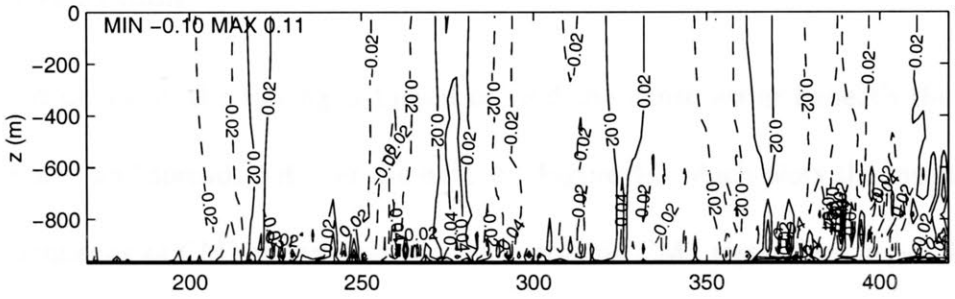

(d) Across-shelf velocity

Figure 4.13: *Along slope sections of (a) salinity, (b) surface tracer concentration (c) alongshore and (d) across-shelf velocities along the slope at x=126 km, depth 970 m after 240 days for the basic experiment in Section 4.2.*

Bulk flow of the plume

Figure 4.14 plots the mean salinity anomaly, thickness, Ekman number, speed and direction of the dense plume on the slope at depths $H = 970$ m and 1,492 m between $y = 340$ and 430 km. The Ekman number is calculated from equations 3.29 and 3.31. The theoretical speed and direction are calculated from equations 3.27 and 3.28 and plotted with the speed and direction of the plume in the model.

The plume reaches depth $H = 970$ m on the slope when $t = 120$ days. The plume continues to thicken and becomes denser throughout winter. At the end of winter, $t = 240$ days, the mean salinity anomaly of the plume $\overline{S'}_{pl} = 0.35$ psu, the plume is 338 m thick, and has an Ekman number of $2{\times}10^{-5}$, implying that the flow is generally stable. The plume travels at a speed of 0.050 m s^{-1} at an angle of 1.4° downslope of the isobaths. This is in agreement with the theoretical speed and direction of a plume determined from equations 3.27 and 3.28, which is 0.063 m s^{-1} and 3° offshore. The salinity and the thickness of the plume increases during winter.

The plume reaches a depth of $H = 1,492$ m by day 180. Figure 4.14 shows that the plume is thinner, the $\overline{S'}_{pl}$ decreases and the alongshore velocity decreases.

Summer relaxation

At the end of winter the forcing is turned off and the dense water beneath the forcing region relaxes and spreads out over the bottom. Figure 4.3 which plots the mean Brunt-Vaisala frequency of CM1 shows that the water column CM1 restratifies in ~8 days. At the end of the summer $t = 360$ days, the mean stratification is $N^2 = 3 \times 10^{-6}$ s^{-2}; this is 4 times greater than the initial stratification.

During summer $t = 240 - 360$ days, the mean salinity beneath the forcing region

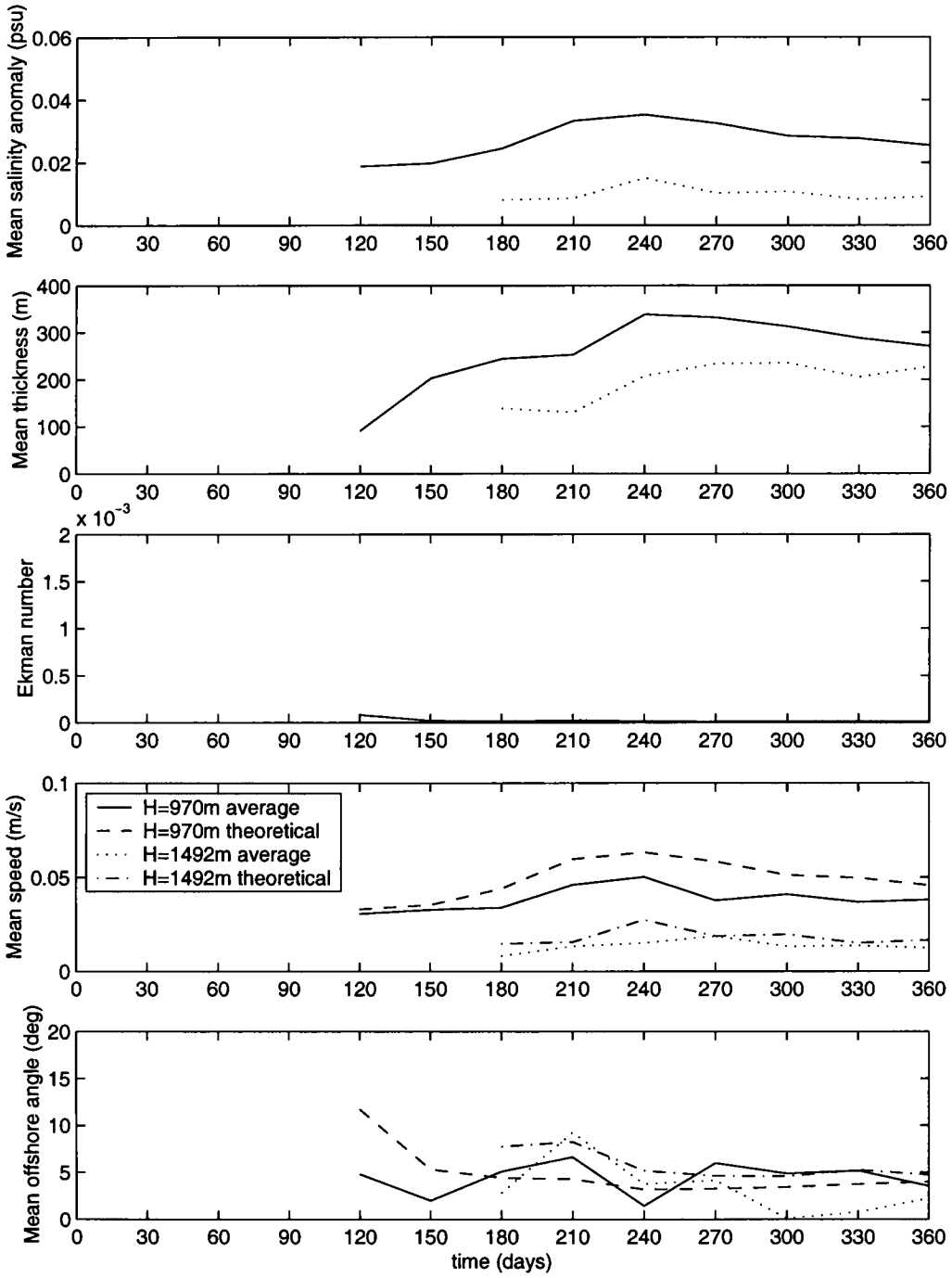

Figure 4.14: *The mean salinity anomaly, thickness, Ekman number, speed and direction of the plume at x=129 km, H=970 m (solid line) and 1,492 m (dotted line), between y = 342 and 432 km. The plume is delineated from the ambient water by a surface tracer concentration of 0.02 for the basic experiment in Section 4.2. The theoretical values for the speed and direction of the plume are calculated from equations 3.28 and 3.28 and plotted for H=970 m (dashed line) and H=1,492 m (dash-dot line).*

shown in Figure 4.4a decreases from 34.626 to 34.452 psu, and the mean salinity on the shelf decreases from 34.563 to 34.495 psu. Figure 4.8 shows a large decrease in the volume of 'intermediate' and 'dense' water masses with $S \geq 34.5$ psu, whereas there is only a small loss of 'dense' water from the depression. The mean salinity of the water in the depression shown in Figure 4.4a decreases only slightly during summer, from 34.654 to 34.636 psu. The age of the water in the depression shown in Figure 4.4b increases with the age of the model, indicating that no more "new" dense water moves into the depression.

4.3 The effect of size of the forcing region, and the strength of forcing

Two additional experiments were carried out with the same bathymetry and same total salt flux as the previous experiment, one with a weaker buoyancy flux over a larger region, and the other with a stronger buoyancy flux over a narrower region extending 20 km from the coast. The ice formation rate was chosen such that the total ice formation and therefore salt flux produced by this forcing is the same as the basic experiment in Section 4.1.1.

4.3.1 Large weak forcing region

This experiment has a forcing region of radius 90 km and a decay width of 10 km. The area of the forcing region is thus 18,000 km^2, and the open water area $A_{OW} = 14,900$ km^2. The forcing region covers the entire depression and extends out to the shelf break. The ice formation rate was set at 3.5 cm day^{-1}, equivalent to a buoyancy

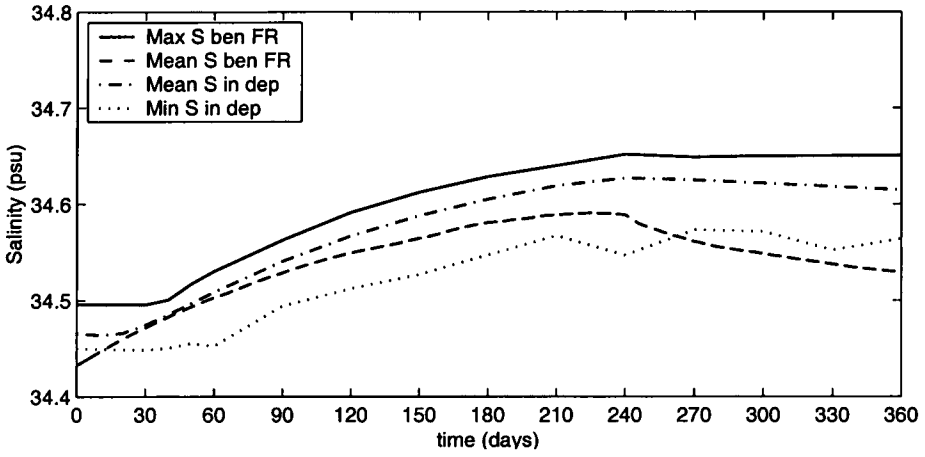

Figure 4.15: *Mean and maximum salinities beneath the forcing region and mean and minimum salinities in the depression below 500 m for the experiment with the weak forcing over a large forcing region described in Section 4.3.1.*

flux of 8.3×10^{-8} m^3 s^{-2}.

Figure 4.3 plots the mean Brunt-Vaisala frequency for the water column CM1. It takes 19 days for the CM1 water column to homogenise, which is in agreement with the time calcuated from equation 3.17. Once the water column is homogenised the time predicted by equation 3.18 for the water columns beneath the forcing region to mix is $t_{\text{mix}} = 0.5 - 0.9$ days. The youngest water parcel on the bottom beneath the forcing region has a mean value of 0.8 days during the winter, which is within the range of predicted values.

The theoretical time required to reach equilbrium listed in Table 4.1 is 79 days. The mean and maximum salinities beneath the forcing region, and the mean salinity in the depression plotted in Figure 4.15 are still increasing at $t = 79$ days, in fact at the end of winter $t = 240$ days, the salinties are still increasing, though at a slower rate. The maximum salinity at the end of winter beneath the forcing region is 34.652 psu ($S' =$ 0.252 psu). This maximum salinity is 0.054 psu greater than the expected equilibrium salinity calculated using the depth at the coast. The mean salinity beneath the forcing region reaches 34.589 psu ($S' = 0.189$ psu), and this is greater than the maximum

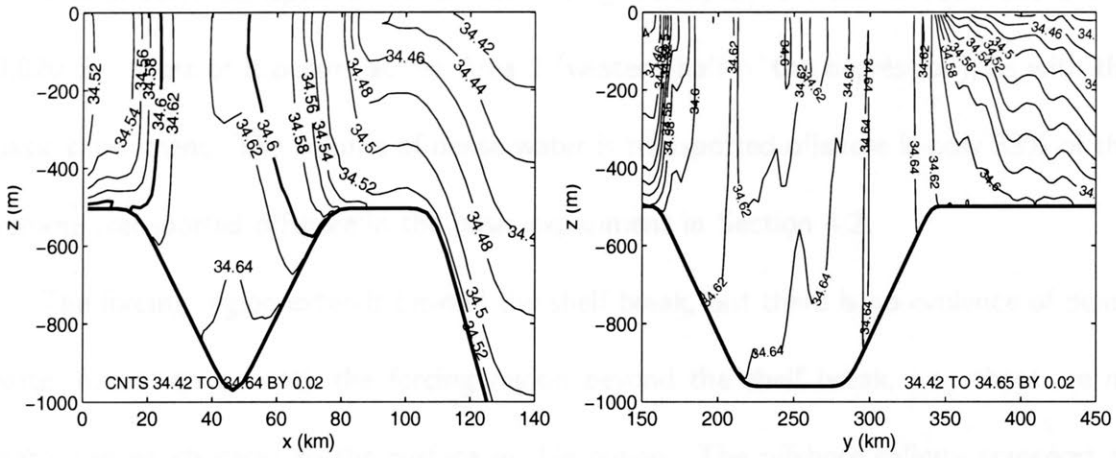

(a) Across-shelf section

(b) Alongshore section

Figure 4.16: *Salinity sections through the centre of the depression after 240 days for the large polynya experiment described in Section 4.3.1. (a) Across-shelf section at y=250 km and (b) alongshore section at x=48 km.*

salinity anomaly calculated from the mean depth, but less than the maximum salinity anomaly calculated from the minimum depth beneath the forcing region.

The cross-shelf and alongshore sections of the salinity in the depression after 240 days are plotted in Figure 4.16. The most saline water is found at the centre of the forcing region which is located above the depression. The dense water forms in the centre of the depression and spreads out into the depression and is trapped there. The mean age, mean salinity and maximum salinity in the depression are listed in Table B.3. The mean age of the water in the depression is 11 days, which is much younger than the mean age of the water in the depression in the basic experiment. This is most likely due to the fact that the water being formed beneath the forcing region has not reached equilbrium and is still increasing in salinity. This means that the newly formed water is denser than the water in the depression, therefore the flushing of the depression is accomplished in less time. The salinities in the depression at the end of winter are 0.02 psu less than the corresponding salinities in the basic experiment.

The offshore transport of dense water ($S \geq 34.6$ psu) is listed in Table B.2 and is 0.020 Sv. Most of it occurs across Area 2 (western half of the depression), as with the basic experiment. The volume of dense water is transported offshore is only 33% of the volume transported offshore in the basic experiment in Section 4.2.

The forcing region extends beyond the shelf break, but there is no evidence of dense water formation beneath the forcing region beyond the shelf break, i.e., there are no isohalines which come to the surface in this region. The offshore salinity transport at $x = 111$ km (offshore of the forcing region) is greater than the offshore salinity transport at the shelf break. This indicates that the surface salt flux offshore of the shelf break contributes to the offshore salinity flux but does not produce dense water that can form bottom water.

The equilibrium depth of the water in the depression is $1,180-1,870$ m. The surface tracer reaches a maximum depth of 1,870 m after 270 days which is the range of the equilibrium depths of the water in the depression.

Large weak forcing continued into winter

To determine the equilibrium time and salinity for the large weak forcing experiment, the same forcing configuration is used but it does not stop after 240 days, instead it continues throughout summer. As stated previously the theoretical time required for this forcing to reach equilibrium listed in Table 4.1 is 79 days. The equilibrium times and salinities for this experiment are listed in Table B.2. The mean salinity of the water beneath the forcing region reaches an equilibrium of 34.592 psu after 250 days. The maximum salinity beneath the forcing region reaches an equilibrium of 34.662 psu after 315 days. The mean salinity in the depression reaches an equilibrium of 34.638 psu after

330 days. The maximum salinity in the depression keeps increasing until it reaches an equilibrium value of 34.663 psu after 345 days.

4.3.2 Strong coastal forcing

The forcing region for this experiment is a half ellipse, with a semi major axis of 50 km alongshore and semi minor axis of 20 km offshore. The depression begins 18 km from the coast and most of the forcing region lies above the shelf between the coast and the depression. The decay width is 10 km and extends over the depression. The area of the forcing region is 4,000 km^2 and overlies a mean depth of 510 m. The ice formation rate is set at 22 cm day^{-1} and results in a buoyancy flux of 5.3×10^{-7} m^2 s^{-3}. In common with the previous experiment, this produces the same amount of ice and total salt flux as the basic experiment in Section 4.2.

The mean Brunt-Vaisala frequecy of the water column CM1 is plotted in Figure 4.3. The water column takes 3 days to homogenise which is in agreement with the time calculated in equation 3.17. However it remains homogeneous for 14% of the winter which is less than half the time compared to the basic forcing experiment. This is due to the forcing region in this experiment being smaller than the basic forcing region, so that the chimney produced is also smaller, and therefore more easily restratified by the lateral advection of less dense water beneath the forcing region. Increased horizontal gradients caused by the stronger forcing can result in baroclinic instability which assists in the irreversible breakdown of the dense water columns.

Once the water column is homogenised the time predicted by equation 3.18 for the water columns beneath the forcing region to mix is $t_{\text{mix}} = 0.2$ days. The youngest water parcel on the bottom beneath the forcing region has a mean value of 0.3 days during

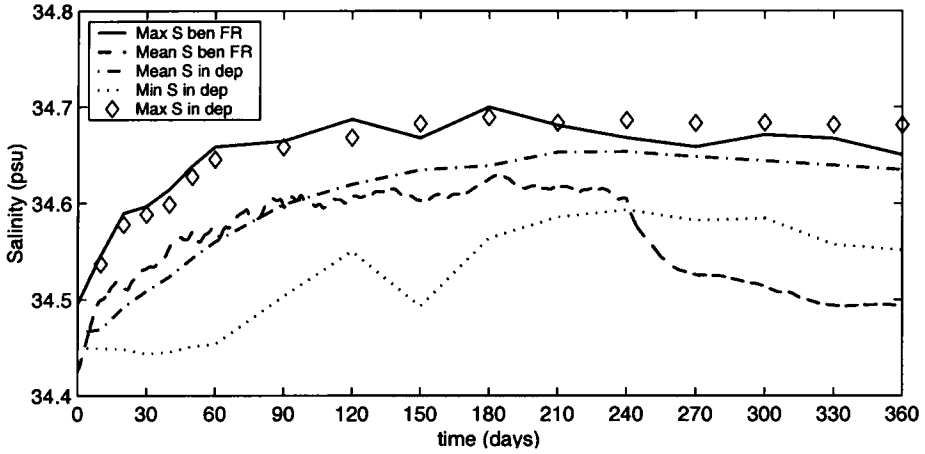

Figure 4.17: *Mean and maximum salinities beneath the forcing region and maximum, mean and minimum salinities in the depression for the coastal forcing experiment described in Section 4.3.2. In experiments with larger forcing regions, the maximum salinity beneath the forcing region included the depression, but because this forcing region is not over the depression, the maximum salinity in the depression has also been plotted.*

the winter, which is in close agreement with the predicted value.

The theoretical equilibrium time and salinities are listed in Table 4.1 and Table B.2 lists the equilibrium times and salinities for this experiment. Figure 4.17 shows that the mean salinity beneath the forcing region does not reach equilibrium until $t = 80$ days, this is 65 days more than the theoretical equilibrium time. The equilibrium mean salinity beneath the forcing region is 34.610 psu ($S' = 0.210$ psu) which is equal to the theoretical equilibrium salinity anomaly calculated using the maximum depth beneath the forcing region. The maximum salinity beneath the forcing region reaches an equilibrium value of 34.687 psu after 120 days, giving a salinity anomaly of 0.287 psu. This equilibrium maximum salinity anomaly is greater than the theoretical equilibrium salinity anomalies.

Dense water forms on the narrow, shallow shelf between the coast and the depression, beneath the forcing region. During winter, the maximum salinity beneath the forcing region represented by the solid line in Figure 4.17, is generally greater than the maximum salinity in the depression represented by the '$\diamond$'. In summer when the dense water stops

forming and drains into the depression, the maximum salinity in the depression is greater than the maximum salinity beneath the forcing region.

The salinities beneath the forcing region fluctuate due to the lateral buoyancy fluxes due to the advection of less dense water from outside the forcing region to the area beneath the forcing region. The maximum salinity in the depression increases steadily with time until it reaches an equilibrium of 34.689 psu after 180 days. The mean and maximum salinity of the water in the depression does not fluctuate because the water in the depression is not subject to this lateral buoyancy flux, though water of lower density does enter the depression dropping the minimum salinity in the depression substantially.

The mean age, mean salinity and maximum salinity in the depression at the end of winter $t = 240$ days is listed in Table B.2. The mean age is greater than the mean age of the basic and large experiments possibly due to the stronger forcing in the smaller forcing region. The stronger forcing results in the mean salinity of the water beneath the forcing region to be higher than those with a weaker forcing region, as the total surface salinity flux for all experiments is the same, it means a smaller volume of dense water is "formed". The mean and maximum salinities in the depression are higher than those of the basic and large experiments.

For the strong coastal forcing experiment the volume of dense water transported offshore is 0.028 Sv. The surface tracer reaches a maximum depth of 1,950 m after 240 days, which is within the range of equilibrium depths of the mean and maximum salinities of the water in the depression, i.e., $1,310 - 2,150$ m.

4.4 Summary

In the experiments described in this chapter, the initial increase of salinity in the water column CM1 at the centre of the polynya is proportional to the buoyancy flux as expected from equation 3.20. The time taken for the water column to homogenise agrees with the time calculated from equation 3.17. Once the area beneath the forcing region has homogenised, the minimum age at the bottom beneath the forcing region, which reflects the time taken for a water column to mix, is close to the time calculated in equation 3.18. Over time, the eddies which develop at the rim of the forcing region move into the centre and the salinity of CM1 is subject to high frequency fluctuations. In order to analyse the effect of the forcing, the maximum and mean salinities of the water beneath the forcing region are calculated.

Table 4.1 lists the theoretical equilibrium times calculated from equations 3.21 and Table B.2 lists the time taken for the mean and maximum salinities beneath the forcing region to reach equilbrium in the model. Only the basic and coastal experiments reached equilibrium and both took longer than the theoretical equilibrium time. The model equilibrium times are 3 to 8 times the theoretical equilibrium times. The theory described in Section 3.4 is based on the situation where there is a buoyancy flux above a flat or uniform gently sloping bottom. The lateral buoyancy flux generated in the theoretical studies assumes an endless supply of ambient water beneath the forcing region, and the uninhibited removal of dense water away from the forcing region. In these experiments, the dense water formed is trapped in the depression near the forcing region, increasing the density of the surrounding water, and lowering the lateral density gradients. This reduces the lateral buoyancy flux, which increases the time required to reach equilibrium. In Section 5.1, the experiment uses a bathymetry with no depression, and the equilibrium

time is found to be much closer to the theoretical value. The presence of the depression in the shelf results in a longer time for the experiment to reach equilibrium than the theoretical value predicted by equation 3.21. Experimental equilibrium times follow the pattern that a larger forcing region takes longer to come to equilibrium.

The theoretical salinities calculated from equation 3.22 and 3.25 using the minimum, mean and maximum depths beneath the forcing region are listed in Table 4.1. The equilibrium mean and maximum salinities beneath the forcing region attained by the experiments are listed in Table B.2. The theoretical equilibrium salinities for the coastal experiment are greater than those of the basic experiment when calculated using the mean and maximum depth beneath the forcing region, and vice versa when calculated using the minimum depth beneath the forcing region. The equilibrium mean salinity beneath the forcing region reached by the coastal experiment is less than the value reached by the basic experiment, but the equilibrium maximum salinity beneath the forcing region is greater for the coastal experiment than it is for the basic experiment. With only two experiments reaching equilibrium it is not possible to develop a more specific trend for the relationship between the equilibrium salinities and the forcing.

All the experiments in this chapter fill the depression with newly formed dense water in $\sim$60 days. As the forcing continues, the experiment with the large weak forcing area takes the shortest time to flush the depression with newly formed dense water and the experiment with the strong coastal forcing takes the longest time to flush. This may be due to the larger forcing region producing a larger volume of water to flush the depression. The mean age of the water in the depression may be related to the salinity of the water in the depression. The large polynya experiment contains the lowest salinity water in the depression, and this lower salinity water is easier to displace than the denser

water formed in the experiments with stronger forcing.

The mean and maximum salinities in the depression at the end of winter in Table B.2 appear to follow the trends of the theoretical equilibrium salinity anomalies calculated using the mean and maximum depths beneath the forcing region in Table 4.1. The large weak forcing region has the lowest mean and maximum salinities and the strong coastal forcing has the highest mean and maximum salinities in the depression.

Table B.3 lists the offshore fluxes of dense water and intermediate water, the onshore flux of MCDW and the net salinity flux. Dense water has $S \geq 34.6$ psu and an undiluted equilibrium depth $> 2,000$ m. The greatest amount of dense water transported offshore is 0.06 Sv in the basic experiment; this is more than twice the amount transported offshore by the large and coastal experiments. Intermediate water has $S = 34.5 - 34.6$ psu and an undiluted equilibrium depth of $1,000 - 2,000$ m. The maximum amount of intermediate water transported offshore occurs in the large forcing area experiment which is 10 times more than that of the coastal forcing experiment. All experiments allow the $\sim$0.2 Sv of MCDW onshore across the shelf break. The net salinity flux in the basic experiment is $\sim$6 times more than for the large and coastal experiments. The maximum salt flux across the shelf break for all experiments so far has been through Area 2, the western half of the depression.

The plume reaches a maximum depth of 1,870 m on the slope in the basic and large experiments, and 1,950 m in the coastal forcing experiment. This corresponds to the equilibrium depths of the salinities found in the depression. The salinity in the depression is greater for the coastal experiment than the other experiments, resulting in the plume reaching greater depths.

Chapter 5

Effect of topography

In this chapter the effects of the topography are investigated by utilising different topographic configurations of the model. The model is configured with a flat shelf in Section 5.1, a sill is configured at the shelf break in Section 5.2, a channel through the sill at the shelf break is configured in Section 6.2, and a second channel is configured through the sill in Section 5.3.4. The forcing used in the experiments in this chapter is the same as the forcing as that used in the basic experiment and described in Section 4.1.1. A summary of the experiments in this chapter is listed in Table B.1.

5.1 Flat shelf

In this section, the effect of the depression in the shelf is studied by configuring the model with a flat shelf instead of a shelf with a depression as configured for the basic experiment in Section 4.2. The forcing used in this experiment is the same as that used in the basic experiment. The results for this experiment are analysed and compared to the results for the basic experiment.

Figure 5.1 shows the minimum, mean and maximum salinities beneath the forcing

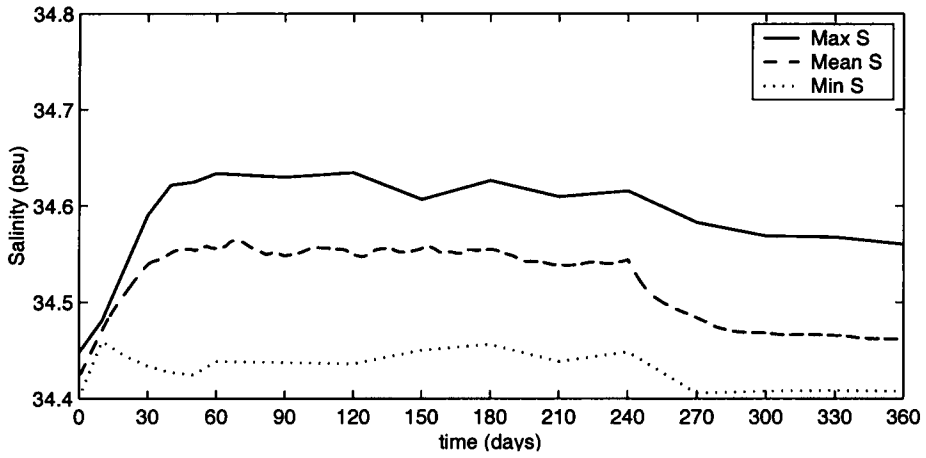

Figure 5.1: *Maximum, mean and minimum salinities beneath for forcing region for the flat shelf experiment in Section 5.1.*

region. Initially the mean salinity increases at a rate of 0.0048 psu day^{-1}, and the maximum salinity increases at a rate of 0.0055 psu day^{-1}. The rate of increase of the maximum salinity beneath the forcing region is in good agreement with the theoretical value calculated from equation 4.3. The rate of increase of the salinity beneath the forcing region for this experiment with the flat shelf is greater than the rate of increase in the basic experiment. This is because the bathymetry beneath the forcing region in this flat shelf experiment is shallower than it is in the basic experiment with the depression in the shelf.

The theoretical time required to reach equilibrium calculated in equation 3.17 is 35 days. This is the same as the theoretical equilibrium time for the basic experiment as equation 3.17 is independent of depth and is dependent on the size of the forcing region and strength of the buoyancy flux. The mean and maximum salinities beneath the forcing region reach equilibrium after 40 and 60 days respectively. The time taken for the mean salinity beneath the forcing region to reach equilibrium is in close agreement with the theoretical equilibrium time. The equilibrium times in this experiment are significantly less than the equilibrium time of the basic experiment listed in Table B.2.

It can be concluded that the presence of a depression in the shelf beneath the forcing region increases the time required for the system to reach equilibrium.

The theoretical equilibrium salinity anomaly is 0.238 psu, this the same as for the basic experiment listed in Table 4.1. The mean salinity beneath the forcing region reaches an equilibrium salinity of 34.551 psu ($S' = 0.151$ psu) and the maximum salinity beneath the forcing region reaches an equilibrium salinity of 34.634 psu ($S' = 0.234$ psu). The equilibrium maximum salinity is in close agreement with the theoretical value. The equilibrium salinities for this flat shelf experiment are much lower than those of the basic experiment with the depression in the shelf listed in Table B.2.

Even though the initial rate of increase of the mean salinity in the flat shelf experiment is greater than it is in the basic experiment, by the end of winter the mean salinity in the flat shelf experiment is less than it is the basic experiment. The flat shelf experiment reaches a lower equilibrium salinity sooner than the basic experiment which takes longer to reach equilibrium and reaches a higher equilibrium salinity. This is because water in the depression is not subject to the lateral advection of less dense water, only the water above the depression ($z > -500$ m) is subject to this lateral buoyancy flux. The depression traps dense water beneath the forcing region allowing it to become more saline thereby increasing the time taken to reach equilibrium and the equilbrium salinity. Without the depression, the dense water on the shelf spreads westward along the shelf away from the forcing region.

The circulation on the shelf is dominated by anti-cyclonic eddies with frequencies of $1 - 2.5$ cycles per day and $10 - 30$ km in diameter. These eddies are formed around the forcing region and travel westward on the shelf with some advecting over the shelf break and onto the slope. The eddies are of the same frequency and size of the eddies

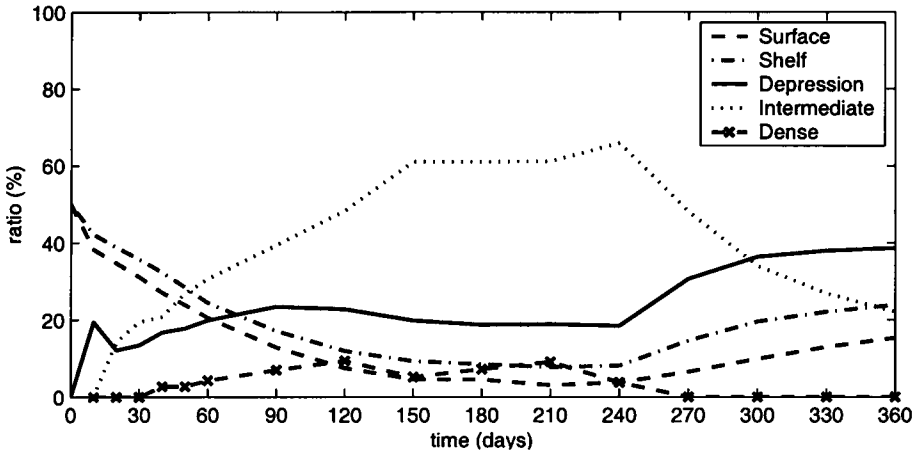

Figure 5.2: *Water mass composition of the water on the shelf for the flat shelf experiment in Section 5.1. The water mass definitions are listed in Table 4.2.*

formed in the basic experiment. The westward flow at the coast is weaker $\sim$0.05 m s^{-1}, and the coastal current is wider $\sim$50 km than it is for the basic experiment.

The buoyancy flux for this flat shelf experiment is the same as the buoyancy flux for the basic experiment. As the equilibrium salinity anomaly for the flat shelf experiment is less than it is for the basic experiment, a greater volume of water is affected than in the basic experiment. The ratio of water masses on the shelf for this experiment and for the basic experiment are plotted in Figure 5.2 and Figure 4.8b, and the water masses are defined in Table 4.2. This experiment has less dense water $S \geq 34.6$ psu and more intermediate water $34.5 \leq S < 34.6$ psu on the shelf than the basic experiment. This trend is also reflected in the transport of these water masses over the shelf break listed in Table B.3.

The offshore transport of dense water is 0.023 Sv, this is 37% of the value of the offshore transport of dense water in the basic experiment. In this experiment, the offshore transport of dense water occurs during winter only, whereas in the basic experiment, the offshore transport of dense water continues at a reduced rate throughout the summer. The offshore transport of intermediate water is 0.135 Sv, this is 50% more than in it is

in the basic experiment. This reflects the fact that there is more intermediate water and less dense water on the shelf in this experiment than in the basic experiment.

At the beginning of summer there is a thin layer ~50 m deep of dense water on the shelf immediately west of the forcing region. Over the next 30 days, this dense water moves westward alongshore leaving no dense water near the forcing region to be transported offshore during summer, nor to be made more saline by the forcing in the following winter. Figure 5.2 shows that all the dense water and 2/3 of the intermediate water on the shelf is 'lost' during summer, $t = 240 - 360$ days. Figure 5.1 shows that the maximum salinity beneath the forcing region decreases from $S = 34.615$ psu at the beginning of summer to $S = 34.560$ psu at the end of summer.

5.2 Effect of the sill at the shelf break

In this section, the effects of a sill at the shelf break are considered. A sill 250 m high is added at the shelf break to the topography of the basic experiment in Section 4.2, so that there is now a depression in the shelf and a sill at the shelf break. The sill is typical of the height of the actual sill at the shelf break in the Adélie Land region, as described in Section 2.1. The sill halves the area available for water to be exchanged between the shelf and the deep ocean, as the depth at the shelf break is 500 m in previous experiments, and for this experiment the depth is 250 m.

The water mass composition of the depression is very similar to the water mass composition of the depression in the basic experiment which is shown in Figure 4.8a. In common with the basic experiment, the depression takes 60 days to fill with newly formed water. Figure 5.3 shows the mean and maximum salinities for the area beneath the forcing region and the mean salinity in the depression. The mean and maximum

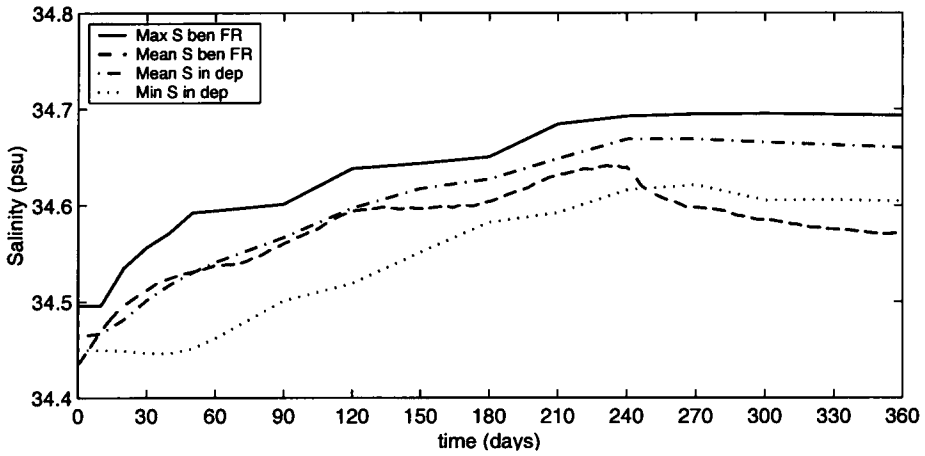

Figure 5.3: *Mean and maximum salinities beneath the forcing region and mean salinity in the depression for the sill experiment in Section 5.2.*

salinities beneath the forcing region increase, plateau and continue to increase again a number of times. The salinities do not appear to come to an equilibrium during the winter forcing period and are greater than the salinities in the basic experiment after ~200 days. The salinities do not come to equilibrium due to the reduction in the lateral buoyancy flux. This reduction in the lateral buoyancy flux is due to the presence of the sill which reduces the exchange of shelf and offshore waters.

The mean salinity in the depression increases steadily throughout winter. At the end of winter the mean salinity of the water in the depression is 34.672 psu, 0.015 psu more than the mean salinity in the basic experiment listed in Table B.2. This follows from the higher salinities beneath the forcing region. The denser water cannot move over the sill at the shelf break, it is trapped on the shelf and in the depression and continues to become more saline during winter.

The mean age of the water in the depression is 24 days, 12 days less than that of the basic experiment. From Figure 5.3 it is evident that the mean salinity beneath the forcing region at the end of winter is still increasing, and as a result this newly formed dense water is able to displace the water in the depression. In contrast the mean

salinity beneath the forcing region in the basic experiment shown in Figure 4.4 reached equilibrium after 150 days, after which the newly formed water is less able to displace water in the depression, resulting in a greater mean age of water in the depression, and a longer flushing time.

The time averaged alongshore velocities are plotted in Figure 5.4. The westward coastal current in this experiment has a speed of $\sim$0.1 m s^{-1} and width of $\sim$20 km, and this is the same as the coastal current in the basic experiment plotted in Figure 4.9. Another westward current of speed $\sim$0.05 m s^{-1} exists on the northern bank of the depression centred above the 500 m isobath. This current is also observed in the basic experiment, though it is weaker here than it is in the basic experiment. An eastward along-sill current with maximum speed of $\sim$0.10 m s^{-1} and averaging 0.05 m s^{-1} exists above the shelf sill, and the current is faster at the surface and $\sim$20 km wide. The current is geostrophic, driven by the sea surface elevation gradient across the sill $d\eta/dx \simeq 10^{-3}$. The sea surface elevation and the current satisfy the theoretical geostrophic current equation given by

$$v = \frac{g}{f}\frac{d\eta}{dx}. \tag{5.1}$$

The anti-cyclonic eddies of frequency $1-2.5$ cycles per day and diameter $10-30$ km are found in the depression and on the shelf to the west of the depression. These are of the same size and frequency of the eddies on the shelf in the basic experiment.

The cross-shelf fluxes at the shelf break are listed in Table B.3. The on and offshore volume fluxes are reduced by 80% in the presence of a sill. The net salinity flux by the end of the year is close to zero. Not only is the salinity trapped on the shelf by the sill, but much of the kinetic energy is trapped on the shelf as well. In trapping this energy on the shelf, a strong alongshore westward current develops, with a core lying at the

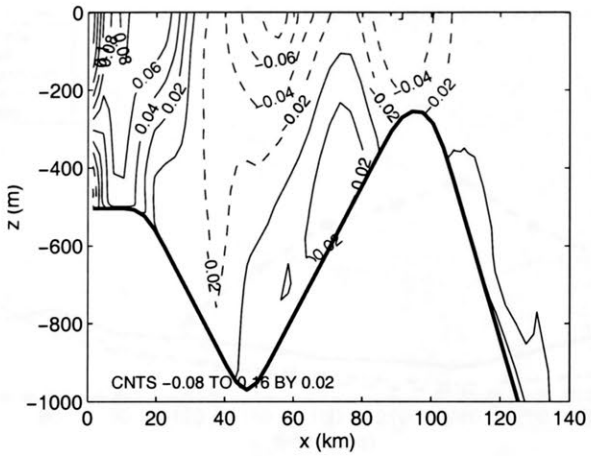

Figure 5.4: *Time averaged alongshore velocity at y=250 km for the sill experiment in Section 5.2.*

surface just shoreward of the sill and reaching speeds greater than 0.12 m s^{-1}.

The water mass composition of the water on the shelf is plotted in Figure 5.5 and the water masses are listed in Table 4.2. More dense water with $S \geq 34.6$ psu is found on the shelf at the end of winter than in the basic experiment without the sill at the shelf break. The volume of dense water on the shelf at $t = 240$ days is 8.23×10^{12} m^3, this is 10% more than the basic experiment. During summer the amount of the dense water on the shelf is reduced by 50%, whereas in the basic experiment without a sill at the shelf break, the volume of dense water on the shelf is reduced by 65%. Yet, no dense water of $S \geq 34.6$ psu is transported over the sill throughout the year, nor any intermediate water of $34.5 \leq S < 34.6$ psu as listed in Table B.3.

Apart from blocking the offshore transport of dense water, the sill also blocks all onshore transport of MCDW. The MCDW is a warm water mass that provides heat to help maintain the polynya and is defined in this study as water with low surface tracer concentration $c < 0.02$ and $S > 34.45$ psu.

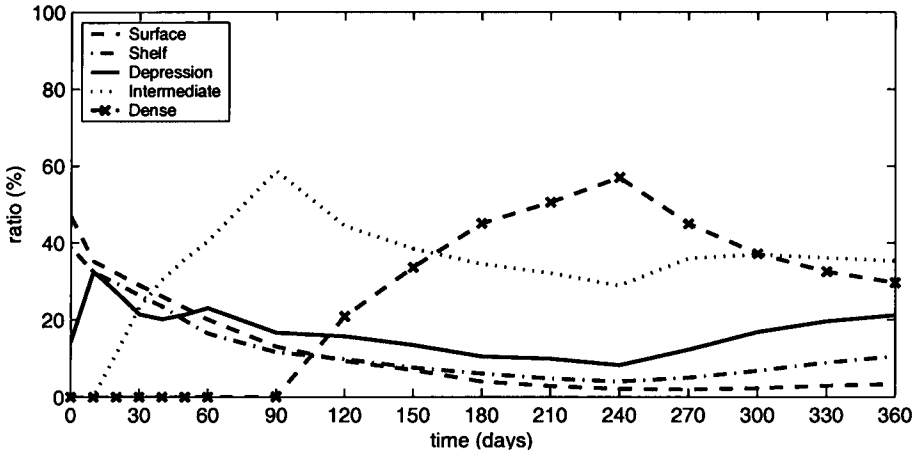

Figure 5.5: *Water mass composition of the water on the shelf for the sill experiment in Section 5.2. The water masses are defined in Table 4.2.*

5.3 The effect of a channel through the sill

In this section, a further change is made to the topography by incorporating a channel 21 km wide and 200 m deep through the sill, in line with the western end of the depression (y = 330 km). Again, the same forcing as used in the basic experiment is applied. In Section 5.3.1 the stratification is the same as the stratification used in the previous experiments given by equation 4.1. In Section 5.3.2 the stratification on the shelf is initialised with stratification similar to the stratification at the end of the summer in the first year experiment, that is increased stratification on the shelf and dense water in the depression.

5.3.1 First year

The mean and maximum salinities beneath the forcing region and mean salinity in the depression are similar to those in the sill experiment without the channel described in Section 5.2. The salinities for the sill experiment are plotted in Figure 5.3. The water mass composition in the depression and on the shelf are also very similar to that of the sill experiment shown in Figure 5.5. The mean age, mean salinity and maximum salinity

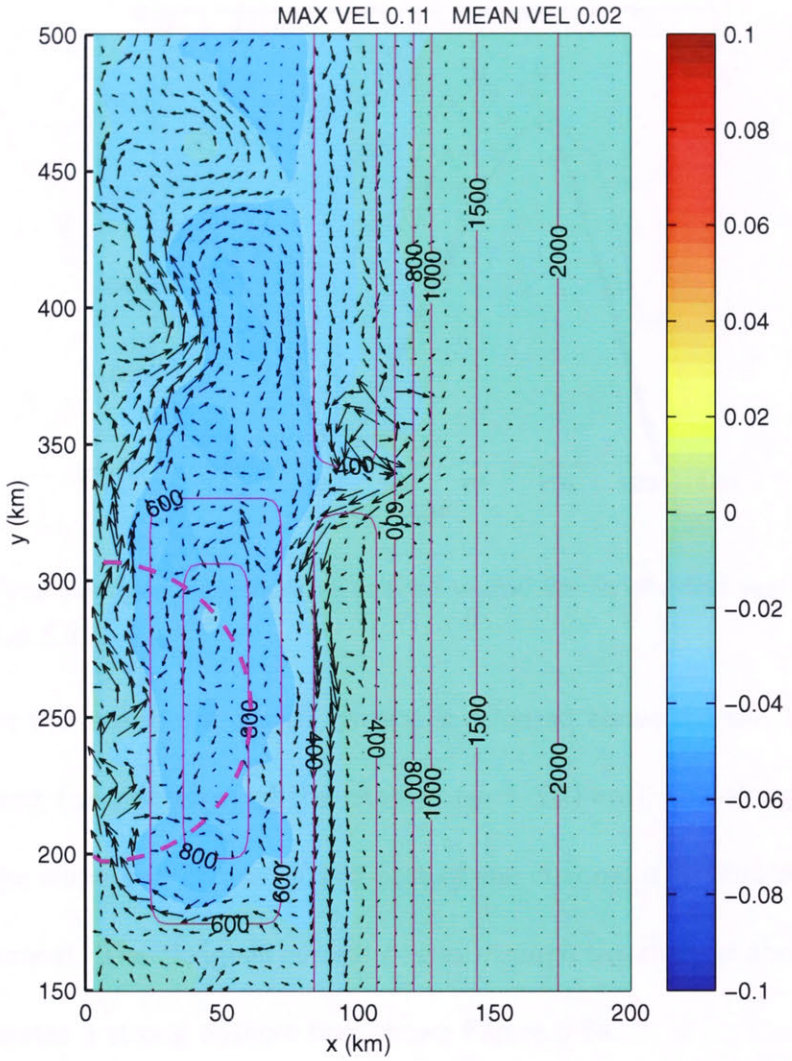

Figure 5.6: *Elevation and barotropic velocities after applying a buoyancy forcing for 240 days for the first year channel experiment in Section 5.3.1. The solid magenta lines are the isobaths labelled in m and the dashed magenta line shows the forcing region. The colourbar for the elevation is labelled in m and the mean and maximum velocities are in* $m\ s^{-1}$.

of the water in the depression at the end of winter are listed in Table B.2, and these values are approximately the same as the sill experiment. The channel through the sill has little effect on the salinities and water masses found on the shelf.

The elevation and barotropic currents for day 240 and the time averaged alongshore velocity at $y = 250$ km are plotted in Figures 5.6 and 5.7, respectively. The westward coastal current and the westward flow above the northern bank of the depression are of the same magnitude as they are in the sill experiment shown in Figure 5.4. In the

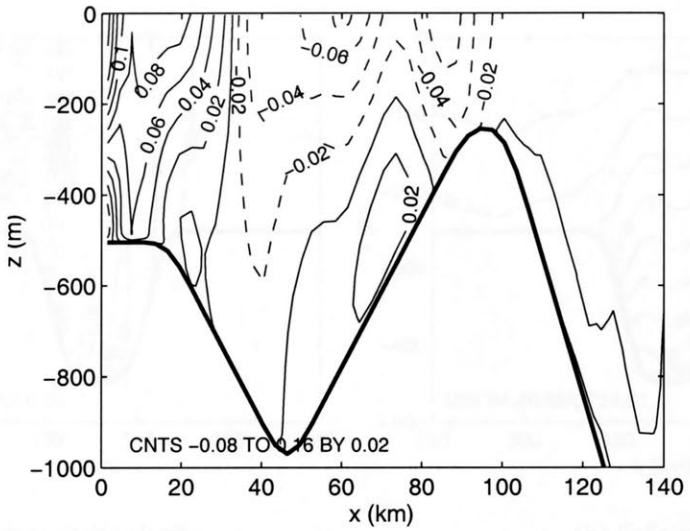

Figure 5.7: *Time averaged alongshore velocity at y=250 km for the first year channel experiment in Section 5.3.1.*

sill experiment the eastward along-sill current is centered above the sill. In this channel experiment west (or upstream) of the channel ($y > 330$ km), the along-sill current is situated on the slope side of the sill and east of the channel it is situated on the shelf side of the channel. The along-sill current passes through the channel above the eastern half and generates a strong onshore flow shown Figure 5.8a.

The onshore flow has been observed by Rintoul (1998) and Bindoff, Rintoul, and Massom (2000a) during winter. It brings warm offshore water onto the shelf which aids in melting the ice and keeps the polynya open. For this study, MCDW is defined as water with low concentration of surface tracer $c < 0.02$ and $S > 34.45$ psu. The onshore transport of MCDW is 0.012 Sv, most of which occurs above the western side of the channel as shown in Figure 5.8a. Without a channel in the sill the onshore transport is completely blocked.

The offshore velocities through the channel are much weaker than the onshore velocities. The offshore transport is approximately one third of the onshore transport through the channel. The offshore velocities are located on the western side of the channel, and

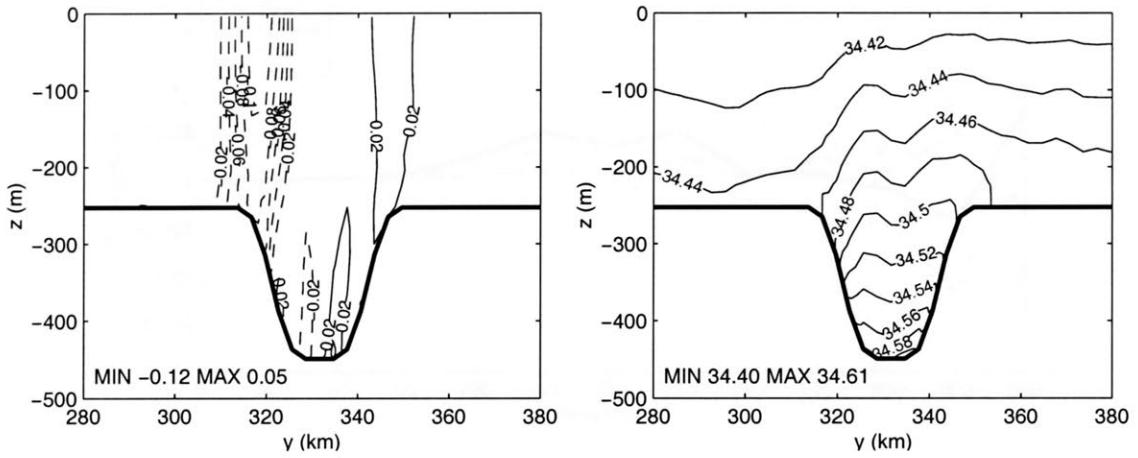

(a) Across-shelf velocity (b) Salinity

Figure 5.8: *Cross channel section at x=96 km of (a) across-shelf velocity (solid lines for offshore and dotted lines for onshore) and (b) salinity for day 240 at the sill in the region around the channel with buoyancy flux for Section 5.3.1.*

the water on the western side is more saline than the water on the eastern side of the channel as shown in Figure 5.8b. The offshore velocity at the western side of the channel transports dense water offshore.

The shelf break is conceptually divided into 3 sections shown in Figure 4.1 to describe the cross-shelf flow: Area 1 is the area west of the channel; Area 2 incorporates only the channel; and Area 3 is the area east of the channel. The channel facilitates cross-shelf flow at the shelf break, and the on and offshore transports increase by 52 and 38%, respectively, compared to the sill experiment. The large increase in onshore transport is a result of the along-sill current which meanders through the channel shown in Figure 5.6. Most of the cross-shelf flow across the shelf break occurs through the channel, and the precentage of on and offshore transport through the channel is 67 and 30%, respectively. This is a disproportionately large percentage of the flow through the channel considering the ratio of area of the channel to the total area of the shelf break.

The salinity fluxes across the shelf break are plotted in Figure 5.9. These salinity

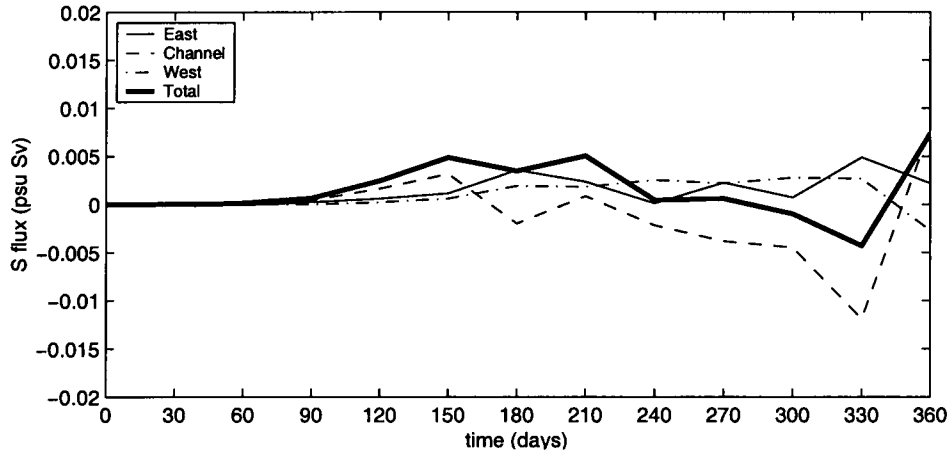

Figure 5.9: *Salinity fluxes across the shelf break in experiment with a channel through the sill. The 270 km length of the shelf is broken into the area above the channel y=316–349 km, east of the channel y=160–316 km and west of the channel y=349–430 km.*

fluxes do not follow the same pattern as the volume fluxes. The on and offshore salinity fluxes across the shelf break increase by 28 and 52%, respectively, compared to the sill experiment. The percentage of on and offshore salinity flux through the channel 52 and 72% respectively. The channel increases the offshore salinity flux.

The channel allows intermediate water with $34.5 \leq S < 34.6$ psu and dense water with $S \geq 34.6$ psu to move from the continental shelf onto the slope whereas the sill experiment in Section 5.2 configured with a continuous sill and no channel prevents water with $S \geq 34.5$ psu from flowing over the shelf sill. The offshore transports of these water masses are listed in Table B.3. The offshore transports of intermediate and dense water are 8 and 16% of the amounts transported offshore in the basic experiment without the sill or channel.

The properties of the plume of dense water on the slope at depth 970 m are plotted in Figure 5.10. The plume is less dense and thinner than the plume in the basic experiment plotted in Figure 4.14, and this is expected from the decrease in dense water flow over the shelf break. The plume reaches depth 970 m after 150 days when it is 18 m thick, the thickness increases to 217 m by the end of summer, and the salinity anomaly of the

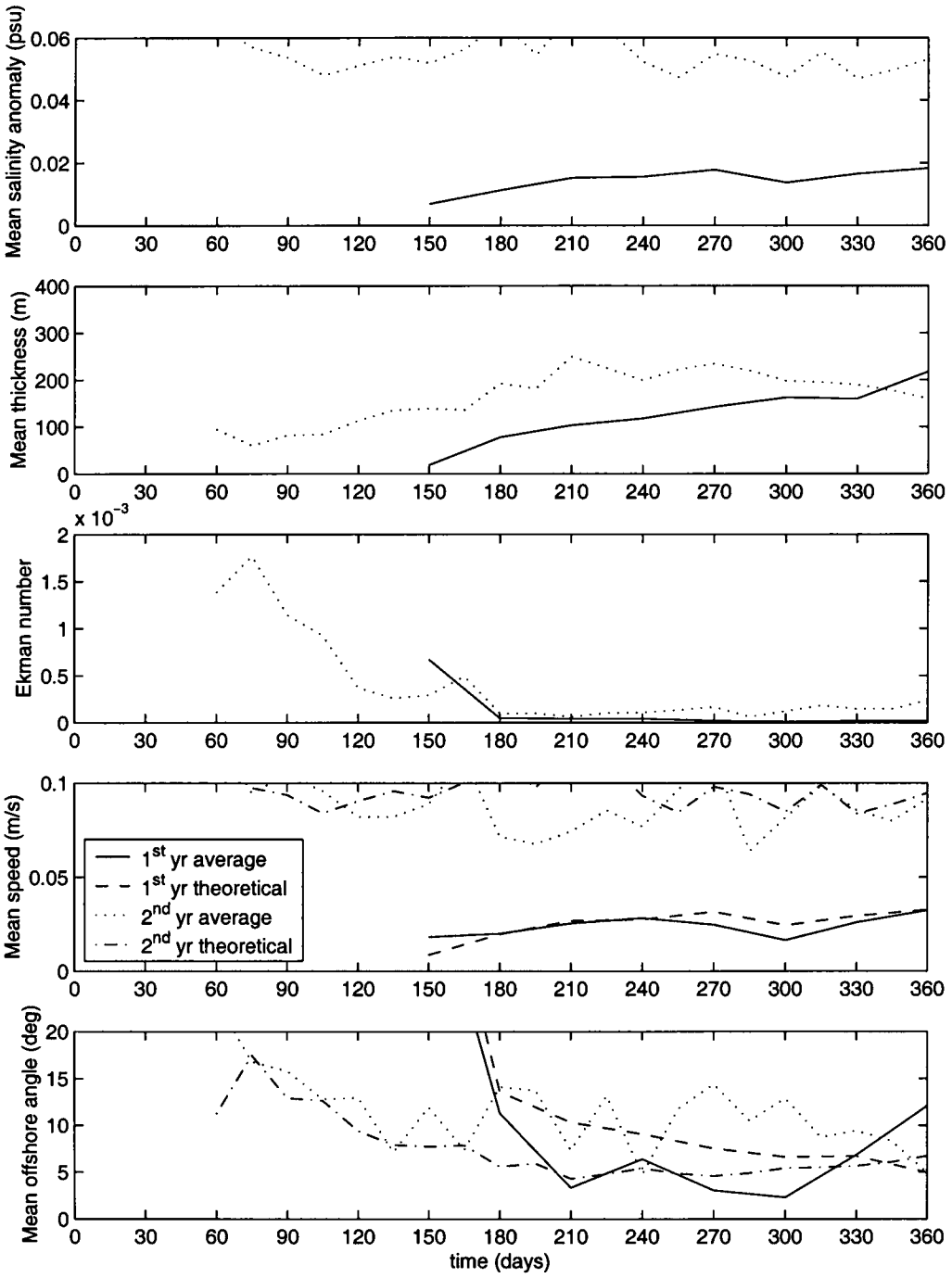

Figure 5.10: *The mean salinity anomaly, thickness, Ekman number, speed and direction of the plume at x=129 km, H=970 m, between y=342 and 432 km. The plume is delineated by a surface tracer concentration c > 0.02 for the channel experiments in Section 5.3. The solid line shows the first year results in Section 5.3.1 and the dotted line shows the second year results from Section 5.3.2. The theoretical values for the speed and direction of the plume are calculated from equations 3.28 and 3.27 and plotted for the first year (dashed line) and second year (dash-dot line).*

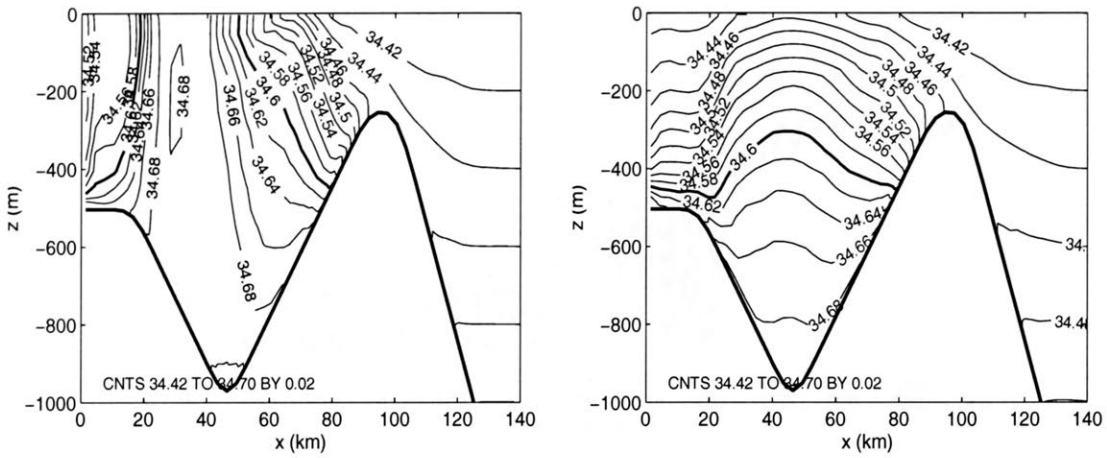

(a) t = 240 days (b) t = 360 days

Figure 5.11: *Salinity at (a) the end of winter and (b) the end of summer for the first year channel experiment in Section 5.3.1.*

plume increases from 0.007 psu to 0.018 psu. The speed of the plume remains around 0.024 m s^{-1} but the direction turns from more offshore to alongslope as expected from equation 3.27 for a greater plume thickness. The maximum downslope extent of the plume is 1,260 m, which is reached on day 240.

Figure 5.11 shows the salinity at the end of winter and the end of summer. The water columns at the end of winter are homogeneous beneath the forcing region. During summer these water columns are restratified. Dense water spreads along the bottom and ambient water moves in above the dense water. The water column CM1 takes 12 days to restratify and the stratification is 4 times the initial stratification of the water column. The mean salinity on the shelf is 34.579 psu at the end of winter, and by the end of summer it drops to 34.526 psu. In the depression the salinity maintains values between 34.59 and 34.70 psu through out the summer with a mean salinity of 34.66 psu.

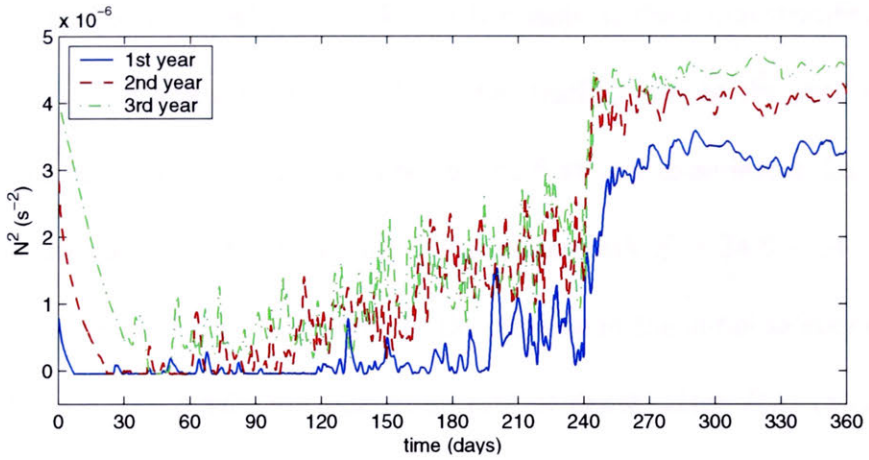

Figure 5.12: *Mean stratification of the water column CM1 for the first, second and third year experiments in Sections 5.3.1, 5.3.2 and 5.3.3.*

5.3.2 The second year

This experiment is initialised with increased stratification on the shelf and dense water in the depression as found at the end of summer in the previous experiment. This method of configuring the second year experiment was chosen over a continuous run over two years from the the end of first year due to the constraints on the numerical stability of the model. The finite size of the model and the not so perfect boundaries reflect energy back into the domain of the model which cumulates to generate noise of the same order of the eddies of interest in this study.

In this section, the previous experiment described in Section 5.3.1 is referred to as the first year experiment, and this experiment is referred to as the second year experiment. The initial stratification is given by

$$S_0(z) = \begin{cases} 34.4 - \frac{0.4}{1000} z & \text{if } z \geq -500 \text{ m and } x \leq 96 \text{ km} \\ 34.6 - \frac{0.2}{1000}(z + 500) & \text{if } z < -500 \text{ m and } x \leq 96 \text{ km} \\ 34.4 - \frac{0.1}{1000} z & \text{if } x > 96 \text{ km}. \end{cases} \tag{5.2}$$

The stratification off the shelf ($x > 96$ km) is the same as the initial stratification of the first year experiment given in equation 4.1. The stratification on the shelf is typical of the conditions found at the end of summer of the first year experiment, i.e., four times the initial stratification on the shelf with dense water with $S = 34.6 - 34.7$ psu in the depression as shown in Figure 5.12. Due to the increase in the initial salinity on the shelf $\overline{S}_{\text{shelf}} = 34.5$ psu, the maximum production rate of dense water P_{DW} calculated from equation 4.2 has increased. For $S_{\text{DW}} = 34.6$ psu, $P_{\text{DW}} = 1$ Sv.

Equation 3.14 gives the condition for deep convection. In this second year case $NH \simeq \gamma(B_0 r)^{1/3}$ suggesting that the system is borderline between deep convection (when the system comes to equilibrium before the homogeneous mixed layer reaches the bottom) and shallow convection (when the system comes to equilibrium after the homogeneous layer reaches the bottom). The equilibrium time calculated from equation 3.15 is 19 days, the equilibrium depth is 498 m resulting in an equilibrium salinity of 34.6 psu. The system does not reach equilibrium in 19 days. Figure 5.12 shows that the water column CM1 homogenises in 22 days in agreement with equation 3.17, showing that shallow convection occurs. The salinity beneath the forcing region shown in Figure 5.13 continues to increase throughout winter. The salinity beneath the forcing region plateaus after 100 days before increasing again after 150 days. The system does not appear to reach equilibrium within the 240 day winter.

The initial flushing of the depression takes 75 days, 15 days longer than for the first year experiment. The statistics for the depression at the end of winter are listed in Table B.2. The salinity in the depression shown in Figure 5.13 increases throughout winter. At the end of winter the mean age of the water in the depression is 37 days, 12 days more than it is in the first year experiment. The mean and maximum salinities

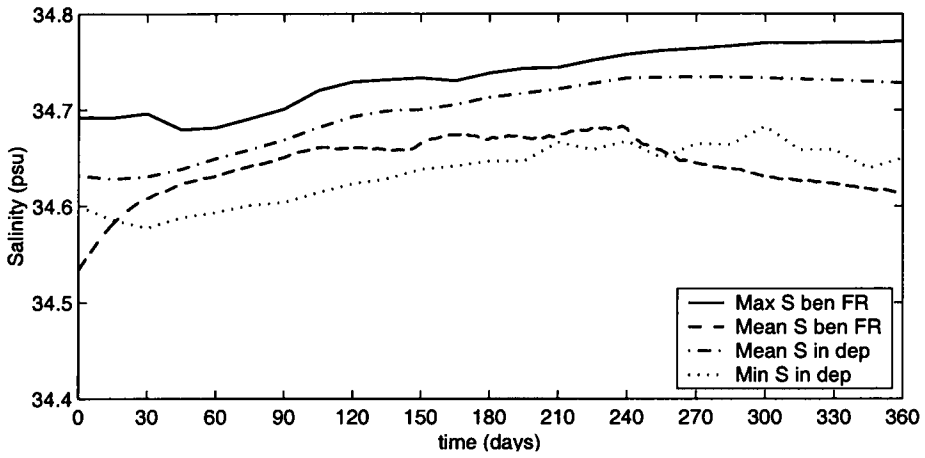

Figure 5.13: *Maximum and mean salinities beneath the forcing region, mean and minimum salinities in the depression for second year channel experiment in Section 5.3.2.*

Water mass	Initial depth		Salinity range
	shelf	deep ocean	
	$-z$ (m)	$-z$ (m)	(psu)
Surface	0 – 125	0 – 250	34.4 – 34.425
Shelf	125 – 500	250 – 2000	34.425 – 34.6
Dense	500 – 1000	2000 – 3000	34.6 – 34.7
Very dense	1000 –	3000 –	34.7 –

Table 5.1: *Water mass definitions for second year experiments. The initial depth of the water masses on the shelf and the deep ocean are shown. The shelf water for the second year experiments makes up the shelf, depression and intermediate water masses for the first year experiment defined in Table 4.2.*

of the water in the depression are ~0.06 psu more than they are for the first year experiment.

Figure 5.14a shows the breakdown of water masses in the depression for the second year experiment. The water masses for the second year experiment are listed in Table 5.1, and these are different to the first year water mass definitions in Table 4.2 due to the different initialisation. The water on the shelf at depths $-500 < z < -125$ m is initialised with water that was defined as shelf, depression and intermediate water in the first year experiment $34.425 \leq S < 34.6$ psu. The depression ($-1000 < z < -500$ m) is initialised with dense water $34.6 \leq S < 34.7$ psu. During winter, the dense water in the depression is replaced with a denser water mass, referred to as very dense water

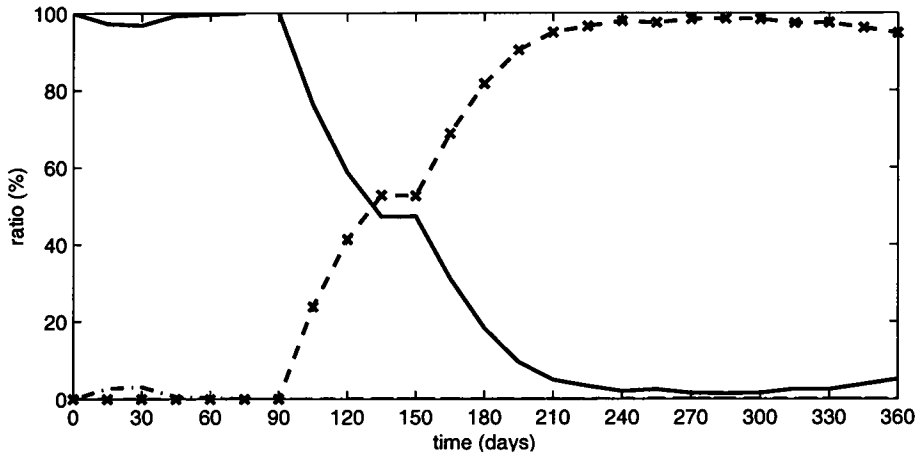

(a) Depression

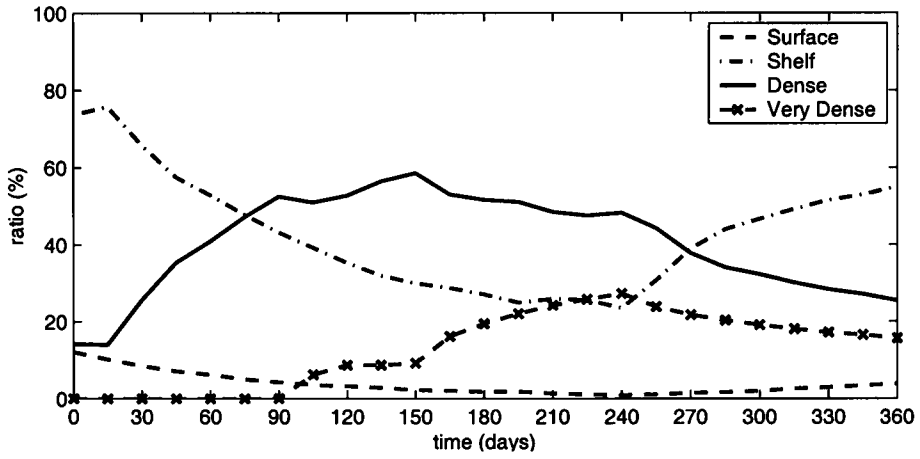

(b) Shelf

Figure 5.14: *Breakdown of water masses (a) in the depression and (b) on the shelf for the second year experiment described in Section 5.3.2. The water masses are defined in Table 5.1.*

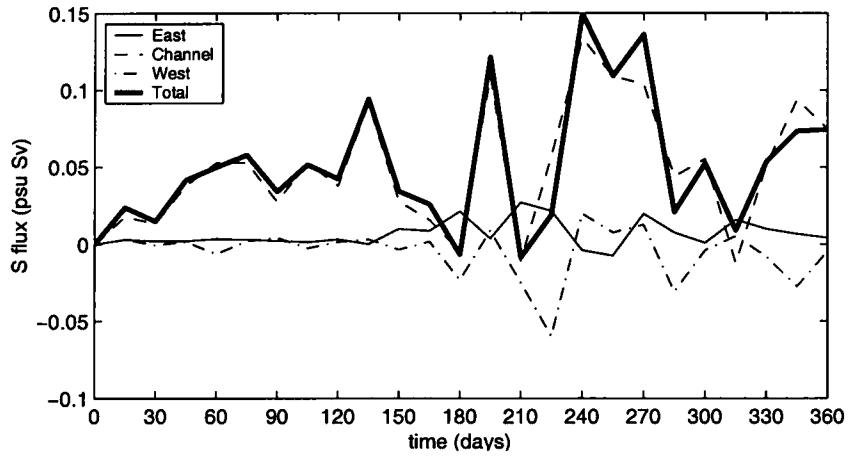

Figure 5.15: *Salinity fluxes across the shelf break (x=96 km) for the second year experiment divided into three areas; east of the channel, the channel and west of the channel.*

($S \geq$ 34.7 psu). By the end of winter, nearly all the water in the depression has $S \geq$ 34.7 psu.

Figure 5.15 shows the salinity fluxes across the shelf break for the three sections: east of the channel, the channel, and west of the channel. The offshore salinity flux above the channel dominates the salinity transport across the shelf break. The offshore transport of salt is intermittent throughout the year in agreement with Foster (1995). The structure of the salinity section and the across-shelf velocity section across the channel is similar to the sections across the channel during the first year shown in Figure 5.8. On the eastern side of the channel there are strong onshore velocities, and on the western side the flow is offshore. The high salinity water is generally found at the bottom on the western side of the channel. The salinity in the second year is higher than the first year experiment. The maximum salinity in the channel at the end of the second year winter is 34.70 psu, 0.09 psu higher than it is at the end of the first winter. The maximum offshore velocity at the end of the second year winter is 0.21 m s^{-1}, four times more than the velocity at the end of the first winter.

Figure 5.10 plots the properties of the plume produced in the second year alongside

the plume properties of the first year. The plume reaches the 970 m isobath on day 60, 90 days earlier than in the first year experiment. The plume is on average 3.8 times more saline than the plume produced in first year. Initially the plume is thicker, but by the end of summer the first year plume is slightly thicker than the second year plume. As expected from the greater density of the plume the speed of the plume in the second year is 3.7 times greater than it is for the first year. For days 60 to 90, the Ekman number of the plume is greater than 10^{-3} which does not fall into the threshold for stable flows (Condie, 1995). The flow at this time does not appear to be unstable and does not form eddies. The plume reaches the bottom of the slope by the end of winter.

At the end of winter when the forcing stops, the second year experiment takes 5 days to restratify compared to the 13 days taken in the first year experiment. The resulting restratification after the second summer results in 1.5 times the stratification at the beginning of the second year. The expected time for restratification is inversely proportional to the stratification ($\tau_{\text{restrat}} \propto 1/N$, equation 3.16), so when the water is 4 times more stratified (i.e., $N^2 = 4 \times N_0^2$) the restratification time is halved.

The water masses on the shelf are shown in Figure 5.14b. The very dense water in the depression remains trapped in the depression, as shown in Figure 5.14a, while the very dense water that is not in the depression relaxes alongshore or is transported through the channel onto the slope. Like the first year experiments, the dense water on the shelf relaxes and spreads out during summer such that only 53% of the dense water on the shelf at the end of winter is found on the shelf by the end of summer.

The total volume of dense and very dense water ($S \geq 34.6$ psu) transported offshore over the shelf break is 4.23×10^{12} m^3 throughout the year. The highest offshore transport occurs at the end of winter and the beginning of summer and all offshore transport of

the dense water is through the channel. Averaged over the year the offshore transport of dense water is 0.136 Sv, 148 times greater than that transported offshore in the first year.

5.3.3 Third year

The effect of the forcing on the initial configuration in the first year experiment in Section 5.3.1 is a four fold increase in stratification, as shown in Figure 5.12. The proportion of water found on the shelf at the end of the first year that is dense enough to adiabatically sink to the "bottom" of the ocean (2000 m in this model), i.e., requires a salinity of at least 34.6 psu, increases from none at the start of the year to 30% at the end of the year. The transport of dense water off the shelf in the first year is 0.0009 Sv.

In the second year, the stratification at the beginning of the year has increased by 33%. The proportion of water that is dense enough to adiabatically sink to the bottom of the ocean has increased from 13% at the beginning of the year to 41% at the end of the second year (but this water is denser than the water found at the beginning of the year). The transport of dense water off the shelf during the second year is 0.1362 Sv.

Due to the significant increase in dense water production from first to second year, a third year run was carried out in order to see what increases would occur from the second to the third year. The third year simulation was initialised with the very dense water mass found in the depression at the end of the second year simulation. The third

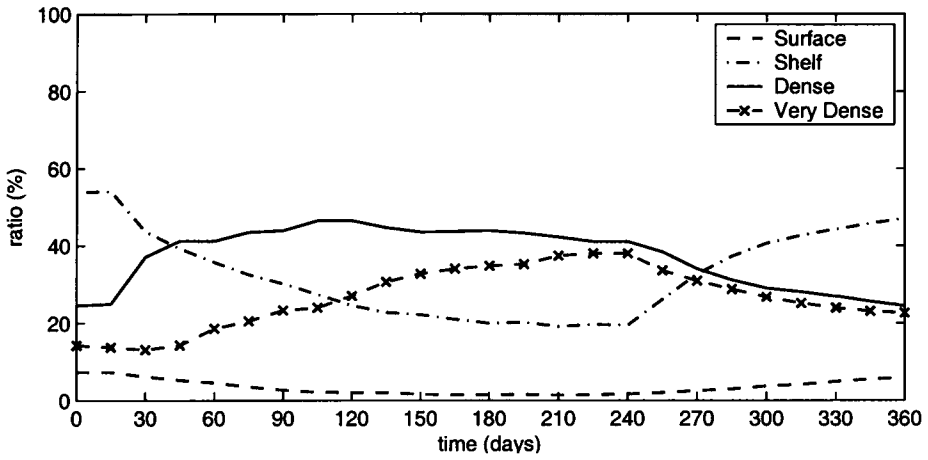

Figure 5.16: *Breakdown of water masses on the shelf for the third year experiment described in Section 5.3.3. The water masses are defined in Table 5.1.*

year run is initialised with the salinity

$$S_0(z) = \begin{cases} 34.4 - \frac{0.6}{1000} z & \text{if } z \geq -500 \text{ m and } x \leq 96 \text{ km} \\ 34.7 - \frac{0.1}{1000}(z + 500) & \text{if } z < -500 \text{ m and } x \leq 96 \text{ km} \\ 34.4 - \frac{0.1}{1000} z & \text{if } x > 96 \text{ km.} \end{cases} \tag{5.3}$$

The water masses on the shelf in the third year simulation are plotted in Figure 5.16. This is similar to the the breakdown of water masses found in the second year experiment plotted in Figure 5.14. The main differences are that there is more dense water and very dense water as defined in Table 5.1 on the shelf. The breakdown of the water masses at the end of the summer of the third year simulation are very similar to the breakdown of water masses that the third year experiment was intialised with. Eventually it is expected that the breakdown of water mass on the shelf is the same at the end of summer as it is at the beginning of the simulation. That is that the forcing during winter and the relaxation during summer is balanced. From Figure 5.12 the stratification at the end of summer is nearly the same as it is at the beginning of the year.

The offshore transport of dense water, $S \geq 34.6$ psu is 0.427 Sv, three times more

than the transport in the second year. With this bathymetric configuration, initial conditions and forcing, it is expected that the dense water production will asymptote to this value.

5.3.4 A second channel through the sill

Rintoul (1998) suggests that a second channel through the sill at at the eastern end of the depression (147°30'E) could be the source of cold, fresh plumes that have been observed at 146°30'E. However, the bottom water on the slope between the two channels connecting the Adélie Depression to the deep ocean is dominated by warm, saline RSBW, suggesting that the outflow at this second channel is relatively weak compared to the outflow at the channel at western end of the depression at 143°E (Rintoul, 1998).

In the model, a second channel identical to the first channel at the western end of the depression ($y = 330$ km) is configured at the eastern end of the depression ($y = 170$ km). All other conditions such as the stratification and the forcing are the same as the first year experiment with one channel described in Section 5.3.1.

The mean and maximum salinities beneath the forcing region and the minimum and mean salinities in the depression are approximately the same as those for the one channel experiment in Section 5.3.1 and the sill experiment shown in Figure 5.3. The salinities fluctuate by ± 0.01 psu about the salinities in the one channel experiment. By the end of winter and during summer the maximum and mean salinity in the depression is 0.01 psu less than the corresponding salinities in the one channel experiment listed in Table B.2.

Figure 5.17 shows the surface tracer concentration and velocity on the bottom sigma level at $t = 210$ days. A plume of dense water comes out of each channel which results in dense water on the slope between $y = 170$ and 330 km, in contrast to the one channel

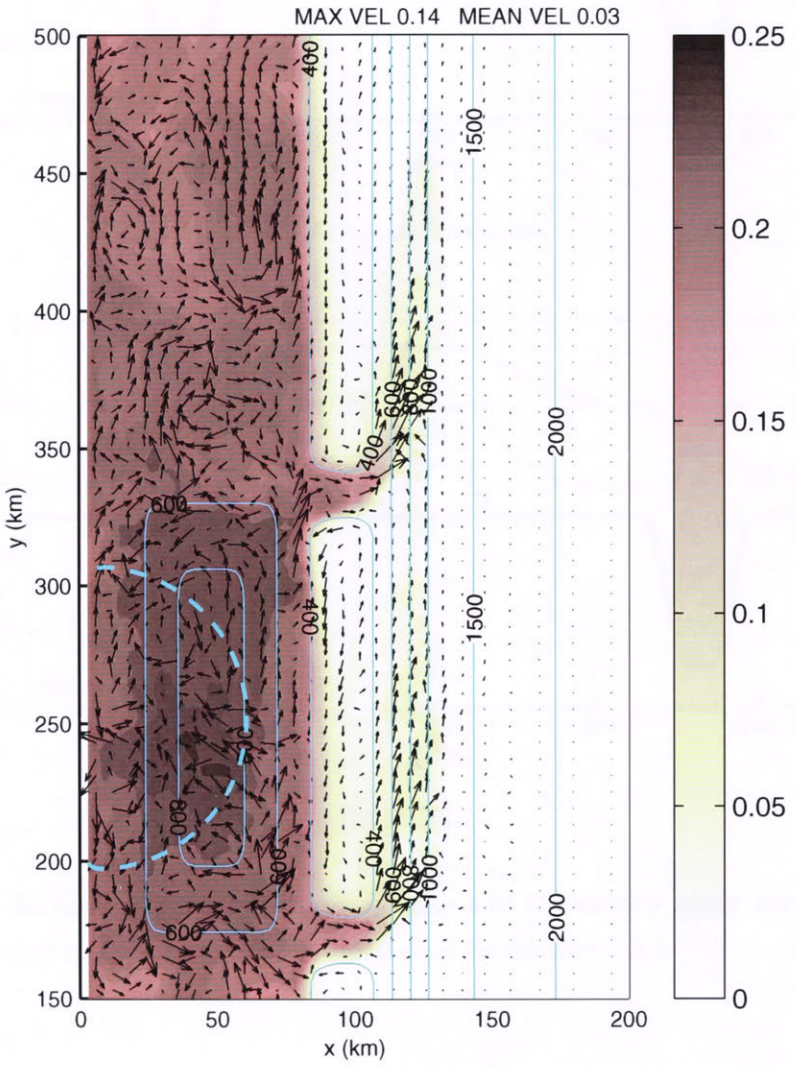

Figure 5.17: *Surface tracer concentration and velocities at the bottom for the two channel experiment in Section 5.3.4 after 210 days. The solid cyan lines are the isobaths labelled in m and the dashed cyan line shows the forcing region. The colourbar is for the surface tracer concentration and the mean and maximum velocities are in* $m\ s^{-1}$.

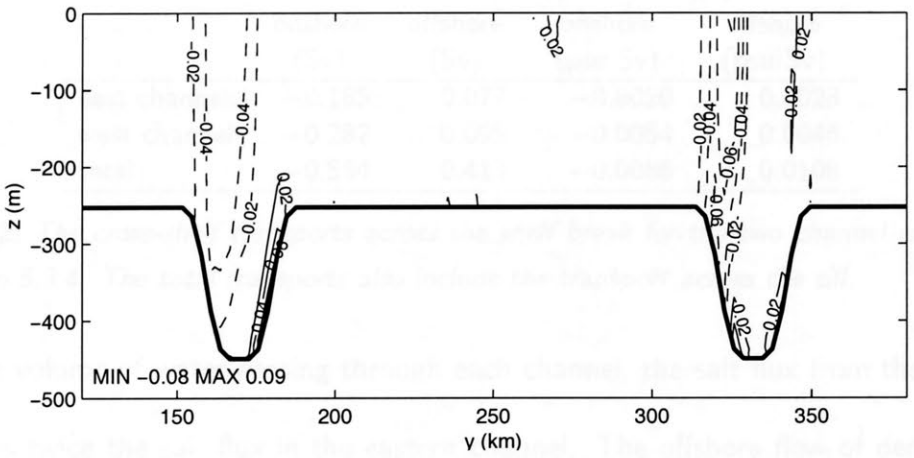

(a) Across-shelf velocity

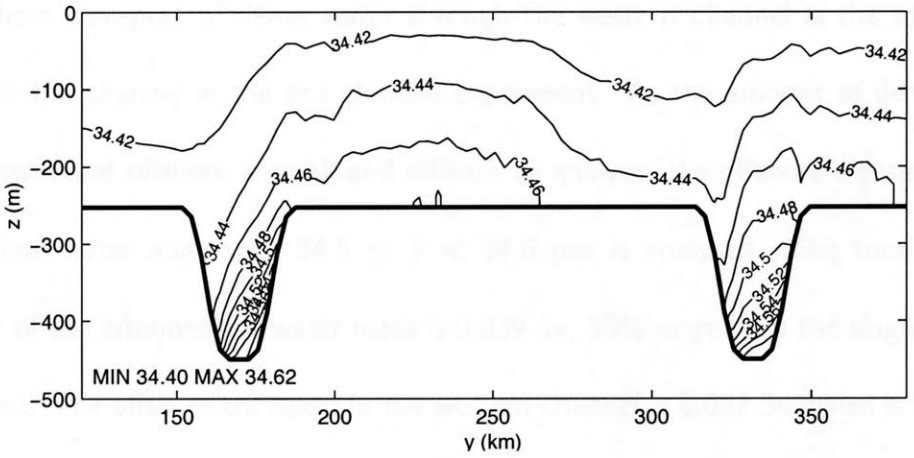

(b) Salinity

Figure 5.18: *Sections of (a) across-shelf velocity and (b) salinity along the shelf break at x=96 km showing the two channels at t=210 days for Section 5.3.4.*

experiment.

Figure 5.18a and b show the across-shelf velocity and salinity at the shelf sill after 210 days. In common with the one channel experiment, the onshore flow through the channel is three times stronger than the offshore flow shown in Figure 5.8a. The cross-shelf fluxes for these experiments are listed in Table B.3. The second channel through the sill increases the on and offshore transports by 20 and 2% respectively. The on and offshore volume and salinity transports are listed in Table 5.2. Though there is nearly

	Volume		Salinity	
	onshore (Sv)	offshore (Sv)	onshore (psu Sv)	offshore (psu Sv)
east channel	−0.185	0.077	−0.0020	0.0023
west channel	−0.282	0.095	−0.0054	0.0046
total	−0.564	0.413	−0.0086	0.0108

Table 5.2: *The cross-shelf transports across the shelf break for the two channel experiment in Section 5.3.4. The total transports also include the transport across the sill.*

the same volume of water passing through each channel, the salt flux from the western channel is twice the salt flux in the eastern channel. The offshore flow of dense water $S \geq 34.6$ psu is 0.0018 Sv, this is double the amount in the one channel experiment. The offshore transport of dense water through the western channel is the same as it is through the channel in the one channel experiment. As the amount of dense water being transported offshore is small and difficult to analyse, the offshore transport of an intermediate water mass with $34.5 \leq S < 34.6$ psu is analysed. The total offshore transport of the intermediate water mass is 0.039 Sv, 38% more than the single channel experiment. The offshore transport in the western channel is 0.027 Sv which is the same as the transport in the channel in the single channel experiment. Another 0.012 Sv of intermediate water is transported offshore in the eastern channel.

The total onshore transport is 0.56 Sv, this is an increase of 18% compared to the one channel experiment. The onshore transport through the western channel is about the same as the onshore transport through the single channel. The total onshore transport of MCDW for the two channel and one channel experiment in the same. In the one channel experiment 85% of the MCDW enters through the channel, for the two channel experiment 60% enters through the western channel and 32% enters through the eastern channel.

5.4 Summary

The westward current at the coast is a consistent feature over a range of topographic configurations. With a depression present, the current is trapped in a narrow band between the coast and the depression. In the absence of the depression, the current is wider and weaker. The eddies on the shelf show an anti-cyclonic signal in a frequency range of $1 - 2.5$ cycles per day and are $10 - 30$ km in diameter. They spread westward along the shelf. In experiments with a depression in the shelf, there is a secondary westward current on the bottom above the northern bank of the depression and a return eastward flow at the surface above the deepest part of the depression. In experiments with a sill at the shelf break, an eastward flow above the sill exists. If there is a channel through the sill, the along-sill current meanders from the slope side of the the sill upstream (west) of the channel, onshore through the channel and continues on the shelf side of the sill downstream (east) of the channel.

In the flat shelf experiment, the equilibrium is reached sooner and the equilibrium salinity is lower than the equilibrium for the basic experiment with the depression in the shelf. The theoretical time for the system to reach equilibrium is dependent on the strength of the buoyancy flux and the size of the forcing region, and should be independent of the depth according to equation 3.21. The additional time required for the system to reach equilibrium is due to the shape of the topography. The water in the depression is not subject to the lateral advection of less dense water into the area beneath the forcing region and prevents the advection of dense water away from the forcing region. This reduces the lateral buoyancy flux between the area beneath the forcing region and that outside of the forcing region. According to equation 3.24, the salinity equilibrium is inversely proportional to the depth beneath the forcing region.

The topography beneath the forcing region in the flat shelf experiment is shallower and equation 3.24 predicts a higher equilibrium salinity. This does not occur. A depression beneath the forcing region is able to effectively trap dense water and allows this trapped water to become denser than it would in the absence of a depression.

With a sill present at the shelf break, an equilibrium is not reached during the 240 day winter forcing period. The salinity in the depression at the end of winter with a sill at the shelf break is greater than the salinity in the depression in the basic experiment without a sill. The sill reduces the amount of water exchanged between shelf and the deep ocean. The reduced supply of ambient offshore water reduces the supply of less dense water on the shelf. This reduces the lateral buoyancy flux between the area beneath the forcing region and area outside, thereby increasing the time that the system requires to reach equilibrium and allowing a greater increase of salinity beneath the forcing region.

In common with the sill experiment, the salinities beneath the forcing region in the one and two channel experiments do not come to equilibrium during the 240 day winter period. The salinity on the shelf for these experiments with the channel is very close to the salinity for the sill experiment without a channel. The presence of a channel in the sill allows the onshore transport of MCDW and the offshore transport of dense water between the shelf and the slope which does not occur in the sill experiment. The presence of a second channel at the eastern end of the depression increases the cross-shelf exchange and provides another source of dense water onto the slope.

For all first year experiments the maximum initial salinity on the shelf is 34.5 psu and is found in the depression. It takes 90 days before dense water with $S \geq 34.6$ psu is found on the shelf. Due to the time to produce this dense water, only a small amount is advected over the shelf break to potentially form bottom water. In the second year

experiment, the water in the depression is initialised with the range of salinity found at the end of the first year experiment, i.e., $S = 34.6 - 34.7$ psu, and the water on the shelf is also initialised to be more stratified and more saline i.e., $S = 34.4 - 34.6$ psu. As a result, more dense water is formed and the flux of dense water over the shelf break is $\sim$150 times greater in the second year experiment than it is in the first year experiment.

Chapter 6

Wind Driven Effects

This chapter describes the effect of wind on dense water formation. The topographic configuration used in this chapter is the same as used in the channel experiment in Section 5.3.1 which contains a depression in the shelf, a sill at the shelf break and a channel through the sill. The stratification is as used in the basic experiment given by equation 4.1. The basic wind configuration uses a 10 m s^{-1} easterly wind, providing a wind stress of 0.2 Pa, constant in time and uniform[1] in space. The easterly wind simulates the katabatic winds of Antarctica that are described in Section 2.2. Section 6.1 concerns the effects of the topography and the basic wind without a buoyancy flux. Section 6.2 concerns the basic wind configuration together with the basic buoyancy forcing as described and used in Section 4.1.1. The response to a pulsating wind of period 10 days and amplitude 10 m s^{-1} applied uniform in space is addressed in the Section 6.3, and Section 6.4 concerns the response to a wind stress curl.

The conditions in Sections 6.2 and 6.3 that produced dense water with the weak first year stratification were used in conjunction with increased stratification and dense water

[1]To differentiate between variables which remain the same over either space or time, the word "constant" is used to refer to something that does not change over time and the word "uniform" is used to refer to something that does not change in space.

in the depression to simulate the second year of dense water production. The initial salinity is given in equation 5.2.

6.1 Effect of a uniform wind only

The effect of the wind on the circulation is described in this section. No buoyancy flux is considered here. The constant easterly wind results in an onshore Ekman transport in a surface Ekman layer ~50 m thick. The onshore transport across the sill is 1.18 Sv, as listed in Table B.3.

The onshore transport of surface water makes up 99% of the total onshore flow, and the volume of surface water on the shelf increases from 47 to 82% of the volume of water on the shelf. The composition of water masses on the shelf are shown in Figure 6.1b and the water masses are defined in Table 4.2. As the shelf fills with surface water, shelf water is driven off the shelf.

The composition of water masses in the depression is plotted in Figure 6.1a. The water in the depression is initialised with salinity between 34.45 and 34.5 psu. After 360 days of wind forcing, 47% of the water in the depression is replaced with lighter shelf water (34.425 $< S <$ 34.45 psu) and 4% is replaced with surface water ($S <$ 34.425 psu). The minimum salinity drops from 34.450 psu to 34.408 psu and the mean salinity of the water in the depression drops by 0.013 psu.

The onshore transport increases the sea surface elevation above the shelf and produces a negative elevation gradient above the sill which in turn drives a westward along-sill current shown in Figure 6.2. East or upstream of the channel ($y <$ 330 km) the along-sill current follows the 400 m isobath on the shelf side. Here the sea surface elevation gradient $d\eta/dx \simeq 10^{-6}$ and the alongshore current $v \simeq$ 0.12 m s^{-1} satisfy

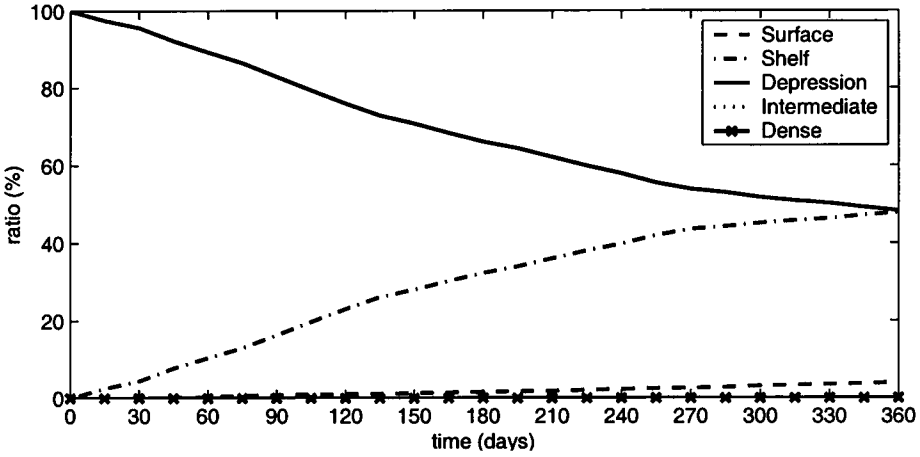

(a) Depression

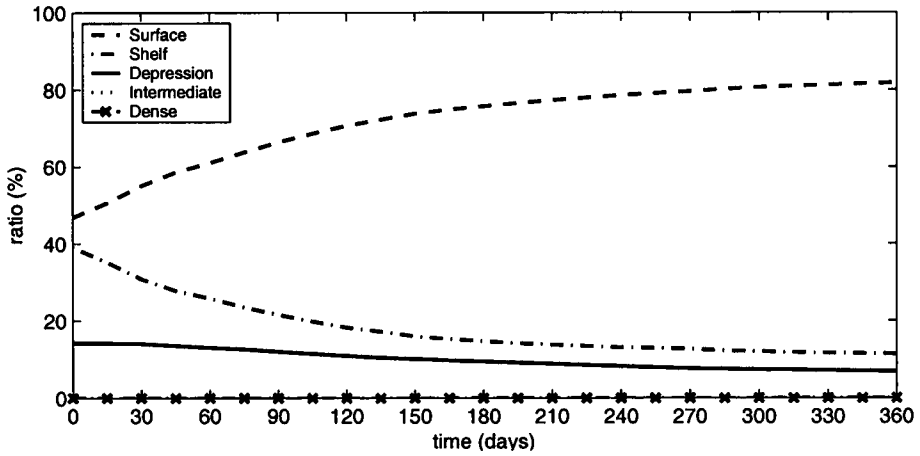

(b) Shelf

Figure 6.1: *Breakdown of water masses (a) in the depression and (b) on the shelf for the wind only experiment described in Section 6.1. The water masses are defined in Table 4.2.*

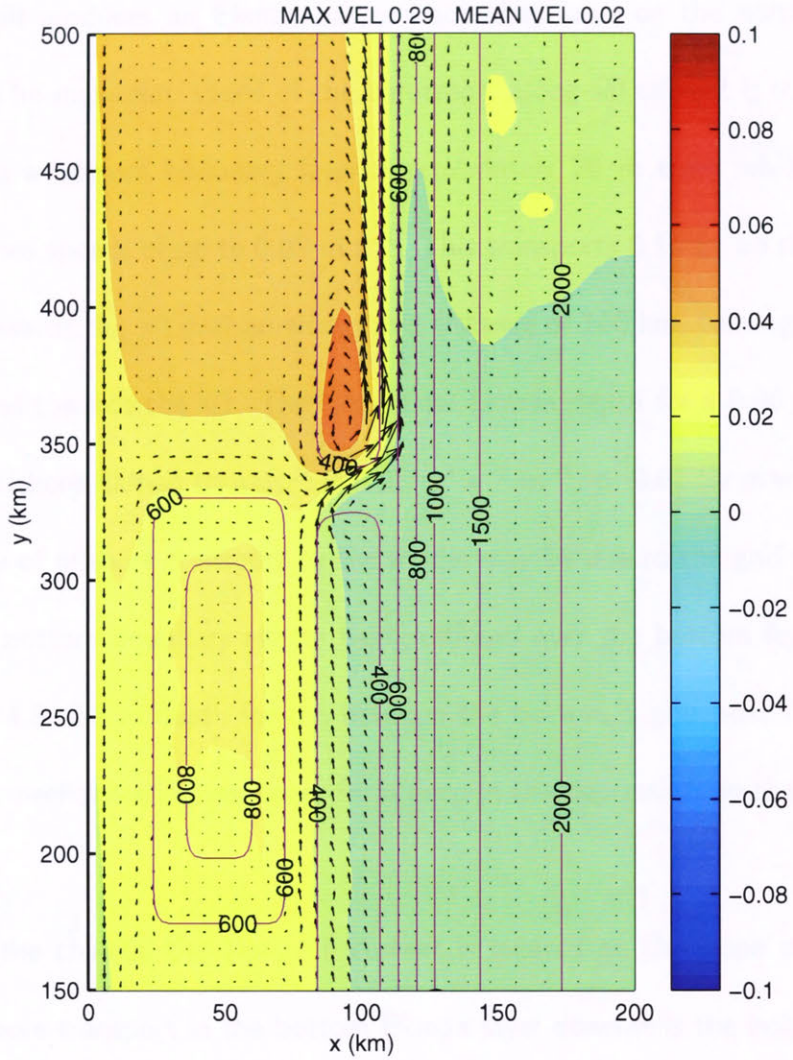

Figure 6.2: *Elevation and barotropic velocities in the wind only experiment in Section 6.1 at t=240 days. The solid magenta lines are the isobaths labelled in m. The colourbar for the elevation is labelled in m and the mean and maximum velocities are in* $m\ s^{-1}$.

the geostrophic velocity equation 5.1. At the channel, the current is diverted offshore through the channel then continues to follow the 400 m isobath on the slope side of the sill west or downstream of the channel ($y > 330$ km). The offshore velocity through the channel is strong with velocities > 0.20 m s^{-1} and an offshore transport of 1.52 Sv. Note that this along-sill current is in the opposite direction of the eastward along-sill current and onshore flow through the channel shown in Figure 5.6 generated in the channel experiment without a wind.

The along-sill current east (upstream) of the channel which is located on the shelf

side of the sill produces an Ekman bottom boundary layer on the north bank of the depression. The maximum speed of the barotropic along-sill current is 0.06 m s^{-1} and this produces a bottom boundary layer approximately 20 m thick while the offshore velocity reaches speeds of up to 0.02 m s^{-1}. This transports 0.14 Sv up the bank of the depression towards the sill over an alongshore distance of 160 km, causing the isohalines to be upwelled towards the sill. The theoretical Ekman depth for a 0.06 m s^{-1} current is 2 m and offshore Ekman transport is 0.07 m^3 s^{-1} m^{-1}, or 0.01 Sv over 160 km. The over estimate of offshore transport by the model may be due to the grid spacing at the bottom, the bottom boundary effects being diffused over the bottom few layers which are 2.4, 2.4, 4.8, 9.6 m depth for the between the bottom 5 grid points at a depth of 500 m. This mechanism moves water from deep in the depression up the bank towards the sill.

West of the channel the along-sill current is located on the slope side of the sill, and the offshore transport in the bottom Ekman layer downwells the isohalines. As the current moves through the channel it splits; part of it recirculates back onto the shelf creating a small eddy, and the remaining water follows the 400 m isobath on the slope side of the sill and continues to travel westward. Most of the energy goes into the alongshore current on the offshore side of the sill. The maximum offshore transport at the shelf break is associated with this meander through the channel. The speed of the current is maximum at the western head of the channel (0.28 m s^{-1}) and it decays to 0.15 m s^{-1} 100 km downstream, close to the observed speed of the East Wind Drift. The slope current is 22 km wide and extends out to the 800 m isobath. The bottom boundary layer generated by the along slope current in this experiment is $\sim$40 m thick and transports 1.22 m^3 s^{-1} m^{-1} offshore. For 0.15 m s^{-1} to 0.28 m s^{-1} velocities, the

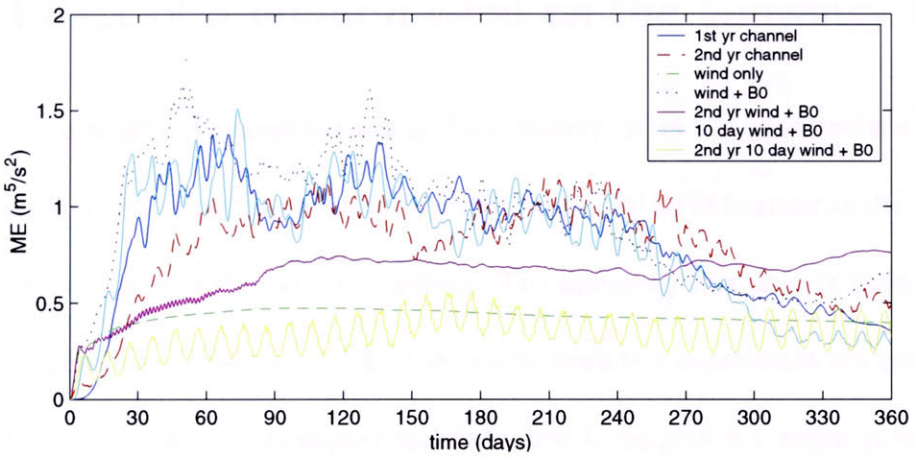

Figure 6.3: *Total mechanical energy on the shelf for the first year channel experiment in Section 5.3.1; second year channel experiment in Section 5.3.2; wind-only experiment in Section 6.1; wind and buoyancy flux experiment in Section 6.2; second year wind and buoyancy flux experiment in Section 6.2.1; 10 day pulsating wind and buoyancy flux experiment in Section 6.3; and second year 10 day pulsating wind and buoyancy flux experiment in Section 6.3.2.*

.

theoretical Ekman depth ranges from 6 to 11 m and the offshore transport ranges from 0.42 to 1.47 $m^3\ s^{-1}\ m^{-1}$.

The total mechanical energy can be calculated by

$$\mathrm{ME} = \int g\eta^2 + \frac{1}{2}(H+\eta)(u^2+v^2)\ dA \tag{6.1}$$

where η is the sea surface elevation, H is the water depth, and (u, v) are the barotropic velocities. Figure 6.3 shows the total mechanical energy on the shelf for this wind-only experiment. The mechanical energy generated in the channel experiment forced by the buoyancy forcing only in Section 5.3.1 is twice the mechanical energy generated by the wind forcing in this experiment.

6.2 Effect of a uniform wind on the buoyancy flux

The combined effects of a constant and uniform easterly 10 m s^{-1} wind and the buoyancy flux are investigated using the same bathymetry and initial stratification as the wind-only experiment described in the previous section. The buoyancy flux used is as in the basic experiment described in Section 4.1.1. The results from this experiment are compared to the results from the wind-only experiment described in Section 6.1 which is forced with the same wind but without the buoyancy flux and the channel experiment described in Section 5.3.1 which is forced with the same buoyancy flux but without the wind forcing.

The water column CM1 marked in Figure 4.1 takes 6 days to homogenise, the same time taken for the channel experiment. The salinity of CM1 increases at the same rate as it does in the channel experiment, $dS/dt = 0.0045$ psu day^{-1}. This value agrees with the expected value calculated from equation 4.3.

Water masses

Figure 6.4b depicts the breakdown of the water masses on the shelf. The water masses are defined in Table 4.2. The onshore flux of surface water replenishes the supply of less dense water on the shelf so that the decrease in low salinity water masses (surface, shelf and depression water) is less than it is in the channel experiment without the wind. The intermediate and dense water masses are created at a slower rate in this experiment than the channel experiment without the wind.

Figure 6.4a shows the ratio of the water masses in the depression. The water in the depression is initially replaced with intermediate water. After day 90, the depression begins to fill with dense water until 91% of the depression is filled with dense water at the beginning of summer. During the summer some dense water is flushed out of the

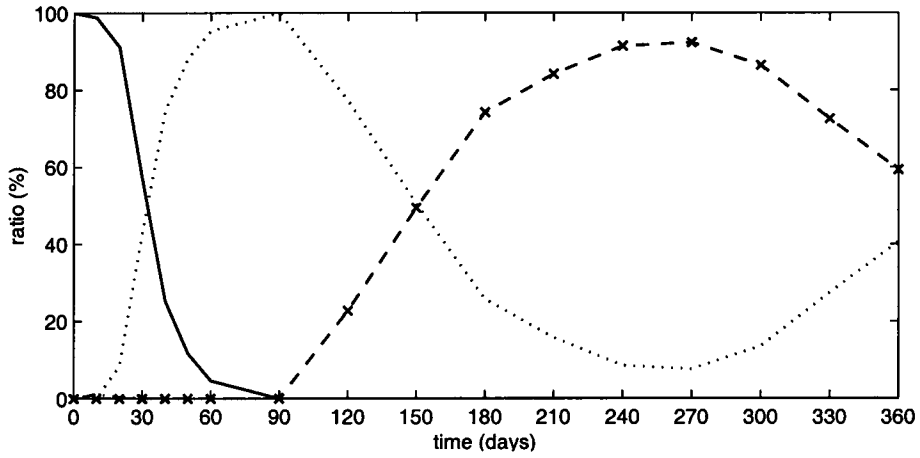

(a) Depression

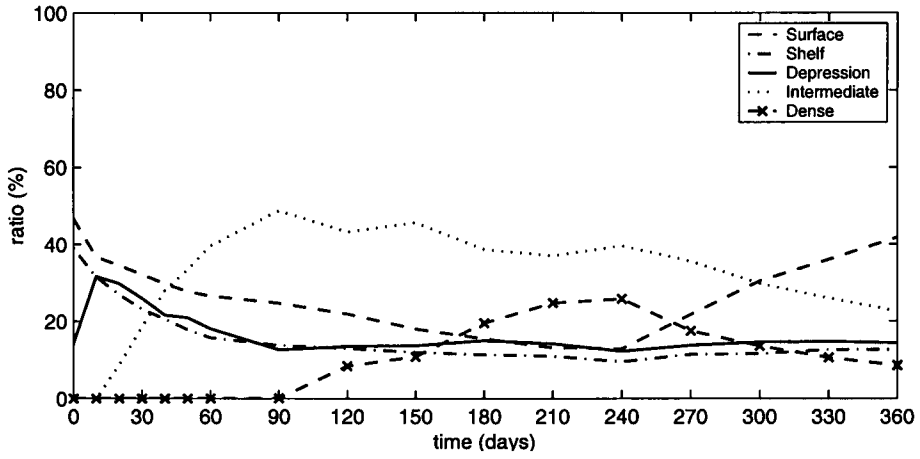

(b) Shelf

Figure 6.4: *Breakdown of water masses (a) in the depression and (b) on the shelf for the uniform wind and buoyancy flux experiment described in Section 6.1. The water masses are defined in Table 4.2.*

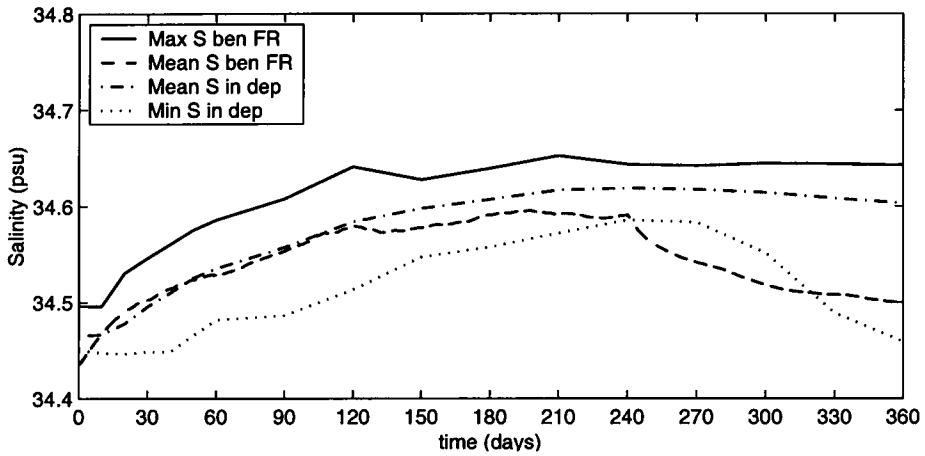

Figure 6.5: *Maximum and mean salinities for the uniform wind and buoyancy flux experiment in Section 6.2.*

depression and is replaced with intermediate water. In the experiments without the wind the dense water is not flushed from the depression during summer.

Equilibrium

The lateral buoyancy flux between the area beneath the forcing region and the area outside is increased by the onshore transport of surface water generated by the wind. This reduces the time for the area beneath the forcing region to reach equilibrium. The mean and maximum salinities beneath the forcing region shown in Figure 6.5 reach equilibrium after 120 days. Whereas the channel experiment without the wind described in Section 5.3.1 does not reach equilibrium within the 240 day winter period. The equilibrium salinity of the water beneath the forcing region is less than the equilibrium salinities reached by all previous experiments configured with a depression in the shelf and no wind, these salinities are listed in Table B.2.

Figure 6.5 plots the maximum and mean salinities beneath the forcing region and the mean and minimum salinity in the depression. The mean salinity beneath the forcing region after 30 days is 0.01 psu less saline in this experiment than in the channel exper-

iment without the wind described in Section 5.3.1. This difference grows to 0.06 psu at the end of winter. The same trend occurs with the mean salinity in the depression.

At the end of winter, the mean age of the water in the depression is 60 days, 35 days older than the channel experiment without the wind. This is caused by

1. water produced by the forcing region being less dense than it is in the experiment without the wind, and not having as much potential to displace water in the depression; and

2. wind-generated currents advecting the dense water away from the forcing region and the depression so that there is less dense water to flush the depression.

Flow on the shelf

The elevation and the barotropic currents at the end of winter are shown in Figure 6.6 and the time averaged alongshore currents at $y = 250$ km are shown in Figure 6.7. The westward along-sill current is stronger than the along-sill current in the wind only experiment. The westward flow at the coast is due to the westward movement of dense water along the coast and is absent in the wind-only experiment. The eastward flow at the surface above the deepest part of the depression is present in the channel experiment and this experiment but is absent from the wind-only experiment.

The total mechanical energy on the shelf is plotted in Figure 6.3. The mechanical energy generated by the wind and the buoyancy flux on the shelf during winter is 16% more than the experiment forced with buoyancy flux alone and 2.6 times the energy generated by the wind alone over the same bathymetry. The mechanical energy resulting from the combined buoyancy and wind forcing is less than the sum of the mechanical energy due to buoyancy forcing alone and the wind forcing alone. The mechanical energy

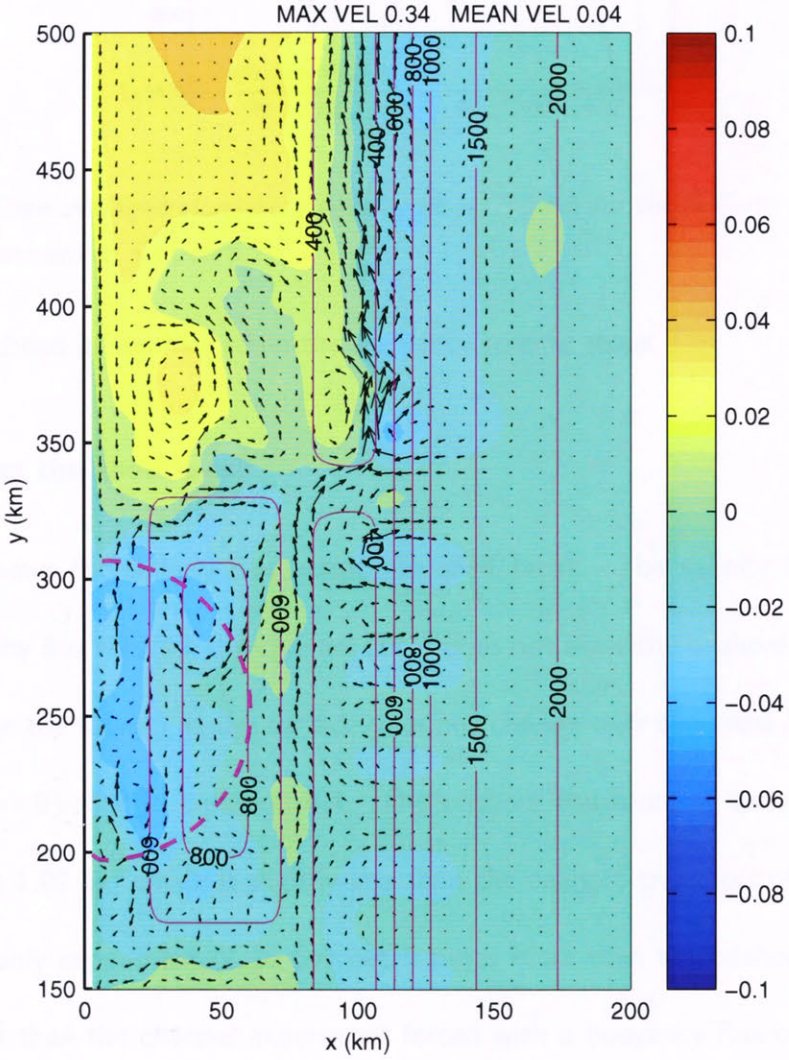

Figure 6.6: *Elevation and barotropic velocities for the constant uniform wind and buoyancy flux experiment in Section 6.2. The solid magenta lines are the isobaths labelled in m and the dashed magenta line shows the forcing region. The colourbar for the elevation is labelled in m and the mean and maximum velocities are in* $m\ s^{-1}$.

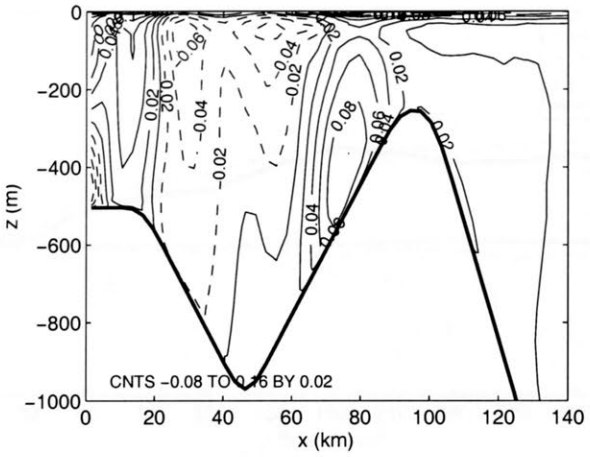

Figure 6.7: *Time averaged alongshore velocity at y=250 km for the uniform wind and buoyancy flux experiment in Section 6.2.*

on the shelf drops in summer when the buoyancy forcing stops.

Fluxes across the shelf break

Figure 6.8 shows the salinity flux across the shelf break. The salinity flux shows the offshore salinity flux through the channel but it does not show the onshore flux of surface water because the salinity at the surface does not change over time and $S(x_0, y, z, t) - S(x_0, y, z, t = 0) \approx 0$ in equation 4.4. The onshore transport of surface water $S \leq 34.425$ psu is 1.07 Sv, which is slightly less than the onshore transport of surface water in the wind-only experiment (1.16 Sv) but 5 times more than the onshore transport of surface water than the channel experiment forced with a buoyancy flux only.

The along-sill current above the northern bank of the depression generates offshore transport in the bottom boundary layer and moves the dense water towards the sill where some of it moves over the sill and down the slope. Above the 400 m isobath on the shoreward side of the sill in Area 1 (east of the channel, $162 < y < 318$ km) the offshore transport for the year is 0.26 Sv, this is 1.8 times the offshore transport for the experiment with no buoyancy forcing in Section 6.1.

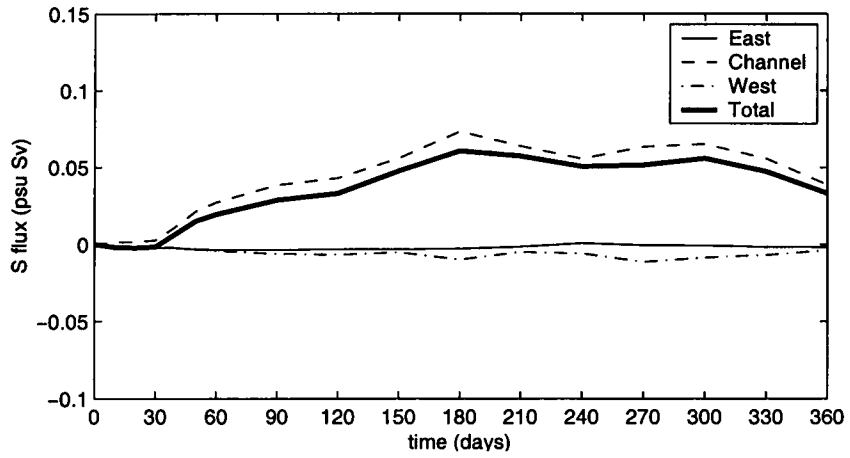

Figure 6.8: *Salinity fluxes across the shelf break (x=96 km) for the uniform wind and buoyancy flux experiment in Section 6.2. The 270 km length of the shelf is broken into the area above the channel y=316–349 km, east of the channel y=160–316 km and west of the channel y=349–430 km.*

Flow through the channel

The cross-shelf velocities through the channel are shown in Figure 6.9a. The cross-shelf transport is dominated by the offshore transport through the channel. The offshore transport through the channel is 1.20 Sv for this experiment, which accounts for 84% of the total offshore transport across the shelf break. The offshore transport is 21% less than the offshore transport through the channel for the wind-only experiment and 9 times more than the transport for the channel experiment forced by a buoyancy flux only. This flow through the channel is predominantly generated by the offshore flow due to the meander of the along-sill current through the channel, the greater offshore flow through the channel for the wind-only experiment is somewhat surprising as the along-sill flow is greater in the wind and buoyancy flux experiment. This may be due to the fact that the along-sill current in the wind-only experiment is a steady current whereas the along-sill current in this experiment has many meanders and some of the energy is fed into the eddies instead of being diverted through the channel.

The on and offshore transports across the shelf break for this experiment are 1.35

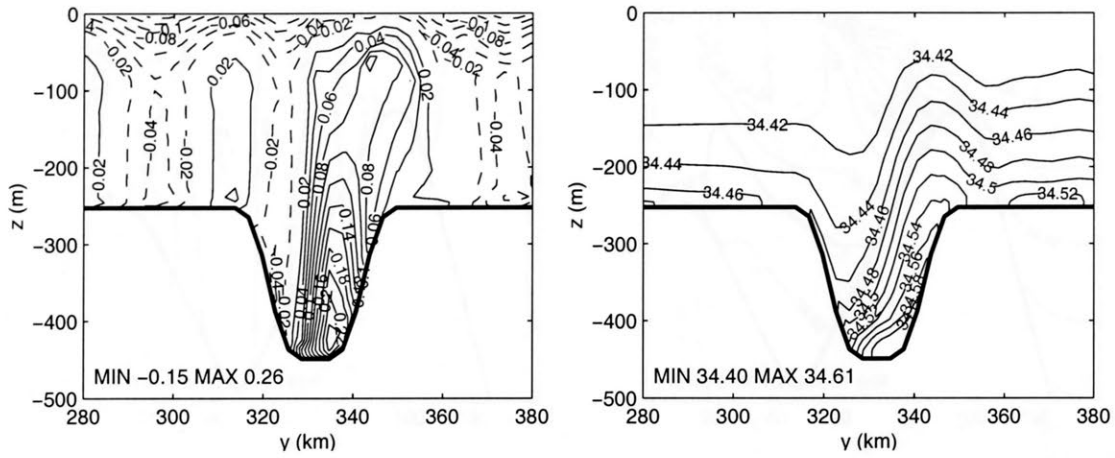

(a) Across-shelf velocity

(b) Salinity

Figure 6.9: *Cross channel section at x=96 km of (a) across-shelf velocity (solid lines for offshore and dotted lines for onshore) and (b) salinity for day 240 for the uniform wind and buoyancy flux experiment in Section 6.2.*

and 1.43 Sv, respectively. This is ∼3 times those of the experiment without the wind in Section 5.3.1 and similar to the on and offshore transport as the wind-only experiment in Section 6.1.

The salinity in the vicinity of the channel is plotted in Figure 6.9b. More saline water is found on the western side of the channel where the flow is offshore. The salinity and cross-shelf velocities are used to calculate the cross-shelf salinity flux using equation 4.4. The averaged offshore salinity transport through the channel is 0.048 psu Sv. The net salinity transport is reduced by the onshore salinity flux in the surface Ekman layer. The net salinity transport at the end of the year is 0.040 psu Sv offshore. Most of the onshore flux occurs west of the channel, close to the forcing region.

Dense water plume

The transport of dense water with $S \geq 34.6$ psu over the shelf break is 0.013 Sv. The volume of dense water transported offshore is 14 times more than the channel

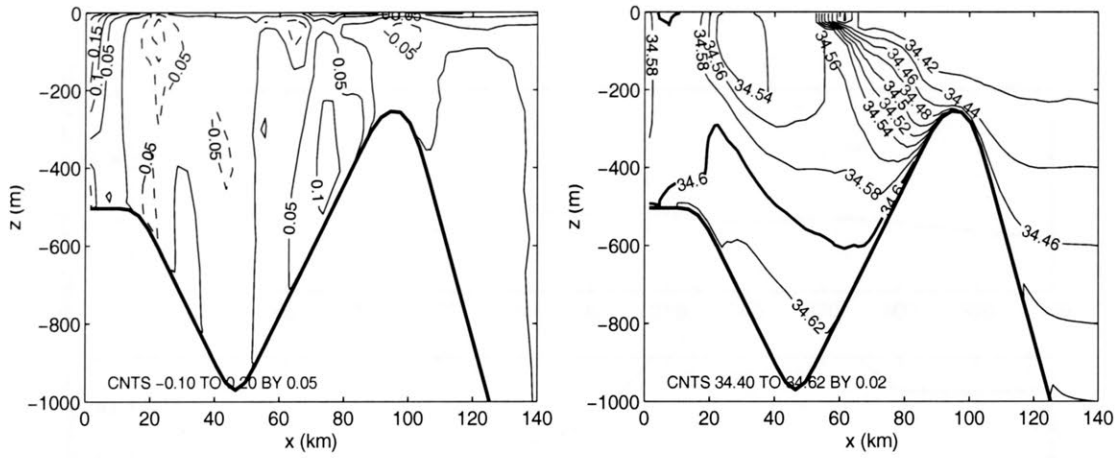

(a) Along shore velocity

(b) Salinity

Figure 6.10: *Across-shelf section at y=250 km of (a) alongshore velocity (solid lines show westward flow into the page and dashed lines show eastward flow) and (b) salinity through the depression after 240 days for the uniform wind and buoyancy flux experiment in Section 6.2.*

experiment without the wind in Section 5.3.1. All offshore transport of dense water passes through the channel, and no dense water passes over the sill even with the assistance of the offshore transport in the Ekman bottom boundary layer. The dense water in the depression accumulates on the southern bank of the depression, as shown in Figure 6.10b. The westward velocity above the northern bank of the depression shown in Figure 6.10a drives a thin 20 m bottom boundary layer to the right, up towards the sill. This draws dense water up the bank of the depression to the 400 m isobath, however, the denser water is not raised quite enough to reach the sill at depth 250 m. The volume of intermediate water with salinity between 34.5 and 34.6 psu transported over the shelf break is 0.27 Sv. Of that 99% is transported out through the channel. The sill at the shelf break is high enough to trap dense water on the shelf. A small amount of intermediate water is transported over the sill in the bottom boundary layer.

The salinity, thickness, speed and direction of the plumes occurring in this experiment are plotted in Figure 6.11. The thickness of the plume is determined by the distance

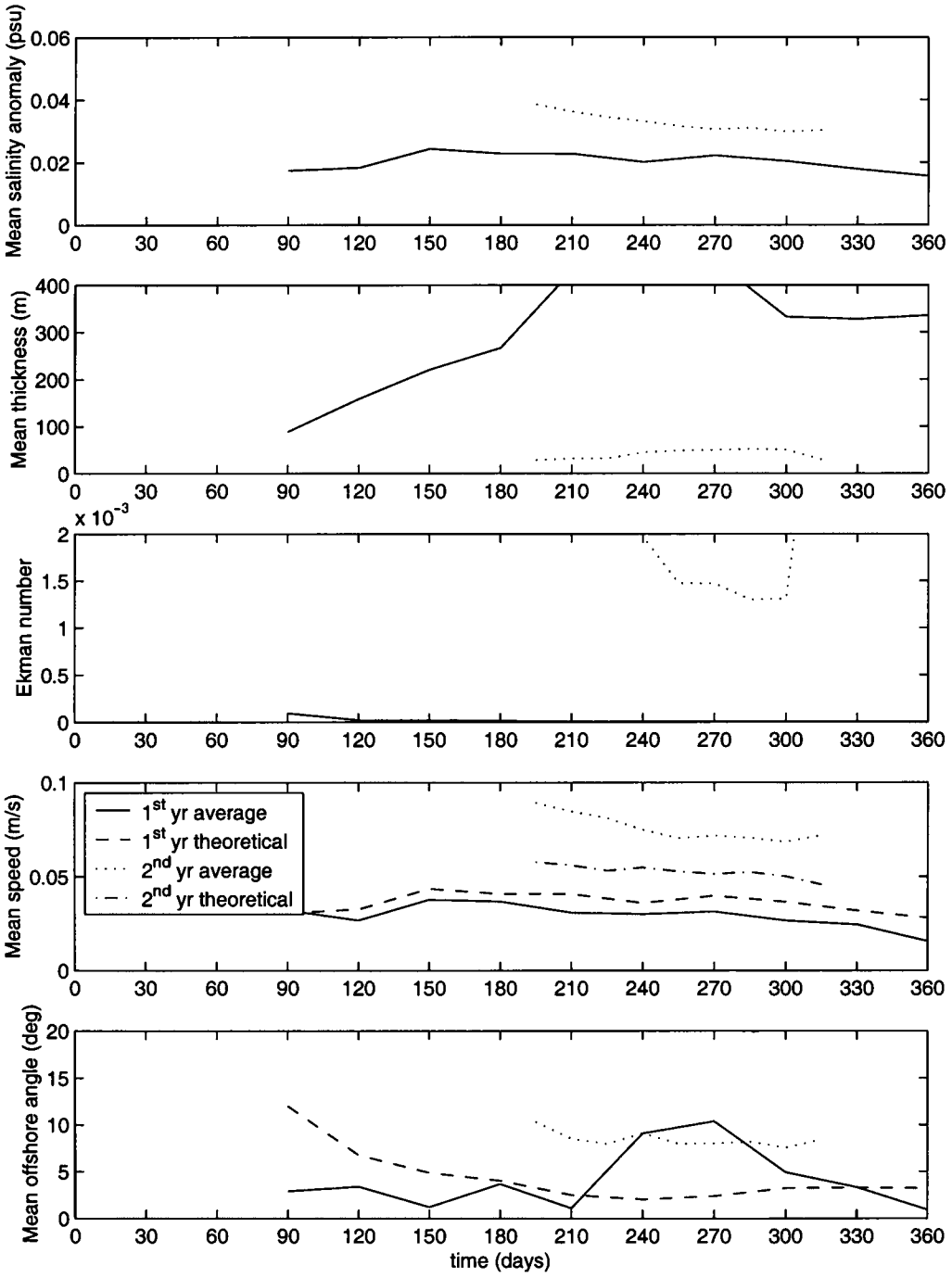

Figure 6.11: *The mean salinity anomaly, thickness, Ekman number, speed and direction of the plume at x=129 km, H=970 m, between y=342 and 432 km. The plume is delineated from the ambient water by a surface tracer concentration of c>0.02 for the the first year uniform wind and buoyancy flux experiment in Section 6.2 (solid line) and second year experiment in Section 6.2.1 (dotted line). The theoretical values for the speed and direction of the plume are calculated from equations 3.28 and 3.28 and plotted for the first year experiment (dashed line) and second year experiment (dash-dot line).*

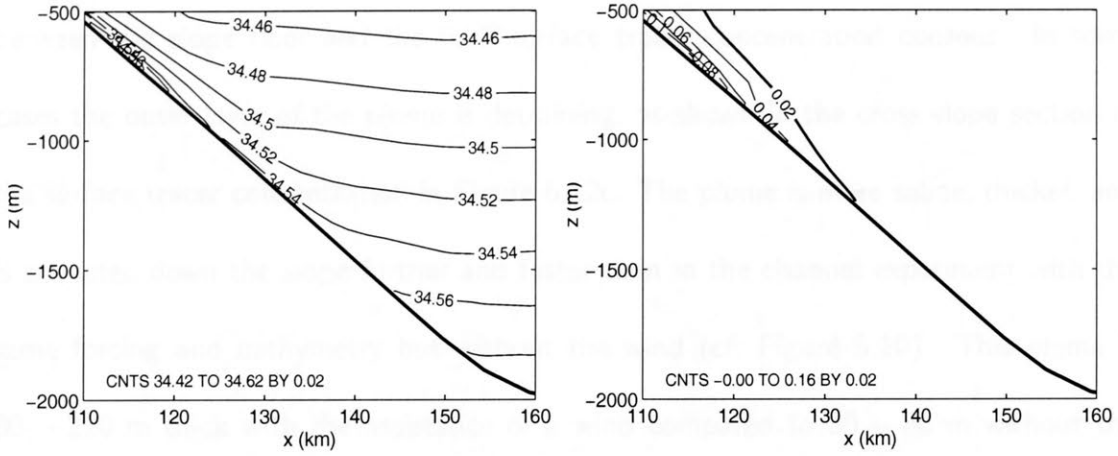

(a) Salinity (b) Salinity anomaly

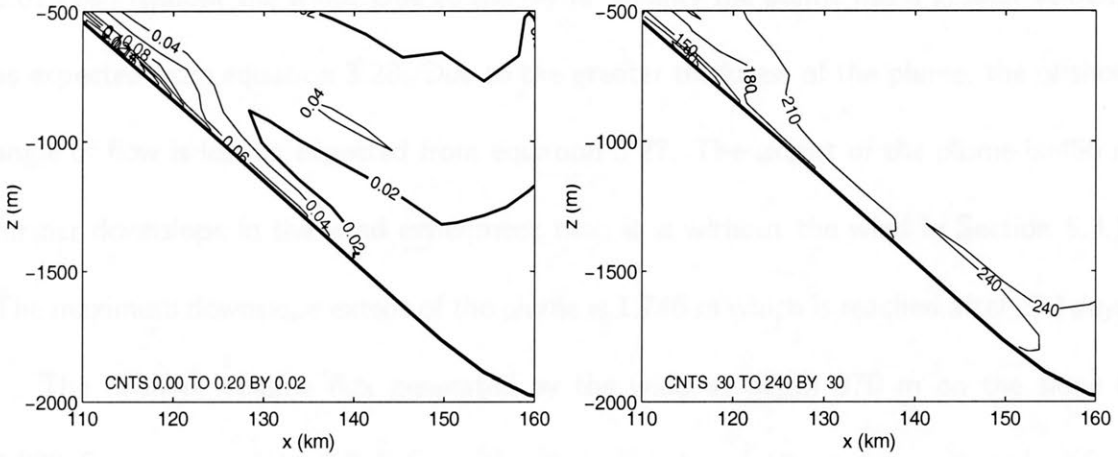

(c) Surface tracer concentration (d) Age

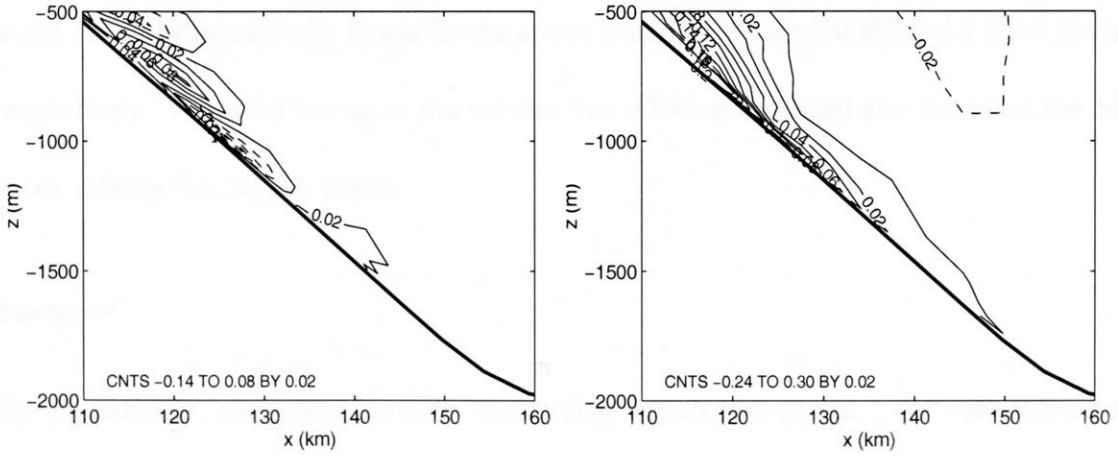

(e) Across-shelf velocity (f) Alongshore velocity

Figure 6.12: *(a) Salinity (psu), (b) salinity anomaly (psu), (c) surface tracer concentration, (d) age (days), and (e) across-shelf and (b) alongshore velocities (m s^{-1}) on the slope at y=372 km after t=240 days for the uniform wind experiment in Section 6.2.*

between the slope floor and the 0.02 surface tracer concentration contour. In some cases the outer layer of the plume is detraining, as shown in the cross slope section of the surface tracer concentration in Figure 6.12c. The plume is more saline, thicker, and is advected down the slope further and faster than in the channel experiment with the same forcing and bathymetry but without the wind (cf. Figure 5.10). This plume is $80 - 220$ m thick with the assistance of a wind compared to $30 - 80$ m without the wind. The mean salinity anomaly after 240 days is 0.020 psu with the wind, compared to 0.015 psu without the wind. Due to the higher salinity the plume has a greater velocity, as expected from equation 3.28. Due to the greater thickness of the plume, the offshore angle of flow is less as expected from equation 3.27. The extent of the plume is 486 m further downslope in the wind experiment than it is without the wind in Section 5.3.1. The maximum downslope extent of the plume is 1,746 m which is reached after 270 days.

The offshore volume flux generated by the wind at depth 970 m on the slope is 0.902 Sv, compared to 0.317 Sv without the wind and the same topography (Section 5.3.1). Thus the wind ultimately assists in the movement of dense water down the slope. The offshore salinity fluxes for the above experiments are 0.0067 and 0.0015 psu Sv, respectively. The wind increases the volume flux offshore threefold and increases the offshore salinity flux by 4.5 times.

Summer

During summer, the water beneath the forcing region restratifies. The restratification is facilitated by the onshore transport of surface water in the surface Ekman layer. The restratification takes 5 days in this wind and buoyancy flux experiment instead of 13 days that it takes in the experiment without the wind. The stratification on the shelf

is ~4 times the initial stratification. The water mass composition on the shelf shown in Figure 6.4b shows that the amount of surface water on the shelf increases substantially, whereas the amount of intermediate and dense waters decrease. The channel experiment loses approximately the same amount of dense water as this experiment, but the water is replaced with water masses which are more dense than the surface water i.e., $34.6 < S < 34.425$ psu. The mean salinity on the shelf decreases from 34.523 psu at the beginning of summer to 34.453 psu at the end, this decrease is 0.02 psu more than the channel experiment without the wind.

6.2.1 Second year

Section 5.3.2 demonstrates that the initial stratification of the model makes a large difference to the results. This experiment uses the same stratification that is used in the second year channel experiment described in Section 5.3.2 with dense water in the depression and increased stratification on the shelf. The initial salinity is given in equation 5.2. The buoyancy flux and the wind forcing used are the same as those used in the previous experiment, which will be referred to as the first year experiment in this section.

The onshore transport of surface water is 1.11 Sv. As the same wind forcing is used as the first year experiment, the onshore transport of surface water is nearly the same.

The mechanical energy on the shelf is shown in Figure 6.3. The mechanical energy on the shelf generated during winter in this experiment is 55% less than the mechanical energy generated by the first year experiment which used the same forcing but was initialised with the weaker stratification on the shelf than this experiment. This reduction in mechanical energy is expected as increased stratification inhibits the penetration of

wind-driven circulation (Spall and Pickart, 2003). If the stratification is strong enough, the wind driven circulation can be decoupled from the bathymetry which may also result in the eddies associated with local topography not being formed, which will further reduce the amount of mechanical energy in the region compared to the less stratified first year experiment. For the first year experiment, the mean mechanical energy decreased from winter to summer. In this experiment, the mean mechanical energy remains constant at 0.69 $m^5\ s^{-1}$ in the second half of winter to summer.

The buoyancy flux is unable to homogenise the water column at CM1, in contrast with the previous experiment with the weaker stratification and same wind that took 6 days, or the second year channel experiment without a wind described in Section 5.3.2 which homogenised the water column of the same initial stratification as this experiment in 22 days. The mechanical energy on the shelf for the first 25 days is greater in the second year experiment with the wind than it is for the second year channel experiment without the wind in Section 5.3.2. This initial energy on the shelf prevents shallow convection from occurring. Only deep convection occurs and no water denser than that which is already present on the shelf is formed in this experiment.

The depression takes 225 days to flush and the mean age of the water in the depression at the end of winter is 184 days. Figure 6.13a shows the breakdown of the water masses in the depression for the second year experiment. In common with the wind-only experiment, the water in the depression is flushed out by shelf water that is less dense than the water initially in the depression. The mean age of the water in the depression is 39 days less than the age of the water in the depression in the wind-only experiment in Section 6.1. This long flushing time occurs because water formed beneath the forcing region is not as dense as the water in the depression, in fact the mean salinity beneath

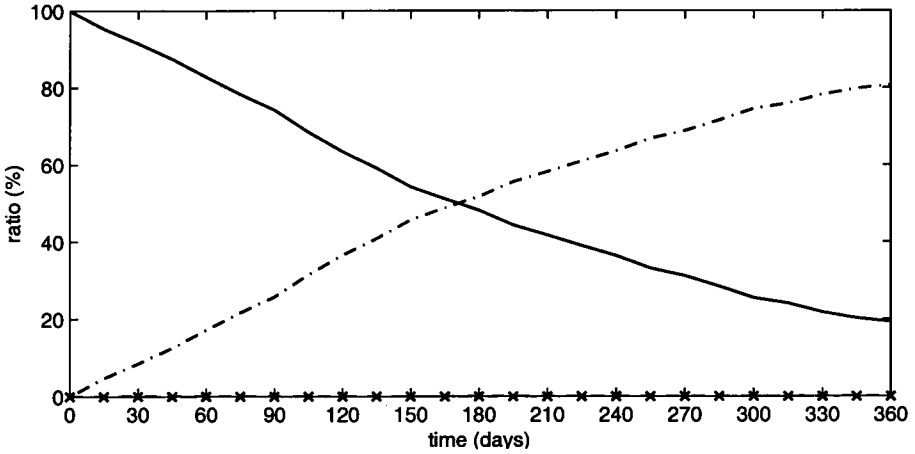

(a) Depression

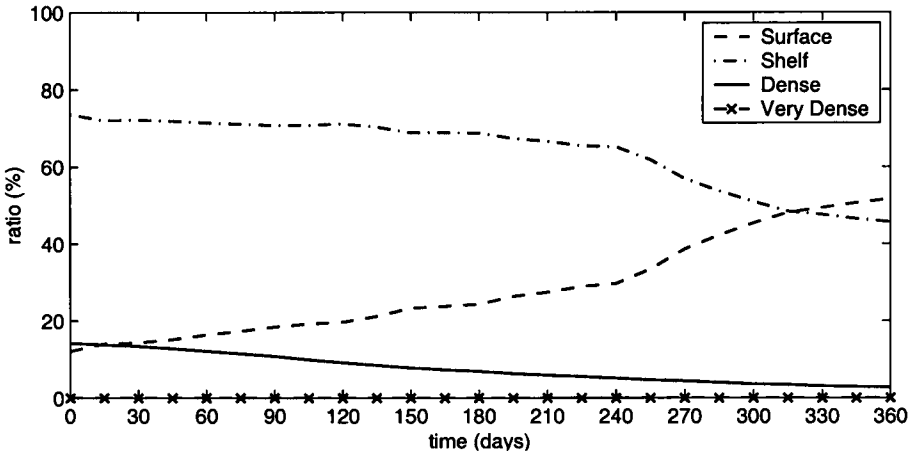

(b) Shelf

Figure 6.13: *Breakdown of water masses (a) in the depression and (b) on the shelf for the second year, uniform wind and buoyancy flux experiment described in Section 6.2.1. The water masses are defined in Table 5.1.*

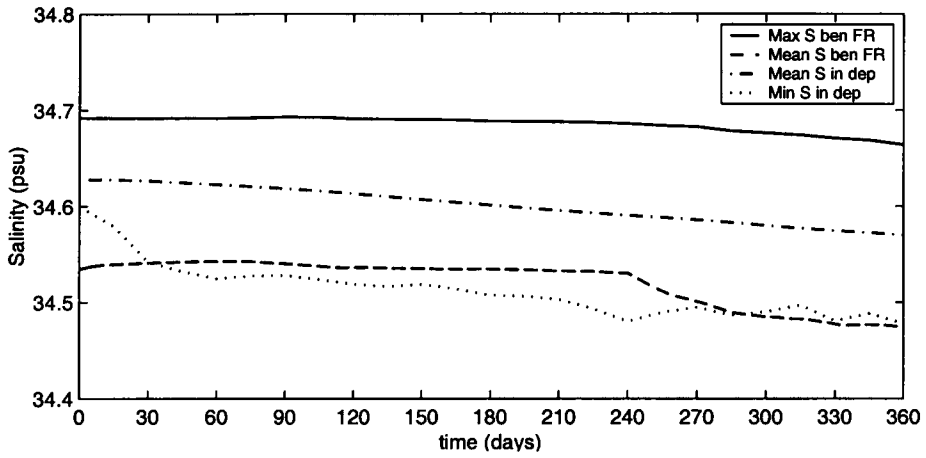

Figure 6.14: *Maximum and mean salinities beneath the forcing region and mean and minimum salinities in the depression for the second year, uniform wind and buoyancy flux experiment described in Section 6.2.1.*

the forcing region decreases over time due to an onshore flux of surface waters directly beneath the forcing region. By the end of the year 81% of the dense water initially in the depression has been flushed out.

Figure 6.14 shows the maximum and mean salinities beneath the forcing region, and the minimum and mean salinities in the depression. The salinities beneath the forcing region and in the depression decrease with time, dominated by the effects of onshore transport of surface water in the wind driven Ekman layer shown by the increasing amount of surface water on the shelf during winter shown in Figure 6.13b.

The offshore transport of dense water $S \geq 34.6$ psu across the shelf break is 4×10^{-4} Sv. This is 5% of the transport in the previous experiment with the first year stratification. Unlike the first and second year channel experiments without the wind described in Sections 5.3.1 and 5.3.2, the initial higher stratification on the shelf and the presence of dense water in the depression does not increase the dense water formation.

Figure 6.11 shows the properties of the plume at $H = 970$ m on the slope. The plume appears here only between days 195 and 315. It is thinner and more saline than the plume produced by the first year experiment. The Ekman number is greater than

10^{-3} (up to 7×10^{-3}) suggesting that the flow may not be stable, but the velocity field of the plume is uniform alongshore and there are no eddies. The maximum extent of the plume is only 1,060 m.

Once the forcing stops, it takes 5 days to restratify, similar to the time taken for the first year wind and buoyancy forcing experiment, and to the time taken for the second year channel experiment with no wind in Section 5.3.2. Figure 6.13b shows that the amount of surface water on the shelf increases at a faster rate during summer than winter.

6.3 Periodic Wind

In order to simulate the pulsating katabatic winds described in Section 2.2 a pulsating wind is used in this experiment. The intention here is to see if how a pulsating wind affects the production and circulation of dense water versus the constant wind. The buoyancy flux used in this experiment is the same as that used in the basic experiment described in Section 4.2. The spatially uniform easterly wind pulses, such that the wind stress defined in equation 3.5 varies according to

$$\tau^y = \tau^y_{\text{max}} \left(\frac{1}{2} - \frac{1}{2} \sin \left(\frac{2\pi t}{T} \right) \right)$$

where the period $T = 10$ days and $v_{\text{wind max}} = 10$ m s^{-1}. The mechanical energy produced on the shelf is shown in Figure 6.3. As a result the total surface momentum flux is 50% of the uniform 10 m s^{-1}wind. During winter the mechanical energy in this experiment is 87% of the energy produced by the first year uniform wind and buoyancy flux experiment in Section 6.2. A spectral analysis of the mechanical energy reveals that

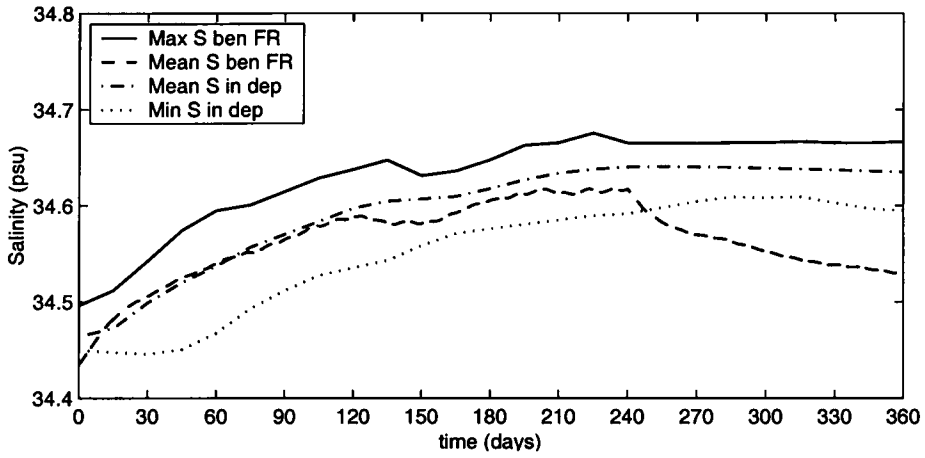

Figure 6.15: *Maximum and mean salinities for the experiment with the sill at the shelf break and channel through the sill forced by the standard buoyancy flux and uniform in space 10 m s^{-1} easterly wind which pulsates with a period of 10 days.*

it has a very strong signal at a 10 day period. The mechanical energy builds up very rapidly in the first 30 days of winter and oscillates a around a mean value of 0.98 m^5 s^{-2} during the second half of winter. During summer, the mean mechanical energy is halved.

The cross shore transports across the shelf break are listed in Table B.2. The reduction in total momentum flux across the surface due to the pulsating wind instead of the uniform wind results in reduced cross-shelf transport. The on and offshore transports for this experiment are ~65% of the corresponding transports in the uniform wind experiment in Section 6.2.

The onshore transport of surface water is 0.65 Sv. This is 61% of the onshore transport of surface water in the uniform wind experiment in Section 6.2. The maximum and mean salinities beneath the forcing region and the mean and minimum salinities in the depression are plotted in Figure 6.15. The mean salinity beneath the forcing region increases, plateaus at day 120 at 34.588 psu, then increases again reaching an equilibrium salinity of 34.617 psu after 200 days. The salinity fluctuates about this equilibrium until the end of winter. The maximum salinity beneath the forcing region plateaus at 34.647 psu at day 135, and then reaches an equilibrium maximum salinity

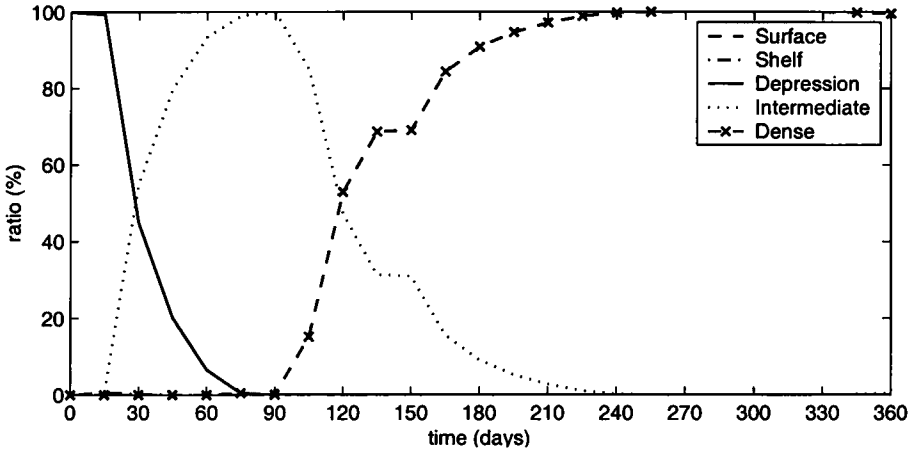

Figure 6.16: *Ratio of water masses in the depression for the first year periodic wind experiment in Section 6.3. See Table 4.2 for the definition of the water masses.*

of 34.675 psu on day 225. The mean salinity beneath the forcing region is greater than it is for the uniform wind experiment but less than the channel experiment without the wind. The same trend applies to the mean salinity in the depression.

The age of the water in the depression at the end of winter is 43 days. The age of the water in the depression is older than for the channel experiment with no wind forcing, but younger than for the uniform wind experiment where the mean salinity beneath the forcing region reached equilibrium before the end of winter, so that the newly formed water does not have the potential to displace the water in the depression.

The ratio of water masses in the depression are shown in Figure 6.16 and the water masses are defined in Table 4.2. The water in the depression fills with intermediate water that is denser than the water that is initially in the depression. Eventually the depression fills with dense water $S \geq 34.6$ psu, whereas in the uniform wind experiment described in Section 6.2, only 91% of the depression fills with dense water in winter, and then during summer some of the dense water is flushed out of the depression by less dense intermediate water. In this experiment the depression completely fills with dense water by the end of winter and the dense water remains in the depression during summer.

Dense water with $S \geq 34.6$ psu is transported across the shelf break through the channel only. The offshore transport of dense water is 0.019 Sv. This is 45% more than the amount transported by the uniform wind experiment, even though the total offshore transport is 38% less. The alongshore current at the coast produced by the uniform wind tends to advect the dense water alongshore. In this experiment the current is not as strong and the water tends to remain near the forcing region, depression and channel allowing the dense water to be transported through the channel and onto the slope.

Once the forcing stops, the water beneath the forcing region takes 9 days to restratify. This is longer than the time for restratification in the uniform wind experiment but less than for the experiment with no wind. The stratification on the shelf is $\sim$4 times the initial stratification, the same as the uniform wind and buoyancy flux experiment and the channel experiment without wind forcing. As the onshore transport of surface water is less for this experiment than the uniform wind experiment, the amount of surface water on the shelf is less at the end of winter. The mean salinity on the shelf decreases from 34.554 to 34.489 psu during summer. This decrease in mean salinity on the shelf is slightly less than in the uniform wind experiment.

6.3.1 Using a stronger wind

As the total momentum flux for the pulsating 10 m s^{-1} wind in Section 6.3 is only 50% of that of the constant 10 m s^{-1}, a second periodic wind experiment a greater wind speed of 14.1 m s^{-1} is used to force the model so that the total momentem flux is the same as that of the constant 10 m s^{-1} wind. All other conditions are the same as Section 6.3. The mechanical energy produced on the shelf in this experiment is only 6% more than the produced in the constant wind experiment.

It takes 14 days more for the 14.1 m s^{-1} pulsating wind experiment to reach equibrium than for the 10 m s^{-1} constant wind experiment and equilibrium salinity attained is 0.01 psu higher. It takes approximately the same amount of time to flush the depression as it does for the 10 m s^{-1} constant wind experiment. The same momentum flux appears to result in the similar flushing times for the depression.

The onshore transport generated by this wind is greater than it is for the constant 10 m s^{-1} wind. The total onshore transport is nearly twice as much and the onshore trasport of MCDW is nearly 100 times as much.

The volume of dense water with $S > 34.6$ psu is 0.016 Sv, this more than it offshore dense water transport in the constant wind experiment but less than the transport of dense water for the 10 m s^{-1} pulsating wind experiment. Both pulsating wind experiments transport more dense water offshore than the constant wind experiment. The 14.1 m s^{-1} pulsating wind experiment will transport less dense water off the shelf than the 10 m s^{-1} pulsating wind.

For the experiments forced with the same total momentum flux and buoyancy forcing whether as a constant wind or as a pulsating wind, the mechanical energy on the shelf, the equilibrium salinity beneath the forcing region and the age and salinity of the water in the depression at the end of winter is nearly the same. The longer period of time for the 10 m s^{-1} pulsating wind experiment to reach equilibrium is likely to be due to the reduction in the total momentum flux. The volume of dense water transported offshore is greater for both pulsating wind experiments than it is for the constant wind experiment.

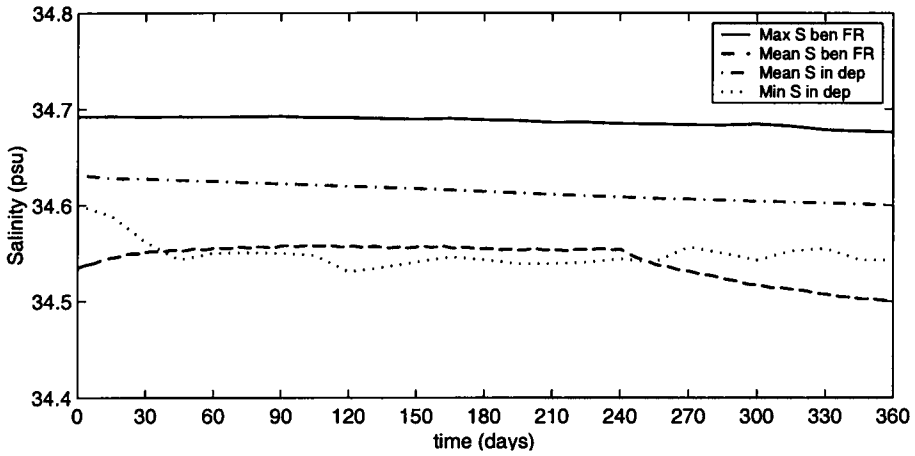

Figure 6.17: *Maximum and mean salinities for second year 10 day pulsating wind and buoyancy flux experiment in Section 6.3.2.*

6.3.2 Second year

This experiment uses a 10 m s^{-1} pulsating wind and buoyancy flux, same as the experiment in Section 6.3 but is initialised with the second year stratification described in Section 5.3.2. The initial stratification on the shelf is four times more than the initial stratification for the previous experiment and the depression is initialised with dense water.

The onshore transport of surface water is 0.69 Sv. As the same wind forcing is used as the previous experiment, the onshore transport of surface water is nearly the same.

The mechanical energy is plotted in Figure 6.3. The mechanical energy produced on the shelf during the year is 69% less than the first year experiment. The production of mechanical energy appears to be related to the production of dense water. In the first year experiment, a lot of dense water is produced, in the second year experiment very little dense water is formed. This also happens in the case with the constant uniform wind in Sections 5.3.1 and 5.3.2. The mechanical energy produced in the second year experiment with the pulsating wind is 52% of the mechanical energy with the uniform wind in the first year experiment.

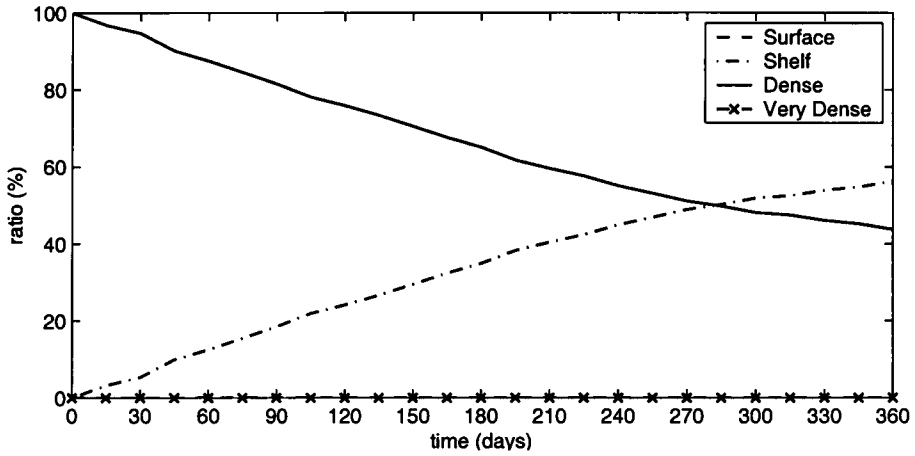

(a) Depression

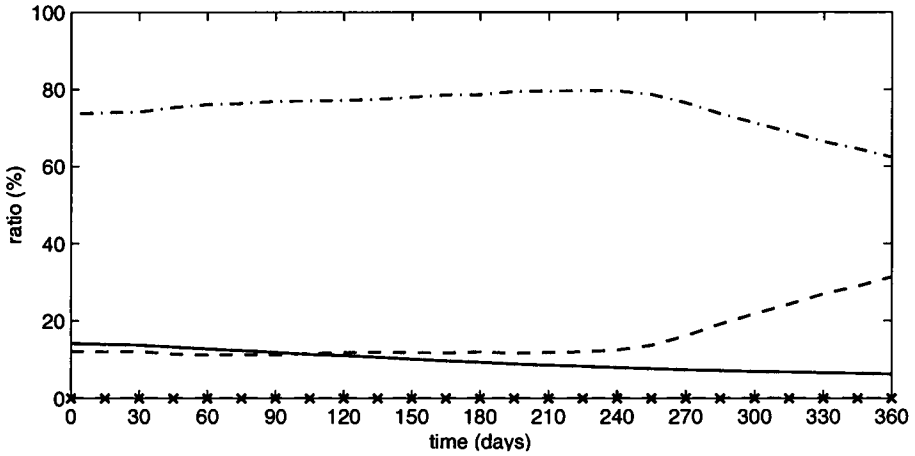

(b) Shelf

Figure 6.18: *Breakdown of water masses (a) in the depression and (b) on the shelf for the second year, 10 day pulsating wind and buoyancy flux experiment described in Section 6.3.2. The water masses are defined in Table 5.1.*

Figure 6.17 shows the maximum and mean salinities beneath the forcing region and the mean and minimum salinities in the depression. In common with the second year uniform wind experiment, these salinities decrease with time because of the onshore flux of surface water in the wind driven Ekman surface layer. The minimum, mean and maximum salinities in this experiment do not decrease as much as they do in the second year uniform wind experiment where the onshore flux of surface water is greater than it is in this experiment.

Figure 6.18a shows the ratio of the water masses in the depression. Initially the depression is filled with dense water $S > 34.6$ psu. Gradually the water in the depression is replaced with less dense water. The rate of replacement is slower than it is for the second year experiment with the uniform wind, as shown in Figure 6.13a. By the end of winter only 44% of the water in the depression is dense water.

Figure 6.18b shows the ratio of the water masses on the shelf. During winter the volume of surface water on the shelf, 1.71×10^{12} m^3 (or 12% of the shelf volume) does not increase as it does in the second year uniform wind experiment, instead the buoyancy flux is able to balance the onshore flux of surface water and maintain a constant amount of surface water on the shelf. In common with the second year uniform wind experiment, the amount of dense water on the shelf decreases during winter, but it decreases at a slower rate so that there is 56% left on the shelf at the end of winter compared to 36% in the second year uniform wind experiment.

In this experiment 1.65×10^{10} m^3 (0.5×10^{-3} Sv) of dense water $S > 34.6$ psu is transported over the shelf break. This accounts for 0.8% of the dense water in that is initially in the depression. The dense water transported offshore in this experiment is 15% less than what is was in the second year experiment with the uniform wind. As with the uniform wind experiment, most of the dense water in the depression is modified by mixing with less dense water.

6.4 The wind stress curl

In this experiment the model is forced with the basic buoyancy flux described in Section 4.1.1 and an easterly wind which decays offshore. The easterly wind is 10 m s^{-1} at the coast and decays to zero over a distance of 50 km offshore, creating a wind stress

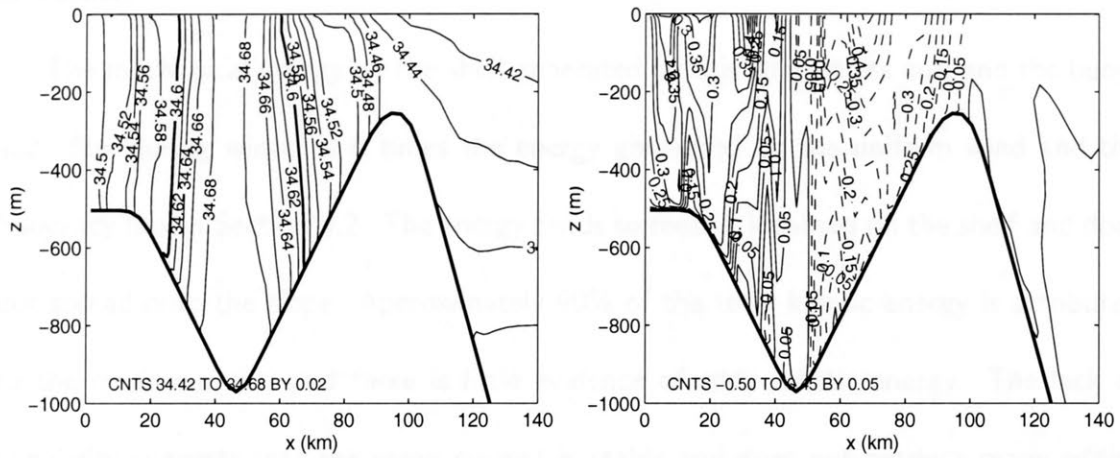

(a) Salinity (b) Alongshore velocity

Figure 6.19: *(a) Salinity and (b) alongshore velocities after at the end of winter (t = 240 days) through y = 250 km for the wind stress curl experiment in Section 6.4.*

curl, $d\tau^y/dx = -4 \times 10^{-6}$ N m^{-3}. The bathymetry used in this experiment is the same as used throughout this chapter consisting of a depression, sill and channel and the stratification is the first year stratification given by equation 4.1.

The wind stress moves water from the centre of the shelf towards the coast, creating a depression in the sea surface above the centre of the shelf. At the end of winter, the sea surface elevation above the depression at $x = 50$ km is -0.21 m. The offshore sea surface elevation gradient between the coast and the centre of the depression ($0 < x < 50$ km) is $d\eta/dx = -4 \times 10^{-6}$. The theoretical geostrophic barotropic current calculated from equation 5.1 is $v = 0.29$ m s^{-1}. The alongshore velocity after $t = 240$ days is plotted in Figure 6.19b, the velocity at the coast is in close agreement with the theoretical geostrophic velocity.

The sea surface elevation rises between the depression and the sill $50 < x < 100$ km resulting in an eastward current above the northern bank of the sill. Cross-shelf currents at the eastern and western ends of the depression create a cyclonic gyre in the depression. Current speeds of up to 0.37 m s^{-1} are observed above the 500 m isobath around the

depression.

The mechanical energy on the shelf generated by this wind stress curl and the buoyancy flux during winter is 8 times the energy generated by the uniform wind and the buoyancy flux in Section 6.2. The energy tends to remain localised on the shelf and does not spread onto the slope. Approximately 90% of the total kinetic energy is attributed to the mean current, and there is little evidence of eddy kinetic energy. The lack of variability suggests that the mean current is stable and does not produce many eddies (Nezlina and McWilliams, 2003).

The water column CM1 takes 6 days to homogenise, the same amount of time as the first year experiment with and without the wind forcing.

Figure 6.19a shows that the isohalines are nearly vertical after 240 days. CM1 is homogeneous for 39% of the winter which is less than the channel experiment without the wind (44%) in Section 5.3.1 and more than the experiment forced with the constant uniform wind (36%) in Section 6.2. The mean stratification of CM1 during winter is $N^2 = 0.1 \times 10^{-6}$ s^{-2}, this is lower than the stratification in the experiment forced with the uniform wind and the channel experiment without the wind.

The mean salinity beneath the forcing region increases from an initial value of 34.436 psu to 34.609 psu at the end of winter, and the mean salinity in the depression increases from 34.464 psu to 34.646 psu. Figure 6.20 shows that these mean salinities do not reach equilibrium by the end of winter. As newly formed water continues to be denser than the water already in the depression, the newly formed water is able to easily flush out the water in the depression. As a result the flushing time of the depression is short and the mean age of the water in the depression is 18 days. Beneath the forcing region the water is most saline at the centre of the depression during winter. During

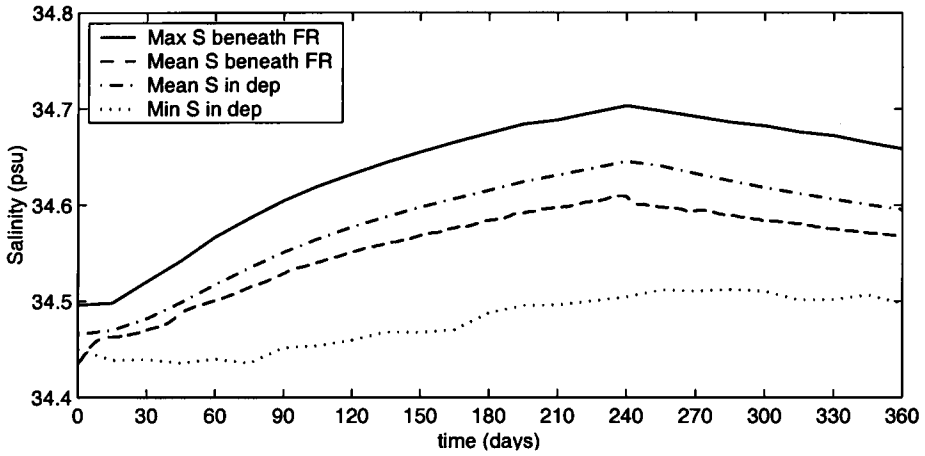

Figure 6.20: *Mean and maximum salinities beneath the forcing region and the mean and minimum salinity in the depression for the experiment with the sill at the shelf break and channel through the sill forced by the standard buoyancy flux, and 10 m* s^{-1} *wind decaying offshore.*

summer the dense water sinks into the depression and forms a dome. These salinities are less than the salinities in the experiment with no wind but greater than those with the uniform wind.

The composition of water masses in the depression and on the shelf are plotted in Figure 6.21. These water masses are defined in Table 4.2. A small amount of water in the depression is initially flushed by less dense shelf water resulting in a slight decrease in the minimum salinity in the depression shown in Figure 6.20. This shelf water in the depression is only present for 30 days. After day 15 the water in the depression is firstly replaced with intermediate water, and then dense water. The ratio of water masses in the depression changes in a similar way to the first year experiment with the uniform wind shown in Figure 6.4a.

The wind stress does not extend beyond the shelf break, so no Ekman surface layer is produced above the shelf break. As a result the 1.16 Sv of surface water transported onto the shelf in the wind-only experiment Section 6.1 does not occur here. In fact, the onshore transport of surface water across the shelf break in this wind stress curl

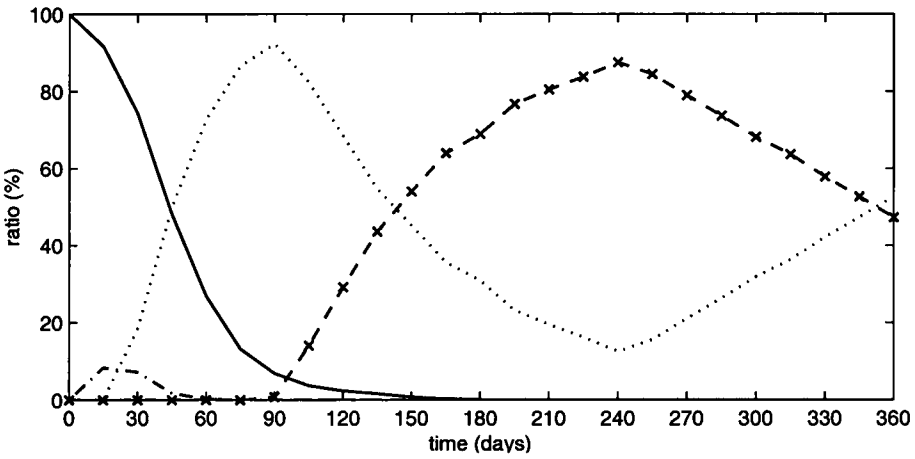

(a) Depression

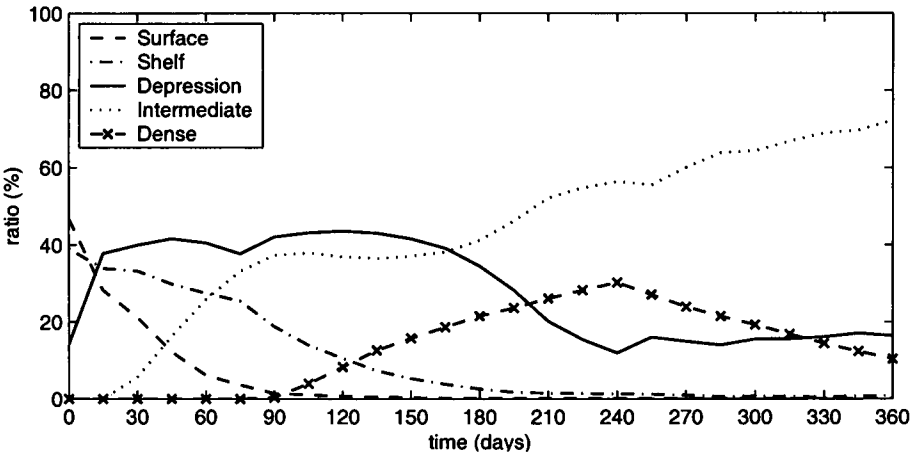

(b) Shelf

Figure 6.21: *Breakdown of water masses (a) in the depression and (b) on the shelf for the wind stress curl and buoyancy flux experiment described in Section 6.4. The water masses are defined in Table 4.2.*

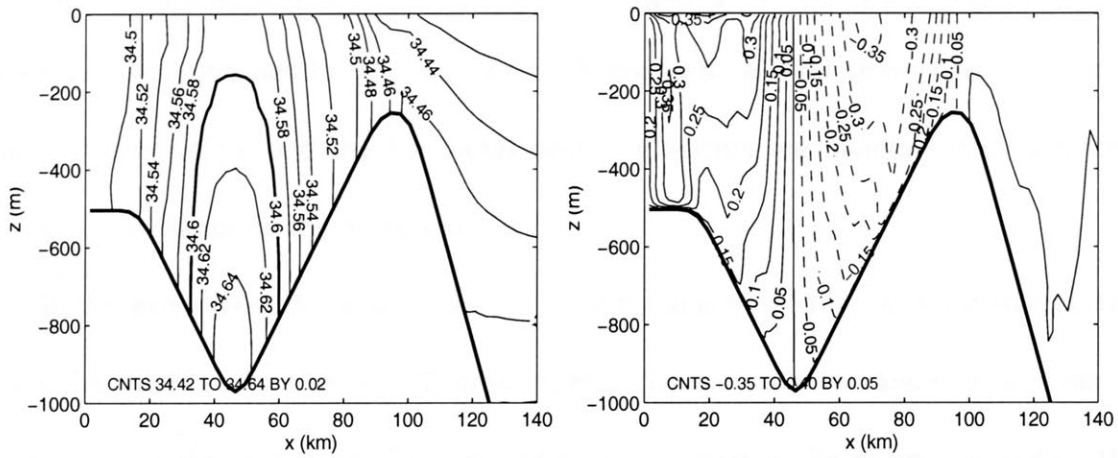

(a) Salinity

(b) Along shore velocity

Figure 6.22: *(a) Salinity and (b) alongshore velocity at the end of summer (t = 360 days) for buoyancy flux and wind stress curl experiment.*

experiment is 0.10 Sv, which is less than the 0.22 Sv onshore transport of surface water in the channel experiment in Section 5.3.1 with no wind forcing. Figure 6.21b shows that there is no surface water on the shelf after 90 days.

The cross-shelf transports across the shelf break are listed in Table B.3. The on and offshore transports are greater in this experiment than the channel experiment forced with a buoyancy flux only by 19 and 51% respectively. However these transports are less than half of that in the uniform wind experiment.

Figure 6.22 shows the salinity and the alongshore velocity at the end of summer. The dense water in the depression does not relax into the depression in the same way it does in the channel experiment forced with a buoyancy flux only and the uniform wind experiments. The mean stratification of the water column CM1 does not restratify during summer as it does in all other experiments. The mean stratification during summer is $N^2 = 0.5\times10^{-6}$ s^{-2}, which is lower than the initial stratification of $N^2 = 0.8\times10^{-6}$ s^{-2}. In all other buoyancy forced experiments, the stratification in summer is greater than the initial stratification. The isohalines at the end of summer for the channel experiment

forced with a buoyancy forcing only shown in Figure 5.11b are nearly horizontal. By contrast the isohalines for the experiment forced with a wind stress curl maintain a vertical orientation, and the horizontal density gradients are maintained by a strong cyclonic circulation in the depression.

In this experiment dense water with $S \geq 34.6$ psu is formed but it is not transported over the shelf break. Figure 6.22 shows that all dense water is trapped in a dome at the centre of the depression. The amount of dense water in the depression and on the shelf shown in Figure 6.21 decreases during summer. It mixes with less dense water resulting in an increase in the volume of intermediate water with $34.5 \leq S < 34.6$ psu. The volume of intermediate water in the other experiments tends to decrease during summer, this is the only experiment where the volume of intermediate water increases. The offshore transport of intermediate water is listed in Table B.3. The net offshore transport of intermediate water mass is 0.016 Sv, which is approximately the same as the experiment without the wind, but less than the experiments forced with the uniform winds.

6.5 Summary

The spatially uniform easterly winds in Sections 6.2 and 6.3 act to drive surface waters onto the shelf. This results in a decrease in salinity on the shelf and an increase in sea surface elevation. The surface water that is transported onshore beneath the buoyancy forcing region lowers the salinity of the waters beneath the buoyancy forcing region. This increases the lateral buoyancy flux and decreases the time required to reach equilibrium to 120 and 200 days for the uniform wind and pulsating wind experiments respectively, whereas equilibrium is not reached by 240 days in the channel experiment without the

wind. The increase in sea surface elevation above the shelf creates a negative sea surface gradient above the shelf sill which drives a westward along-sill current. This current flows in the opposite direction to the along-sill current in the experiments without a wind where the sea surface elevation gradient is positive. The sea surface elevation above the shelf in the experiments without wind forcing decreases due to the compression of the water columns beneath the forcing region. Young (1998), Bindoff et al. (2001) report observations of westward currents above the shelf sill.

The wind driven along-sill current creates a strong offshore flow through the channel. East (or upstream) of the channel, the current is located on the shelf side of the sill. At the channel, the current passes through the channel, and continues alongshore on the slope side of the sill. This increases the offshore shelf transport significantly. These uniform wind experiments, both constant and pulsating in time result in increased offshore transport of dense water for the first year experiments.

In the wind stress curl experiment, the applied wind stress extends as far as 50 km offshore but does not extend beyond the shelf break situated 96 km from the coast. The result is a strong westward barotropic current at the coast and eastward current at the sill. These currents are strong enough to prevent the production of eddies which might otherwise break down the dense water formation beneath the depression. Instead the westward current at the coast advects ambient water beneath the forcing region at the coast, but dense water formed beneath the centre of the buoyancy forcing region is undisturbed, and therefore attains a higher salinity than the uniform wind experiments, but not as high as the experiment with no wind.

The addition of a wind increases the lateral buoyancy flux thereby reducing the effectiveness of the buoyancy flux in producing dense water. In the first year experiments

with the wind the mean salinity beneath the forcing region is less than it is in the basic experiment in Section 4.2 which has the same buoyancy forcing. The reduced effectiveness of the buoyancy flux when a wind is added is particularly noticeable in the experiments with second year stratification, where the buoyancy flux is unable to homogenise the water column. Deep convection rather than shallow convection takes place, and the resultant mixing limits the density of the shelf waters.

Chapter 7

Comparison of numerical results to observations

In this chapter the results of the numerical simulations described in Chapters 4 through 6 are compared with observations from the Adélie Land region reported by Gordon and Tchernia (1972), Bindoff et al. (2001), Rintoul (1998), Bindoff et al. (2000a), Bindoff et al. (2000b), Foster (1995), Jacobs (1991), Gill (1973), Whitworth et al. (1998), and Baines and Condie (1998). A summary of the numerical simulations is listed in Table B.1.

7.1 Water masses

The four water masses identified by Bindoff et al. (2001) on the shelf during winter are summarised in Section 2.5. Temperature and salinity sections annotated with the water masses are plotted in Figure 7.1. The cold fresh Ice Shelf Water (ISW) found at the coast has the same density as the warm saline Highly Modified Circumpolar Deep Water (HMCDW) which intrudes onto the shelf break from offshore. The densest water mass found on the shelf is the High Salinity Shelf Water (HSSW) which is found in the

bottom of the depression. The Winter Water (WW) found above the HSSW is denser than both the ISW and HMCDW. The cross-shelf sections of temperature and salinity from Gordon and Tchernia (1972) in the Adélie Depression during summer are plotted in Figure 7.2. Gordon and Tchernia (1972) classified the water in the bottom of the depression as shelf water and the water above it as warmer water which replaced the shelf water during summer.

7.1.1 Water at the coast

ISW is produced by the melting of ice shelves which makes the water colder, fresher and less dense. In the present numerical simulations, variations in salinity model the changes in density while the temperature is kept constant. The buoyancy flux due to sea-ice formation is simulated by applying a salinity flux at the surface, but no lateral salinity flux is applied at the coast to simulate the effects of the ice shelves. As a result no ISW is produced through buoyancy fluxes. However, in the present numerical simulations, lower salinity water is present at the coast as a result of the advection of ambient water from outside the forcing region by the coastal current.

During the early stages of winter in the first year channel experiment, the water at the coast is the most saline water on the shelf due to the greater effect of buoyancy flux over the shallow topography and the absence of the coastal current. As a coastal current develops the dense water travels westward along the coast and less saline water east of the forcing region is advected along the coast. The presence of less saline water at the coast beneath the forcing region in the middle of winter is shown in Figure 7.3a. By the end of winter the salinity at the coast is nearly the same as at the shelf break. These water masses are separated by denser water representative of the winter water

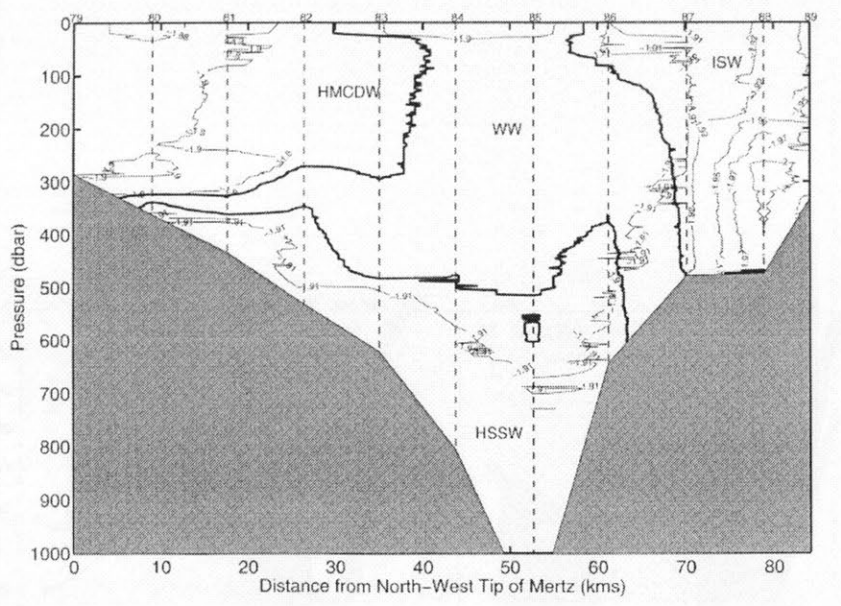

(a) Temperature

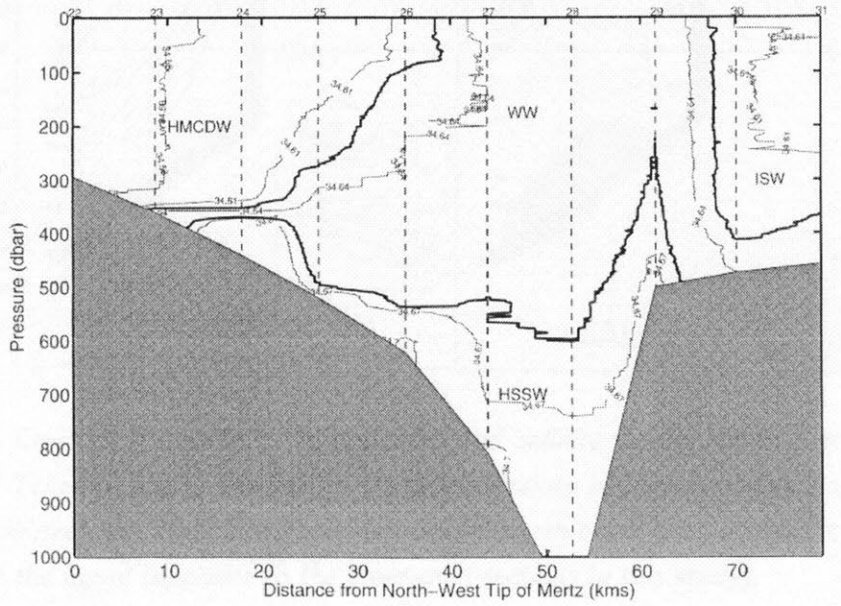

(b) Salinity

Figure 7.1: *(a) Temperature and (b) salinity sections in the Adélie Depression at 145° E during winter. Figures 2 and 3 from Bindoff et al. (2001). The four water masses are annotated on the sections. The figure is oriented north-south with the coast on the right hand side of the figure (opposite to the cross-shelf sections in this study).*

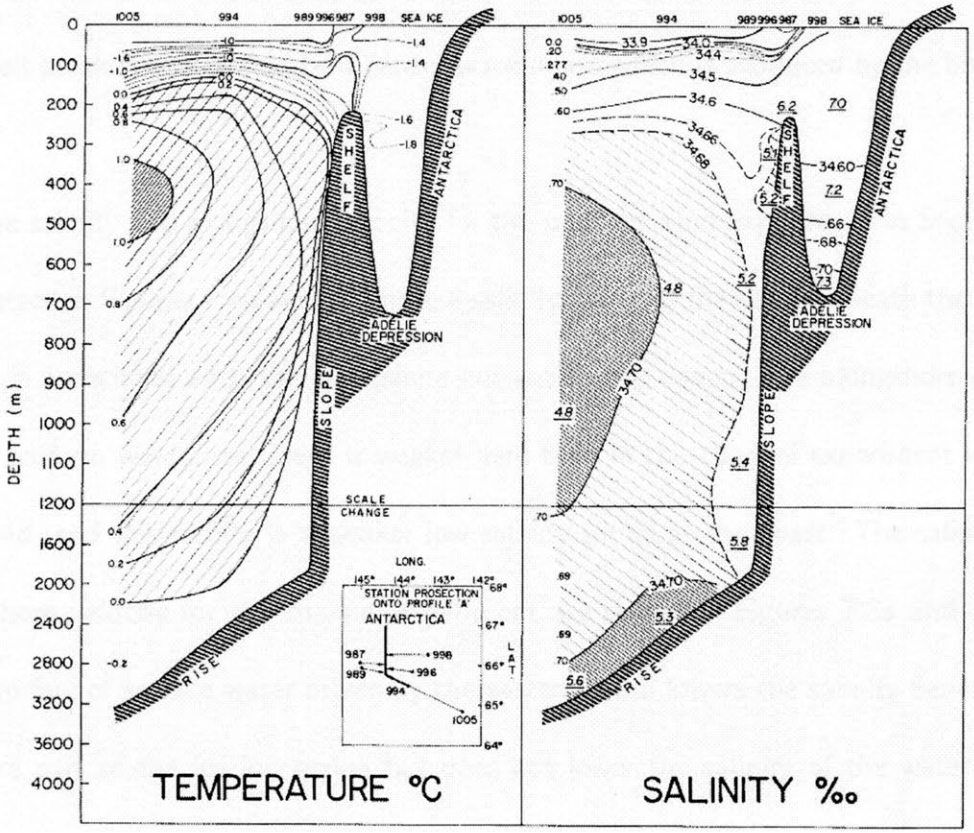

Figure 7.2: *Cross shelf section of temperature and salinity during summer at 144°E from Gordon and Tchernia (1972, Figure 5). Underlined values in the salinity section are oxygen values in millilitres per litre. The figure is oriented north-south with the coast on the right hand side of the figure (opposite to the cross-shelf sections in this study).*

above the depression which is produced by the buoyancy flux.

The second year channel experiment described in Section 5.3.2 is initialised with saltier water on the shelf than offshore. Throughout the winter of the second year experiment, the salinity at the coast is greater than the salinity at the shelf break. This is because the water that is on the shelf has been initialised so that it is denser than the water at the shelf break. Like the first year experiment, the water at the coast and the shelf break are separated by a denser water mass which is produced by the buoyancy flux.

The salinity and alongshore velocity for the uniform wind experiment in Section 6.2 are plotted in Figures 7.4a and c. The low salinity water at the coast beneath the forcing region is associated with the alongshore current at the coast. The alongshore current in the uniform wind experiment is weaker here than in the channel experiment without the wind, and this results in a weaker low salinity signal at the coast. The salinity and alongshore velocity for the channel experiment are shown in Figures 7.3a and c. The onshore flux of surface water driven by the easterly wind lowers the salinity beneath the offshore part of the forcing region but does not lower the salinity of the water at the coast. The wind stress curl experiment produces a very strong westward current at the coast over a width of 50 km. This current advects large amounts of water along the coast resulting in low salinity water being advected beneath the forcing region.

The results from the numerical simulations are in agreement with the observation of less dense water at the coast. This less dense water is a result of the alongshore advection of less dense water from outside the forcing region. The ISW that is observed at the coast is believed to be formed by freshening and cooling of WW due to melting of the ice shelves (Bindoff et al., 2001).

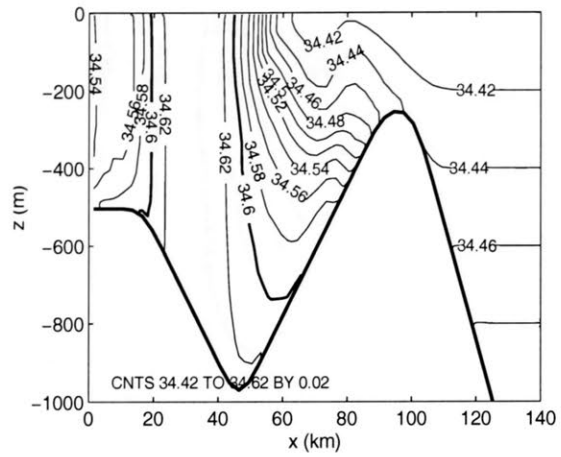

(a) Salinity after 120 days

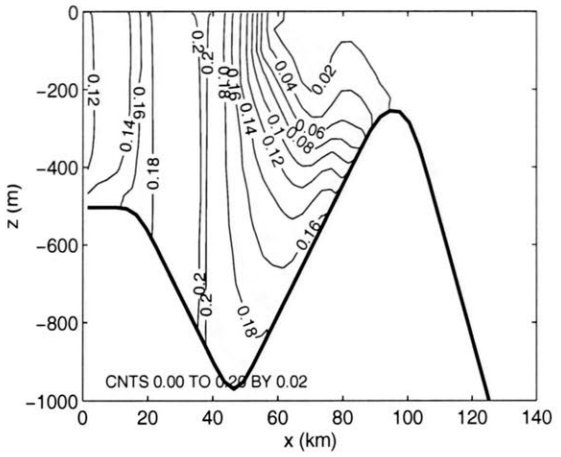

(b) Surface tracer after 120 days

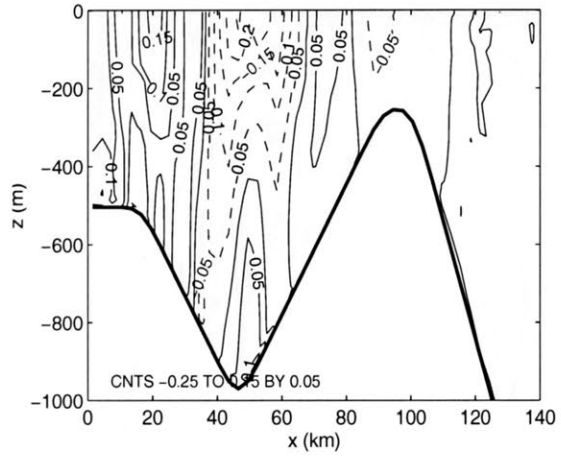

(c) Alongshore velocity after 120 days

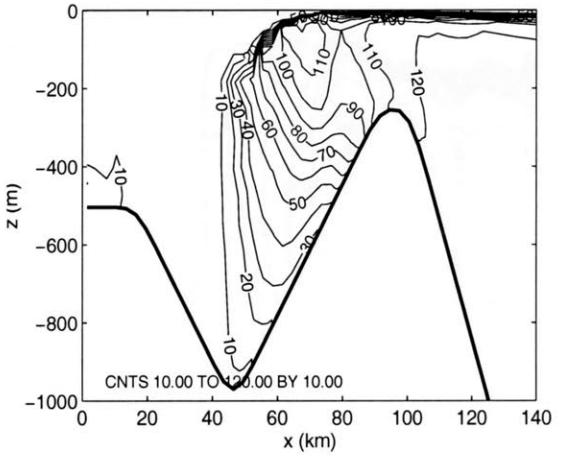

(d) Age after 120 days

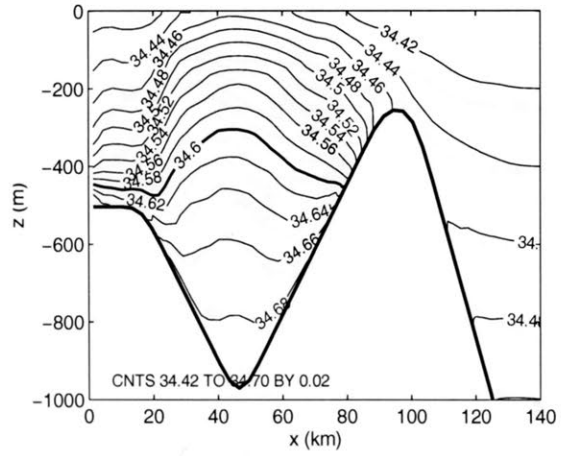

(e) Salinity after 360 days

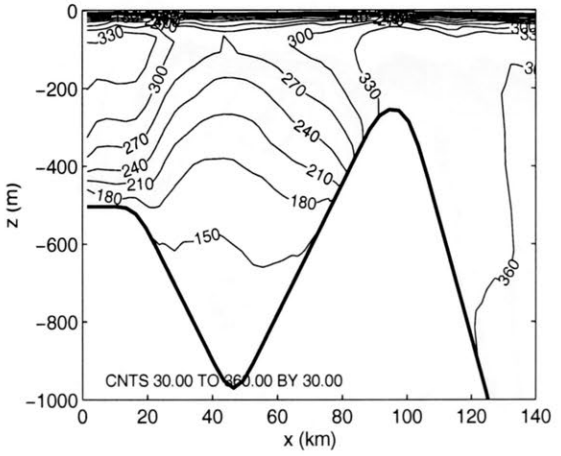

(f) Age after 360 days

Figure 7.3: *(a) Salinity, (b) surface tracer, (c) alongshore velocities and (d) age after 120 days and (e) salinity and (f) age after 360 days through y=250 km for the experiment with depression, sill and channel forced by a buoyancy flux in Section 5.3.1.*

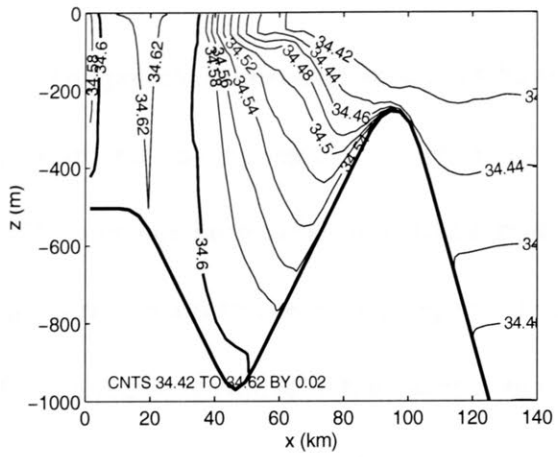

(a) Salinity after 120 days

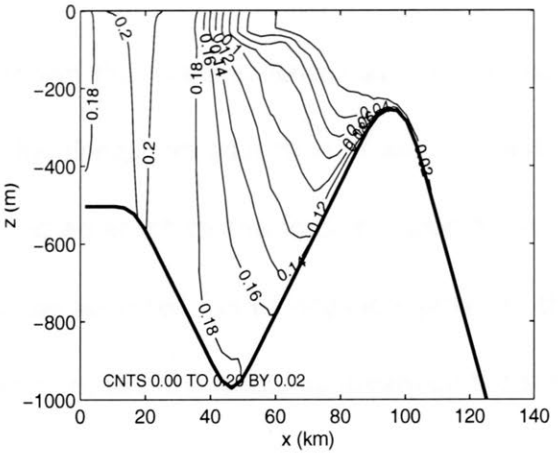

(b) Surface tracer after 120 days

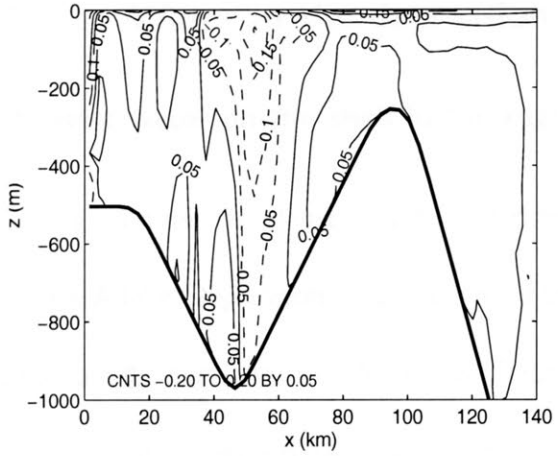

(c) Alongshore velocity after 120 days

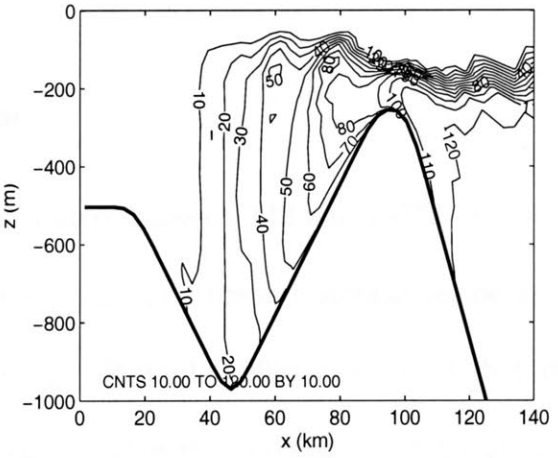

(d) Age after 120 days

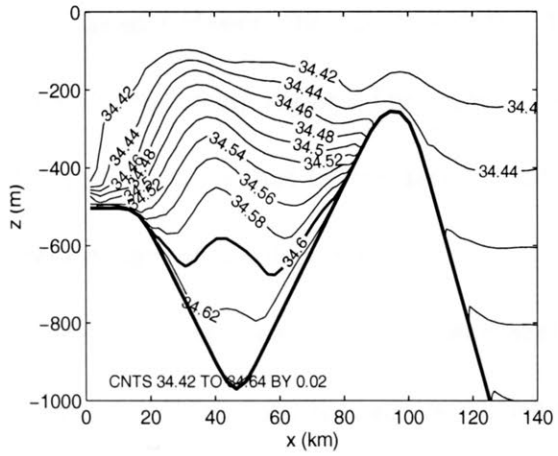

(e) Salinity after 360 days

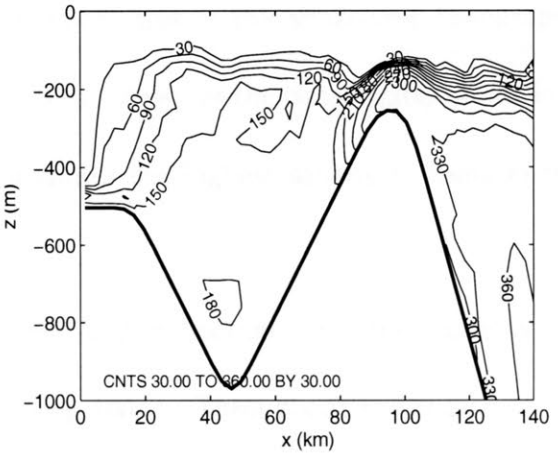

(f) Age after 360 days

Figure 7.4: *(a) Salinity, (b) surface tracer, (c) alongshore velocities and (d) age after 120 days and (e) salinity and (f) age after 360 days through y=250 km for the experiment with depression, sill and channel forced by a buoyancy flux and constant and uniform wind in Section 6.2.*

The present numerical simulations have shown that the less dense water at the coast beneath the forcing region can result from the alongshore advection of ambient water. ISW does not necessarily need to be produced adjacent to the forcing region for it to be present beneath the forcing region. It can be advected from alongshore provided the forcing region is limited in the alongshore direction, the ISW exists upstream on the shelf and the coastal current is strong enough.

7.1.2 Water in the depression

Densest water on the shelf in the region

During summer the densest and most saline waters between 142 and 147°E are found in the Adélie Depression (Gordon and Tchernia, 1972). These historical temperature and salinity sections are plotted in Figure 7.2. Rintoul (1998) also found that the densest water between 142.5 and 145.5°E was found in the depression. At the start of winter in the first year model experiments the highest salinity is normally found over the seabed between the coast and the depression, this is the shallowest topography beneath the forcing region. Throughout the course of winter the dense water drains into the depression so that by the second half of winter the highest salinity is found in the deepest part of the depression.

In the second year channel experiment described in Section 5.3.2 the model is initialised with high salinity dense water in the depression. Throughout the course of the simulation the densest water continues to be found in the depression, and during the winter period, the salinity in the depression increases. For the second year model experiments with the wind in Sections 6.2.1 and 6.3.2, the highest salinity on the shelf is initialised in the depression but it does not increase during winter; in fact it decreases

slightly due to mixing.

The presence of the depression in the shelf traps dense water so that the densest water in the model is generally found in the depression as was observed by Gordon and Tchernia (1972) and Rintoul (1998). In this model the densest water is sometimes found over the shallower regions of the shelf where the buoyancy flux is most effective in producing dense water. This effect tends to be transitory, as the dense water either flows along the coast or it flows into the depression.

Thus the model and the observations are consistent qualitatively in that in the presence of a depression in the model, the densest water on the shelf is generally found in the depression.

Water in the depression during winter

Winter Water (WW) is found above the High Salinity Shelf Water (HSSW) in the depression. During winter Bindoff et al. (2001) observed that (1) the mean potential density of the WW is 0.03 kg m^{-3} less than that of the HSSW, (2) while the WW mass tends to be homogeneous and the HSSW tends to be stratified, and (3) the HSSW has a higher oxygen content than the WW, i.e., the HSSW in the depression is younger than the WW above it.

The initial stratification on the shelf in the numerical simulations is eroded by the negative buoyancy flux. In all experiments where the forcing region extends above the depression the homogeneous layer of WW observed by Bindoff et al. (2001) is replicated.

In the experiments where the buoyancy flux is strong enough for shallow convection to take place, the water columns beneath the forcing region are homogenised. If the buoyancy forcing is located above the depression then the water column in the depression

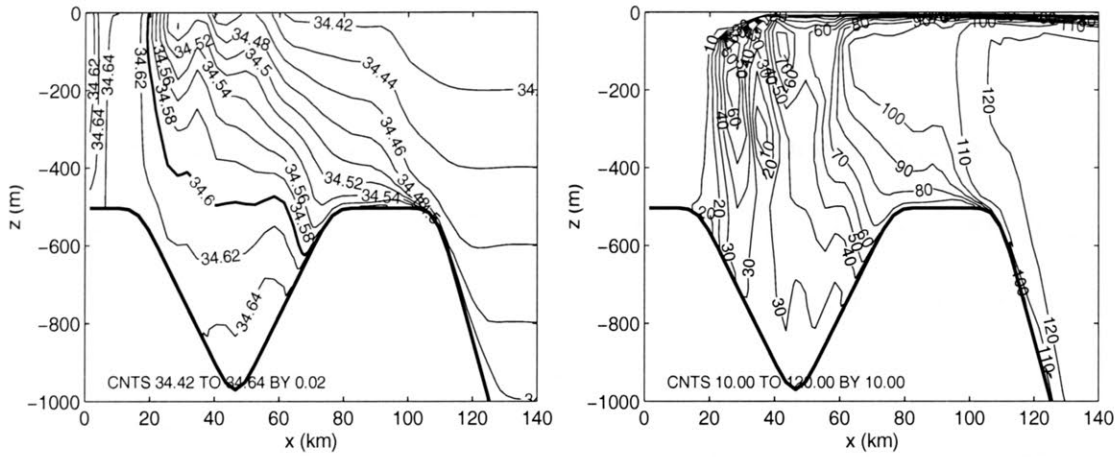

(a) Salinity (b) Age

Figure 7.5: *(a) Salinity and (b) age after 120 days through y=250 km for the experiment with depression forced by a strong buoyancy flux at the coast in Section 4.3.2.*

is homogenised during winter. The homogeneous water columns are depicted by the vertical salinity contours in Figure 7.3a, but the waters away from the forcing region ($x > 50$ km) are stratified. For the basic forcing and the weak forcing over a large area, it is only during the early stages of winter while the buoyancy flux is eroding away the stratification that the water above the depression is homogeneous and the water in the depression is stratified. This replicates the winter time observations of stratified water in the depression reported by Bindoff et al. (2001). Later in winter the whole water column is homogenised.

The salinity and age after 120 days for the coastal forcing experiment in Section 4.3.2 are plotted in Figure 7.5. In this experiment the dense water in the depression tends to be stratified as smaller volumes of the water beneath the forcing region are formed and they do not flush the depression with a uniform water mass as in the experiments with larger forcing regions. The water in the depression is still less stratified than the water above it. The strong stratification of the water above the depression is a result of lateral advection of less dense water.

Active dense water formation does not occur in the second year model experiments which are forced with a uniform wind (Sections 6.2.1 and 6.3.2). The strong stratification on the shelf is eroded by the buoyancy flux. The increased lateral buoyancy forcing due to the onshore transport of surface water in the wind driven Ekman layer brings the system to equilibrium before the water columns in the depression are homogenised. This results in the water in the depression retaining its initial stratification.

The densest water formed beneath the forcing region sinks into the depression so that the mean density of the water in the depression is greater than the mean density of the water above the depression. This newly formed dense water in the depression is "younger" than the water above the depression, except in the experiments which are forced with a wind. In these experiments the wind creates a young surface mixed layer. Figure 7.3d plots the cross-shelf section of the age after 120 days for the channel experiment which is forced with a buoyancy flux only. A cross-shelf section of the age after 120 days for the uniform experiment is plotted in Figure 7.4d. The wind stress creates a deep mixed layer which erodes the "old" water, and the mean age of the water above the depression is the same as the mean age of water in the depression.

The model is able to simulate the homogeneous water mass which is observed by Bindoff et al. (2001) during winter when dense water formation is active. The stratified water in the depression during winter (Bindoff et al., 2001) is reproduced in the numerical simulations when active dense water formation does not occur above the depression, i.e., in the early stages of winter, in the strong coastal forcing experiment, and in the second year experiments which are forced with a buoyancy flux and uniform wind. In experiments where dense water formation occurs, the water in the depression is denser and younger than the water above the depression which is in agreement with the observations from

Bindoff et al. (2001). The model is able to simulate the observations in the Adélie Depression during winter reported by Bindoff et al. (2001) in isolation but is unable to simulate simultaneously the homogeneous water above the depression, and the stratified, younger and denser water in the depression.

Water in the depression during summer

In summer, the water in the depression is younger, denser and more stratified than the water above, similar to the water column structure found during winter. Temperature, salinity and oxygen observations during summer from Gordon and Tchernia (1972) are shown in Figure 7.2. The temperature and salinity sections show that the water in the depression is much more stratified than the water above it, and the oxygen values show that the water in the depression is younger than the water above it. The cross-shelf section of density during summer observed by Foster (1995) is shown in Figure 7.6a. On the shoreward side of the shelf break the stratification of the water beneath the pycnocline and above the depth of the sill at the shelf break ($100 < z \lesssim -450$ m) is approximately half the stratification of the water on the shelf below the level of the sill ($z \gtrsim -450$ m).

Once the buoyancy forcing in the model ceases, the dense water beneath the forcing region relaxes and sinks to fill the depression. The water above the depression is restratified by the lateral advection of less dense water from the area outside the forcing region. The water above the depression is highly stratified. The dense water in the depression is younger than the water above it.

The numerical simulations are able to replicate the observations of young dense water in the depression during summer by Gordon and Tchernia (1972). The model was not

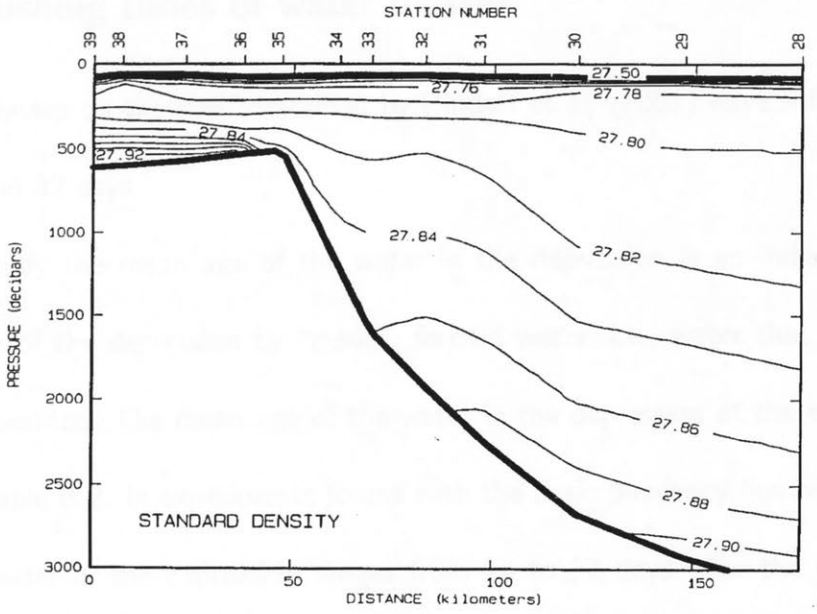

(a)

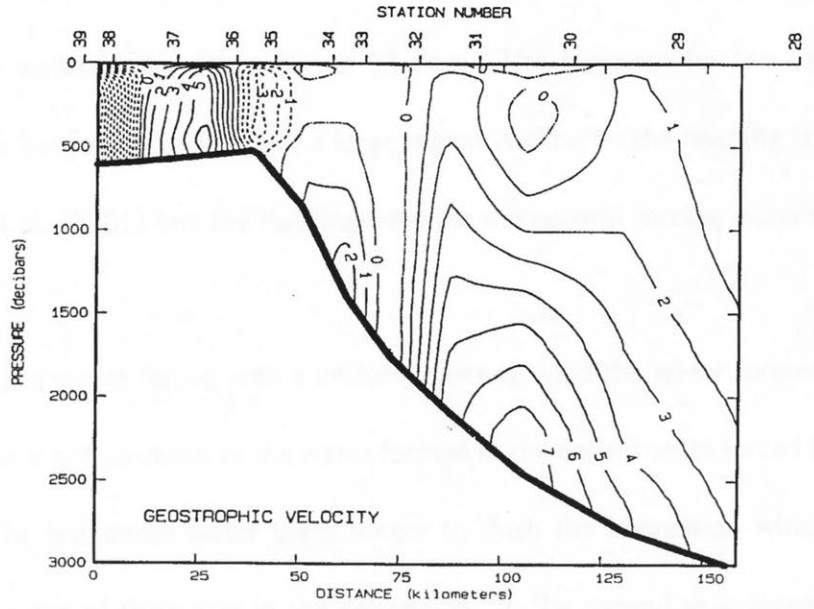

(b)

Figure 7.6: *Standard density and geostrophic velocities calculated from the density section at 151° E Foster (1995). Solid lines show westward flow and dashed lines show eastward flow, units are in cm* s^{-1}.

able to reproduce the homogeneous water mass above the depression.

7.1.3 Flushing times of water masses

The water masses on the shelf described by Bindoff et al. (2001) have a flushing time between 6 and 32 days.

In this study the mean age of the water in the depression is an indication of the flushing time of the depression by "newly" formed water, i.e., water that has recently been at the surface. The mean age of the water in the depression at the end of winter is listed in Table B.2. In experiments forced with the basic buoyancy flux only the mean age of the water in the depression ranges from 24 to 37 days. For the weak forcing over a large area the mean age of the water in the depression is a low 11 days which is within the limits estimated by Bindoff et al. (2001). For the strong coastal forcing the mean age of water in the depression is 53 days. The response for the basic buoyancy and the weak buoyancy forcing over a large region is close to the flushing time estimated by Bindoff et al. (2001) but the flushing time for the coastal forcing experiment is much longer.

In the experiments forced with a uniform easterly wind the water formed beneath the forcing region is not as dense as the water formed in the experiments forced by a buoyancy flux only. The less dense water takes longer to flush the depression which results in a greater mean age of the water in the depression. In the second year experiments where the depression is initialised with dense water, the flushing times are 3 to 5 times those of the first year experiments because of the denser water in the depression.

The flushing times in experiments that are forced by a basic buoyancy flux or a weak buoyancy flux over a large region without the assistance of a wind are close to the times

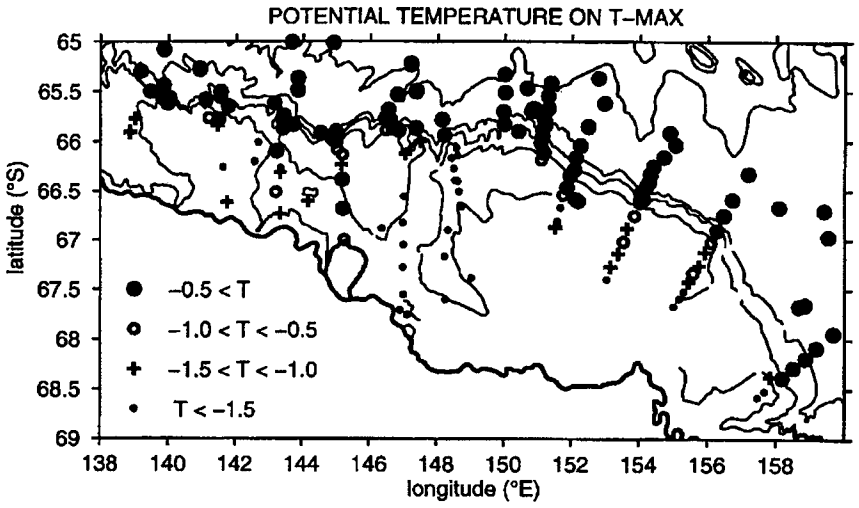

Figure 7.7: *The potential temperature of the potential temperature maximum of the MCDW from Figure 7 in Rintoul (1998). The thick contour shows the coastline and the thin lines are the 500, 1000, 2000 and 3000 m isobaths. Note the presence of warm water $T > -0.5°C$ in the Adélie Depression between 143 and 145°E.*

estimated by Bindoff et al. (2001). The addition of a uniform easterly wind increases the flushing time of the water in the depression by reducing the effectiveness of the buoyancy forcing in producing dense water.

7.1.4 Intrusions of MCDW onto the shelf

Modified Circumpolar Deep Water (MCDW) is a mixture of Circumpolar Deep Water and surface water and/or shelf water. It is found offshore of the shelf break beneath the surface layer and is characterised by warm temperatures. Figure 7.7 shows the potential temperature maximum of the MCDW, and temperatures as high as +0.5°C have been observed in the Adélie Depression (Rintoul, 1998). The onshore movement of MCDW is blocked by the sill at the shelf break but channels through the sill allow water from the slope onto the shelf, e.g., through the channel near the Adélie Depression. MCDW is found in the Adélie Depression but it is not found on the shelf immediately to the east nor west (Rintoul, 1998; Bindoff et al., 2000a).

In the model the temperature is kept constant and dense water is produced by a salinity flux. A surface tracer flux equivalent to the salinity flux is also forced at the surface, this marks newly formed dense water so that it can be differentiated from the water not formed beneath the forcing region. MCDW is defined as having a low surface tracer concentration $c < 0.02$ and $S > 34.45$ psu which has an initial depth of $z < -500$ m for the experiments initialised with first year stratification. The only water on the shelf which is initialised with this salinity is in the depression; all other water initialised with this salinity is found in the deep ocean. The onshore transport of MCDW in the model runs is listed in Table B.3.

For the experiments without the sill at the shelf break in Chapter 4, there are onshore intrusions of MCDW all along the shelf break. This is inconsistent with the observation of Rintoul (1998) and Bindoff et al. (2000a) that MCDW is only found in the vicinity of the Adélie Depression.

The presence of a continuous sill at the shelf break in Section 5.2 prevents all onshore transport of MCDW onto the shelf. The addition of a channel through the sill in Section 5.3.1 allows 0.012 Sv of MCDW to be transported onshore, 85% of the onshore transport of MCDW enters through the channel. This MCDW is advected onshore through the eastern side of the channel shown in Figure 5.8a and then eastward above the northern bank of the depression by the barotropic current shown in Figure 5.6.

The experiments forced with a easterly wind produce a surface Ekman layer which transports surface water onshore but this Ekman transport does not assist in the transport of MCDW that is found beneath the surface layer. In the wind only experiment in Section 6.1 no MCDW is transported onshore. In the combined uniform wind and buoyancy flux experiments for the experiments initialised with the first year stratification

the onshore transport of MCDW is 0.001 and 0.007 Sv for the constant (Section 6.2) and pulsating (Section 6.3) winds, respectively.

This study has demonstrated that the sill at the shelf break blocks the transport of MCDW onto the shelf and the presence of a channel in the sill allows MCDW to flow onto the shelf into the region near the Adélie Depression in agreement with the observations reported by Rintoul (1998) and Bindoff et al. (2000a). The uniform easterly wind drives a surface Ekman layer which transports surface water onshore and does not assist in the onshore transport of MCDW in the experiments forced with a wind only. This study has been able to show the effect of the topography and wind forcing on the intrusion of MCDW onto the shelf.

7.2 Circulation on the Shelf

Bindoff et al. (2001) measured the ADCP velocities on the shelf during winter, and the velocities are shown in Figure 7.8. The velocity field on the shelf is largely barotropic. The strongest flow is a narrow westward current with speeds exceeding 0.20 m s^{-1} adjacent to the coast. Over the depression, in depths greater than 500 m, the flow field is eastward. Above the northern bank of the depression, in water shallower than 500 m, the flow changes back to being westward. The alongshore transport beneath the Mertz polynya associated with the above currents comprises 1.2 ± 0.5 Sv westward transport of ISW adjacent to the coast, 2.0 ± 0.7 Sv eastward transport of WW and HSSW above the depression and 0.7 ± 0.5 Sv westward transport of HMCDW at the shelf break.

The velocities during mid-winter $t = 120$ days for the channel experiment in Section 5.3.1 are shown in Figure 7.3c. The current at the coast is westward and exceeds speeds of 0.20 m s^{-1}. The westward coastal current extends out above the 700 m

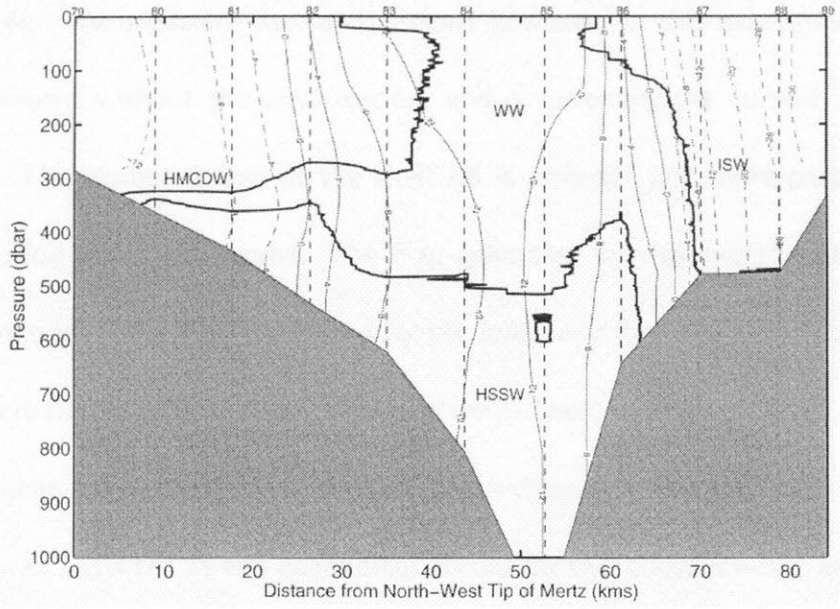

Figure 7.8: *Observations of east-west velocities in the Adélie Depression during winter (Bindoff et al., 2001, Figure 4). Dashed lines show westward currents and solid lines show eastward currents, the contour labels are in cm s^{-1}. The figure is oriented north-south with the coast on the right hand side of the figure (opposite to all cross-shelf sections in this study).*

isobath on the southern bank of the depression. The flow above the deepest part of the depression is predominantly eastward, consistent with the observations. The flow above the sill tends to be eastward near the surface and westward on the bottom. In the numerical simulations the flow above the depression is not uniformly eastward like the observations, instead there are cells of eastward and westward flow. The alongshore transports calculated from the time averaged velocities plotted in Figure 4.9 are 0.65 Sv westward along the coast; 0.92 Sv eastward above the depression; and 0.17 Sv westward above the northern bank of the depression. The westward transport at the coast predicted by the model lies at the lower end of the range of observations of westward transport of ISW along the coast, and the simulated eastward transport above the depression and the simulated westward transport above the shelf break are lower than the corresponding transport observations of Bindoff et al. (2001).

The alongshore velocities after 120 days for the uniform wind experiment are plotted

in Figure 7.4c. The westward flow at the coast is weaker in this experiment than it is in the experiment without the wind forcing, and occasionally the current at the coast is reversed. The westward flow at the shelf sill is stronger and more persistent when an easterly wind forces the model. The flow generated by this experiment appears to be a combination of the flow generated by the buoyancy flux alone and the wind only experiments in Sections 5.3.1 and 6.1, respectively. The currents generated by the wind only experiment are eastward at the coast and westward above the sill. The flow at the coast turns eastward in the experiment forced by the buoyancy flux and the wind forcing when the buoyancy forcing stops during summer. The transport associated with the alongshore velocities are 0.33 Sv westward at the coast, 0.70 Sv eastward above the depression, and 0.85 Sv westward above the northern bank of the depression. The westward transport at the coast and the eastward transport above the depression are both lower than the observed values, but the westward transport above northern bank of the depression is within the range of the observations.

The ratio of barotropic to baroclinic energy for the wind forced experiments in Chapter 6 is greater than it is for the experiments forced by a buoyancy flux only in Chapter 5. In the channel experiment which is forced by buoyancy forcing only, the ratio of barotropic to baroclinic energy at $y = 250$ km on the shelf is $\sim$2:1. Where a wind and a buoyancy flux force the model, the ratio of barotropic to baroclinic energy at $y = 250$ km on the shelf is $\sim$4:1. For the wind forcing only with ratio of barotropic to baroclinic energy is $\sim$8:1.

The density differences on the shelf are greater than those that are observed. This leads to greater horizontal density gradients in the model. From the thermal wind equations this results in vertical shear in the velocities which results in baroclinic flow.

The mean potential density of the ISW and the HMCDW observed in the Adélie Land region is ~27.85 kg m^{-3} and the mean potential density of the WW and the HSSW above and in the Adélie Depression are 27.89 and 27.92 kg m^{-3} respectively. The density difference between the mean potential density of the HMCDW and the HSSW is 0.07 kg m^{-3}. When dense water begins forming on the shelf in the model, the salinity difference between the dense water with $S \geq 34.6$ psu representative of the HSSW and water with $S < 34.6$ psu representative of HMCDW above the shelf break is 0.10 psu which is equivalent to a density difference of 0.08 kg m^{-3}. This difference increases to 0.16 psu (0.13 kg m^{-3}) at the end of winter, this is greater than the density difference that is observed.

The observed westward current at the coast is reproduced in the experiments that produce dense water. The observed eastward flow above the depression is produced in the models forced with a buoyancy flux. The observed westward flow at the shelf break is reproduced in the experiments forced with a uniform easterly wind.

The direction of the currents observed by Bindoff et al. (2001) in the Adélie Land region are reproduced by the numerical simulations, though the transports tend to be slightly less than the observed values. The modelled currents tend to be more baroclinic than barotropic due to the density differences in the model being larger than those observed.

7.3 Antarctic Slope Front

The Antarctic Slope Front is generally observed above the upper continental slope (Jacobs, 1991). It separates the shelf water from the offshore waters. A lateral temperature gradient of 3°C ($\Delta\rho \simeq 0.16$ kg m^{-3}) over 25 km is the best indicator of the front. Where

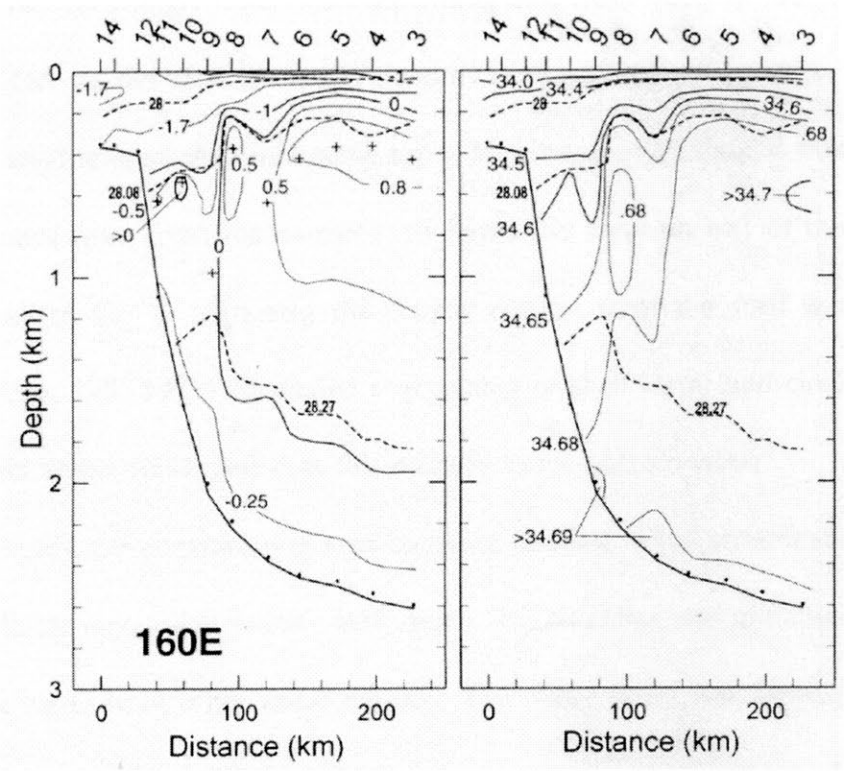

(a)

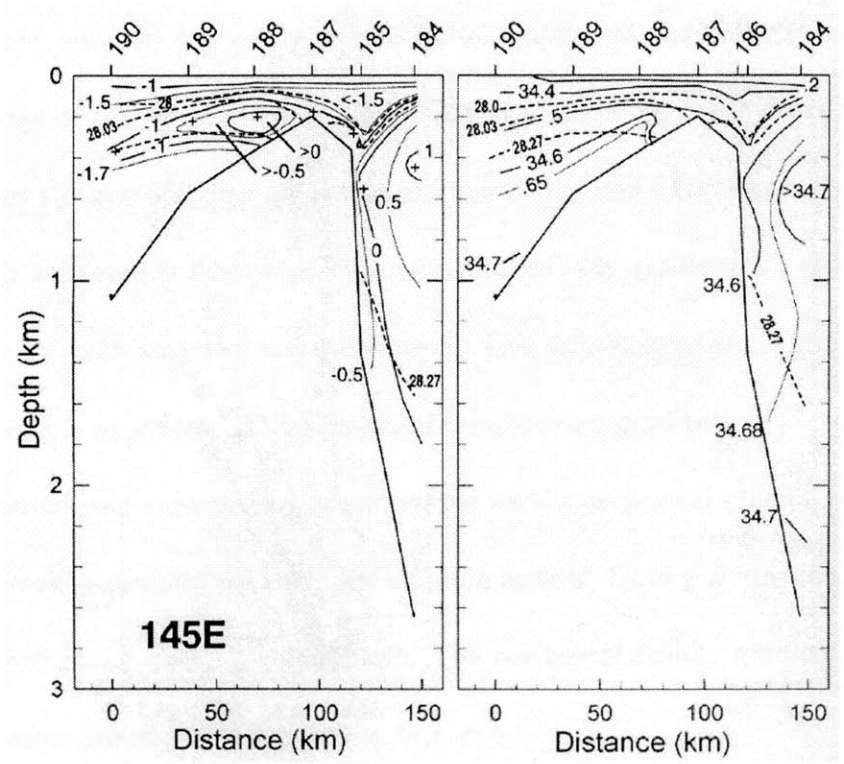

(b)

Figure 7.9: *Cross-shelf sections of temperature and salinity at (a) 160°E and (b) 145°E reproduced from Whitworth et al., (1998, Figures 6 and 7).*

the shelf is narrow a single front exists separating cold fresh water of the coastal current from the CDW at the shelf break (Whitworth et al., 1998) as shown in Figure 7.9a. Where the shelf is wide, the front some times appears as a 'V' shaped front, where the aforementioned front from the narrow shelf forms the northern half of the 'V' and the southern half of the 'V' separates the coastal current from the shelf water as shown in Figure 7.9b. Gill (1973) concluded that mixing of shelf water and circumpolar deep water occurs at the front, and that this mixture forms bottom water.

In this study, temperature was kept constant and the initial stratification was modelled by a linear increase in salinity with depth. No halocline was initialised to separate the surface water from other water masses. The dense water was formed on the shelf by a salinity flux at the surface and a front between the shelf water and the ambient offshore water is to be found in the numerical simulations.

The front between the newly formed dense water and the ambient water is found near the edge of the forcing region for the first year experiments. A cross section of the salinity after 120 and 360 days are shown in Figures 7.3a and e for the channel experiment forced with a buoyancy flux only. The horizontal salinity gradient is $\sim$0.16 psu/12 km ($\simeq$ 0.26 kg m^{-3}/25 km) at the end of winter. This salinity gradient is stronger than the density gradient equivalent of the observed temperature gradient.

The second year experiments are initialised with a horizontal salinity gradient across the shelf break separating the shelf and offshore waters. During winter the front remains near the shelf break where it is initialised. The horizontal salinity gradient at the end of winter is about the same as it is in the first year.

The horizontal salinity gradients in the first year experiments forced with a uniform wind are half of what they are for the experiment without the wind because the dense

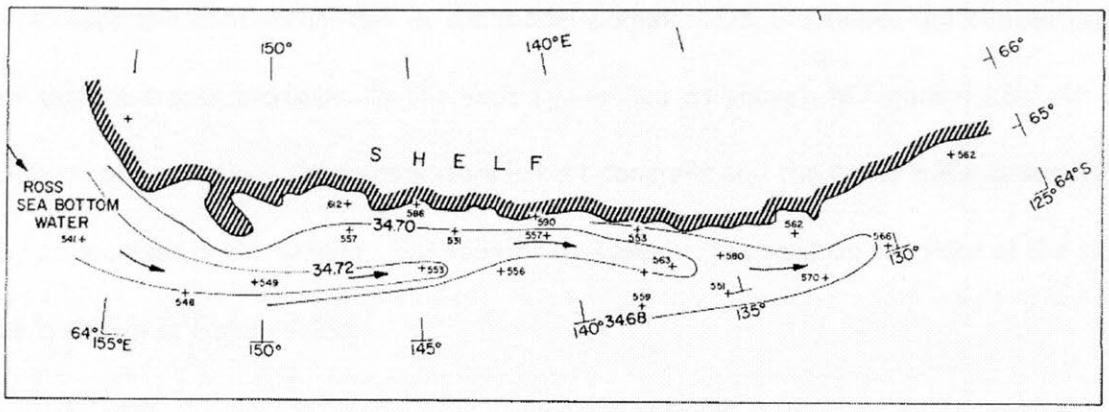

Figure 7.10: *Bottom salinity contours and O_2 values next to crosses from the continental rise off the Adélie Coast (Gordon and Tchernia, 1972, Figure 9).*

water produced in the former experiments is not as dense as the dense water produced in the latter. A cross section of the salinity after 120 and 360 days are shown in Figures 7.4a and e for the experiment forced with a buoyancy flux and constant and uniform wind.

The model produces a front between the dense water formed on the shelf and the less dense water offshore; this reproduces the southern half of the 'V' shaped front. As the cold fresh coastal current that is observed above the shelf break in Antarctica is not configured into the model, the northern half of the 'V' shaped front is not reproduced.

7.4 Flow on the slope

7.4.1 Water properties

The oxygen values on the continental rise increase from east to west as shown in Figure 7.10 from Gordon and Tchernia (1972). The bottom water from the Ross Sea flows westward. As it passes the Adélie Land region, the Ross Sea Bottom Water signal is eroded and replaced by newly formed bottom water from the Adélie Land region which is fresher and has a higher oxygen content.

In the numerical simulations the dense water plume travels along the slope and does

not reach the continental rise in the model domain. On the slope, the concentration of surface tracer increases to the west ($y \rightarrow \infty$) as shown in Figure 4.13b. In the numerical simulations the temperature is kept constant and the dense water is simulated by an increase in the salinity. The salinity increases to the west on the floor of the slope as is shown in Figure 4.13a.

7.4.2 Barotropic currents

Observations of buoy tracks show current speeds over the continental slope to be 0.16 m s^{-1} westward for water less than 500 m, decreasing to zero for depths of 3,800 m and turning eastward for depths greater than 3,800 m (Bindoff et al., 2000b). East of the channel at 150°E between 65.92 and 64.8°S the barotropic flow is westward and the barotropic transport over the 124 km is 39.5 Sv; west of the channel at 139.8°E the flow is westward between 65.71 and 65.4°S, over this distance of 34 km the transport is 8.5 Sv. Farther north the currents turn eastward and become part of the Antarctic Circumpolar Current (Bindoff et al., 2000b) which is not modelled in this study.

In experiments without wind forcing the net barotropic transport is eastward. In the experiment with no sill at the shelf break in Section 4.2 the barotropic velocities are dominated by eddies at the shelf break and there is no continuous current, although the net alongshore transport is eastward. In the experiment with a continuous sill at the shelf break there is a strong continuous barotropic eastward current above the sill. For the first year channel experiment in Section 5.3.1, the barotropic eastward current has transport similar to the sill experiment without the channel. The position of the current in the channel experiment is not directly above the sill as it is in the sill experiment, instead it is positioned on the slope side of the sill upstream of the channel, then passes

through the channel and then to the shoreward side of the sill downstream of the channel. In the second year channel experiment in Section 5.3.2, the offshore transport of dense water is increased substantially and the dense water plume that moves westward along the slope is able to capture the water columns and produce westward barotropic flow. The velocities reach 0.23 m s^{-1} on the upper part of the slope west of the channel. The westward transport generated by this barotropic flow is 0.60 Sv.

The experiments forced with a uniform westward wind forcing produce onshore transport in the surface Ekman layer. The onshore transport raises the sea level above the shelf and creates a negative sea surface elevation gradient (decreasing offshore) above the shelf sill. This drives a geostrophic westward current along the sill. In the wind only experiment in Section 6.1, east of the channel the core of the along-sill current lies above the 400 m isobath on the onshore side of the sill and has a speed of 0.06 m s^{-1} and has a barotropic westward transport of 1.00 Sv. The current passes through the channel and west of the channel the core of the current is on the offshore side of the sill above the 400 m isobath and has a speed of 0.16 m s^{-1} and a barotropic westward transport of 1.60 Sv. The barotropic current produced by the combination of the buoyancy forcing and the wind forcing in Section 6.2 is similar to the barotropic current produced by the wind blowing over the same topography in Section 6.1.

The barotropic westward current generated by (1) the dense water plume moving along the slope or (2) the uniform easterly wind reaches speeds of 0.16 m s^{-1}, similar to the observed current speed. The extent of the model is configured such that the maximum depth is 2,000 m and the model is 700 km alongshore (only 270 km of which have been analysed in this study). In these numerical simulations the westward current only extends as far as the 1,500 m isobath. Observations show that the current extends

out to the 3,800 m isobath. As the current in the numerical simulations is not as wide as the observed current, the alongshore transport in the model is less than that observed. The Antarctic Slope Current is virtually circumpolar and is not driven by purely local forcing but by many sources around the continent.

The observed barotropic westward current over the sill and slope is reproduced in the numerical simulations that produce a lot of dense water which overflows onto the slope producing a dense water plume that captures water columns and results in barotropic westward flow. Experiments forced with a uniform easterly wind result in a sea surface elevation gradient that drives a westward current of the same magnitude as the observed currents above the sill and slope, though the alongshore transport is not as great.

7.4.3 Baroclinic currents

The baroclinic westward transport measured by Bindoff et al. (2000b) east of the channel at 150°E between 65.92 and 64.8°S (a distance of 124 km) was 9.1 Sv; and west of the channel at 139.8°E between 65.71 and 65.4°S (a distance of 34 km) was 1.4 Sv. The westward baroclinic flow at 150°E is due to the westward flow of dense water formed in the Ross Sea which is not modelled in this study, and the flow at 139.8°E is most likely to be due to the dense water formed in the Adélie Land region.

The baroclinic westward flow west of the channel is stronger than it is east of the channel for experiments that produce dense water that flows onto the slope. The maximum baroclinic westward current is produced in the second year experiment with no wind in Section 5.3.2. This experiment also has the greatest amount of dense water transported over the shelf break (see Table B.2).

The maximum baroclinic transport in the numerical simulations produced by the

second year experiment in Section 5.3.2 is 0.56 Sv, which is nearly half the observed value of 1.4 Sv. This is most likely due to less dense water being produced in the model than in the Adélie Land region.

7.4.4 Plume

The dense water plumes on the slope around Adélie Land region are observed to be 100 – 300 m thick (Baines and Condie, 1998). In most numerical simulations the plume thickness on the slope ranges from 100 – 500 m, where the plume is defined as water on the slope with surface tracer concentration $c > 0.02$.

The plume appears on the slope offshore and west of the forcing region for the experiments without a sill at the shelfbreak. The plume is thin offshore of the forcing region and the thickness increases westward. The plume thickness is plotted in Figure 4.14, it ranges from 100 and 350 m thick.

For experiments configured with a sill and channel, the plume is found on the slope west of the channel. The plume thickness for the first and second year channel experiments without the wind is plotted in Figure 5.10. The plume takes 150 days to reach the 970 m isobath in the first year and is initially less than 100 m thick. After 210 days it is 100 m thick and over time it becomes thicker. In the second year the plume appears at the 970 m isobath after 60 days, and reaches a maximum thickness of 200 m by the end of summer.

The uniform wind assists in moving the plume down the slope. The plume reaches the 970 m isobath after 90 days instead of 150 days for the experiment without the wind. The thickness of the plume is difficult to determine due to the detrainment of the outer layers of the plume, but it is plotted in Figure 6.11. From $t = 180$ to 270 days

the plume thickness is 260 to 530 m thick. The cross-slope section of concentration of surface tracer in Figure 6.12c shows that detrainment is occurring, this increases the estimates of plume thickness. The plume thickness for the wind driven case ranges from $88 - 360$ m, excluding the plume thickness data between $t = 180$ to 270 days while detrainment is occurring. This is close to the range of plume thicknesses reported by Baines and Condie (1998).

Where there is a continuous sill at the shelf break, no plume is found on the slope because the dense water is trapped on the shelf and is unable to flow over the sill onto the slope. Also, in the wind stress curl experiment, no plume is found on the slope. Where a plume is produced in these experiments it is up to 400 m thick which is of the order of the thickness of dense water plumes found on the slopes of Antarctica where dense water formation occurs (Baines and Condie, 1998).

7.4.5 Geostrophic velocity structures

Figure 7.6b shows the geostrophic velocities calculated from a cross-shelf density section shown in Figure 7.6a at 151°E in Eastern Wilkes Land from Foster (1995, Figure 5). The velocity field has features that are consistent with the velocity field generated by shelf waves (Foster, 1995). This section is east of our study area and west of the Ross Sea, which is the most likely source of dense water on the slope at this section. The cross sections of alongshore velocity from the numerical simulations are compared to the geostrophic velocity section in Figure 7.6b.

The geostrophic velocity structure in Figure 7.6b is reproduced by experiments that produce dense water that overflows onto the slope. All occurrences of this velocity structure are found to the west of the forcing region, in the direction that the dense

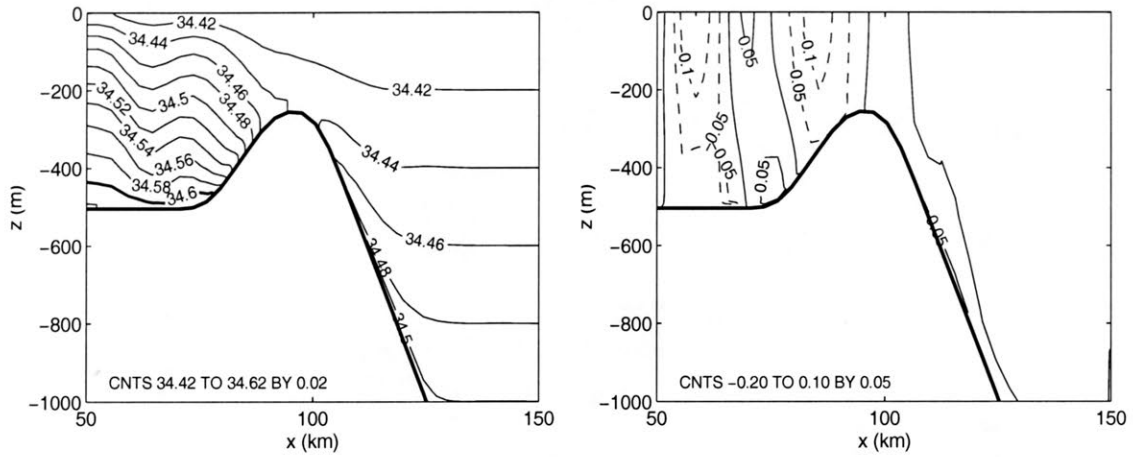

(a) Salinity

(b) Alongshore velocity

Figure 7.11: *(a) Salinity and (b) alongshore velocity at y=372 km after 150 days for Section 5.3.1 to compare with the geostrophic velocities calculated by Foster (1995) reproduced in Figure 7.6. Solid lines are westward flow and dashed lines are eastward flow, velocity in* $m\ s^{-1}$.

water travels along the slope. Figure 7.11 shows a cross section of salinity and alongshore velocity west of the channel at $y = 372$ km after 150 days from the channel experiment described in Section 5.3.1. This velocity structure is similar to the structure shown in Figure 7.6b. The eastward velocity at the shelf break in the numerical simulation is stronger than it is in Foster (1995) and the westward velocity over the upper slope is confined to a thinner layer on the slope. In the second year channel experiment in Section 5.3.2 velocity structures similar to the geostrophic velocity are more common, the pattern of eastward and westward are the same, but the alongshore velocities are of the order of 10 times stronger. The velocity pattern is also reproduced in the simulations with the combined uniform wind and buoyancy flux in Sections 6.2 and 6.3, and in the experiment configured without the sill or the channel in Section 4.2 where dense water is present on the slope.

The geostrophic velocity pattern calculated by Foster (1995) is not reproduced where no dense water is present on the slope. Table B.3 lists that the sill experiment, the wind

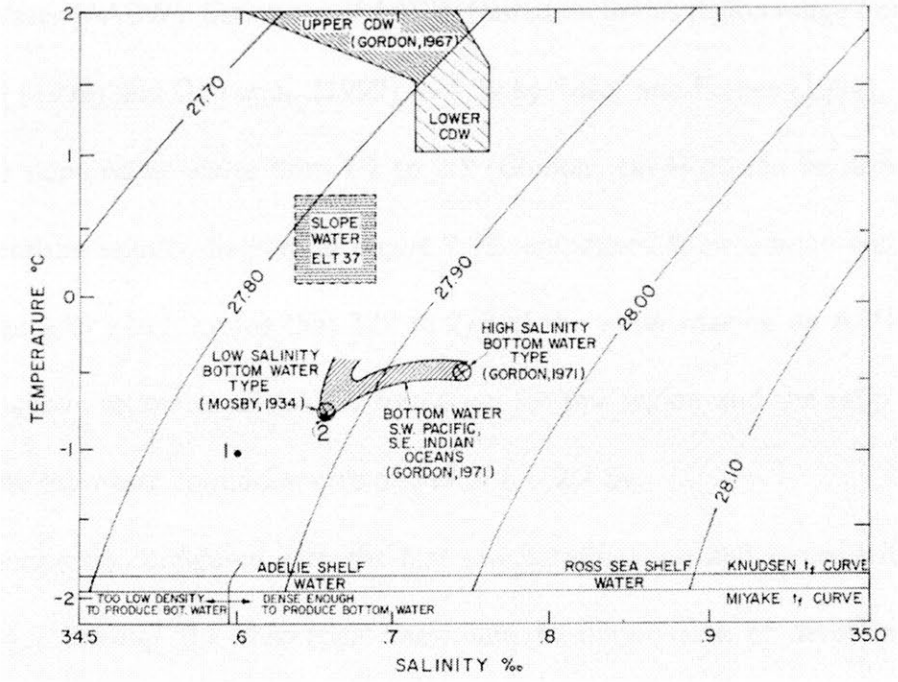

Figure 7.12: *Schematic temperature-salinity diagram showing the core layer values of Antarctic water masses from Gordon (1972, Figure 8).*

only experiment and wind stress curl experiment do not transport dense water across the shelf break onto the slope. These experiments do not replicate the geostrophic velocity structure in Foster (1995).

The geostrophic velocity structure from Foster (1995) is, however, reproduced when dense water is present on the slope. The alongshore velocities are greater in magnitude; this is due to the strong density gradients from the close proximity of dense water source i.e., less than 200 km, whereas in Foster (1995) the source of the dense water is the Ross Sea which is over 1,000 km away.

7.5 Rates of dense water formation

In the numerical simulations dense water is produced by a buoyancy flux over a limited forcing region above the shelf. This production of this dense water mass is analogous to observed processes producing Shelf Water (SW) which is a component of Antarctic

Bottom Water (AABW). Estimates of AABW formation in this region range from 2−3 Sv by Rintoul (1998) and Orsi et al. (1999) to 4 Sv by Speer and Forbes (1994). The ratio of shelf to slope water varies from 1:1 to 2:1 (Gordon, 1974) as can be deduced from the temperature-salinity diagram in Figure 7.12 reproduced from Gordon and Tchernia (1972, Figure 8) which means that 1/2 to 2/3 of the water making up AABW is SW. From the above estimates of AABW formation for this region and the ratio of SW in AABW, the estimated formation rate of SW is $1 - 2.7$ Sv.

In experiments configured with the first year stratification and forced with the basic buoyancy forcing, the theoretical maximum formation rate of dense water with $S \geq 34.6$ psu is 0.4 Sv (equation 4.2). This rate is far short of the rates of SW formation estimated from observations for this region. The greatest amount of dense water transported offshore over the shelf break for an experiment initialised with first year stratification and forced with the basic buoyancy flux is 0.062 Sv for the experiment configured without a sill at the shelf break in Section 4.2. This is 6% of the lowest estimate of SW formation from the above cited literature. Even if the alongshore transport of dense water of 0.020 Sv to the west and 0.010 Sv to the east on the shelf is taken into account, assuming at some stage it will move over the shelf break, the amount of dense water formed is 13% of the estimate of SW formation. With a configuration that contains a sill and channel, the offshore transport of dense water across the shelf break is 0.001 Sv. With the additional forcing of a constant uniform wind the offshore flux of dense water is 0.013 Sv and with a pulsating uniform wind the offshore flux of dense water is 0.019 Sv. All dense water transports over the shelf break are significantly lower than the estimated production rates of SW, thus the first year simulation is clearly not consistent with observations.

At the end of the first year simulation, dense water with $S \geq 34.6$ psu is found in the depression and the stratification on the shelf is four times the initial stratification, this results in a greater mean salinity on the shelf. For an experiment initialised with the these conditions on the shelf, the theoretical maximum formation rate of dense water is 0.7 Sv, which is only 70% of the lower estimate of SW formation for this region. In this numerical study the maximum amount of dense water $S \geq 34.6$ psu transported over the shelf break is 0.136 Sv for the second year channel experiment in Section 5.3.2, forced by a buoyancy flux only. The alongshore transport of dense water on the shelf is 0.028 and 0.020 Sv to the west and east respectively, resulting in a total dense water production of 0.184 Sv leaving the forcing region. This is 3 times the production rate of the maximum production rate of dense water from a first year model experiment. It is still less than the estimated shelf water production for the Adélie Land region. This shows that initial conditions drastically affect the amount of dense water formed. Most but not all the dense water passes through the channel onto the slope.

In the third year simulation in Section 5.3.3, dense water with $S \geq 34.6$ psu makes up more 40% of the initial water on the shelf. Forcing the third year initial configuration with the basic forcing can produce a theoretical maximum formation rate equal to the lower estimate of SW formation (1 Sv). The offshore transport of dense water in this experiment was 0.427 Sv. The net alongshore transport of dense water on the shelf is 0.047 Sv to the west. This is still short of the estimates of SW formation in this region. As it is expected that further simulations will be the similar to the third year simulation as described in Section 5.3.3, and further simulations for these conditions are not expected to produce much more dense water.

The model initialisation and the buoyancy forcing produce 1/5 of the amount of

dense water that is estimated for this region. This study has been able to show that dense water can be formed in this region and is able to show how various features affected dense water formation. The next section describes factors that could be improved or included in the model that may increase the production of shelf water and make the model more "realistic".

7.6 Improvements to the model

This study has been simplified and is limited in the observations it is able to reproduce. Further additions to the model that might allow closer agreement with the existing observations could include:

- the incorporation of other bathymetric features in the Adélie Land region shown in Figure 2.1 e.g., the ridge on the shelf west of the Adélie Depression, the Mertz Glacier Tongue, the ridges and canyons in the slope,

- modelling the variation in temperature as well as salinity, to enable better classification of water masses, allowing two water masses to have similar densities with different temperature and salinity properties. The incorporation of varying temperature in the numerical simulation would allow CDW and the Antarctic Slope Front (ASF) to be modelled. CDW is an important component of AABW. The ASF and its associated current are instrumental in the production of AABW (Whitworth et al., 1998),

- more realistic initial conditions. For example, high density water on the shelf would most likely reduce strong along shelf density gradients. This would alleviate the problem of strong alongshore buoyancy fluxes which remove dense water from the

forcing region and advect less dense water to beneath the forcing region,

- more realistic modelling of the sea-ice formation. The uniform buoyancy forcing produces a dense water mass of uniform quality. Buoyancy forcing that is varied over time provided the variation in time occurs over a time scale that is greater than the response time of the ocean so that the ocean does not integrate the effects of the forcing or buoyancy flux variation in space may produce dense water of varying densities resulting in stratified water in the depression,

- more realistic modelling of the winds, including evaporative effects which would add to the buoyancy flux and the production of dense water and

- the effects of the ice shelves which would "super cool" the water but at the same time, melting of ice shelves would freshen the water and possibly these effects would balance each other resulting in a very small net effect.

Due to constraints on the numerical stability of the model, it was only run for one year at a time. To simulate the second and third years, the model was initialised with salinity structure found at the end of the first year runs, i.e., increased stratification on the shelf and dense water in the depression and then run again. As demonstrated by the second year channel experiment the initialisation has a drastic effect on the production of dense water.

7.7 Summary

This study was able to reproduce some of the observations of circulation and water column structure from the Adélie Land region. The numerical simulations were in agreement with the following observations.

- When there is a depression in the shelf, the densest water along the shelf is found in the depression (Rintoul, 1998; Bindoff et al., 2000a).

- Homogeneous water columns are found beneath the forcing region during winter, simulating the winter water found above the depression (Bindoff et al., 2001).

- Stratified high salinity shelf water (HSSW) in the depression is found during winter in the strong coastal forcing experiment where dense water formation occurs on the shelf between the coast and the depression. It is also found in the second year wind experiments where the buoyancy flux combined with the wind is unable to erode away the stratification in the depression (Bindoff et al., 2001).

- The HSSW in the depression is denser and younger than the WW above it (Bindoff et al., 2001).

- The mean age of the water in the depression is in good agreement with the flushing times of the depression (Bindoff et al., 2001).

- In the presence of a sill at the shelf break and a channel through the sill, MCDW enters through the channel and is found on the north bank of the depression (Rintoul, 1998; Bindoff et al., 2000a).

- Patterns of westward flow at the coast, eastward flow above the depression and westward flow above the north bank of the depression are replicated. The numerically simulated velocity structure tends to be noisier than the observations (Bindoff et al., 2001).

- The southern half of the 'V' of the Antarctic Slope Front is formed between the dense water on the shelf and the less dense water offshore (Jacobs, 1991;

Whitworth et al., 1998).

- Increase in the oxygen values from east to west along the slope (Gordon and Tchernia, 1972) are simulated by the increase in surface tracer concentration from east to west.

- Barotropic westward flow above the upper slope (Bindoff et al., 2000b) is replicated in experiments which are forced with a uniform easterly wind. The flow is also replicated in the second year experiment where the dense water plume produced on the slope is strong enough to capture the water column.

- Baroclinic westward flow (Bindoff et al., 2000b) is produced when dense water moves onto the slope and moves westward along the slope.

- The geostrophic alongshore velocity structures calculated from density sections (Foster, 1995) are simulated in sections where dense water is travelling along the slope.

- Dense water is produced in this region, is transported onto the slope and travels westward along the slope (Gordon and Tchernia, 1972).

Chapter 8

Discussion and Conclusion

In the Adélie Land region, persistent sea-ice formation during winter in the Mertz polynya results in significant Antarctic Bottom Water (AABW) production. Key topographic features of the Adélie Land region including a depression in the shelf, a sill at the shelf break and a channel through the sill, are included and the role of these features in modifying circulation and AABW formation is determined. The effects of winds are also studied. The effects of the Mertz polynya are reported in Chapter 4, the effect of topographic features including the depression, the sill at the shelf break and the channel through the sill are reported in Chapter 5 and the effect of the wind is reported in Chapter 6. The results of the numerical simulations are compared to observations in Chapter 7.

The horizontal model resolution on the shelf is 3 km, sufficient to resolve the perturbations that break up the convective chimney. The model is able to simulate the stages of convection in accordance with the theories of Send and Marshall (1995), Visbeck et al. (1996), Gawarkiewicz and Chapman (1995) as described in Section 3.2.

The equilibrium time and salinity anomaly for the experiment configured with a flat

shelf described in Section 5.1 is in good agreement with the theoretical equilibrium time and salinity of a convective event discussed in Section 3.4. The theories described in Section 3.4 which were developed by Send and Marshall (1995), Gawarkiewicz and Chapman (1995), Gawarkiewicz (2000) were developed for a surface buoyancy flux over a flat bottom and thus do not predict the equilibrium state for the experiment with a depression in the shelf.

8.1 The effect of topographic features

The effect of the topography is determined in Chapter 5. The model configuration is such as to resolve the key topographic features on the shelf which are generally too small to be resolved in larger scale models and are therefore generally omitted from Oceanic General Circulation Models (OGCM). The present model includes a depression in the shelf, the sill at the shelf break and the channel through the sill.

8.1.1 Depression

A buoyancy forced system reaches equilibrium when the buoyancy forcing at the surface is balanced by the lateral buoyancy fluxes which remove salty dense water from beneath the forcing region and advect fresher ambient water to the area beneath the forcing region. A depression beneath the forcing region increases the time taken to reach equilibrium since water in the depression is shielded from the incoming advection of less dense water. The denser water formed beneath the forcing region fills the depression and does not spread away from the forcing region as readily as it does on a flat shelf. As denser water forms, it flushes less dense water out of the depression. Because the dense water in the depression is resident longer than it would on a flat shelf, it is exposed to the forcing for

a longer period of time and reaches a higher density and salinity anomaly.

The time to reach equilibrium for the basic experiment with the depression is 4 times more than the time required by the flat shelf experiment without the depression. Also, the equilibrium salinity anomaly acquired is 0.01 psu greater.

The depression stores dense water on the shelf during summer. The maximum salinity on the shelf at the end of summer with a depression in the shelf is 34.68 psu compared to 34.58 psu on the flat shelf. This means that there is already dense water on the shelf at the beginning of the following winter. In the second year channel experiment the offshore transport of dense water increases by a factor of 50 compared to the first year channel experiment.

8.1.2 Sill

The sill blocks cross-shelf flow between shelf and deep ocean waters beneath the height of the sill at a depth of 250 m. The reduction in cross-shelf flow thereby increases the time taken for the water to reach equilibrium and increases the equilibrium salinity. Equilibrium is not reached in the sill experiment within the 240 day forcing period, whereas in the basic experiment without the sill the salinity reached equilibrium after 150 days. The mean salinities beneath the forcing region at the end of winter are 34.640 for the sill experiment and 34.626 psu for the experiment without the sill at the shelf break.

During summer, the sill stops the dense water from flowing off the shelf. The salinity on the shelf decreases by a greater amount in the experiment without the sill than it does in the experiment with the sill. Thus at the beginning of the following winter dense water is already present on the shelf, which in turn can increase production of dense

water in the following year.

The sill stops offshore flow of intermediate and dense waters from leaving the shelf and moving onto the slope. Concurrently the sill also stops onshore flow of Modified Circumpolar Deep Water (MCDW) from the deep ocean onto the shelf. The MCDW provides warm water to the shelf which helps melt the sea-ice and maintain the polynya.

8.1.3 Channel

The channel through the sill provides a path for cross-shelf flow between shelf and deep ocean waters. Dense water is able to move from the shelf onto the slope and a small amount of MCDW is able to move from the deep ocean onto the shelf.

The limited amount of MCDW on the shelf helps maintain the polynya. This allows continued high production rates of sea-ice, and without a polynya the rate of sea-ice formation is lower. Larger amounts of MCDW on the shelf as found in the experiments without a sill would be likely to melt greater amounts of ice resulting in fresher less dense water.

In the first year channel experiment, there is a small amount of dense water with $S \geq 34.6$ psu transported offshore. However no offshore transport of dense water occurs in the experiment without a channel through the sill. For an intermediate water mass with $34.5 \leq S < 34.6$ psu, the experiment without a channel does not allow this water mass to move over the sill into the deep ocean, whereas the experiment with the channel transports 0.029 Sv of this water through the channel.

8.2 Wind

The uniform easterly wind increases the cross-shelf exchange at the shelf break through the generation of eddies and a surface Ekman layer which advects surface water onshore. The Ekman transport created by the uniform wind advects surface water from offshore beneath the forcing region, and reduces the time to reach equilibrium. The uniform wind experiment reaches equilibrium after 120 days, while the channel experiment without the wind does not reach equilibrium in 240 days. The second year uniform wind experiment is unable to homogenise the water column due to the increased onshore advection of less dense surface water to the area beneath the forcing region.

The increased onshore transport in the wind driven surface Ekman layer does not increase the amount of MCDW transported onto the shelf because the MCDW is found below a depth of 500 m, which is outside of the surface Ekman layer. In the wind only experiment no MCDW is transported onshore.

The eddies generated at the shelf break by the uniform easterly wind also assist in the movement of water off the shelf, and the offshore volume transport across the shelf break is 4 times greater in the experiment with the wind than for the experiment without the wind. But the volume of dense water with $S \geq 34.6$ psu transported offshore is only 21% of that which is transported offshore due to the lower volume of dense water on the shelf. This is due to the overall reduction in salinity of the shelf waters with the easterly wind.

For a pulsating wind with the same total momentum flux as the constant wind, the time for the system to reach equilibrium and the equilibrium salinity reached is similar. The volume of dense water transported offshore is greater for the pulsating wind.

When the wind speed is reduced for the pulsating wind, the lateral advection of less

dense water from outside the forcing region to the area beneath the forcing region in the pulsating wind experiment is not as great as it is for the uniform wind experiment. Within the numerical simulations, it takes longer for the system to reach equilibrium with a pulsating wind than it does for a stronger momentum flux. The resulting equilibrium salinity anomaly is 0.04 psu more saline in the reduced momentum flux experiment. The reduction in the momentum flux results in more dense water being transported offshore than the constant wind or pulsating wind of greater speed. Though the stronger winds do not assist in the offshore transport of dense water, the experiment with no wind does not assist in producing cross shelf transports and offshore transport of dense water.

The situation for the wind stress curl wherein the easterly wind decays to zero over a distance of 50 km offshore is completely different. The increase in salinity for this experiment is close to that of the no wind experiment. The circulation pattern generated by the wind stress curl does not aid in the offshore transport of dense water from the shelf break onto the slope.

8.3 Relevance to other areas

Though this study was configured for the Adélie Land region, it is generally relevant for other regions of the Antarctic continental shelf, such as the Filchner Depression in the Weddell Sea, and the Amery Depression in Prydz Bay.

The Prydz Bay region is a possible source of bottom water according to Middleton and Humphries (1989). Prydz Bay is similar to the Adélie Land region in that the Amery Depression is separated from the deep ocean by the Fram Bank and Four Ladies Bank and is connected to the ocean by the Prydz Channel (Wong, Bindoff, and Forbes, 1998). The Prydz Bay polynya is located in front of the Amery Ice Shelf, and just west

of the Amery Depression. Between 1987 and 1994 the size of the polynya ranged from 6,000 and 22,000 km^2 (Massom et al., 1998). In general the mean size of the Prydz Bay polynya is 59% of that of the Mertz polynya. This polynya is maintained by a combination of the effects of a western boundary of grounded icebergs which block the westward flow of ice around the continent into the polynya and the upwelling of warm Circumpolar Deep Water (CDW), in a similar fashion to the Mertz polynya.

8.4 Conclusion

This study has shown that topographic features play an important part in the production of deep convection and AABW in the Adélie Land region of Antarctica. In particular, the effects of a depression in the shelf, a sill at the shelf break and a channel within the sill have been examined. Without the presence of a depression in the shelf, dense water is not formed. A sill at the shelf break reduces exchange of shelf and deep ocean waters. A channel through the sill allows a limited amount of exchange between shelf and deep ocean waters. This is enough to allow the dense water to flow off the shelf onto the slope.

The model successfully simulates many of the salient features of the observations from the Adélie Land region. The presence of the densest water in the depression, the presence of younger water in the depression than the water above it, the onshore flow of MCDW through the channel, and the westward flow of dense water on the slope have been observed and successfully simulated. The model has also shown active dense water formation (1) above the shallow region between the coast and the depression in the coastal forcing experiment and (2) above the depression for experiments with a larger forcing region. These latter features remain to be confirmed by observation.

Appendix A

The Princeton Ocean Model

The Princeton Ocean Model (POM) was developed by Alan Blumberg and George Mellor in 1977 and has been further developed by various people since then. Currently it is widely used for various modelling applications. The model is a a sigma coordinate, free surface, primitive equation ocean model. The model uses the boussinesq and hydrostatic approximations, and includes the Smagorinsky horizontal diffusion scheme and the Mellor-Yamada 2.5 turbulence closure model for vertical mixing. The model has a baroclinic and barotropic mode. The model uses an Arakawa-C staggered grid and a leapfrog (centred in space and time) time step (O'Connor, 1991).

Due to the 3-dimensional nature of the model, it can be used to model situations which are difficult to analyse through analytical models. The model is able to handle variations in topography which allow it to model dense water formation and its movement on the slope.

Governing Equations

The governing equations used in this model are three-dimensional and non-linear. They describe the velocity field $\mathbf{u} = (u, v, w)$, the surface elevation $\eta = \eta(x, y)$, the salinity

$S = S(x, y, z)$ and the potential temperature $\theta = \theta(x, y, z)$.

The continuity equation for incompressible flow is given by

$$\nabla \cdot \mathbf{u} = 0 \ , \tag{A.1}$$

where

$$\nabla = \left(\frac{\partial}{\partial x}, \frac{\partial}{\partial y}, \frac{\partial}{\partial z} \right) \ .$$

The horizontal momentum equations are

$$\frac{\partial u}{\partial t} + \mathbf{u} \cdot \nabla u - fv = -\frac{1}{\rho_0} \frac{\partial p}{\partial x} + \frac{\partial}{\partial z} \left(K_M \frac{\partial u}{\partial z} \right) + F_x \tag{A.2}$$

$$\frac{\partial v}{\partial t} + \mathbf{u} \cdot \nabla v + fu = -\frac{1}{\rho_0} \frac{\partial p}{\partial y} + \frac{\partial}{\partial z} \left(K_M \frac{\partial v}{\partial z} \right) + F_y \ . \tag{A.3}$$

The conservation equations for potential temperature and salinity are

$$\frac{\partial \theta}{\partial t} + \mathbf{u} \cdot \nabla \theta = \frac{\partial}{\partial z} \left(K_H \frac{\partial \theta}{\partial z} \right) + F_\theta \tag{A.4}$$

$$\frac{\partial S}{\partial t} + \mathbf{u} \cdot \nabla S = \frac{\partial}{\partial z} \left(K_H \frac{\partial S}{\partial z} \right) + F_S \ . \tag{A.5}$$

The hydrostatic assumption is

$$\rho g = -\frac{\partial p}{\partial z} \ . \tag{A.6}$$

If the natural Rossby number Ro^* given in equation 3.19 is small, then the geostrophic adjustment is relatively fast and the convection is quasi two-dimensional (Molemaker

and Dijkstra, 2000). The pressure is found by

$$p(x,y,z,t) = p_a + g\rho_0\eta + g\int_z^0 \rho(x,y,z',t)\,dz' \tag{A.7}$$

and the density $\rho = \rho(\theta, S)$ is calculated using the UNESCO equation of state.

The terms F_x, F_y, F_θ and F_S represent the small scale processes unresolved by the model grid. They are parameterised in terms of horizontal mixing processes, analogous to diffusivity. They are represented by (Blumberg and Mellor, 1987, page 3)

$$F_x = \frac{\partial}{\partial x}\left(2A_M\frac{\partial u}{\partial x}\right) + \frac{\partial}{\partial y}\left(A_M\left(\frac{\partial u}{\partial y} + \frac{\partial v}{\partial x}\right)\right) \tag{A.8}$$

$$F_y = \frac{\partial}{\partial y}\left(2A_M\frac{\partial v}{\partial y}\right) + \frac{\partial}{\partial x}\left(A_M\left(\frac{\partial u}{\partial y} + \frac{\partial v}{\partial x}\right)\right) \tag{A.9}$$

$$F_{\theta,S} = \frac{\partial}{\partial x}\left(A_H\frac{\partial(\theta,S)}{\partial x}\right) + \frac{\partial}{\partial y}\left(A_H\frac{\partial(\theta,S)}{\partial y}\right) \tag{A.10}$$

where A_M and A_H are the horizontal kinematic viscosity ($m^2\ s^{-1}$) and horizontal heat diffusivity ($m^2\ s^{-1}$). These values are determined by the Smagorinsky model.

$$A_M = C\,\Delta x\,\Delta y\sqrt{\left(\frac{\partial u}{\partial x}\right)^2 + \left(\frac{\partial v}{\partial y}\right)^2 + \frac{1}{2}\left(\frac{\partial u}{\partial y} + \frac{\partial v}{\partial x}\right)^2} \tag{A.11}$$

where C is a constant. These terms are used to damp out noise in the numerical model, as the grid spacings become smaller, A_M goes to zero. In this study $C = 0.2$, and values of A_M of order 100 $m^2\ s^{-1}$ are generated in the model.

The horizontal heat diffusivity A_H (also used for salinity) is set to the same value as the horizontal kinematic viscosity A_M, as used by Jiang and Garwood (1995, 1998) in modelling dense water plumes and overflows on a slope.

Boundary Conditions

The boundary conditions at the free surface $z = \eta$ are

$$\rho_o K_M \left(\frac{\partial u}{\partial z}, \frac{\partial v}{\partial z} \right) = (\tau_s^x, \tau_s^y) \tag{A.12}$$

$$\rho_o K_H \left(\frac{\partial S}{\partial z}, \frac{\partial \theta}{\partial z} \right) = (\langle wS(0) \rangle, \langle w\theta(0) \rangle) \tag{A.13}$$

$$q^2 = B_1^{2/3} \, | \, (\tau_s^x, \tau_s^y) \, |^2 \tag{A.14}$$

$$q^2 l = 0 \tag{A.15}$$

$$w = u\frac{\partial \eta}{\partial x} + v\frac{\partial \eta}{\partial y} + \frac{\partial \eta}{\partial t} \tag{A.16}$$

Where (τ_s^x, τ_s^y) represents the wind stress vector and $\langle wS(0) \rangle, \langle w\theta(0) \rangle$ represent the salt flux and temperature flux at the surface, $\frac{q^2}{2}$ is the turbulent kinetic energy, $B_1^{2/3} = 6.51$ is a constant and l is the turbulence macroscale determined from the turbulence closure scheme.

At the bottom the salt and temperature gradients are zero, so there are no advective and diffusive salt and temperature fluxes through these boundaries. At the bottom the boundary conditions are

$$\rho_o K_M \left(\frac{\partial u}{\partial z}, \frac{\partial v}{\partial z} \right) = (\tau_b^x, \tau_b^y) \tag{A.17}$$

$$q^2 = B_1^{2/3} u_{\tau b}^2 \tag{A.18}$$

$$q^2 l = 0 \tag{A.19}$$

$$w_b = -u_b \frac{\partial H}{\partial x} - v_b \frac{\partial H}{\partial y} \tag{A.20}$$

where $u_{\tau b}$ is the bottom friction velocity and is related to the bottom frictional stress, (τ_b^x, τ_b^y). The parameters, $K_M, B_1, (\tau_b^x, \tau_b^y)$ are determined by the turbulence closure

scheme. These boundary conditions represent the turbulent bottom boundary.

The coastal boundary ($i = 1, x = 0$) is closed. The offshore boundary ($i = IM, x =$ 392 km) uses a simple zero gradient boundary condition. The alongshore boundaries ($j = 1, JM$) are open boundaries, which use the following boundary conditions. The Martinsen plus Roed local solution (MRO in Palma and Matano, 1998) which uses a relaxation to a local solution at the boundary is used for the barotropic variables. The flow relaxation scheme (FRS in Palma and Matano, 2000) is used for the scalar variables of temperature and salinity. Orlanski radiation conditions are used for the baroclinic velocities (ORI in Palma and Matano, 2000). The Martinsen sponge used in the relaxation alongshore boundary conditions uses 10 points.

These open boundary conditions were found to be the best for these simulations as the Martisen sponge damped much of the energy from the interior that travelled towards the boundary. The radiation condition was then able to radiate the remaining energy causing little reflection back into the interior.

Turbulence Closure Scheme

The vertical mixing co-efficients K_M and K_H in the governing equations A.2 and A.3 are determined by the Mellor-Yamada 2.5 Model (Blumberg and Mellor, 1987, equations 15a and 15b)

$$K_M = lqS_M$$

$$K_H = lqS_H$$

where S_M and S_H are stability functions (equations 17a and 17b, Blumberg and Mellor, 1987)

$$\begin{aligned} S_M[6A_1A_2G_M] + S_H(1 - 2A_2B_2G_H - 12A_1A_2G_H) &= A_2 \\ S_M(1 + 6A_1^2G_M - 9A_1A_2G_H) - S_H(12A_1^2G_H + 9A_1A_2G_H) &= A_1(1 - 3C_1) \end{aligned}$$

where (equations 16a and 16b, Blumberg and Mellor, 1987)

$$\begin{aligned} G_M &= \frac{l^2}{q^2}\sqrt{\left(\frac{\partial U}{\partial z}\right)^2 + \left(\frac{\partial V}{\partial z}\right)^2} \\ G_H &= -\frac{l^2}{q^2}N^2 \end{aligned}$$

where

$$N^2 = -\frac{g}{\rho_0}\frac{\partial \rho}{\partial z}$$

and the numerical constants determined from laboratory experiments are (Mellor and Yamada, 1982)

$$(A_1, B_1, A_2, B_2, C_1) = (0.92, 16.6, 0.74, 10.1, 0.08).$$

$S_M(G_M, G_H)$ and $S_H(G_M, G_H)$ are plotted in Figure A.1. When the water column is statically unstable i.e., $N^2 < 0 \Rightarrow G_H > 0$ then the stability functions S_M and S_H increase, which results in increasing the vertical diffusivity mixing co-efficient K_H for salinity and temperature and the vertical kinematic viscosity momentum co-efficient K_M.

The bottom stress (τ_b^x, τ_b^y) is matched to the bottom velocities by the logarithmic

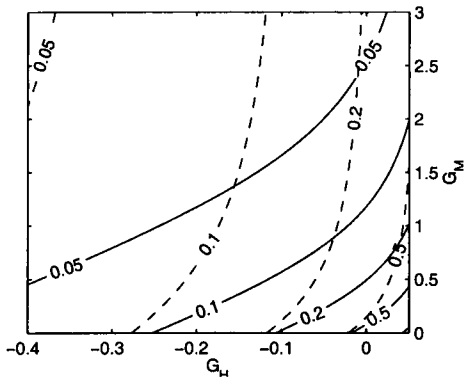

Figure A.1: *The stability functions $S_M(G_M, G_H)$ (solid lines) and $S_H(G_M, G_H)$ (dashed lines).*

law of the wall,

$$(\tau_b^x, \tau_b^y) = \rho_o \, c_D \, |U_b| \, U_b \tag{A.21}$$

where the dimensionless drag co-efficient c_D is determined by

$$c_D = \left[\frac{1}{\kappa} \ln \left(\frac{H + z_b}{z_o} \right) \right]^{-2} \tag{A.22}$$

where $\kappa = 0.4$ is the von Karman constant, $z_o = 1$ cm is the roughness parameter and z_b is the depth just above the bottom, $H + z_b$ is the grid spacing between the bottom grid points. As the grid spacing at the bottom becomes larger c_D decreases.

Sigma (σ) Co-ordinates

The above equations are transformed from the ordinary (x, y, z, t) co-ordinate system to (x^*, y^*, σ, t^*) co-ordinates where

$$x^* = x \qquad y^* = y \qquad \sigma = \frac{z - \eta}{H + \eta} \qquad t^* = t \; . \tag{A.23}$$

This co-ordinate system follows the topography, so that the free surface, $z = \eta$ becomes $\sigma = 0$ and the bottom, $z = -H$ is $\sigma = -1$.

The advantages of a σ co-ordinate system over a z level co-ordinate system is the smooth representation of the bottom topography which allows more accurate modelling of the bottom boundary layer (Mellor, Häkkinen, Ezer, and Patchen, 1999).

Finite Differencing

The governing equations were discretised by using centred in space differential operators

$$\overline{F(x,y,\sigma,t)}^{x} \equiv \frac{F(x+\frac{\Delta x}{2},y,\sigma,t)+F(x-\frac{\Delta x}{2},y,\sigma,t)}{2} \tag{A.24}$$

$$\frac{\partial}{\partial x}F(x,y,\sigma,t) \equiv \frac{F(x+\frac{\Delta x}{2},y,\sigma,t)-F(x-\frac{\Delta x}{2},y,\sigma,t)}{\Delta x} \tag{A.25}$$

$$\frac{\partial}{\partial x}\overline{F(x,y,\sigma,t)}^{x} \equiv \frac{F(x+\Delta x,y,\sigma,t)-F(x-\Delta x,y,\sigma,t)}{2\Delta x} \tag{A.26}$$

$$\overline{F(x,y,\sigma,t)}^{xy} \equiv \overline{\overline{F(x,y,\sigma,t)}^{x}}^{y}$$

$$\equiv \overline{\overline{F(x,y,\sigma,t)}^{y}}^{x} \tag{A.27}$$

Numerical Scheme

There are two modes of calculation, the internal (or baroclinic) mode and the external (or barotropic) mode. The external mode calculation calculates the surface elevation, and the vertically averaged velocities UA and VA. The slow moving internal mode calculates the internal velocities $\mathbf{u} = (u, v, w)$, the salinity $S(x, y, z)$, the temperature $\theta(x, y, z)$ and the turbulence quantities. The internal velocities are adjusted so that their vertical integrals are equivalent to the vertically averaged velocities calculated in the external mode.

The time steps are limited by the Courant-Freidrichs-Levy (CFL) computational sta-

bility condition, the external mode time step is constrained by the condition

$$\Delta t \leq \frac{1}{C_t}\left(\frac{1}{\Delta x^2}+\frac{1}{\Delta y^2}\right)^{-1/2} \tag{A.28}$$

where $C_t = 2\sqrt{gh} + U_{max}$, and U_{max} is the maximum velocity expected. The internal mode time step is constrained by

$$\Delta T \leq \frac{1}{C_T}\left(\frac{1}{\Delta x^2}+\frac{1}{\Delta y^2}\right)^{-1/2} \tag{A.29}$$

where $C_T = 2C + U_{max}$, and C is the maximum internal wave speed based on the gravest mode and is set to 2 m s^{-1}.

Passive tracers

Two passive tracers where added to this model, an age tracer and a surface tracer. The surface tracers use the same advection and diffusion scheme used by the scalars salinity and temperature. The age tracer uses the advection and diffusion schemes used by the scalars plus the age increases with the age of the model.

The surface tracer is initialised to zero every where and tracer flux at the surface is the same as the surface salinity flux. Therefore the values of the tracer expected in the model are of the order of the salinity anomalies. The advantage of the surface tracer concentrations is that they do not decrease as the water descends to greater depths where the ambient salinity is greater, unlike the salinity anomalies which do. The surface tracer is used as a marker of water that is formed in the forcing region. It gives an indication of the initial time taken to flush the depression. It marks the plume on the slope. The absence of the surface tracer $c < 0.02$ together with $S > 34.5$ psu is an

indicator of Modified Circumpolar Deep Water.

The age tracer is initially set to 1 day everywhere so that water initially in the model is one day "older" than the model. The age of the water at the surface is reset to zero at each timestep.

Parameters used in this study

Parameter	Value
IM	75
JM	170
KB	21
DX	3–12 km
DY	3–10 km
DTI (ΔT)	240 s
DTE (Δt)	8 s
HORCON (C)	0.2

Other ocean models

A number of other ocean models exist which could have been used for this study. This section describes some of the other models.

Regional Ocean Modelling System (ROMS) developed by the modelling groups at Rutgers University and University of California, Los Angeles, it is a rewrite of the S-Coordinate Rutgers University Model (SCRUM). ROMS solves the same primitive equations on a similar grid to POM but the numerical alogorithms, code structure and modelling concepts are completely different (Ezer, Arango, and Shchepetkin, 2002). ROMS is a modular ocean model which makes the newest algorithms avaliable and has larger flexibility whereas POM has simple stand-alone code with fewer options. ROMS allows a larger internal time step than POM, but POM is more stable at shorter internal time steps. ROMS requires more computational time than POM, but taking into account

the larger time step allowed by the numerical stability of the model, the computional time required for the same time period of integration is about the same. With all the additional options avaliable to ROMS, it is possible that it may have been better suited to this problem but at the time this study was started, POM was more readily avaliable.

Miami Isopycnic Coordinate Ocean Model (MICOM) has height as a prognostic variable and potential density as the vertical co-ordinate. Advantages of a isopycnic model are that sub-grid scale processes are made adiabatically, however complications at the boundaries are introduced and the model has difficulty when incorporating an accurate equation of state (Bleck and Smith, 1990).

Hamburg Ocean Primitive Equation (HOPE) and Dietrich Center for Air Sea Technology (DieCAST) model are z-coordinate models which are not suitable for the density flows down a slope modelled in this study.

Appendix B

Tables of experiments

Section	Description	Bathymetry	Forcing
		Chapter 4	
4.2	Basic	Shelf with depression	Basic buoyancy flux (B_0)
4.3.1	Large	"	Large polynya with weak forcing
4.3.2	Coastal	"	Coastal polynya with strong forcing
		Chapter 5	
5.1	Flat shelf	Flat shelf	B_0
5.2	Sill	Depression with sill	B_0
5.3.1	Channel/1st year	DSC	B_0
5.3.2	Channel/2nd year	DSC	B_0
5.3.3	Channel/3rd year	DSC	B_0
5.3.4	Double channel	Depression and sill with 2 channels	B_0
		Chapter 6	
6.1	Wind only	DSC	Constant and uniform 10 m s^{-1} easterly wind
6.2	Uniform wind/1st yr	DSC	B_0 + constant uniform 10 m s^{-1} wind.
6.2.1	Uniform wind/2nd yr	DSC	"
6.3	Pulsating wind/1st yr	DSC	B_0 + 10 day pulsating uniform 10 m s^{-1} wind.
6.3.1	Pulsating wind/1st yr	DSC	B_0 + 10 day pulsating uniform 14.1 m s^{-1} wind.
6.3.2	Pulsating wind/2nd yr	DSC	"
6.4	Wind stress curl	DSC	B_0 + wind stress curl 10-0 m s^{-1}/50 km

Table B.1: *Summary of experiments. DSC refers to depression, sill and channel configuration. B_0 refers to the basic buoycancy flux.*

Section	Description	Equilibrium Forcing region				Day 240 Depression		
		time (days)	mean S (psu)	time (days)	max S (psu)	mean age (days)	mean S (psu)	max S (psu)
Chapter 4								
4.2	Basic	150	34.623	150	34.677	36	34.654	34.677
4.3.1	Large	250*		315*		11	34.635	34.649
4.3.2	Coastal	80	34.610	120	34.687	53	34.661	34.686
Chapter 5								
5.1	Flat shelf	40	34.551	60	34.634			
5.2	Sill					24	34.669	34.692
5.3.1	Channel/1st yr					25	34.672	34.706
5.3.2	Channel/2nd yr					37	34.733	34.758
5.3.3	Channel/3rd yr	175	34.658			49	34.765	34.786
5.3.4	Double channel					26	34.662	34.694
Chapter 6								
6.1	Wind only					223	34.455	34.495
6.2	Uniform wind/1st yr	120	34.579	120	34.641	60	34.619	34.642
6.2.1	Uniform wind/2nd yr					184	34.591	34.686
6.3	Pulsating wind/1st yr	200	34.617	225	34.675	43	34.640	34.666
6.3.1	Pulsating wind/1st yr	134	34.586	165	34.644	62	34.617	34.644
6.3.2	Pulsating wind/2nd yr					192	34.608	34.685
6.4	Wind stress curl					18	34.645	34.701

Table B.2: *Summary of results for experiments in Chapters 4 through 6. Equilibrium times and salinities beneath the forcing region. Age, mean and max salinities for the water in the depression at the end of winter (day 240). Note that the initial mean salinity in the depression is 34.464 psu and the maximum salinity is 34.50 psu (except for the second year experiments which have an initial mean salinity of 34.628 psu and maximum of 34.7 psu). *For the large weak forcing experiment in Section 4.3.1 which did not reach equilibrium within the 240 day winter, the forcing was continued in another experiment to determine the equilbrium time and salinity.*

Section	Description	Volume fluxes (Sv)					Salinity flux (psu Sv)
		Total onshore	Total offshore	MCDW onshore	IW	DW	
Chapter 4							
4.2	Basic	−1.607	1.393	−0.0747	0.0909	0.0621	0.0203
4.3.1	Large	−1.919	1.506	−0.0466	0.1255	0.0203	0.0038
4.3.2	Coastal	−1.502	1.197	−0.0969	0.0115	0.0282	0.0029
Chapter 5							
5.1	Flat shelf	−2.055	1.476	−0.1104	0.1348	0.0234	0.0100
5.2	Sill	−0.312	0.293				−0.0001
5.3.1	Channel/1st yr	−0.472	0.404	−0.0120	0.0149	0.0009	0.0016
5.3.2	Channel/2nd yr	−1.173	1.221	n/a	0.2067	0.1362	0.0530
5.3.3	Channel/3rd yr	−1.732	1.974	−0.0077	0.2562	0.4269	0.1310
5.3.4	Double channel	−0.564	0.413	−0.0118	0.0255	0.0015	0.0022
Chapter 6							
6.1	Wind only	−1.176	1.606				−0.0142
6.2	Uniform wind/1st yr	−1.347	1.427	−0.0012	0.2585	0.0132	0.0398
6.2.1	Uniform wind/2nd yr	−1.358	2.033	n/a	0.3630	0.0004	0.0591
6.3	Pulsating wind/1st yr	−0.913	0.882	−0.0069	0.1691	0.0190	0.0258
6.3.1	Pulsating wind/1st yr	−2.149	1.092	−0.1087	0.0941	0.0163	0.0074
6.3.2	Pulsating wind/2nd yr	−1.039	1.418	n/a	0.4138		0.0592
6.4	Wind stress curl	−0.563	0.606	−0.0213	0.0157		0.0082

Table B.3: *Summary of cross-shelf transports at the shelf break ($x = 96$ km) between $y = 160$ and 430 km. The cross-shelf transports are divided into on and offshore volume transport, onshore transport of MCDW ($u < 0$, $S < 34.45$ psu and $c < 0.02$), net transport of intermediate water (IW, $34.5 \leq S < 34.6$ psu) and dense water (DW, $S \geq 34.6$ psu) and net salinity flux calculated from equation 4.4. Positive numbers indicate offshore transport.*

Bibliography

Adolphs, U. and Wendler, G. (1995). A pilot study on the intereactions between katabatic winds and polynya at the Adélie coast, Eastern Antarctica. *Antarctic Science*, *7*(3), 307–314.

Baines, P. G. and Condie, S. (1998). Observations and modelling of Antarctic downslope flows: a review. In Jacobs, S. and Weiss, R. F. (Eds.), *Ocean, Ice, and Atmosphere: Interactions at the Antarctic Continental Margin*, Vol. 75 of *Antarct. Res. Ser.*, pp. 29–49. AGU, Washington.

Beckmann, A., Hellmer, H. H. and Timmermann, R. (1999). A numerical model of the Weddell Sea: Large-scale circultion and water mass distribution. *J. Geophys. Res.*, *104*(C10), 23375–23391.

Beckmann, A. and Pereira, A. F. (2003). Lateral tidal mixing in the Antarctic marginal seas. *Ocean Dynamics*, *53*, 21–26.

Bindoff, N. L., Williams, G. D. and Allison, I. (2001). Sea-ice growth and water mass modification in the Mertz Glacier, East Antarctica, during winter. *Ann. Glaciol.*, *33*, 399–406.

Bindoff, N. L., Rintoul, S. R. and Massom, R. (2000a). Bottom water formation and

polynyas in Adélie Land Antarctica. *Papers and Proc of Roy Soc of Tasmania*, *133*(3), 51–56.

Bindoff, N. L., Rosenberg, M. A. and Warner, M. J. (2000b). On the circulation and water masses over the Antarctic continental slope and rise between 80° and 150°E. *Deep-Sea Res II*, *47*, 2299–2326.

Bleck, R. and Smith, L. T. (1990). A wind-driven isopycnic co-ordinate model of the north and equatorial Atlantic ocean. 1 model deveopment and supporting experiments. *J. Geophys. Res.*, *95*(C3), 3273–3285.

Blumberg, A. F. and Mellor, G. L. (1987). A description of a three-dimensional coastal ocean circulation model. In Heaps, N. S. (Ed.), *Three-Dimensional Coastal Ocean Models*, Vol. 4 of *Coastal and Estuarine Series*, pp. 1–16. American Geophysical Union, Washington, D. C. 208 pp.

Böning, C. W. and Semtner, A. J. (2001). High-resolution modelling of the thermohaline and wind-driven circulation. In Siedler, G., Church, J. and Gould, J. (Eds.), *Ocean Circulation and Climate*, Vol. 77 of *International Geophysics Series*, pp. 59–77. Academic Press, London.

Broecker, W. S. (1991). The great ocean conveyor. *Oceanography*, *4*(2), 78–89.

Broecker, W. S., Sutherland, S. and Peng, T.-H. (1999). A possible 20th-century slowdown of the Southern Ocean deep water formation. *Science*, *286*, 1132–1135.

Carmack, E. C. (1977). Water characteristics of the Southern Ocean south of the Polar Front. In Angel, M. V. (Ed.), *A Voyage of Discovery*, Vol. 24 (Suppl.) of *Deep-Sea Res.*

Carmack, E. C. and Foster, T. D. (1975). On the flow of water out of the Weddell Sea. *Deep-Sea Res.*, *22*, 711–724.

Carmack, E. C. and Killworth, P. D. (1978). Formation and interleaving of abyssal water masses off Wilkes Land, Antarctica. *Deep-Sea Res.*, *25*, 357–369.

Cavalieri, D. J. and Martin, S. (1985). A passive microwave study of polynyas along the Antarctic coast Wilkes Land coast. In Jacobs, S. (Ed.), *Oceanology of the Antarctic Shelf*, Vol. 43 of *Antarct. Res. Ser.*, pp. 227–252. AGU, Washington.

Chapman, D. C. (1998). Setting the scales of the ocean response to isolated convection. *J. Phys. Oceanogr.*, *28*, 606–620.

Chapman, D. C. (1999). Dense water formation beneath a time-dependent coastal polynya. *J. Phys. Oceanogr.*, *29*, 807–820.

Chapman, D. C. (2000). The influence of an alongshore current on the formation and offshore transport of dense water from a coastal polynya. *J. Geophys. Res.*, *105*(C10), 24,007–24,019.

Chapman, D. C. and Gawarkiewicz, G. (1997). Shallow convection and buoyancy equilibration in an idealized coastal polynya. *J. Phys. Oceanogr.*, *27*, 555–566.

Condie, S. A. (1995). Descent of dense water masses along continental slopes. *J Mar Res*, *53*, 897–928.

Cushman-Roisin, B. (1994). *Introduction to Geophysical Fluid Dynamics*. Prentice-Hall, Englewood Cliffs, New Jersey. 320 pp.

Davis, A. M. J. and McNider, R. T. (1997). The development of Antarctic katabatic winds and the implications for the coastal ocean. *J Atmos Sci*, *54*, 1248–1261.

England, M. H. (1992). On the formation of Antarctic Intermediate and Bottom Water in the Ocean General Circulation Models. *Deep-Sea Res.*, *22*, 918–926.

Ezer, T., Arango, H. and Shchepetkin, A. F. (2002). Developments in terrain-following ocean models: intercomparisons of numerical aspects. *Ocean Modelling*, *4*, 249–267.

Fofonoff, N. P. (1956). Some properties of sea water influcencing the formation of Antarctic bottom water. *Deep-Sea Res.*, *4*, 32–35.

Foldvik, A., Middleton, J. H. and Foster, T. D. (1990). The tides of the southern Weddell Sea. *Deep-Sea Res.*, *37*, 1345–1362.

Foster, T. D. (1995). Abyssal water mass formation off the eastern Wilkes Land coast of Antarctica. *Deep-Sea Res.*, *42*, 501–522.

Foster, T. D. and Carmack, E. C. (1976). Frontal mixing zone and Antarctic bottom water formation in the southern Weddell Sea. *Deep-Sea Res.*, *23*, 301–317.

Foster, T. D. and Middleton, J. H. (1980). Bottom water formation in the western Weddell Sea. *Deep-Sea Res.*, *27*, 367–381.

Foster, T. D. and Middleton, J. H. (1987). Mixing and bottom water formation in the shelf break region of the southern Weddell Sea. *Deep-Sea Res.*, *34*, 1771–1794.

Gawarkiewicz, G. (2000). Effects of ambient stratification and shelfbreak topography on offshore transport of dense water on continental shelves. *J. Geophys. Res.*, *105*(C2), 3307–3324.

Gawarkiewicz, G. and Chapman, D. C. (1995). A numerical study of dense water for-

mation and transport on a shallow, sloping continental shelf. *J. Geophys. Res.*, *100*(C3), 4489–4507.

Gill, A. E. (1973). Cirlculation and bottom water production in the Weddell Sea. *Deep-Sea Res.*, *20*, 111–140.

Gill, A. E. (1982). *Atmosphere-Ocean Dynamics*. Academic Press, New York. 662 pp.

Goosse, H., Campin, J.-M. and Tartinville, B. (2001). The sources of Antarctic bottom water in a global ice-ocean model. *Ocean Modelling*, *3*(1-2), 51–65.

Gordon, A. L. (1974). Varieties and variabilty of Antarctic bottom water. In *Processus de formation des eaux océaniques profondes*, No. 215 in Colleques Internationaux du C.N.R.S., pp. 33–45.

Gordon, A. L. and Tchernia, P. (1972). Waters of the continental margin off the Adélie Coast, Antarctica. In Hayes, D. E. (Ed.), *Antarct. Res. Ser.*, Vol. 19, pp. 59–69. American Geophysical Union.

Grumbine, R. W. (1991). A model of the formation of high salinity shelf water on polar continental shelves. *J Geophys Res Oceans*, *96*(C12), 22049–22062.

Häkkinen, S. (1995). Seasonal simulation of the Southern Ocean coupled ice-ocean system. *J. Geophys. Res.*, *100*(C11), 22733–22748.

Hellmer, H. H. and Beckmann, A. (2001). The Southern Ocean: A ventilation contributor with multiple sources. *Geophys. Res. Letters*, *28*(15), 2927–2930.

Jacobs, S. S. (1991). On the nature and significance of the Antarctic Slope Front. *Marine Chemistry*, *35*, 9–24.

Jiang, L. and Garwood, Jr, R. W. (1995). A numerical study of three-dimesional dense bottom plumes ona Southern Ocean continental slope. *J. Geophys. Res.*, *100*(C9), 18471–18488.

Jiang, L. and Garwood, Jr, R. W. (1998). Effects of topographic steering and ambient stratification on overflows on continental slopes: A model study. *J. Geophys. Res.*, *103*(C3), 5459–5476.

Jones, H. and Marshall, J. (1993). Convection with rotation in a neutral ocean: A study of open-ocean deep convection. *J. Phys. Oceanogr.*, *23*, 1009–1039.

Jones, H. and Marshall, J. (1997). Restratification after deep convection. *J. Phys. Oceanogr.*, *27*, 2276–2287.

Kikuchi, T., Wakatsuchi, M. and Ikeda, M. (1999). A numerical investigation of the transport process of dense shelf water from a continental shelf to a slope. *J. Geophys. Res.*, *104*(C1), 1197–1210.

Land-Serff, G. F. and Baines, P. G. (1998). Eddy formation by dense flows on slopes in a rotating fluid. *J. Fluid Mech.*, *363*, 229–252.

Lytle, V. I., Worby, A. P., Massom, R., Paget, M. J., Allison, I., Wu, X. and Roberts, A. (2001). Ice formation in the Mertz Glacier polynya, East Antarctica, during winter. *Ann. Glaciol.*, *33*, 368–372.

Marshall, J., Hill, C., Perelman, L. and Adcroft, A. (1997). Hydrostatic, quasi-hydrostatic and non-hydrostatic ocean modeling. *J. Geophys. Res.*, *102*(C2), 5733–5752.

Marsland, S. and Wolff, J.-O. (1998). East Antarctic seasonal sea-ice and ocean stability: a model study. *Ann. Glaciol.*, *27*, 477–482.

Massom, R. A., Harris, P. T., Michael, K. J. and Potter, M. J. (1998). The distribution and formative processes of latent-heat polynyas in East Antarctica. *Ann. Glaciol.*, *27*, 420–426.

Massom, R. A., Hill, K. L., Lytle, V. I., Worby, A. P., Paget, M. and Allison, I. (2001). Effects of regional fast-ice and iceberg distributions on the behavior of the Mertz Glacier Polynya, East Antarctica. *Ann. Glaciol.*, *33*, 391–398.

Mellor, G. and Yamada, T. (1982). Development of a Turbulence Closure Model for Geophysical Fluid Problems. *Rev. of Geophys. Space Phys.*, *20*, 851–875.

Mellor, G., Häkkinen, S., Ezer, T. and Patchen, R. (1999). A generalization of a sigma coordinate ocean model and an intercomparison of model vertical grids. In Pinardi, N. (Ed.), *Ocean Forecasting: Theory and Practice*. Springer-Verlag.

Middleton, J. H. and Foster, T. D. (1977). Tidal currents in the central Weddell Sea. *Deep-Sea Res.*, *24*, 1195–1202.

Middleton, J. H., Foster, T. D. and Foldvik, A. (1982). Low-frequency currents and continental shelf waves in the southern Weddell Sea. *J. Phys. Oceanogr.*, *12*, 618–634.

Middleton, J. H. and Humphries, S. E. (1989). Thermohaline sturcture and mixing in the region of Prydz Bay, Antarctica. *Deep-Sea Res.*, *36*(8), 1255–1266.

Molemaker, M. J. and Dijkstra, H. A. (2000). Stability of a cold core eddy in the presence of convection: Hydrostatic versus nonhydrostatic modeling. *J. Phys. Oceanogr.*, *30*, 475–494.

Narimousa, S. (1997). Dynamics of mesoscale vortices generated by turbulent convection at large aspect ratios. *J. Geophys. Res.*, *102*(C3), 5615–5624.

Nezlina, N. P. and McWilliams, J. C. (2003). Satellite data, empirical orthogonal functions, and the 1997–1998 El Niño off California. *Remote Sens Environ*, *84*(2), 234–254.

Nøst, O. A. and Foldvik, A. (1994). A model of ice shelf-ocean interactions with application to the Filchner-Ronne ice shelves. *J. Geophys. Res.*, *99*(C7), 14243–14254.

O'Connor, W. P. (1991). *A User's Manual for the Princeton Numerical Ocean Model.* Institute for Naval Oceanography.

Orsi, A. H., Johnson, G. C. and Bullister, J. L. (1999). Circulation, mixing, and production of Antarctic Bottom Water. *Progress in Oceanography*, *43*(1), 55–109.

Orsi, A. H., Jacobs, S. S., Gordon, A. L. and Visbeck, M. (2001). Cooling and ventilating the abyssal ocean. *Geophys. Res. Letters*, *28*(15), 2923–2926.

Palma, E. D. and Matano, R. P. (1998). On the implementation of passive open boundary conditions for a general circulation model: The barotropic mode. *J. Geophys. Res.*, *103*(C1), 1319–1341.

Palma, E. D. and Matano, R. P. (2000). On the implementation of passive open boundary conditions for a general circulation model: The three-dimensional case. *J. Geophys. Res.*, *105*(C4), 8605–8627.

Parish, T. R. and Wendler, G. (1991). The katabatic wind regime at Adelie Land, Antarctica. *Int J Climatol*, *11*, 97–107.

Parish, T. R. and Bromwich, D. H. (1987). The surface windfield over the Antarctic ice sheets. *Letters to Nature*, *328*, 51–54.

Pease, C. H. (1987). The size of wind-driven coastal polynyas. *J. Geophys. Res.*, *92*(C7), 7049–7059.

Pond, S. and Pickard, G. L. (1995). *Introductory Dynamical Oceanography*. Butterworth-Heinemann Ltd.

Potter, M. J. (1995). An evaluation of polynyas in East Antarctica. Honour's thesis, IASOS, Univ Tas.

Rintoul, S. R. (1998). On the origin and influence of Adélie Land bottom water. In Jacobs, S. S. and Weiss, R. F. (Eds.), *Ocean, Ice and Atmosphere: Interactions at the Antarctic Continental Margin*, Vol. 75 of *Antarct. Res. Ser.*, pp. 151–171. American Geophysical Union.

Roberts, A., Allison, I. and Lytle, V. I. (2001). Sensible and latent heat flux estimates over the Mertz Glacier Polynya from in-flight measurements. *Ann. Glaciol.*, *33*, 337–384.

Saunders, P. M. and Thompson, S. R. (1993). Transport, heat, and freshwater fluxes within a diagnostic numerical model (FRAM). *J. Phys. Oceanogr.*, *23*, 452–464.

Send, U. and Marshall, J. (1995). Integral effects of deep convection. *J. Phys. Oceanogr.*, *25*, 855–872.

Shapiro, G. I. and Hill, A. E. (1997). Dynamics of dense water cascades at the shelf edge. *J. Phys. Oceanogr.*, *27*, 2382–2394.

Smith, W. H. F. and Sandwell, D. (1997). Global seafloor topography from satellite alitimetry and ship depth soundings. *Science*, *277*, 1957–1962.

Spall, M. A. and Chapman, D. C. (1998). On the efficiency of baroclinic eddy transport across narrow fronts. *J. Phys. Oceanogr.*, *28*, 2275–2287.

Spall, M. A. and Pickart, R. S. (2003). Wind-driven recirculations and exchange in the Labrador and Irminger Seas. *J. Phys. Oceanogr.*, *33*(8), 1829–1845.

Speer, K. G. and Forbes, A. (1994). A deep western boundary current in the South Indian basin. *Deep-Sea Res.*, *41*(9), 1289–1303.

Stevens, D. P. and Killworth, P. D. (1992). The distrubution of kinetic energy in the Southern Ocean: a comparison between observations and an eddy resolving general circulation model. *Philosophical Transactions of the Royal of Society London B*, *338*, 251–257.

Stevens, I. G. and Stevens, D. P. (1999). Passive tracers in a general circulation model of the Southern Ocean. *Annales Geophsicae*, *17*, 971–982.

Stössel, A. and Kim, S.-J. (1998). The impact of southern ocean ice in a global ocean model. *J. Phys. Oceanogr.*, *28*(10), 1999–2018.

The FRAM Group (1991). An eddy-resolving model of the Southern Ocean. *Eos Trans*, *22*(15), 169, 174–175.

Toggweiller, J. R. and Samuels, B. (1995). Effect of sea ice on the salinity of Antarctic Bottom Waters. *J. Phys. Oceanogr.*, *25*, 1980–1997.

Visbeck, M., Marshall, J. and Jones, H. (1996). Dynamics of isolated convective regions in the ocean. *J. Phys. Oceanogr.*, *26*, 1721–1734.

Wendler, G., Stearns, C., Weidner, G., Darguad, G. and Parish, T. (1997). On the extraordinary katabatic winds of Adelie Land. *J. Geophys. Res.*, *102*(D4), 4463–4474.

Whitworth, III, T. (2002). Two modes of bottom water in the Australian-Antarctic basin. *Geophys. Res. Letters*, *29*(5).

Whitworth, III, T., Orsi, A. H., Kim, S.-J. and Nowlin, Jr, W. D. (1998). Water masses and mixing near the Antarctic slope front. In *Ocean, Ice, and Atmosphere: Interactions at the Antarctic Continental Margin*, Vol. 75 of *Antarct. Res. Ser.*, pp. 1–27. AGU, Washington.

Wong, A. P. S., Bindoff, N. L. and Forbes, A. (1998). Ocean-ice shelf interaction and possible bottom water formation in Prydz Bay, Antarctic. In Jacobs, S. S. and Weiss, R. F. (Eds.), *Ocean, Ice, and Atmosphere: Interactions at the Antarctic Continental Margin*, Vol. 75 of *Antarct. Res. Ser.*, pp. 173–187. AGU, Washington.

Worby, A. P., Bindoff, N. L., Lytle, V. I., Allison, I. and Massom, R. A. (1996). Winter ocean / sea ice interactions studied in the East Antarctic. *Eos Trans*, *77?*, 453, 456–457.

Worby, A. P., Massom, R. A., Allison, I., Lytle, V. and Heil, P. (1998). East Antarctic sea ice: A review of its structure, properties and drift. In Jefferies, M. O. (Ed.), *Antarctic Sea Ice: Physical Processes, Interactions and Variability*, Vol. 74 of *Antarct. Res. Ser.*, pp. 41–67. AGU, Washington.

Young, N. W. (1998). Antarctic iceberg drift and ocean currents derived from scatterometer image series. In *Proceedings in a Joint EDA-Eumetsat Workshop on*

Emerging Scatterometer Applications - From Research to Operations, ESA SP-424, pp. 125–132 Noordwijk, The Netherlands. ESTEC.

Zwally, H. J., Comiso, J. C. and Gordon, A. L. (1985). Antarctic offshore leads and polynyas and oceanographic effects. In Jacobs, S. (Ed.), *Oceanology of the Antarctic Shelf*, Vol. 43 of *Antarct. Res. Ser.*, pp. 203–226. AGU, Washington.